

UNIVERSITÀ DEGLI STUDI DI TRIESTE

XVIII CICLO DEL
DOTTORATO DI RICERCA IN FISICA

MULTIWAVELENGTH APPROACH TO THE JOINT FORMATION AND EVOLUTION OF GALAXIES AND AGNS

Settore scientifico-disciplinare
FIS/05 ASTRONOMIA E ASTROFISICA

DOTTORANDO:
FABIO FONTANOT

COORDINATORE DEL COLLEGIO DEI DOCENTI:
PROF. GAETANO SENATORE
Dipartimento di Fisica Teorica Università di Trieste

TUTORE:
DOTT. PIERLUIGI MONACO
Dipartimento di Astronomia Università di Trieste

CORRELATORE:
PROF. STEFANO CRISTIANI
INAF - Osservatorio Astronomico di Trieste

Contents

| | | |
|----------|---|-----------|
| 0 | Overview | 1 |
| 1 | Galaxies and Galactic Properties | 7 |
| 1.1 | Galaxies | 7 |
| 1.1.1 | Milky Way | 7 |
| 1.1.2 | Morphological Classification of Galaxies | 8 |
| 1.1.3 | Large Scale Structure | 9 |
| 1.2 | Observations | 10 |
| 1.2.1 | Multiwavelength Observations of Galaxies | 10 |
| 1.2.2 | Stellar Population properties | 14 |
| 1.2.3 | Statistical properties | 17 |
| 1.2.4 | Structural relations | 22 |
| 1.3 | Cosmological Context | 24 |
| 1.3.1 | Basic Equations | 25 |
| 1.3.2 | The Standard Cosmological model | 28 |
| 1.3.3 | Growth of structures in the Universe | 30 |
| 1.3.4 | Merger Trees | 35 |
| 1.4 | Physical processes in galaxy formation | 37 |
| 1.4.1 | Thermal Processes | 37 |
| 1.4.2 | Gravitational Processes | 43 |
| 1.5 | Models of galaxy formation and evolution | 48 |
| 1.5.1 | Semi-analytical models | 49 |
| 2 | Active Galactic Nuclei and Quasars | 61 |
| 2.1 | Unified Model for AGNs | 63 |
| 2.2 | Multiwavelength AGN observations | 65 |
| 2.2.1 | Building up a QSO template spectra library | 67 |
| 2.3 | AGN–Galaxy connection | 68 |
| 2.4 | Redshift evolution of AGNs | 70 |
| 3 | High Redshift QSOs in the GOODS | 73 |
| 3.1 | The Database | 74 |
| 3.1.1 | Bright QSOs from the SDSS | 74 |
| 3.1.2 | Faint QSOs from the GOODS | 75 |
| 3.2 | Computing the Luminosity Function of high- z QSOs | 81 |
| 3.2.1 | QSO template library | 82 |
| 3.2.2 | QSOs color prediction | 82 |

| | | |
|----------|---|-----------|
| 3.2.3 | Completeness against selection criteria | 83 |
| 3.2.4 | Simulated catalogues | 84 |
| 3.2.5 | Computing the QSO LF | 86 |
| 3.3 | Conclusions on the QSO LF | 89 |
| 4 | GALRISE Model for the Joint Evolution of Galaxies and AGNs | 95 |
| 4.1 | Outline of the model | 95 |
| 4.1.1 | DM halos and galaxies | 95 |
| 4.1.2 | Baryons | 96 |
| 4.1.3 | Algorithm | 97 |
| 4.1.4 | Mass flows | 99 |
| 4.1.5 | Energy flows | 100 |
| 4.1.6 | Metal flows | 102 |
| 4.1.7 | Other variables | 102 |
| 4.1.8 | External flows | 103 |
| 4.1.9 | Initial conditions | 103 |
| 4.1.10 | Cosmology and units | 104 |
| 4.2 | DM halos | 104 |
| 4.2.1 | DM merger trees | 104 |
| 4.2.2 | DM halo properties | 106 |
| 4.3 | Galaxy mergers, destruction and stripping | 107 |
| 4.3.1 | Dynamical friction on satellites | 107 |
| 4.3.2 | Galaxy merger trees | 109 |
| 4.3.3 | Galaxy mergers | 109 |
| 4.4 | Halo gas | 110 |
| 4.4.1 | Equilibrium model for the hot phase | 110 |
| 4.4.2 | Shock heating | 112 |
| 4.4.3 | Cooling | 113 |
| 4.4.4 | Infall | 115 |
| 4.4.5 | Galaxy super-winds and cosmological fall-back | 117 |
| 4.5 | Bulge and Disc structure | 118 |
| 4.5.1 | Discs | 118 |
| 4.5.2 | Bulges | 120 |
| 4.6 | Feedback | 122 |
| 4.6.1 | Kinetic feedback and the velocity dispersion of cold clouds | 124 |
| 4.6.2 | Thin systems | 125 |
| 4.6.3 | Thick systems | 128 |
| 4.7 | Metals | 130 |
| 4.8 | AGN activity | 131 |
| 4.8.1 | Accretion onto black holes | 131 |
| 4.8.2 | Feedback from jets | 132 |
| 4.8.3 | Quasar winds | 133 |
| 4.9 | Parameters | 133 |
| 4.10 | Post Processing | 134 |
| 4.11 | Results | 135 |
| 4.12 | Conclusions | 143 |

| | | |
|----------|--|------------|
| 5 | Feedback from Quasars in Star-forming Galaxies and the triggering of Massive Galactic Winds | 149 |
| 5.1 | The model for feedback | 152 |
| 5.2 | Feedback from the quasar | 156 |
| 5.2.1 | The effect of radiative heating | 156 |
| 5.2.2 | Radiation pressure on the expanding super-shell | 159 |
| 5.2.3 | Feedback from AGN in presence of other stellar feedback regimes | 163 |
| 5.3 | Shining quasars in the hierarchical context | 163 |
| 5.3.1 | Low-angular momentum gas and the triggering of the wind | 164 |
| 5.3.2 | An example | 166 |
| 5.4 | Conclusions on QSO Feedback | 169 |
| 6 | The Effect of Stellar Feedback and Quasar Winds on the AGN Population | 173 |
| 6.1 | Modeling AGNs in GALRISE | 174 |
| 6.1.1 | Accretion onto BHs | 174 |
| 6.1.2 | Quasar-triggered winds | 174 |
| 6.1.3 | Computing LFs and X-ray background | 176 |
| 6.2 | Results | 178 |
| 6.2.1 | X-ray number counts and background | 186 |
| 6.2.2 | Predictions | 188 |
| 6.3 | Conclusions on the Effect of Stellar Feedback and Quasar Winds on the AGN Population | 189 |
| 7 | The assembly of massive galaxies in the hierarchical cosmogony. | 193 |
| 7.1 | Spectrophotometric Codes | 194 |
| 7.1.1 | Computing Galactic Spectra | 195 |
| 7.1.2 | Dust | 197 |
| 7.1.3 | Bruzual & Charlot (2003) | 198 |
| 7.1.4 | GRASIL | 199 |
| 7.2 | From physical to astronomical quantities | 200 |
| 7.2.1 | Interfacing the Spectrophotometric code with GALRISE | 200 |
| 7.2.2 | Luminosity functions, number counts and redshift distributions | 202 |
| 7.3 | Results | 204 |
| 7.3.1 | <i>K</i> -band LF | 204 |
| 7.3.2 | 850 μ m counts | 207 |
| 7.4 | Conclusions on the Assembly of Massive Galaxies | 208 |
| 8 | Conclusions | 211 |

List of Tables

| | | |
|-----|---|-----|
| 1.1 | Comparison between different models of Galaxy formation and evolution | 60 |
| 3.1 | Parameters for the new field definition in the GOODS | 75 |
| 3.2 | QSO candidates. | 91 |
| 3.3 | Additional QSO candidates | 92 |
| 3.4 | Best fit parameters of the Luminosity Function | 93 |
| 4.1 | Mass and energy flows | 98 |
| 4.2 | GALRISE Parameters | 147 |

List of Figures

| | | |
|------|---|-----|
| 1.1 | Hubble's Morphological Classification of Galaxies | 8 |
| 1.2 | Johnson photometric system | 11 |
| 1.3 | SDSS photometric system | 12 |
| 1.4 | GOODS photometric system | 12 |
| 1.5 | Color-Magnitude Diagram in the SDSS sample | 15 |
| 1.6 | Observed Color Bimodality in the SDSS sample | 16 |
| 1.7 | Comparison between optical and infrared luminosity functions | 20 |
| 1.8 | Constraints on cosmological parameters | 30 |
| 1.9 | Example of Dark Matter merger tree | 36 |
| 1.10 | Cooling Functions | 39 |
| | | |
| 2.1 | Examples of AGN spectra | 62 |
| 2.2 | Unified model for AGNs | 64 |
| 2.3 | Composite spectrum of Type I QSO | 66 |
| 2.4 | Template library spectra | 68 |
| 2.5 | Observative M_{bul} vs M_{BH} relation | 69 |
| 2.6 | Downsizing in X-ray bands | 71 |
| | | |
| 3.1 | Candidates Spectra | 78 |
| 3.2 | $V_{660} - i_{775}$ versus $i_{775} - z_{850}$ color in HDF-N and CDF-S | 80 |
| 3.3 | Distribution of real objects in the Redshift versus M_i space | 81 |
| 3.4 | Comparison between different estimates of IGM absorption | 83 |
| 3.5 | Color diagrams for the confirmed QSOs in DR3QSO | 84 |
| 3.6 | Evolution of QSO colors with redshift | 85 |
| 3.7 | Completeness of QSO selection criteria | 86 |
| 3.8 | Analytical fits to the high- z QSO LF | 88 |
| | | |
| 4.1 | General scheme of mass flows in a model galaxy | 99 |
| 4.2 | Example of ordering of the PINOCCHIO merger trees | 105 |
| 4.3 | Mass flows for the one-phase version | 122 |
| 4.4 | Feedback regimes | 123 |
| 4.5 | DM halos at $z = 0$ | 135 |
| 4.6 | Star mass function of galaxies at $z = 0$ | 136 |
| 4.7 | Cosmic star formation history | 137 |
| 4.8 | Star mass density as a function of redshift | 138 |
| 4.9 | Mass function of cold gas and evolution of the cold gas density | 139 |
| 4.10 | Mass versus surface density | 140 |
| 4.11 | Schmidt-Kennicutt law for the model disc component | 141 |

| | | |
|------|--|-----|
| 4.12 | Baryonic Tully-Fisher relation | 142 |
| 4.13 | Structure of elliptical galaxies | 143 |
| 4.14 | Metal content | 144 |
| 5.1 | Evolution of a toy spheroid with the feedback model of Monaco (2004a) | 155 |
| 5.2 | Evolution of a toy spheroid in case of runaway radiative heating | 157 |
| 5.3 | Evolution of the main progenitor of an elliptical galaxy | 165 |
| 5.4 | Star formation rates | 167 |
| 5.5 | Bulge and Black Hole masses as a function of k_{resv} | 168 |
| 6.1 | 2-10 keV X-ray Luminosity Function | 179 |
| 6.2 | 0.5-2 keV X-ray Luminosity Function | 180 |
| 6.3 | B-band Luminosity Functions | 181 |
| 6.4 | The evolution of QSOs number density with redshift | 182 |
| 6.5 | $M_{\text{bulg}} - M_{\text{BH}}$ relation | 183 |
| 6.6 | The BH mass function | 184 |
| 6.7 | The evolution of QSOs number density as a function of σ_0 | 185 |
| 6.8 | Source Number Counts in x-ray bands | 186 |
| 6.9 | X-ray background | 187 |
| 6.10 | Evolution of the BH-bulge relation | 188 |
| 6.11 | Average accretion rates | 189 |
| 7.1 | Local K -band Luminosity Function | 195 |
| 7.2 | Fraction of stars in the central galaxy or in the halo | 196 |
| 7.3 | K -band Source Number Counts | 201 |
| 7.4 | Redshift source distribution | 203 |
| 7.5 | LF Redshift Evolution | 205 |
| 7.6 | 850μ Source Number Counts | 206 |
| 7.7 | Predicted Redshift Distribution for 850μ sources | 207 |
| 7.8 | SFR function at $z = 2.5$ | 208 |

Chapter 0

Overview

Nowadays stellar astrophysics has reached a high level of maturity. Many stellar processes are well understood and a standard model for stellar evolution exists. This progress has led to the development of stellar evolution models which are able to reproduce the main observational properties of stellar populations in great detail (i.e. synthetic color-magnitude diagrams of globular or open clusters). There are some aspects escaping a full understanding, mainly related to the problem of convection in stellar interiors, to the modeling of late evolutionary stages of intermediate mass stars (i.e. the problem of dredge-ups in Asymptotic Giant Branch Stars) and to the need for a refined model for stellar atmospheres, but we can reasonably assume that we are able to follow the main path of stellar evolution in a quantitative way for a wide range of stellar masses and metallicities.

On the contrary, *galactic astrophysics* is an open, expanding field. There are many differences between the study of stars and galaxies. Stars can be considered as isolated systems: stellar interactions in galaxies are negligible (with the remarkable exception of multiple systems, but these can be also considered isolated systems with respect to the other stellar systems). Stars can be considered “simple” systems: hydrostatic equilibrium, local thermodynamical equilibrium and spherical symmetry hold. None of the previous hypothesis holds in galactic astrophysics: galaxies are non-isolated systems, their interactions with the environment have a considerable importance; galaxies are “complex” systems, their properties being the result of the interplay of many physical processes (gravitational, dynamical, thermal, stellar, nuclear). The complexity of the problem is increased by the scalelength range required to describe such processes, from the Mpc scale of cosmological evolution to the Km scale of supernovae explosions. Galaxy formation and evolution is correlated to the large scale structure of the Universe, which is determined by the matter fluctuations imprinted at the epoch of inflation and still visible as temperature anisotropies of the Cosmic Microwave Background (CMB). The combined study of distant supernovae and of the CMB leads to the evidence that we live in a Universe dominated by cosmological constant and by dark matter ($\Omega_\Lambda = 70\%$, $\Omega_{DM} = 26\%$, $\Omega_b = 4\%$). The evolution of large scale structure determines the formation of virialized density peaks,

Dark Matter Halos, which assemble hierarchically: small, low-mass halos are thought to form first, then merge to form larger halos. The most massive halos form at recent times. This framework has a deep impact on galaxy studies, due to the fact that galaxies form inside dark matter halos, where the density is high enough to trigger the chain of physical processes acting on the baryonic gas. Galaxies are not static objects, but suffer a continuous evolution. These processes can be both due to the properties of the object itself, or due to the interactions of the galaxy with the surrounding environment. Physical processes acting on baryons are more complex than those felt by dark matter, which is subject only to gravitational interactions: it is not obvious that galaxies should obey the dark matter bottom-up assembly process. Moreover galaxies are not homogeneous systems, but they show at least two main components, a central spheroidal region and a disc-like structure; the different physical conditions of these components need different physical models in order to reproduce the observed galactic properties. Evidence has also grown that non-stellar processes giving rise to the *Active Galactic Nucleus* (AGN) phenomenology have also a great impact on the evolution of the galaxy as a whole. Only in recent years the physical description of these processes and of their impact on galaxy evolution has started to provide valuable insight.

In recent years we have witnessed a relevant increase of the available observational data. Most interestingly we are now able to observe the properties of extra-galactic samples in different electromagnetic bands. This *multiwavelength approach* has gained increasing importance owing to the fact that different wavebands trace different emission mechanisms and then different components (old and young stars, gas, dust, AGN). Multiwavelength surveys are often used to select galaxy and AGN populations on the basis of their relative emission at different wavebands. It is clear that in order to fully understand the overall formation and evolution of galaxies and AGN we need to devise models that reproduce all this spectrophotometric information at the same time. This is not a simple task due to the fact that observational strategies change considerably among different wavebands. Presently, a great deal of information about galaxy formation is now available due to the development of dedicated multiwavelength surveys such as the *Great Observatories Origins Deep Survey* (GOODS), which are designed to observe the same region of the sky with different instruments that are operative at different wavelengths. The selection of complete AGN and galaxy samples and the determination of their space densities is of fundamental importance to follow the joint evolution of the galaxies and the supermassive black holes hosted at their centers. High-redshift ($z > 3.5$) observations are even more useful, because they sample these objects at early times. For instance the study of the faint AGN population at high-redshift gives robust constraints both for models of AGN and galaxy formation and for the QSO contribution to the ultra-violet background. Despite its importance the properties of the high-redshift faint AGN population are almost unconstrained due to the challenging magnitude limits.

There are aspects of galaxy formation and evolution that are not fully

understood, but we are approaching a realistic description. A first aspect is related to the uncertainties in the physical description of the relevant physical processes involved in the formation and evolution of galaxies, such as cooling, star formation, feedback and the presence of AGN. We have only a partial understanding and can deal with them only approximately. Early work in this field assumed simple descriptions of these processes, most of the times based on rough parameterizations. An increasing attention has been devoted in recent years in order to provide reliable descriptions of these processes taking into full account the thermodynamical properties of gas. A key role in this research field is played by N -body simulation coupled with hydrodynamical equation solvers (like SPH or AMR simulations). They provide at the same time the solution for both the motion of particles under self-gravity and the thermodynamical state of the gas. On the other hand analytic work has provided prescriptions for physical processes relevant on galactic scale. These numerical and analytical works allow a more stringent constraining of the physical processes involved.

A second aspect of the problem of galaxy formation and evolution is related to the complex interplay and relative importance of these different processes. To face this aspect it is necessary to compare models with large samples of galaxies. This is a very difficult task for N -body hydro simulations, owing to the fact that present day computational power does not allow the analysis of large cosmological volumes up to the scales relevant for galaxy formation and evolution. It is possible to overcome this limit by selecting single dark matter halos from the output of a large volume and “re-simulate” them with higher resolution. However the number of objects that can be studied with this technique is also limited by the computational time required to re-simulate them.

In order to gain better insight on both problematic aspects (the description of the physical processes involved and their interplay), in the last decades a new approach to the problem of galaxy formation and evolution has been proposed by several groups. The *Semi-Analytic Models* of galaxy formation and evolution have been proven to be a very useful tool. They allow to follow the assembly history of galaxies taking into account with analytic recipes and parameterizations all major physical processes involved. Their analytic formulation allows the user to study large cosmological volumes with the desired resolution, so as to compare model galaxies with large surveys. Semi-analytic codes are much faster than SPH simulations: this is a very important feature because it allows the user to run multiple realizations, with different physical recipes and assumptions, in a moderate amount of time. Semi-analytical models are able to fit a large number of local galactic properties such as luminosity functions, source number counts, the Tully-Fisher relation, the relationship between the mass of galactic spheroidal components and the mass of the hosted super-massive black holes, the galaxy two-point correlation function, the ratio between galactic morphological types, galactic disc sizes, gas fractions in discs as a function of B -band luminosity. However, despite those relevant success, some backdraws hold. Many specific models have been unsuccessful in reproducing constraints like the level of α -enhancement in

elliptical galaxies, the bimodality of galaxy colors, the redshift distribution of K-band sources, the surface density of EROs, the sub-mm counts. One of the most long-standing problems regards the formation of the massive elliptical galaxies; hierarchical models tend to predict that these galaxies form late by the merging of already assembled discs, which is at variance with the evidence from stellar populations; in particular, the tightness of the fundamental plane, the evolution of the color-magnitude relation and the local $Mg_2 - \sigma$ relation suggest that ellipticals formed early, while the level of α -enhancement with respect to iron suggests that they formed quickly, in a short burst of star formation. Moreover, these pieces of evidence all converge in indicating that the most massive ellipticals are the oldest and most α -enhanced ones. Besides, recent studies on the AGN luminosity function highlight the fact that the number density of more luminous AGNs peaks at earlier epochs with respect to the number density of their low luminosity counterparts. Owing to the fact that more luminous AGNs are thought to be connected with more massive black hole, this observational result can be seen as another evidence of the fact that more massive objects assemble earlier than low mass objects, at variance with the dark matter evolution. This behavior has been named *downsizing*.

Difficulties of Λ CDM models in reproducing the evidence of downsizing can be ascribed either to an intrinsic inability of hierarchical models to describe the physical processes leading to the assembly of the observed galaxy populations, or to the simplistic modeling of the physical processes involved. In this work we present a new model for galaxy formation and evolution. This model improves with respect to previous semi-analytical models in several aspects. Each model galaxy is subdivided into three components (halo, bulge and disc) and in each one the gas is modeled as a two-phase medium. The evolution of each component is followed taking into account the evolution of the thermal and kinetic energies of both the hot and the cold gas. Gas and stars are allowed to flow from one component to another as the result of physical processes, such as gas cooling, disc instabilities and merger events. Besides, discs and spheroids are considered as different environments and physical processes such as star formation and feedback are modeled with different recipes. Our model also takes into account self-consistently the presence of a supermassive black hole at the galactic center. This central black hole is supposed to shine as an AGN each time it accretes matter and to release an amount of energy into the ISM. We model this heating in terms of a QSO feedback. We conclude that radiative heating from the central AGN is able to influence the stellar feedback regime in the host galaxy. Besides, we take advantage of an improved modeling for the formation of gas reservoirs and for the matter accretion onto supermassive black holes. This allows us to follow with great detail the joint mass assembly of galaxies and central supermassive black holes.

We show that this model is able to correctly predict observed quantities (such as local luminosity functions, local baryonic mass function, cosmic star formation history), which are already assessed by previous semi-analytic models, but also is able to reproduce *at the same time* the downsized evolution of the AGN luminosity function, and the early assembly history of massive

galaxies (reproducing both the near-infrared distribution of sources and sub-millimetric observations), assuming simple reasonable recipes based on local observations for the Initial Mass Function.

This work is organized as follows.

- In chapter 1 and 2 we will briefly discuss multiwavelength observational properties of galaxies and AGNs. We will also discuss the standard cosmological Λ CDM model, the physical mechanisms involved in galaxy formation and evolution, and we will give a review of semi-analytical models present in literature.
- In chapter 3 we will present our observational results relative to the computation of the AGN luminosity function at $3.5 < z < 5.2$. We will present our selection of quasar candidates in the GOODS fields, based on optical and x-ray observations. We will also present our algorithm for the computation of the luminosity function starting from a combined sample of GOODS and SDSS observations. Our results provide reliable constraints on the faint end of the luminosity function, which are useful for understanding the process of BH assembly. *The results presented in this chapter will be submitted for publication in Fontanot, Cristiani, Monaco, et al. (2006)*
- Chapter 4 is devoted to the presentation of our model for the joint evolution of galaxies and AGNs, GALRISE. In this chapter we will describe in full detail our prescription for the various physical processes involved, with particular emphasis on cooling, infall and feedback. Besides we will present in the same chapter the model predictions on the galaxy stellar mass function, cosmic star formation rate, stellar mass density, structural properties of galaxies and compare them with observations. *The results presented in this chapter will be submitted for publication in Monaco, Fontanot & Taffoni (2006)*
- In chapter 5 we will focus our attention on the role of AGN feedback as a trigger of massive galactic winds. This topic has been developed in the framework of stellar feedback model of Monaco (2004ab): as an independent result we show that AGN feedback is able to change the physical conditions for stellar feedback in galactic spheroidal components and we discuss the physical conditions for the triggering of a galactic wind. *The results presented in this chapter have been published in Monaco & Fontanot (2005).*
- In chapter 6 we will analyse the properties of the predicted AGN population, with particular emphasis on the redshift evolution of the luminosity function in the optical and x-ray bands. The most relevant result is the correct prediction of the downsizing behavior of the AGN

population. We stress that kinetic feedback in bulges is the key mechanism to reproduce such a behavior. *The results presented in this chapter will be submitted for publication in Fontanot, Monaco et al. (2006a).*

- Finally, in chapter 7 we will present the near-infrared and sub-millimetric properties of our model galaxies. We will show that GALRISE is able to reproduce at the same time the redshift distribution of K -selected galaxies, the redshift evolution of K -band luminosity function and the sub-mm number counts. Combining this pieces of information we can conclude that GALRISE is able to correctly reproduce the early assembly of massive galaxies. *The results presented in this chapter will be submitted for publication in Fontanot, Monaco et al. (2006b).*

Chapter 1

Galaxies and Galactic Properties

1.1 Galaxies

We will start this work analyzing our own stellar system, then we will move to consider the external galaxies.

1.1.1 Milky Way

The word "galaxy" comes from the Greek term "galactos", which means "made of milk" and it refers to the mythological origin of our stellar system. In order to understand the structure of the Milky Way we can use the classical approach, i.e. counting the stars in various directions of the sky. This way various authors in the past come to the conclusion that our galaxy is a flat system with a spheroidal structure at the center. Our star, the Sun, is located $8.5Kpc$ away the center of the galaxy.

More quantitatively we nowadays divide the Milky Way into four structures, by mean of differences in geometry, kinematics and stellar populations.

First of all we have a *Thin Disc* made by stars, gas and dust. It extends $\sim 20Kpc$ in radius with a width of about $200pc$. It contains almost all the gas present in the galaxy (10% in mass). The stars in the disc belong to population I, which means that they are young, blue, metallic¹ stars. In the disc we find also open clusters: young, gravitationally weakly bound stellar aggregates. The kinematics of the disc is quite simple: gas and stars rotate around the center of the galaxy. The rotation is differential: it means that the angular velocity of rotation depends on the distance from the center. We have also random motions superimposed to the differential rotation, but they are about an order of magnitude lower than the ordered motions.

At the center of the galaxy we find a spheroidal structure called *Bulge*. It has a radius of about $3Kpc$. It consists mainly by old, metal enriched, red

¹In this thesis we consider as "metals" all chemical elements heavier than Helium

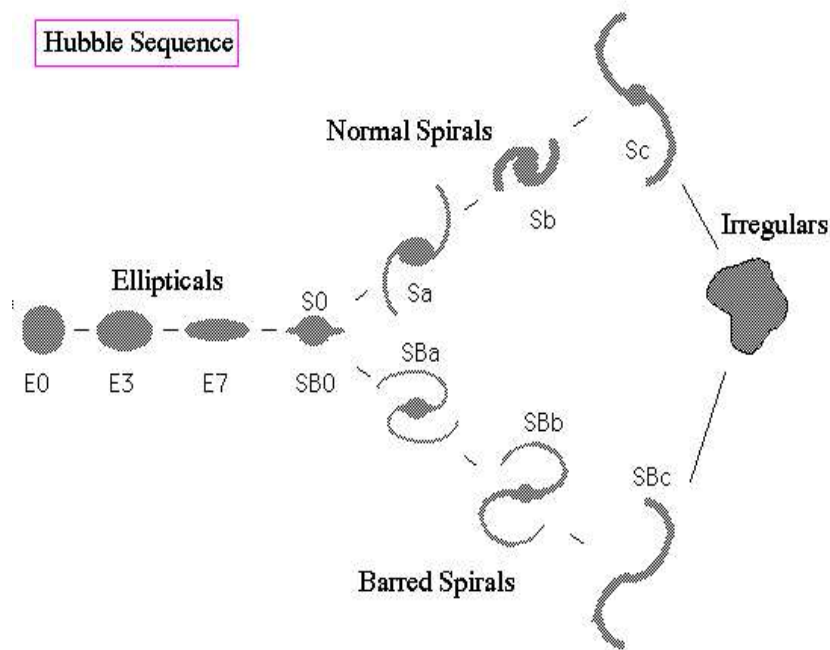


Figure 1.1: Hubble's Morphological Classification of Galaxies (Image taken from <http://abyss.uoregon.edu/~js/ast123/lectures/lec11.html>)

stars. The kinematic of the bulge is dominated by random chaotic motions with a rotational component.

The *Halo* of the Milky Way is a spheroidal structure with a radius of about $30Kpc$. It consists of isolated stars and globular clusters (old, gravitationally stable stellar aggregates). Its gas and dust content is very low. The halo stars are old and metal poor population II stars. Their kinematics are dominated by random motions.

We can also identify an additional disk-like component of the galaxy: the *Thick Disc*. Its properties are intermediate between the halo and the thin disc. Stars rotate with kinematics similar to thin disc stars but they have also relevant random motions. The properties of stellar population are also intermediate between population I and II.

1.1.2 Morphological Classification of Galaxies

The most diffuse classification of external galaxies was proposed by Edwin Hubble (fig. 1.1). It is also known as the *Hubble Sequence* and it relies on visual analysis of the morphology of objects. Galaxies are divided mainly into two groups: *Early Type* or *Elliptical* Galaxies and *Late Type* or *Spiral* Galaxies.

Elliptical Galaxies appear as structureless ellipsoids. They have various ellipticities and are classified on the basis of the ratio between the major and minor semiaxes of their sky projection. These galaxies are characterized by an

old stellar population (mainly metallic stars with an age of about 10^{10} years). They have a little amount of interstellar gas and nearly no sign of ongoing star formation.

Spiral galaxies are stellar system very similar to the Milky Way. They show the same structures of our galaxy (disc, bulge, halo). Spiral bulges show analogies with elliptical galaxies both in terms of stellar populations and gas content. Discs consist of a mixture of young and old stars, with a relevant amount of interstellar gas and dust. Young blue stars and *HII* regions (regions where hot, blue stars are pouring large amounts of ultraviolet radiation into the surrounding cloud from which they were recently formed keeping it ionized), corresponding to regions of ongoing star formation, trace the typical spiral pattern. Observed spirals show a wide range of spiral patterns, and this leads to a sub-classification of spirals. *Sa* and *Sb* Spirals have prominent bulges and wounded spiral arms, on the contrary *Sc* and *Sd* Spirals have small bulges and loosely wound spiral arms. About 50% of spirals show an elongated structure that crosses the bulge and from which spiral arms begin, called *Bar*.

There are also some other kinds of galaxies in the Hubble sequence.

Lenticular galaxies have intermediate properties between Ellipticals and Spirals. They have always a relevant bulge with respect to a small disc without a spiral pattern.

Irregular galaxies have no clear structure and show traces of a young stellar population due to a recent event of star formation.

The previous classification refers to bright objects. However there are also galaxies with small dimensions and low luminosity. We usually refer to these objects as *Dwarf* galaxies. These galaxies are difficult to detect because of their low surface brightness but they may result as the dominant in number galactic population. They are classified in a sequence with respect to their bright counterparts, but this classification is still controversial. In particular it is still unclear how to divide dwarf galaxies from luminous galaxies and it is still under debate if the properties of dwarfs correspond to the properties of the corresponding bright galaxies.

1.1.3 Large Scale Structure

Galaxies do not fill homogeneously the sky. On the contrary they show a tendency to aggregate into complex structures. The spatial distribution of such structure forms the so called *Large Scale Structure of the Universe*.

Galaxies are rarely isolated objects. The majority a such objects are found in gravitationally bound systems. These systems are classified according to the number of members. Typically *Groups* contain from 3 up to 100 galaxies. On the other end, *Clusters* consist of a larger number of galaxy members. Clusters are classified on the basis of their richness in galaxies. Rich clusters can have thousands of members. Galaxies and clusters are often connected to form larger non-virialized structures called *Superclusters*. Superclusters tend to have no regular geometry, often they are flat structures. These structures are connected trough filaments made by galaxies to form a web, which surrounds large areas

where only few galaxies can be found. These regions are called voids. The overall configuration with underdense regions surrounded by overdense nearly two-dimensional structures can be well represented with the image of a sponge.

The distribution of Hubble types in the Universe is not uniform. Elliptical galaxies are more numerous in dense environments (as clusters), while spirals are more numerous in the field. As an example in typical clusters we find $\sim 40\%$ ellipticals, $\sim 40\%$ lenticulars and only $\sim 20\%$ of spirals, while in the field $\sim 10\%$ ellipticals, $\sim 70\%$ lenticulars and $\sim 70\%$ of spirals².

We will show in the next sections how the formation of structures in our Universe can be explained in a cosmological context.

1.2 Observations

In this section we describe the most relevant observational properties of galaxies. We will focus our attention on the pieces of information, we can infer from multiwavelength observation of their Spectral Energy Distribution (hereafter SED). In this section we do not treat the AGN contribution to the galactic emission: this will be the subject of section 2.2.

1.2.1 Multiwavelength Observations of Galaxies

UV – Optical

The optical window goes from 3000 \AA up to 7000 \AA . At higher energies we enter the Ultraviolet (UV) region, subdivided into soft-UV ($912 \text{ \AA} < \lambda < 3000 \text{ \AA}$) and extreme-UV (EUV: $100 \text{ \AA} < \lambda < 912 \text{ \AA}$). The 912 \AA wavelength corresponds to the Lyman discontinuity, i.e. to the ionization energy for an hydrogen atom ($E=13.6 \text{ KeV}$).

The wavelength range of maximum stellar emission falls into the optical window. Optical observations trace the stellar populations of galaxies and are based on photometric systems: an example of photometric system is given in fig. 1.2, which shows the *Johnson photometric system*. Each wavelength interval is called *band*. Optical bands are defined in terms of sensitivity of the instrument at a given wavelength: it is possible to change the range of sensitivity of the instrument by changing the interposed *filter*, in order to sample different regions of the optical spectrum. Multi-band photometry is a key tool in astronomy, due to the fact that different spectral regions sample different galactic properties. The luminosity of a source in an optical band it is expressed in terms of magnitudes. The difference between the magnitude in two bands is called *color* and represents an estimate of the ratio between the fluxes in the two wavelength regions. The study of galactic colors provides fundamental information about the underlying stellar populations. Early type galaxies show red colors, because their spectra are dominated by old red stars, while late type galaxies have blue colors because they are dominated by young blue stars.

²Percentages are computed on bright galaxies with $L > L_*$

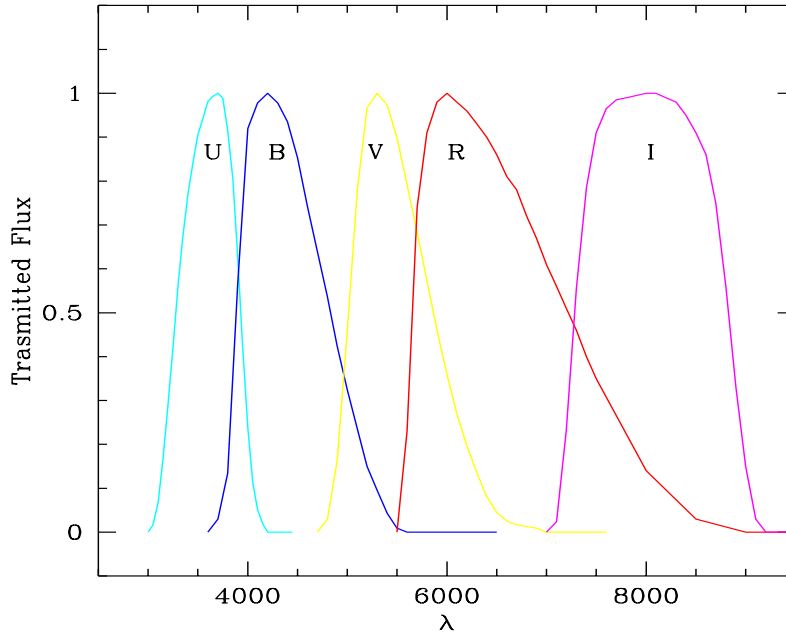


Figure 1.2: Johnson photometric system

In recent years it became possible to design photometric systems optimized to study galaxy spectra. Among the various photometric systems present in literature we want to introduce these that we will use in this work: the SDSS photometric system (Fukugita et al. 1996, fig. 1.3) and HST/ACS photometric system (Williams et al. 1996, fig. 1.4).

At higher energies and lower wavelengths we enter the UV region. The importance of soft-UV spectroscopy for stellar studies is related to the fact that the strongest resonant lines lie in the soft-UV region. Moreover UV emission lines allow to study stellar coronae and chromospheres and in particular the phenomenon of mass-loss in Wolf-Rayet stars. Interstellar UV absorption lines are useful to study local interstellar clouds. Galactic UV emission comes from young stars and is directly related to the process of star formation. In fact we are able to reconstruct the star formation history of the Universe from the observation of rest-frame UV LF.

Infrared Observations

Conventionally the Infrared band covers a wavelength range from 7000 Å to 1 millimeter. It can be subdivided into several sub-bands: Near-Infrared (NIR) band (from 7000 Å up to 5 μm); Mid-Infrared (MIR) band (from 5 μm up to 30 μm); Far-Infrared (FIR) band (from 30 μm up to 300 μm); sub-millimeter (sub-mm) band (from 300 μm up to 1 mm).

The Infrared emission of galaxies is dominated by thermal emission coming from two kind of sources: cold stars and dust. The relative contribution of

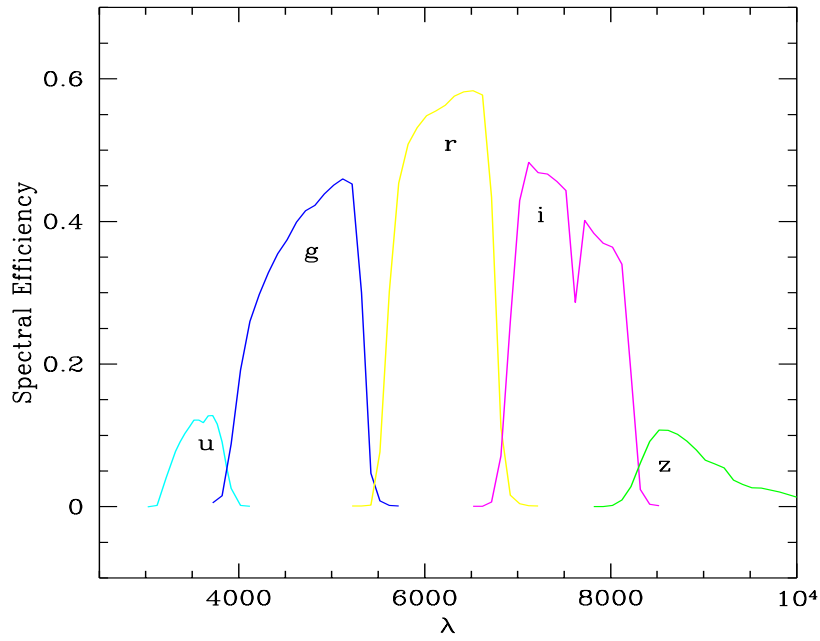


Figure 1.3: SDSS photometric system

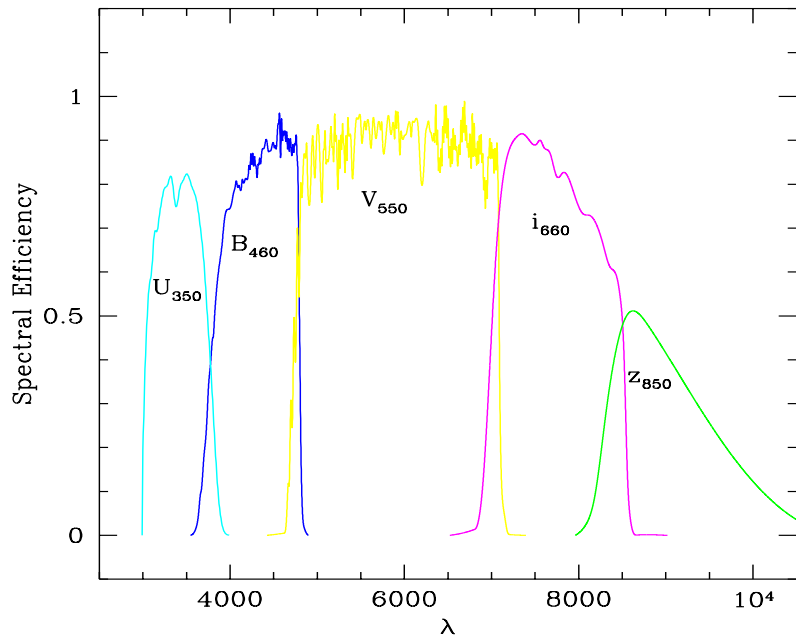


Figure 1.4: GOODS photometric system

the two categories is relevant in order to understand the physical conditions of the observed galaxy as a whole. NIR observations trace essentially the photometric emission of cold stars (red giants): they are able to trace the dominant stellar populations (in mass) of the galaxy. In particular, the K -band ($19600\text{\AA} < \lambda < 24400\text{\AA}$) luminosity is a good tracer of the galactic stellar mass (Gavazzi et al., 1996) and allows to follow the assembly of the bulk of stellar mass, at variance with B -band and UV observations that trace star formation history but are heavily affected by dust obscuration. K -band surveys allow to select galaxies according to their mass up to $z \sim 1.5$ (a galaxy with stellar mass $\sim 10^{11}$ corresponds to a magnitude $18 < K < 20$ at redshifts $1 < z < 2$, see i.e. Cimatti et al., 2002b). For this reason the near-infrared galaxy Luminosity Function (LF) is a good tracer of the Galaxy Stellar Mass Function (GSMF, see i.e. Pozzetti et al., 2003).

MIR and FIR observations are instead dominated by thermal emission from dust. Dust grains associated with star-forming regions reprocess optical and UV photons coming from young stars and reradiate them at FIR wavelengths. For this reason we can infer informations about the cosmic star formation history by taking into account observations in FIR bands; samples selected far-IR/sub-mm wavelengths are dominated by objects with ongoing star-formation. In particular observations with the Sub-millimeter Common-User Bolometer Array (SCUBA) on the James Clerk Maxwell Telescope (JCMT) at $850\mu\text{m}$ have highlighted the presence of a population of high-redshift, star forming galaxies with relevant sub-mm fluxes (Smail et al. 1997).

X-ray observations

The X-ray band covers the wavelength range between 100\AA and 0.002\AA . In X-ray astronomy it is common practice to use photon energies (expressed in KeV) in place of wavelengths. X-ray band limits quoted above can be expressed as 0.12 KeV and 500 KeV , due to the fact that an energy of 1KeV corresponds to a wavelength of 12\AA . X-ray observations are roughly subdivided into two bands: soft-X and hard-X. The division can slightly change from author to author, but in general it falls at energies of a few KeV. In the following we use as soft-X band the energy range between 0.5 and 2 KeV and as hard-X band the energy range between 2 and 10 KeV . This choice is typical of satellite observations (ROSAT, Chandra, XMM).

Soft X-ray photons are easily absorbed by intervening atoms and molecules (bound-free and free-free processes). On the other hand hard-X photons can travel larger distances in the Universe. They are not affected by the previous absorbing processes, however they suffer partial extinction due to Thompson-Compton scattering processes. In order to estimate the amount of absorption it is useful to introduce the concept of *column density* N_H , which is defined as the equivalent density of intervening hydrogen atoms required to produce the observed absorption. It is possible to estimate the column density by comparing the soft X-ray and hard X-ray fluxes of the source (*hardness ratio*). The knowledge of N_H is useful to compute X-ray corrections and to estimate the real amount of X-ray emission.

X-ray emission is related both to thermal and non-thermal processes. Thermal emission is due to free-free processes in hot plasmas $10^6 K < T < 10^8 K$. Non-thermal processes are related both to synchrotron emission from relativistic electrons moving through a magnetic field and to Inverse Compton radiation, in which a low energy photon is scattered by a relativistic electron.

The X-ray emission in spirals is attributed to the superposition of individual sources such as X-ray binary star systems and thermal emission ($10^6 K$ hot gas) associated with supernova remnants (SNRs) and the hot phase of the ISM, while in elliptical galaxies the major contribution is due to diffuse hot interstellar gas (temperature $10^7 K$).

The X-ray emission of normal galaxies is not very relevant ($L_X \sim 10^{38} - 10^{42}$ erg/s). The most important X-ray emitters are AGNs ($L_X \sim 10^{43} - 10^{48}$ erg/s). We will focus our attention on these objects in chapter 2.

Radio

Radio observations cover the wavelength range $\lambda \geq 1mm$. At microwave wavelengths emission is related to thermal processes in warm ($T \sim 10^4 K$) plasma. At longer wavelengths emission is synchrotron radiation due to relativistic electrons moving through magnetic fields.

Emission lines in this band (commonly known as *Radio Lines*) are extensively used to trace interstellar gas because they suffer low interstellar extinction. The 21 cm line is an accurate tracer of *HI* clouds and it is often used to study both the structure of the Milky Way and the rotation curve of external spiral galaxies (see i.e., Zwaan et al., 2005). The molecular lines (*CO*, *OH*, *HCHO*, *H₂CO* and *CS*) are used to detect molecular clouds. The recombination lines of *H*, *He*, *C* are useful both to study the internal structure of *HII* regions and to trace the distribution of these regions in the Milky Way.

Radio emission in galaxies is related to compact objects resulting from the final stages of stellar evolution and is considered as a tracer of star formation (see i.e. Condon et al., 2002). The most luminous galactic radio sources are pulsars and SNRs. Pulsars are characterized by a strong magnetic field and a high angular momentum. These systems are able to generate relativistic electrons emitting synchrotron radiation. Radio emission from SNRs is due both to warm gas and to synchrotron from relativistic electrons generated by the SN event.

However the most powerful radio sources in the Universe are not related to stellar evolution but are AGNs. We will describe such processes in chapter 2.

1.2.2 Stellar Population properties

We have already seen in previous sections that galactic morphological types differ in terms of stellar content. In particular elliptical galaxies are characterized by stars with old ages and high metallicity, while spiral discs show a large number of young population I stars. This different stellar content has fundamental consequences in the observed colors and spectra of these objects

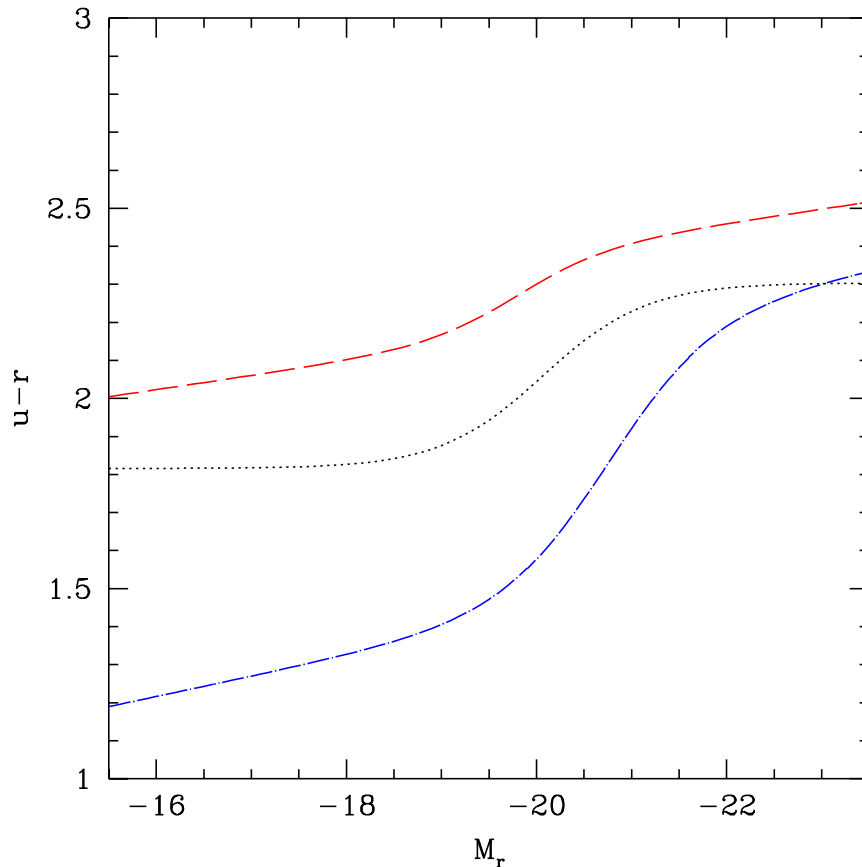


Figure 1.5: Color-Magnitude diagram for SDSS galaxies. Lines refer to the mean rest frame $u - r$ color of blue (dot-dashed) and red (dashed) populations (Baldry et al. 2004). Dotted Line represents the optimal divider between the two distributions.

We obtain the information about stellar population properties from the analysis of galactic spectral energy distributions (SEDs). When we observe a galactic spectrum we analyse photons coming from the unresolved stellar populations. This implies that the dominant stellar population (in terms of luminosity) determines the spectrum of the galaxy. As an example, elliptical galaxies show spectra dominated by absorption lines of red old stars, while spiral galaxy spectra are characterized by absorption lines associated to young blue stars and emission lines from HII regions (ionized regions around young luminous stars).

Galaxy Color Distribution

The colors of galaxies are strongly related with their stellar content. Elliptical galaxies show red colors due to the age and metallicity of the dominant stellar population. On the contrary blue color are associated with spiral disc due to the young blue stellar population.

Baldry et al. (2004) analysed the color-magnitude diagram for the galaxies

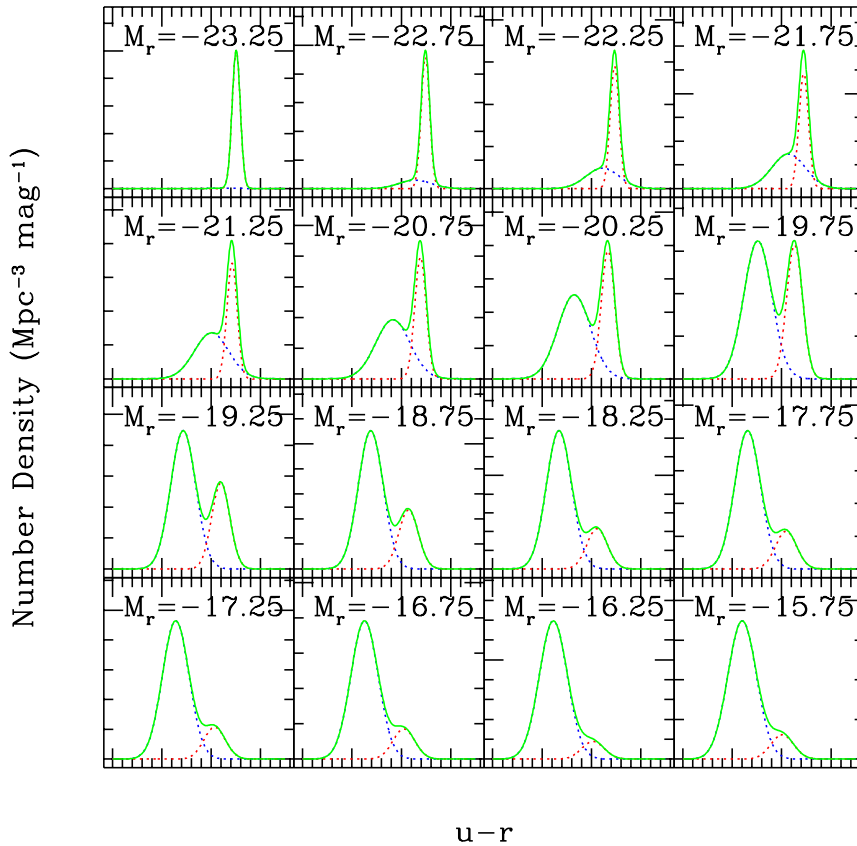


Figure 1.6: Observed Color Bimodality in the SDSS sample (Balogh et al. 2004)

in the Sloan Digital Sky Survey. They found that the whole sample can be subdivided into two different galaxy populations on the basis of the observed color. They found evidence for a red population associated to early type galaxies, and for a blue population associated with spiral galaxies. In fig. 1.5 we show the locus of the mean rest frame $u - r$ color as a function of r magnitude for the two populations. This *color bimodality* appears to be a well defined property of galaxies, and it spans a wide range of galactic magnitudes. Balogh et al. (2004) found that the distribution of galaxies at a given r magnitude in the SDSS sample is well described by the sum of two gaussian distributions (fig. 1.6). This bimodal distribution is a property that holds true for a wide range of magnitudes. Moreover Blanton et al. (2003) claimed that this bimodality spans over several other galactic properties: dividing galaxies into two populations according to their colors highlights the fact that this subdivision is valid also for others galactic properties as emission line strength, luminosity functions, nuclear and star-formation activity.

Extremely Red Objects

Extremely Red Objects (EROs) are defined in terms of their very red colors ($R - K_s > 5$ or $I - K > 4$, Pozzetti & Mannucci, 2000). Such very red colors can be explained by two galactic populations: starbursts hidden by large amounts of dust, which absorb and reprocess stellar radiation, or high-redshift old ellipticals with intrinsically old red stellar populations and large positive K-corrections (Cimatti et al., 2002a; Daddi et al., 2002). EROs are typically found at high redshift ($z > 1$) and provide important constraints for understanding the mass assembly of galaxies. Both the presence of heavy starburst galaxies and red ellipticals, made by old stars (it implies that the redshift of formation of these ellipticals must be even higher), is challenging for model of galaxy formation and evolution (see i.e. Cimatti et al., 2002b).

1.2.3 Statistical properties

Galaxy Catalogues

The most important tools to study statistical properties of galaxies are galaxy catalogues. They are a compilation of observations of magnitude and distances (i.e. redshifts see sec. 1.3) of galaxies over a well defined region of the sky. A catalogue is defined *statistically complete* if it contains all objects satisfying well-defined selection criteria. Useful selection criteria are based on apparent magnitude, angular diameter or color criteria. The statistical completeness is a key property of a catalogue because it allows the study of selection effects. It is possible to define volume complete samples from galaxy catalogues. In this case we consider only the galaxies with a luminosity higher enough to be detected at the maximum distance. Galaxy surveys are commonly classified according to their sky coverage and to their deepness. Due to the increasing observational challenges involved, the deepest surveys are defined on small areas of the sky. On the other hand, large area surveys collect information over thousands galaxies, but they are limited to brighter magnitudes.

In this work we will use data coming from several survey. In particular we want to briefly introduce here the most important.

- The 2dF Galaxy Redshift Survey (2dFGRS, Colless et al., 2001) covers a sky area of about 1500 square degrees and contains about 221414 galaxies brighter than a nominal extinction-corrected magnitude limit of $b_J = 19.45$.
- The Third Data release of the Sloan Digital Sky Survey (SDSS, Abazajian, et al. 2005) covers an area³ of 4188 square degrees and collects 374767 confirmed galaxies brighter than $r = 17.77$.
- The K20 survey (see e.g., Cimatti et al., 2002) contains information about a sample of about 550 galaxies with $K < 20$ observed in a sky area of 52 square arcminutes.

³We consider here the SDSS spectroscopic survey

- The Great Observatories Origins Deep Survey (GOODS) is a public, multiwavelength survey that covers 320 square arcminutes and it consists of two major parts: space based imaging and ground based imaging. This survey is able to detect objects with a limiting magnitude $z_{850} < 27.5$

Large area surveys, such as the 2dFGRS and the SDSS, provide the most relevant sample for local galaxy investigation. On the other hand the combination of these datasets with deep observations (such as K20 and GOODS) is fundamental to study distant objects.

Luminosity Functions

The *Luminosity Function* (LF) $\Phi(L)$ gives the number dN of galaxies present in a volume dV with luminosities between $[L, L + dL]$:

$$dN = \Phi(L)dVdL \quad (1.1)$$

This function can be computed from a galaxy catalogue once the adopted objective selection criteria are specified and the distance of each object is known. In general the shape of the optical LF is well represented by the so called *Schechter Function*:

$$\Phi(L)dL = \Phi^*(L/L^*)^\alpha e^{-L/L^*} d(L/L^*) \quad (1.2)$$

The parameter Φ^* is related to the number of galaxies in the catalogue with typical luminosity L^* :

$$\Phi(L^*) = (\Phi^*/L^*)e^{-1}$$

The Schechter function is specified by the two parameters L^* and α . For luminosities fainter than L^* it reduces to a power-law with slope α ; at brighter luminosities it gets an exponential shape. The parameter L^* is the knee of the LF. The classical form of the Schechter function is valid up magnitudes as faint as about -15 (Trentham, Sampson, & Banerji, 2005). Recent studies on the faint end of the LF (Blanton et al., 2004) show an excess of faint objects with respect to the Schechter function fixed at $L \geq L_*$.

We can analyze separately the LF of different morphological types. As a result of this kind of analysis it is possible to show that the Schechter LF is the combination of various LFs, relative to the different morphological types (see i.e., Marinoni et al., 1999, Baldry et al. 2004b). The shapes of these LFs could also be different from the Schechter form. In particular Early type galaxies are characterized by a gaussian LF, turning into a Schechter function if we consider also dwarf ellipticals and lenticular galaxies. Something similar holds true for early type spirals; on the contrary, late type spirals and irregulars have a Schechter LF with a steeper faint end. The sum of the different components gives rise to the observed Schechter LF. The relative abundance of morphological types in different environments (morphological segregation) gives rise to differences in the related LFs. Marinoni et al. (1999) found that the *B*-band LF for cluster members tends to show brighter values of

M_B^* with respect to the field value. Baldry et al. (2004b) divided the SDSS sample into five bins of increasing environmental density (defined using the projected surface density at the distance of the fifth-nearest neighbor), then studied separately the LF of the blue and red populations (see 1.2.2). They found that the faint end slopes change: in the highest density bin the two population have compatible faint end slopes, whereas in the lowest density bin the red sequence and the blue sequence have respectively a shallower and a steeper slope. Popesso et al. (2004) analysed the LF of SDSS cluster galaxies and compare their results to the analogous work developed by Blanton et al. (2003a) on SDSS field galaxies. They concluded that the LF of field galaxies is flatter than the cluster LF, while the cluster M_* is brighter than the field M_* by about 0.5 mag.

If we move from the optical to other wavelengths the shape of the LF changes. In the near-infrared the LF is well described by a Schechter function, while in far-infrared and radio bands the LF shape does not follow the Schechter function anymore. As an example, Saunders et al., (1990) computed the far-infrared LF using the PSC catalogue (based on IRAS observations). Their best fit LF has the following analytical form:

$$\Phi(L) = \Phi^* \left(\frac{L}{L^*} \right)^{1-\alpha} \exp \left[- \frac{1}{2\sigma^2} \text{Log}^2 \left(1 + \frac{L}{L^*} \right) \right] \quad (1.3)$$

In figure 1.7 we compare eq. 1.3 with a Schechter function.

Number Counts

We can get the number density n of galaxies brighter than L by integrating the luminosity function $\Phi(L)$:

$$\begin{aligned} n(> L) &= \int_L^{+\infty} \Phi(L') dL' \\ &= \Phi^* \int_{x=L/L^*}^{+\infty} x^\alpha e^{-x} dx \\ &= \Phi^* \Gamma(1 + \alpha, L/L^*) \end{aligned} \quad (1.4)$$

where we use the definition of *incomplete gamma function*:

$$\Gamma(j, k) = \int_k^{+\infty} x^{j-1} e^{-x} dx \quad (1.5)$$

The total number density is obtained by integrating the luminosity function up to the luminosity of dwarf galaxies. It is worth noting that it is not possible to integrate the luminosity function up to $L = 0$; in fact the integral diverges because of $\alpha \leq -1$.

When facing the problem of extra-galactic number counts, the distances of sources have to be taken into account. Photons travel with finite velocity c . Due to this fact the information they bring on the emitting source refers to a past epoch on the cosmic history: the farther the galaxy, the younger the Universe we are observing. For this reason we have to take into account evolutionary effects in the definition of number density and define a redshift

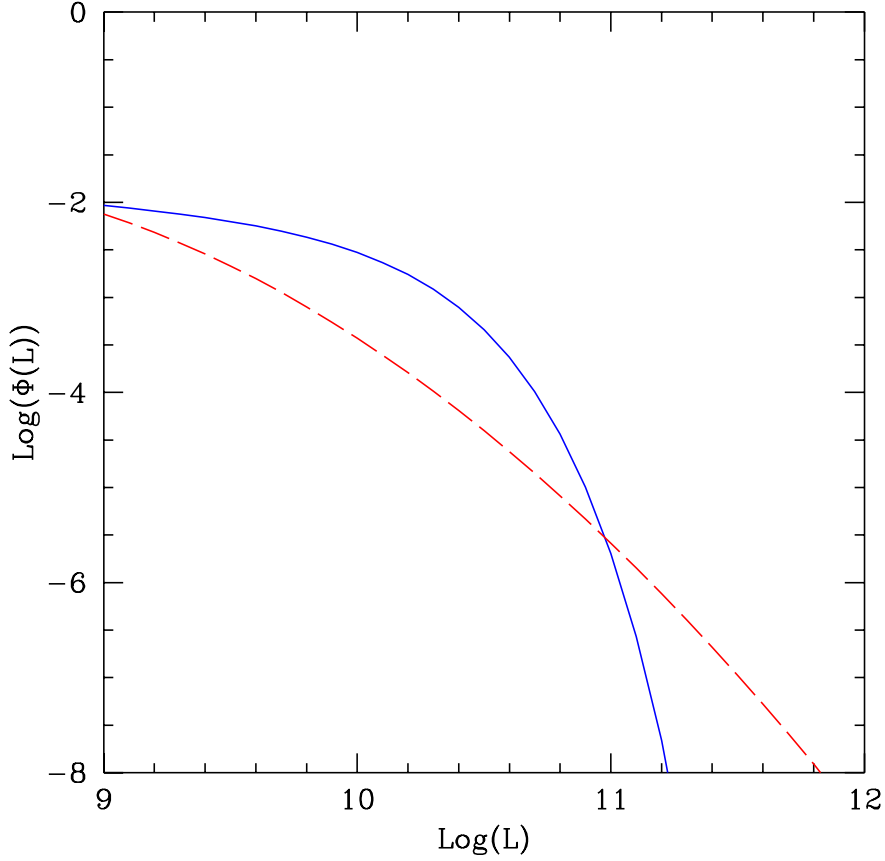


Figure 1.7: Optical and Infrared Galaxy Luminosity Functions. Solid blue line refers to a Schechter Function with parameters $\Phi^* = 0.006$, $L^* = 10^{10}$, $\alpha = -1.2$; dashed red line refers to the Infrared LF (eq. 1.3) with parameters $\Phi^* = 0.026$, $L^* = 10^8$, $\alpha = 1.09$, $\sigma = .72$.

dependent luminosity function $\Phi(L, z)$. The number density of galaxies brighter than L and with a redshift lower than z is then:

$$n(> L, < z) = \int_L^{+\infty} \int_0^z \Phi(L', z') dL' dz' \quad (1.6)$$

The galactic number counts N in a solid angle Ω can be expressed as:

$$N(> L, < z) = \frac{1}{\Omega} \int_L^{+\infty} \int_0^z \Phi(L', z') \frac{dV(z', \Omega)}{dz'} dL' dz' \quad (1.7)$$

where $V(z, \Omega)$ is the cosmological volume subtended by an angle Ω at a redshift z . We can also define the luminosity density ρ_L as:

$$\rho_L = \int_0^{+\infty} L' \Phi(L') dL' = \Phi^* L_* \Gamma(2 + \alpha) \quad (1.8)$$

The evolution of the Universe as a whole affects the properties of distant objects. We will give a more detailed description of the cosmological context in sec. 1.3. When we receive a photon from a distance galaxy the wavelength λ_o we measure differ from the wavelength at emission λ_e , due to the expansion of the Universe. The relation between the emitted and observed wavelengths is given:

$$z = \frac{\lambda_o - \lambda_e}{\lambda_e} \quad (1.9)$$

where z represents the *redshift* of the observed source. If we observe a redshifted galaxy with a passband filter, we are receiving photons emitted at a different wavelength with respect to the spectral response of the filter. In order to correct for this effect it is useful to introduce the K-correction:

$$K(\lambda_o) = -2.5 \log \left[\frac{\phi(\lambda_o/(1+z))}{(1+z)\phi(\lambda_e)} \right] \quad (1.10)$$

where $\phi(\lambda)$ represents the fraction of energy emitted at a wavelength λ . $K(\lambda)$ represents the difference between the observed magnitude at λ and the magnitude that would be observed at restframe. Also the luminosity and the angular diameter of a distant galaxy are affected by the expansion of the Universe. In particular it is possible to show that the luminosity is dimmed by a factor $(1+z)^2$, while the angular diameters are enhanced by a factor $(1+z)$. Due to this combined effects the surface brightness is dimmed by a factor $(1+z)^4$.

Correlation Functions

In this paragraph we analyse the spatial distribution of galaxies in the Universe due to the Large Scale Structure. The most widely used statistical indicator in this field is the *correlation function*. In the following we want to focus our attention on the *two-point correlation function* or *autocorrelation function* $\xi(r)$.

The number of object pairs dN_{pair} with separation $r = |r_1 - r_2|$ in volumes dV_1 and dV_2 is:

$$dN_{pair}(r) = \langle n \rangle^2 (1 + \xi(r)) dV_1 dV_2 \quad (1.11)$$

where $\langle n \rangle$ is the mean object density per unity volume. The mean number of objects at a distance r from a galaxy is then:

$$\langle N(r) \rangle = \int_0^r dN(r) = \frac{4\pi}{3} r^3 \langle n \rangle + 4\pi \int_0^r \xi(r') r'^2 dr' \quad (1.12)$$

The second term in eq.1.12 represents the deviation from a Poissonian distribution. If the Universe is homogeneous on large scales, the following condition (*integral constraint*) holds:

$$4\pi \int_0^\infty \xi(r) r^2 dr = 0 \quad (1.13)$$

Observationally the galaxy correlation function is well described by:

$$\xi(r) \simeq \left(\frac{r}{r_0}\right)^\gamma \quad (1.14)$$

and $\gamma \sim 1.8$. The r_0 parameter is the *correlation length* and it gives an estimate of the strength of the clustering. Norberg et al. (2002) proposed a value between $8.15 \text{ Mpc} < r_0^{\text{early}} < 12.43 \text{ Mpc}$ for early type galaxies and a value $5.3 < r_0^{\text{late}} < 8.0 \text{ Mpc}$ for late types in the 2dFGRS, while Zehavi et al. (2005) proposed $r_0^{\text{red}} = 8.14 \text{ Mpc}$ for red galaxies and $r_0^{\text{blue}} = 5.14 \text{ Mpc}$ for blue galaxies in the SDSS. These results imply a stronger clustering of elliptical galaxies with respect to late type galaxies.

It is possible to define a two-point correlation function also for groups and clusters. The result is always a power law function with a similar γ exponent, but with a higher normalization, growing with the richness of the system ($r_0^{\text{clu}} \sim 17 \text{ Mpc}$ for poor clusters and $r_0^{\text{clu}} \sim 36 \text{ Mpc}$ for rich clusters, Bahcall et al., 2004).

1.2.4 Structural relations

In this section we focus our attention on several structural properties satisfied by galaxies. Different morphological galaxy types satisfy different structural relation. This evidence gives us important hints about the mechanisms leading to the formation of different galaxy types. In this section we introduce the main properties we will discuss in the following chapters.

Luminosity Profiles

The Luminosity Profile $I(r)$ of a galaxy is defined as the surface brightness measured along the major axis of the photometric image of the galaxy. The luminosity profile of early type galaxies is well described by the *De Vaucouleurs' law*:

$$I(r) = I_0 \exp(-(r/r_0)^{1/4}) \quad (1.15)$$

Lenticular and spiral bulges are also well described by a De Vaucouleurs' profile. Spiral discs follow an exponential profile:

$$I(r) = I_0 \exp(-r/r_0) \quad (1.16)$$

Late type spiral bulges might have exponential profiles but the question is still under debate due to the intrinsic difficulties in separating the bulge and disc components.

Observations have revealed the presence of a population of spiral galaxies with values of $I(0)$ below the typical value for spirals ($21.7 \text{ Bmag arcsec}^{-2}$). This population had been systematically lost in previous observations. These objects (*Low Surface Brightness* LSB) have disc as massive as small spirals, but they are larger and less luminous. Deep observations revealed that all spiral discs have similar properties, and they seem to differ only as far as surface brightness is concerned.

Properties of Elliptical Galaxies

Faber & Jackson (1976) noticed a correlation between velocity dispersion and luminosity of elliptical galaxies. In the following years however evidence was reached that the *Faber–Jackson relation* is a projection of a more general relation. This relation holds in a three dimensional space defined by the velocity dispersion σ_{EL} , the effective radius r_e (defined as the major semiaxis of the isophote containing half the luminosity of the object) and the mean surface brightness I_e at the radius r_e . Elliptical galaxies live on a planar region of this space, the so called *Fundamental Plane* (Djorgovski & Davis, 1987; Dressler et al., 1987). It is easy to show that the virial theorem holds and the mass over luminosity ratio M/L is kept constant in elliptical, the following relation holds:

$$I_e r_e \propto \sigma_{EL}^2 \quad (1.17)$$

Bender et al. (1992) showed that the precise inclination of the fundamental plane depends on the variation of M/L as a function of luminosity. Jorgensen et al. (1996) quantify as follows the fundamental plane:

$$\log r_e = 1.20 \log \sigma_{EL} - 0.83 \log I_e + \gamma \quad (1.18)$$

This implies $M/L \propto L^{0.2}$. The fundamental plane shows a small scatter (or order of 0.1 dex in $\log r_e$, Pahre et al., 1995) and this evidence is a strong constraint for models of galaxy formation and evolution (Renzini & Ciotti, 1993).

We saw in 1.2.2 that elliptical galaxies are characterized by red colors. Moreover they show a relation between color and absolute magnitude (see i.e. Bower et al., 1992; Scodreggio, 2001; Terlevich et al., 2001): more luminous galaxies are redder. Redder colors are associated with older stellar populations, so a possible interpretation of the color-magnitude relation is that more massive galaxies have older stellar populations, i.e. they assembled their mass before less massive objects. This is in line with the downsizing scenario mentioned in the overview. However the interpretation of the color-magnitude relation is complicated by the age-metallicity degeneracy. The color of a stellar population is determined by the color of the main sequence turn-off. Unfortunately, if we consider two stellar populations, a first one older and a second one more metal rich, they show the same color of the main sequence turn-off. The situation becomes more complicated if we consider the relationship between the metallicity index Mg_2 and σ_{EL} . The index Mg_2 , computed from the Magnesium absorption lines, is a tracer of the mean metallicity of stars and it correlates with σ_{EL} (see i.e. Dressler et al., 1987). This correlation is interpreted as an evidence that more massive elliptical are more metal rich. Moreover if we analyse some ellipticals with great detail we notice the existence of stellar gradients inside these objects (see i.e. Carollo et al., 1993). In particular inner regions of elliptical galaxies are redder and more metal rich than outer regions. In conclusion, ellipticals are old, and more massive ones are more enriched.

Properties of Spiral Galaxies

In spiral galaxies a well defined relation between luminosity and rotational velocity at a given scale length holds: the *Tully–Fisher relation* (1977). Giovanelli et al. (1997) combine HI velocity profiles with *I*-band photometry and derive the following relation:

$$M_I = -21.00 - 7.68(\log W - 2.5) \quad (1.19)$$

where W is the inclination-corrected width of the HI line profile (e.g. in good approximation twice the maximum rotation velocity). Comparing the results of several authors (see e.g. Strauss & Willick and reference therein) evidence has grown that the slope of the relation depends on the observed bandpass. This difference is due to variations in the mass-to-light ratios of disc with luminosity. The effect is stronger in the *B*-band, whereas it is smaller in the *I*-band. For this reason the *I*-band Tully-Fisher relation is considered more appropriate to be compared with models. Besides we can conclude that the Tully–Fisher relation gives us information more on the structure of the disc than the nature of stellar populations.

We see in 1.2.2 that spiral galaxies are characterized by blue colors. This is a sign of recent stars formation. Star formation is concentrated in the disc, and it traces the typical spiral pattern. For this reason the spiral pattern is interpreted as a density wave able to trigger star formation episodes. On the other hand spiral bulges are characterized by red colors and stellar populations older with respect to the disc.

1.3 Cosmological Context

The knowledge of the cosmological context is of fundamental importance for the complete understanding of this work. In this section we will focus our attention on some relevant concepts we will refer to in the next chapters. We also give some equations that we consider useful for a better comprehension of the text. A more rigorous treatment of cosmological equations can be found for instance in Padmabanabhan (1995) and Peacock (1999).

Nowadays there is a general consensus in the scientific community on the so-called Standard Cosmological Model. The *Cosmological Principle* postulates the homogeneity and isotropy of the Universe; in other words, there is not a privileged observer in the Universe and its statistic properties at a certain time are independent of the position. Both isotropy and homogeneity are confirmed by observations of the mass distribution on large scale (the Large Scale Structure) and of the Cosmic Microwave Background (CMB). On the other hand it is evident that the Universe is neither isotropic nor homogeneous on galactic scales. This discrepancy is due to small primordial fluctuations superimposed on the otherwise homogeneous density field, which grow forming the currently observed galaxies. In this paragraph we focus on the description of the evolution of the Universe as a whole. We will deal with the mechanisms

responsible for the formation of the primordial fluctuations and the subsequent growth of structure in sec. 1.3.3.

1.3.1 Basic Equations

The evidence that the distance between galaxies is increasing with time leads to the idea that at a certain point in the past the observed Universe should have been compressed in a small volume. This model is called *Big Bang*. It is worth noting that the idea of the Big Bang as a “big explosion” is not correct: it is more realistic to figure out the Big Bang as the starting instant of the expansion of the Universe. Starting from the Big Bang the evolution of the Universe follows the equation of the *General Relativity*.

If we solve Einstein’s equations under these hypothesis we get the so called *Robertson–Walker Metric*, describing the space-time geometry:

$$ds^2 = dt^2 - a^2(t) \left[\frac{dr^2}{1 - kr^2} + r^2(d\theta^2 + \sin^2\theta d\phi^2) \right] \quad (1.20)$$

The k parameter can assume the values $-1, 0, 1$ respectively for an open, flat or closed Universe; ds^2 represents the proper time describing the distance of two events; t is the time coordinate, r the radial space coordinate, θ and ϕ the angular coordinates. The quantity $a(t)$ is the *Scale Factor*: it describes how distances in the Universe scale with in time. We can write the following relation:

$$1 + z(t) = \frac{a(t_0)}{a(t)} \quad (1.21)$$

where we introduce the concept of *cosmological redshift*. The classical interpretation of redshift (eq. 1.9) is related to the Doppler Shift due to the velocity of the source with respect to the observer. In a very similar way we can associate a *recession velocity* v to the cosmological redshift. Following our similitude we can write a relation between this ”velocity” and the distance d of the source:

$$d = \frac{\dot{a}(t)}{a(t)} v \quad (1.22)$$

We define the *Hubble Parameter*:

$$H(t) = \frac{\dot{a}(t)}{a(t)} \quad (1.23)$$

the *Hubble Constant*:

$$H_0 = H(t_0) \quad (1.24)$$

\mathbf{r} as the system of physical coordinates and \mathbf{x} the system of *comoving coordinates*:

$$\mathbf{r} = a\mathbf{x} \quad (1.25)$$

The evolution of the scale factor is determined by the *Friedmann Equations*:

$$\begin{aligned} \left(\frac{\dot{a}}{a}\right)^2 &= \frac{8\pi G}{3}\rho - \frac{k}{a^2} + \frac{\Lambda}{3} \\ \ddot{a} &= -\frac{4\pi G}{3}(\rho + 3p) + \frac{\Lambda}{3} \end{aligned} \quad (1.26)$$

The parameter k represent the curvature of the Universe (eq. 1.20); ρ is the mean density of the Universe and p is the pressure. When we compute the density and the pressure we have to take into account both the radiation and the matter content of the Universe. In the cosmological framework matter and radiation evolve in a different way, in particular matter density scales as $a(t)^{-3}$, while the energy density of radiation as $a(t)^{-4}$. For this reason we consider two different epochs in the history of the Universe dominated respectively by matter and radiation. The epoch during which the densities of the two species were almost equal is called the *Equivalence Epoch*. The quantity Λ is called cosmological constant; it was introduced by Einstein, in order to allow for a stationary solution. It was abandoned when the evidence of cosmic expansion was found, but it is now used to express the accelerated expansion of the Universe, discovered using Type I Supernovae. The density of the Universe is directly related to its geometry through the parameter Ω :

$$\Omega = \frac{\bar{\rho}}{\bar{\rho}_{cr}} \quad (1.27)$$

where $\bar{\rho}_{cr}$ is the *Critical Density* of the Universe:

$$\bar{\rho}_{cr}(t) = \frac{3H^2(t)}{8\pi G} \quad (1.28)$$

The value of the parameter $\bar{\rho}_{cr}$ is related to the geometry of the Universe: if Ω is greater than 1 we live in a close Universe; if Ω is lower than 1 we live in an open Universe; if Ω is equal to 1 our Universe is flat.

Power Spectrum

In this paragraph we study the properties of the matter density field in comoving coordinates. First of all we define the *density contrast* as:

$$\delta(\mathbf{x}) = (\rho(\mathbf{x}) - \bar{\rho})/\bar{\rho} \quad (1.29)$$

This quantity represents the deviation of the density field from its mean value $\bar{\rho}$. We can represent the spatial distribution of the density contrast as a superposition of plane waves or a *Fourier Series*. We consider the comoving wavenumber $\mathbf{k} = (n_x \frac{2\pi}{L}, n_y \frac{2\pi}{L}, n_z \frac{2\pi}{L})$ and we impose period boundary condition on a cubic volume $V = L^3$:

$$\delta(\mathbf{x}) = \sum_{n_x, n_y, n_z = -\infty}^{+\infty} \delta_{\mathbf{k}} e^{i\mathbf{k}\cdot\mathbf{x}} \quad (1.30)$$

where $\delta_{\mathbf{k}}$ is the Fourier transform of $\delta(\mathbf{x})$ and is a complex number. If we take an arbitrary large L we can recover the integral form of the *Fourier Transform*:

$$\delta(\mathbf{x}) = \frac{1}{(2\pi)^3} \int \delta_{\mathbf{k}} e^{i\mathbf{k}\cdot\mathbf{x}} d^3k \quad (1.31)$$

$$\delta_{\mathbf{k}} = \int \delta(\mathbf{x}) e^{-i\mathbf{k}\cdot\mathbf{x}} d^3x$$

Assuming $\delta(\mathbf{x})$ is a real quantity implies $\delta_{\mathbf{k}}^* = \delta_{-\mathbf{k}}$. The variance of the field is defined as:

$$\sigma^2 = \langle (\delta(\mathbf{x}) - \langle \delta(\mathbf{x}) \rangle)^2 \rangle = \langle \delta(\mathbf{x})^2 \rangle \quad (1.32)$$

if we consider two vectors \mathbf{x}_1 and \mathbf{x}_2 , the modulus of their difference being $x = |\mathbf{x}_1 - \mathbf{x}_2|$, we define the correlation function $\xi(x)$ as:

$$\xi(x) = \langle \delta(\mathbf{x}_1) \delta(\mathbf{x}_2) \rangle \quad (1.33)$$

If we compare eq.1.33 and eq.1.31 we obtain:

$$\begin{aligned} \xi(x) &= \langle \int \delta_{\mathbf{k}_1} e^{i\mathbf{k}_1\cdot\mathbf{x}_1} d^3k_1 \int \delta_{\mathbf{k}_2} e^{i\mathbf{k}_2\cdot\mathbf{x}_2} d^3k_2 \rangle \\ &= \int d^3k_1 \int d^3k_2 e^{i\mathbf{x}_1\cdot\mathbf{k}_1 + i\mathbf{x}_2\cdot\mathbf{k}_2} \langle \delta_{\mathbf{k}_1} \delta_{\mathbf{k}_2} \rangle \end{aligned} \quad (1.34)$$

We define the *Power Spectrum*:

$$\langle \delta_{\mathbf{k}_1} \delta_{\mathbf{k}_2} \rangle = P(|\mathbf{k}_1 - \mathbf{k}_2|) \delta^D(\mathbf{k}_1 - \mathbf{k}_2) \quad (1.35)$$

The function δ^D represents a Dirac delta function. Comparing eq.1.35, eq.1.34 and eq.1.33 we get:

$$\xi(x) = \frac{1}{(2\pi)^3} \int d^3k P(k) e^{i\mathbf{x}\cdot\mathbf{k}} \quad (1.36)$$

In practice $\xi(x)$ and $P(k)$ are a Fourier pair. The variance is equivalent to $\xi(0)$, and we can express it as:

$$\sigma^2 = \frac{1}{2\pi^2} \int_0^\infty k^2 P(k) dk \quad (1.37)$$

Origin of small fluctuations in the early Universe

The power spectrum $P_{rec}(k)$ at the recombination depends on the linear evolution of gravitational perturbations in the early Universe. In the standard cosmological model structures form from the gravitational collapse of small primordial fluctuation in the density field (*gravitational instability scenario*). The *Inflationary model* is able to explain the origin of these anisotropies in the primordial Universe. This model assumes that the early Universe undergoes a short phase of accelerated expansion, due to a symmetry breaking of a scalar quantum field (the "inflaton") that reaches a new vacuum configuration. The quantistic fluctuations of the inflaton become "classical" owing to the Hubble expansion and are the origin of primordial fluctuations. We can observe these fluctuations of the density field only after the recombination epoch, when the Universe became transparent to radiation. The relation between

the power spectrum of primordial fluctuations P_{prim} and the power spectrum at recombination P_{rec} can be expressed in terms of the *Transfer Function* $T(k)$:

$$P_{rec}(k) = P_{prim}(k) T^2(k) \quad (1.38)$$

The subsequent evolution of perturbations can be followed with perturbative methods (*Linear Theory*), as long as these perturbations are small. At later times their density can become relevant; we refer then to *non-linear perturbations*. As an example, galactic DM halos are in a non-linear regime, whereas Superclusters can be considered in quasi-linear regime. We will deal with this topic in 1.3.3.

Inflation predicts a power law primordial power spectrum:

$$P(k) = Ak^n \quad (1.39)$$

If $n = 1$ we call $P(k)$ *Harrison and Zel'dovich Primordial Spectrum*. The σ_8 parameter, representing the variance of the density field, computed on an $8Mpc/h$ radius sphere, using a *top-hat* filter, is used to parameterize the normalization of $P(k)$. The variance on a finite scale R is:

$$\sigma^2 = \frac{1}{2\pi^2} \int_0^{R^{-1}} k^2 P(k) dk \quad (1.40)$$

We can introduce a filter function W , i.e. a low-pass filter. In this case the variance σ_R^2 on the scale R is:

$$\sigma_R^2 = \frac{1}{2\pi^2} \int_0^\infty k^2 W^2(kR) P(k) dk \quad (1.41)$$

The importance of the σ_8 parameter is related to the fact that this radius roughly corresponds to the typical size fluctuation from which clusters form. In other words it is related both to the normalization of the power spectrum and to the timing of structure formation.

1.3.2 The Standard Cosmological model

In the last decades astronomers found growing evidence of the presence of a mass component that interacts only gravitationally. This mass component does not emit electromagnetic radiation and for this reason it has been called *Dark Matter* (DM). A classic test in favor of the existence of DM consists in the analysis of the rotation curves of spiral galaxies. The prediction of the shape of these rotation curves based on the gravitational effect of the luminous mass does not match with the observed rotation curves. This evidence stimulated astronomers to postulate the existence of a dark mass component sustaining the rotation of spirals up to the observed radii. Nowadays evidence of the presence of DM has been achieved. One of the most important observations is the measure of the mass of galaxy clusters through the measure of their gravitational effect (e.g. through *Gravitational Lensing*).

The nature of DM has strong effects on the cosmology, in particular on the growth of perturbations that give rise to the galaxy population. The proposed

DM models differ in the relativistic or non-relativistic nature of DM particles. In the case of relativistic DM particles (*Hot Dark Matter Models, top-down scenario*), large structures form first, then they fragment in smaller structures. On the contrary, in the case of non-relativistic DM particles (*Cold Dark Matter Models, bottom-up scenario*) small structures form first, then merging to form large structures.

The Λ CDM model gained an increasing importance in recent times; it assumes non-relativistic DM particles and takes into account the cosmological constant Λ . In this model the matter density Ω_m is taken smaller than 1, and a new quantity $\Omega_\Lambda = \rho_\Lambda/\rho_{crit}$ is introduced, in order that the sum of Ω_m and Ω_Λ is 1. Ω_Λ has a similar meaning with respect to Ω_m and is linked to the value of the cosmological constant.

The Λ CDM scenario implies that the Universe was very dense and very hot in the early times. In this conditions matter was completely ionized and all particle species (photons included) were in thermodynamical equilibrium. At these stages the Universe was then opaque to electromagnetic radiation. During the following expansion the temperature decreased, until light nuclei and electrons started to combine in atoms, thus decoupling from photons: from this moment on, photons can propagate freely in the Universe. We can observe at $z = 0$ this radiation as an almost uniform cosmic background in the microwaves. The existence of the CMB is a very stringent confirmation of the Big Bang model. Moreover, due to the coupling of matter and radiation before recombination, small CMB temperature anisotropies trace the fluctuations in the density field at this epoch.

Cosmological Parameters

The Λ CDM scenario is completely described by a set of *cosmological parameters*: a basic set consists of the Hubble constant H_0 , the total matter density Ω_m , the baryon Ω_b , radiation Ω_γ and neutrino Ω_ν densities, the cosmological constant Λ , the density perturbation spectral index n , the density perturbation amplitude σ_8 . These parameters define the overall evolution of the Universe and the growth of structures. The most powerful technique to measure the value of cosmological parameters relies on the measurement of the anisotropies in the CMB. The angular power spectrum C_l of anisotropies, depends on all the cosmological parameters and it had been observed by several groups (see i.e. de Bernardis et al., 2000). The *Wilkinson Microwave Anisotropy Probe (WMAP)* satellite (Bennett et al., 2003) provides to most accurate determination of the CMB fluctuations, and the most accurate measurement of cosmological parameters (Spergel et al., 2003). However to obtain tight constraints other data sets need to be considered in addition to WMAP. Suitable data sets comes from the analysis of galaxy power spectrum (Verde et al., 2002), of galaxy clusters (Borgani et al., 2001; Allen et al. 2003), distant SNe (Supernovae Cosmology Project; Perlmutter et al, 1999; Knop et al., 2003) and the Lyman-alpha Forest power spectrum (Viel et al., 2004). In spite of the different nature of these datasets their results are in good agreement and constrain the cosmological parameters (fig. 1.8) to values

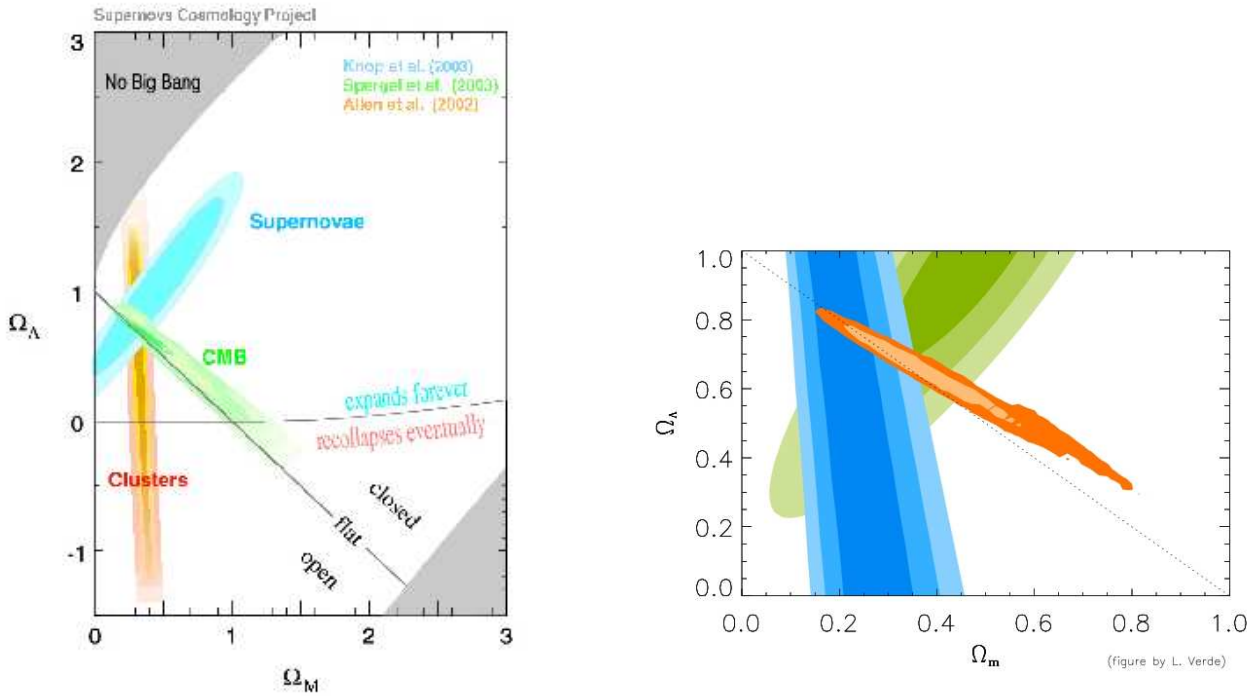


Figure 1.8: Constraints on cosmological parameters. Left Panel: Confidence regions for Ω_m and Ω_Λ with WMAP CMB (green area Spergel et al., 2003), galaxy cluster results (orange area Allen et al., 2002) and Type Ia Supernovae (cyan area Supernova Cosmology Project, Knop et al., 2003) (from Ciardi & Ferrara, 2005). Right Panel: Confidence regions for Ω_m and Ω_Λ with WMAP CMB (orange area Spergel et al., 2003), $2dF$ data (cyan area Verde et al., 2002), Supernovae data from the Supernova Cosmology Project (green area Perlmutter et al., 1999) (figure taken from <http://www.physics.upenn.edu/~lverde/cosmmodel.html>)

$\Omega_m = 0.3$, $\Omega_\Lambda = 0.7$, $\Omega_b = 0.04$, $H_0 = 70 \text{ Km/s}$, $\sigma_8 = 0.9$. In this work we assume the ΛCDM model with these parameter values as our reference cosmological model.

1.3.3 Growth of structures in the Universe

Eulerian approach and Linear Theory

In this paragraph we describe the evolution of primordial perturbations using an *Eulerian approach*. We consider the matter density as a non-collisional fluid, and refer to a fixed comoving coordinate system. We write the following equation system:

$$\nabla_{\mathbf{x}}^2 \phi = 4\pi G(\rho - \bar{\rho})a^2$$

$$\frac{\partial \mathbf{v}}{\partial t} + \frac{1}{a}(\mathbf{v} \cdot \nabla_{\mathbf{x}})\mathbf{v} + \frac{\dot{a}}{a}\mathbf{v} = -\frac{\nabla_{\mathbf{x}}\phi}{a} \quad (1.42)$$

$$\frac{\partial \delta}{\partial t} + \frac{1}{a}\nabla_{\mathbf{x}} \cdot (1 + \delta)\mathbf{v} = 0$$

The first equation represents the *Poisson equation* for the *peculiar gravitational potential* ϕ generated by the density fluctuations; the second one is the *Euler equation* describing the motion of the generic fluid element with peculiar velocity \mathbf{v} and it represents the equation of motion; the last one is the *continuity equation* representing the mass conservation law for the fluid.

We now assume that $\rho(\mathbf{x})$ and \mathbf{v} satisfy the following conditions (t is the cosmic time and d the coherence length of the matter density field):

$$\delta \ll 1 \quad (1.43)$$

$$\left(\frac{vt}{d}\right)^2 \ll \delta$$

Under these assumptions we can simplify the system of equations and write:

$$\frac{\partial^2 \delta}{\partial t^2} + 2\frac{\dot{a}}{a}\frac{\partial \delta}{\partial t} = 4\pi G\bar{\rho}\delta \quad (1.44)$$

This equation admits two solutions. The first one $D_+(t)$ describes the growth of perturbations in time, the other one $D_-(t)$ is a decreasing function of cosmic time and describes the decay of perturbations. After a small interval of cosmic time $D_-(t)$ becomes negligible. We refer to the growing mode as $D(t)$.

The linear evolution of the density field is then written in the form (t_i represent the initial reference time):

$$\delta(\mathbf{x}, t) = \delta(\mathbf{x}, t_i)\frac{D(t)}{D(t_i)} \quad (1.45)$$

Lagrangian approach and the Zel'dovich approximation

An alternative view of the problem is provided by the *Lagrangian approach*. We define a coordinate system in motion with the fluid element (Lagrangian coordinates); this way we can study the evolution of a mass element following its trajectory and deformation in space. We define \mathbf{q} as the Lagrangian coordinate system and $S(\mathbf{q}, t)$ as the displacement vector. We can then write:

$$\mathbf{r}(\mathbf{q}, t) = a(t) \cdot \mathbf{x}(\mathbf{q}, t) = a(t)[\mathbf{q} + S(\mathbf{q}, t)] \quad (1.46)$$

In the previous equation we indicate with \mathbf{r} the Eulerian proper coordinate and with \mathbf{x} the comoving coordinate. We define the quantity *linear density contrast*:

$$\delta_i(\mathbf{q}) = \frac{\delta(\mathbf{q}, t_i)}{D(t_i)} \quad (1.47)$$

which is constant in linear theory and independent of the starting time t_i . If we normalize $D(t)$ as $D(t_0) = 1$ at final time t_0 , δ_l will represent the density contrast linearly extrapolated to t_0 . The peculiar potential in Lagrangian coordinates is rescaled as follows:

$$\varphi(\mathbf{x}) = \frac{2a(t)}{3D(t)H_0^2\Omega_0}\phi(\mathbf{q}) \quad (1.48)$$

and it obeys:

$$\nabla_{\mathbf{q}}^2\varphi(\mathbf{q}) = \frac{\delta(\mathbf{q}, t_i)}{D(t_i)} = \delta_l(\mathbf{q}) \quad (1.49)$$

The velocity vector is rescaled as:

$$\mathbf{u}(\mathbf{q}) = \frac{d\mathbf{x}}{dD} = \frac{\mathbf{v}}{a\dot{D}} \quad (1.50)$$

In linear theory:

$$\mathbf{u}(\mathbf{q}) = -\nabla_{\mathbf{q}}\varphi \quad (1.51)$$

To solve for $S(\mathbf{q}, t)$ in analogy with Eulerian theory, we assume small deviations ($\delta \ll 1$):

$$S(\mathbf{q}, t) = g(t)\mathbf{p}(\mathbf{q}) \quad (1.52)$$

In this case it is possible to demonstrate that:

$$\frac{\delta\rho}{\rho} = -g(t)\frac{\partial p_i}{\partial q_j} = -g(t)\nabla_{\mathbf{q}} \cdot \mathbf{p}(\mathbf{q}) \quad (1.53)$$

Comparing this result with Eulerian theory we can easily get $g(t)$ and $\mathbf{p}(\mathbf{q})$ using an expansion into Fourier series:

$$g(t) \propto D(t) \quad (1.54)$$

$$\mathbf{p}(\mathbf{q}) \propto \mathbf{u}(\mathbf{q}) \quad (1.55)$$

We can now write the so called *Zel'dovich Approximation* (1970):

$$\mathbf{x}(\mathbf{q}, t) = \mathbf{q} + D(t)\mathbf{u}(\mathbf{q}) \quad (1.56)$$

which is very similar to to the equation of motion of a free particle:

$$\mathbf{x}(\mathbf{q}, t) = \mathbf{q} + t \cdot \mathbf{v}(\mathbf{q}) \quad (1.57)$$

We can assume as a first approximation the Universe as an ensemble of dust particles that feel only the effect of gravity. In this example the velocity field can be written as:

$$\mathbf{v} = \nabla\phi$$

This condition is true if the fluid is in laminar regime, i.e. without intersections in the particles trajectories. In the case of the evolution of the Universe this is true only until the first *orbit crossing* happens.

Nonlinear spherical collapse

The relations above are valid in the case of small fluctuations. As structures grow fluctuations on larger and larger comoving scales go non-linear. In this paragraph we focus our attention on the simpler possible detailed model for the formation of an object. We consider a spherical region with uniform overdensity δ_{ov} and radius R_{ov} . A result of General Relativity known as *Birkhoff's Theorem* states that external matter exerts no force on the material within the sphere. We can write the following equation:

$$\frac{d^2R}{dt^2} = -\frac{GM}{R^2} = -\frac{4\pi}{3}\bar{\rho}(1 + \delta_{ov})R \quad (1.58)$$

which is formally equivalent to the equation for the evolution of the cosmological scale factor:

$$\frac{d^2a}{dr^2} = -\frac{4\pi}{3}\bar{\rho}a \quad (1.59)$$

Thus R evolves like a in a “universe” with different density but the same initial time and initial expansion rate. The following parametric solution holds:

$$\begin{aligned} \frac{R}{R_m} &= \frac{1}{2}(1 - \cos\eta) \\ \frac{t}{t_m} &= \frac{\eta - \sin\eta}{\pi} \end{aligned} \quad (1.60)$$

where R_m is the maximum radius of the sphere and is attained at the time t_m . The collapse of the sphere to $R = 0$ occurs at time $2t_m$. This simple model for the collapse of an overdense region is known as spherical top-hat. The assumption that the overdensity is uniform has not been used directly in any passage of the above analysis. We can subdivide the spherical overdensity into several mass shells (provided that they do not cross each other), and repeat the previous analysis for each shell. The previous equations then describe the evolution of any spherical perturbation in which δ_{ov} is a decreasing function of M . In this more general scheme we can write:

$$t_m = \frac{\pi}{2} \left(\frac{R_m^3}{2GM} \right)^{1/2} \quad (1.61)$$

The quantity $t_{coll} = 2t_m$ is called collapse time and it is an estimate of the amount of time necessary for the overdensity to collapse.

N-body simulations

The analytic techniques describe the growth of structures in the linear regime or with spherical symmetry. In order to follow the evolution of cosmological perturbations and the growth of structures beyond these limits, numerical methods are commonly used. These methods are a fundamental tool because they provide the exact solution to the problem of the growth of structure in the non-linear regime. They are classified according to the different mathematical approach to the solution of the dynamic equations into Eulerian

and Lagrangian methods. The Eulerian approach defines a grid (which can be fixed or adaptive) and computes the properties of the fluid at each grid point, while the Lagrangian scheme follows individual mass elements and studies the evolution of their properties. An N -body simulation is a numerical method which follows the evolution of a set of N particles under the effect of gravitational forces (see i.e. Davis et al., 1985). Cosmological simulations are defined on particles in a cubic volume, the so called *box*. An N -body simulation is representative of the evolution of the Universe as a whole, if the volume is large enough to sample scales at which the Universe can be considered homogeneous. A simplified scheme for an N -body is the following: first of all a space grid is defined, then at each timestep the gravitational force acting on each particle is computed as a summation over the gravitational interaction with other particles; finally the new positions and velocities are computed for each particle. A severe limit of N -body simulations is the large amount of computational time they require, which puts limits on the number of particles involved and as a consequence on the reached mass resolution. A number of techniques have been developed in order to decrease the computational time without losing accuracy in the reconstruction of particle positions and velocities. The method involving the direct summation of the gravitational forces is known as *Particle-Particle (PP)* method. PP codes are accurate but they require large computational times. In the *Particle-Mesh (PM)* method the properties of the gravitational field are computed on a grid, then the interaction of each particle with the field is computed. PM codes are fast, with respect to PP, but their resolution is limited by the dimensions of the reference mesh. *Particle-Particle-Particle-Mesh (P^3M)* methods are able to join the velocity of a PM code with the accuracy of a PP code. In P^3M codes the force acting on a particle is divided into two contributions: a short range force, computed using a PP technique and a long range force, computed using PM methods. An alternative to these methods are the so called tree methods. In these schemes the particles are arranged in a hierarchy of groups. When the force on a particle is computed, the force due to distant groups is approximated by their lowest multipole moments. It is common practice (see e.g. Springel, Yoshida & White, 2001) to terminate the expansion after quadrupole moments have been included. The cosmological volume is hierarchically partitioned into a sequence of cubes, where each cube contains eight siblings, each with half the side-length of the parent cube. These cubes form the nodes of the tree structure. The tree is constructed such as each node contains exactly one particle, or is progenitor to further nodes. The force computation proceeds by walking the tree and summing up the contribution from nodes. In the standard formulation the multiple expansion of a node of size l is used if $r < l/\theta$, where r is the distance of the point of reference from the center-of-mass of the cell, and θ is an accuracy parameter. If a node fulfills this criterion the tree walk along this branch is terminated.

1.3.4 Merger Trees

In the standard Λ CDM cosmological model small structures form first than coalesce to form larger and more massive structures. In this section we describe the methods able to follow the assembly history of virialized Dark Matter Halos (DMHs). An example of the hierarchical assembly of a DMH at $z = 0$ is sketched in fig. 1.9: this assembly history is called *DMH merger tree*. Galaxies are thought to form inside DMHs as the result of physical processes (see sec. 1.4): an accurate description of the non-linear evolution of perturbations is thus important in order to model the formation and evolution of galaxies. N -body techniques are able to compute the exact solution of the problem of determining DMH merger trees in a cosmological volume. On the other hand analytic techniques based both on Eulerian or Lagrangian perturbation theory were proposed in order to find an approximate solution of the problem. Analytic techniques have the advantage of being fast and flexible, and are suitable for a Monte-Carlo approach. An analytic description of the DMH assembly processes was first proposed by Press & Schechter (1974). They used heuristic arguments to derive an analytic form for the mass distribution of DMHs present at any given time. Extensions of this theory proposed alternative derivations of the original formalism (see i.e. Cavaliere, Colafrancesco & Menci, 1992; Sheth & Tormen, 1999). The extended Press & Schechter (EPS) theory is used to generate DMH merger trees, (Peacock & Heavens, 1990; Bond et al., 1991; Kauffmann & White, 1993; Lacey & Cole, 1993; Somerville & Kolatt, 1999). The EPS formalism provides an expression for the probability that a halo of given mass m_0 at z_0 has a progenitor of mass m_1 at a given larger redshift z_1 . In order to make the tree finite a minimum mass threshold is usually imposed; the contribution of halos smaller than this limit is taken into account by assuming that their mass is accreted as a diffuse component.

EPS provides a reasonable first approximation to the mass functions of halos (Efstathiou et al., 1988), but it underestimates the number of massive objects and overestimates the number of low mass ones (Governato et al., 1999), with respect to the results of N -body simulations. The merger history of DMHs is reasonably reproduced by EPS, but there are systematic differences when compared with N -body simulations.

Monaco et al. (2002) proposed a new approach for obtaining the information on the assembly history of DMHs, based on Lagrangian Perturbation Theory (LPT see i.e., Moutarde et al., 1991; Buchert & Ehlers, 1993; Catelan, 1995) and on the Zel'dovich (1970) approximation. In this formalism LPT is used in the context of the EPS approach to provide predictions for the collapse of fluid elements in a given numerical realization of a linear density field. Mass elements are assumed to have collapsed after undergoing orbit crossing. The Zel'dovich approximation is used to compute the Eulerian positions of halos at a given time. This algorithm, called PINOCCHIO (PINpointing Orbit-Crossing Collapsed Hierarchical Objects) can accurately reproduce many properties of the DMHs when compared with an N -body simulation that started from the same initial density field. The agreement extends also to the object-by-object level. In fig. 1.9 we show a DMH merger

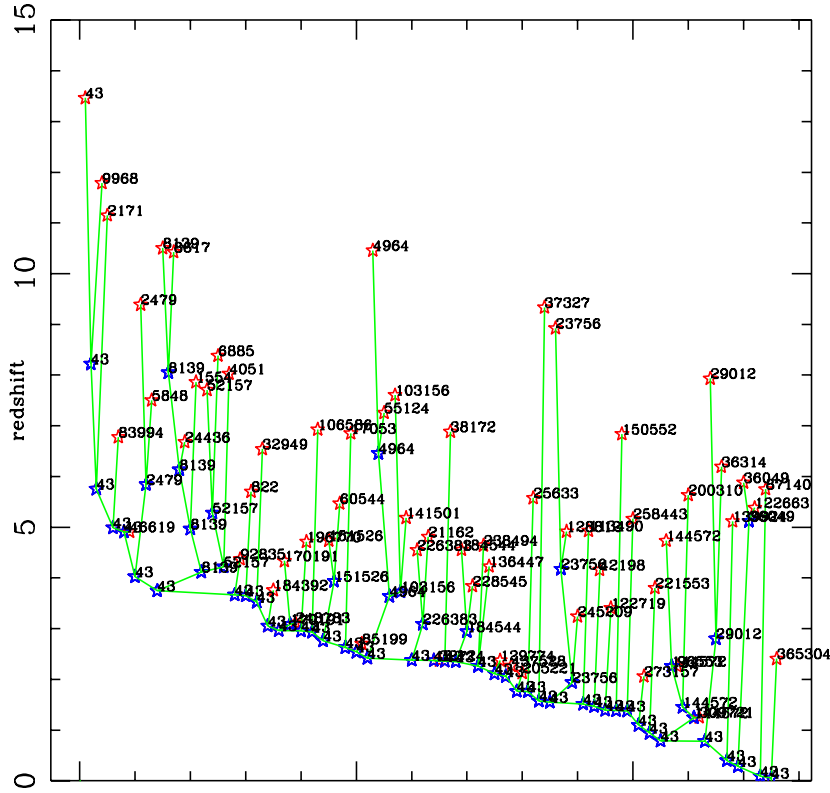


Figure 1.9: Example of Dark Matter Halo merger tree in a PINOCCHIO realization. Numbers identify individual DMHs, red stars mark their formation redshift; blue stars mark merging events.

tree taken from a PINOCCHIO realization.

Comparing the shape of the DMH Mass Function (MF) and the Galaxy Luminosity Function, it is evident that the two functions do not coincide. On the other hand the observed number of L_* galaxies at a given epoch is consistent with the number of expected $10^{12}M_\odot$ DMHs at the same epoch. At masses smaller than $10^{13}M_\odot$ the DMH MF is a power law with a slope much steeper than the faint-end slope of the observed field galaxy luminosity function. Moreover the exponential cut-off of the DM MF (occurring at $\sim 10^{14}M_\odot$) is weaker with respect to the observed luminosity function cut-off: in order to reconcile the bright-end of the LF with the high-mass end of the DM MF, we need a mechanism able to limit star formation in more massive halos.

1.4 Physical processes in galaxy formation

In the previous section we have focused our attention on the purely gravitational aspects of structure formation and hierarchical clustering. This approach provides an adequate description of the evolution of dark matter. However, galaxies are made of baryons and their properties are not determined by gravity alone. In this section we will describe the physical processes that are thought to play a major role in determining the morphology and SEDs of galaxies. Baryonic gas is driven at the center of massive dark matter halos by dissipative and radiative processes, producing a separation between dark and luminous material. Star formation converts cold gas into stellar populations. Finally, energy feedback onto the gas from dying stars and AGNs has severe effects on the state of the gas (and as a consequence on its star formation history).

In the following sections we divide such processes into two categories: thermal and gravitational processes.

1.4.1 Thermal Processes

Shock Heating

As we saw in 1.3.3, when a non-linear perturbation disentangles from the uniform expansion of the Universe as a whole, it starts collapsing as a close Universe. We can assume that after collapse this perturbation reaches a condition of virial equilibrium between its kinetic energy E_K and its potential energy E_Φ :

$$2E_K + E_\Phi = 0 \tag{1.62}$$

which becomes, for spherical systems:

$$M\sigma^2 = \alpha \frac{GM^2}{R} \tag{1.63}$$

where α is a coefficient depending on the mass distribution and σ is the velocity dispersion of the system.

During the collapsing phase the gas is assumed to be heated through violent relaxation processes and shock waves up to an equilibrium temperature called *virial temperature*:

$$T_v = \frac{\mu m_p \sigma_0^2}{3k} \tag{1.64}$$

where μ is the molecular weight of the gas, m_p the proton mass, σ_0 the velocity dispersion and k the Boltzmann constant.

Gas Cooling

We describe gas cooling following the approach of White (1996) The first mechanism of gas cooling is the so-called Compton cooling. Low energy

photons passing through a thermal gas of non-relativistic electrons scatter with Thompson cross section σ_T :

$$\sigma_T = \frac{8\pi}{3} \left(\frac{e^2}{m_e c^2} \right)^2 \quad (1.65)$$

where m_e is electron mass and e electron charge. The tendency to energy equipartition leads to a mean gain in photon energy per collision:

$$h\Delta\nu = \frac{4kT_e}{m_e c^2} h\nu \quad (1.66)$$

where T_e is the electron temperature. In a thermal background of photons with temperature T_γ the mean energy loss rate of electrons is thus:

$$\frac{dE_e}{dt} = \int d\nu n_\nu \sigma_T c h \Delta\nu = \frac{4kT_e}{m_e c^2} \sigma_T a T_\gamma^4 \quad (1.67)$$

where a is the standard radiation constant. A fully ionized gas of primordial composition will cool against the CMB ($T_e \gg T_\gamma(z)$) on the timescale:

$$t_{\text{compcool}} = \frac{3m_e c}{4\sigma_T a T_\gamma^4} \quad (1.68)$$

This timescale is independent of gas density and temperature. However, Compton cooling has a lower efficiency at decreasing redshift. Even at very high redshift ($z \sim 10$) Compton cooling on galactic scale is less effective than radiative cooling.

At temperatures of above $10^6 K$ (the same conclusion holds for enriched gas at $10^7 K$) baryonic gas is almost entirely ionized. The only significant process is then bremsstrahlung due to the acceleration of an electron in a scattering processes with atomic nuclei. The cooling rate of such a process is simply:

$$\frac{dE}{dt} \propto n_e n_H T^{0.5} \quad (1.69)$$

where n_e and n_H are the electron and hydrogen number densities respectively.

As the temperature decreases electrons can recombine with ions, emitting the excess energy with a photon. Partially ionized atoms can be excited by electron collisions thereafter decaying radiatively to the ground state. In both cases the gas loses energy to the radiated photon. Both processes depend strongly on temperature either for the temperature sensitivity of the recombination coefficient, or for the temperature dependence of ion abundance. Assuming ionization equilibrium for the gas we can write the cooling per unit volume for both processes as:

$$\frac{dE}{dt} \propto n_e n_H f(T) \quad (1.70)$$

It can be demonstrated that the second process (collisional excitation of partially ionized atoms) is dominant. The rate of the specific energy loss due to radiative cooling is given by the cooling function $\Lambda(T)$. Figure 1.10 shows

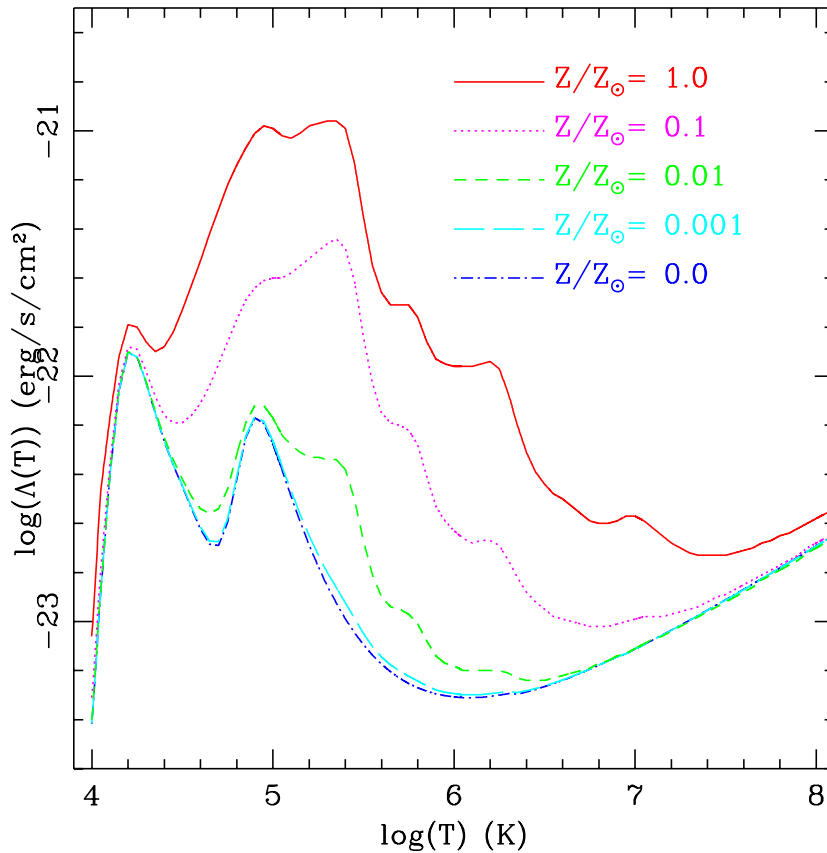


Figure 1.10: Cooling Function $\Lambda(T)$ (Sutherland & Dopita, 1993) at various metallicities.

the cooling function proposed by Sutherland & Dopita (1993) for different gas metallicities. For primordial gas the cooling rate peaks at a temperature $T = 1.5 \times 10^4$ (hydrogen) and $T = 10^5 K$ (helium). Gas with solar metallicity shows another peak at $T = 10^5 K$ due to oxygen, and the presence of a variety of other elements enhances cooling at around $T = 10^6 K$. At temperature below $T = 10^4 K$ gas is predicted to be almost completely neutral and the cooling rate drops quickly. Some cooling due to collisional excitation of molecular vibrations may be possible if molecules are indeed present. Cooling by collisional excitation and subsequent radiative decay can be suppressed in presence of a strong UV background. In this case the abundance of partially ionized elements is reduced by photoionization. This phenomenon depends on the spectrum of the UV background and on the ratio between gas and UV photon densities. Such suppression is therefore most likely to be important at early stages of galaxy formation for low mass objects (see i.e. Efstathiou, 1992; Babul & Rees, 1992).

Star Formation

Star Formation takes place in the cooled gas clouds if their self-gravity is sufficient to overcome thermal pressure. Let us consider an uniform cold gas cloud of radius R , mass M , temperature T , density ρ and mean molecular weight μ . We can express its thermal energy E_K and its gravitational energy E_Φ as:

$$\begin{aligned} E_K &= \frac{3kTM}{2\mu m_p} \\ E_\Phi &= -\frac{GM^2}{R} \end{aligned} \tag{1.71}$$

The condition for the cloud collapse is then:

$$\begin{aligned} M &> M_J \\ M_J &= \left(\frac{3kT}{2G\mu m_p} \right)^{3/2} \left(\frac{4\pi\rho}{3} \right)^{-1/2} \end{aligned} \tag{1.72}$$

M_J is the so called *Jean Mass*; it represents the limiting mass for the collapse of a gas cloud into stars. It can be expressed in terms of the number density n :

$$M_J = 15.4 T^{3/2} \mu^{-2} \left(\frac{n}{1\text{cm}^{-3}} \right)^{-1/2} M_\odot \tag{1.73}$$

The most likely sites for star formation are molecular clouds where density is high enough and temperature quite low. In order to understand the formation of low-mass stars from giant molecular clouds, the hierarchical fragmentation theory was proposed (see i.e. Reed, 1976). According to this theory the collapse of a giant molecular cloud is not uniform, but as the process goes on the mean density of the cloud increases, and some disomogeneities in the cloud can reach their Jeans mass and start to collapse on their own. In order to reach the conditions for priming nuclear reactions, the gas has to loose almost all of its angular momentum. The angular momentum can be transferred both to protostars during the fragmentation process and to the external regions of the cloud due to the interaction of the gas particles with the intracloud magnetic field.

Schmidt (1959) studied star formation in nearby galaxies; he proposed that the amount of gas converted into stars per unit time and unit volume is proportional to a power law of the gas density:

$$\frac{d\rho_{gas}}{dt} \propto \rho_{gas}^m \tag{1.74}$$

Schmidt proposed a value for the exponential $m = 2$, nowadays a value $m < 2$ is commonly assumed (see i.e., Kennicutt, 1998). If $m > 1$ the time scale for gas consumption is proportional to a negative power of gas density: it means that regions with the higher initial density are more efficient in turning their gas into stars.

Semi-analytical models of galaxy formation and evolution proposed several parameterization for the star formation rate \dot{m}_\star (see i.e. Somerville & Primack, 1999) in galactic discs as a function of the cold gas mass m_{cold} . We deal with this topic here for completeness. A more detailed description of the semi-analytical modeling will be presented in sec. 1.5.1. The more general recipe is to consider a star formation in the form:

$$\dot{m}_\star = \frac{m_{cold}}{\tau_\star} \quad (1.75)$$

with the star formation efficiency factor τ_\star taken as a free parameter. Kauffmann et al. (1993) proposed that the timescale for star formation is proportional to the dynamical time of the disc $\tau_{dyn} = r_{disc}/V_C$:

$$\dot{m}_\star = m_{cold} \tau_\star^0 \tau_{dyn} \tau_{dyn} = r_{disc}/V_C \quad (1.76)$$

where r_{disc} is the radius of the disc, V_C its circular velocity and τ_\star^0 is a free parameter of the model. Cole et al. (2000) proposed that the star formation efficiency is a function of the circular velocity of the disc:

$$\dot{m}_\star = \frac{m_{cold}}{\tau_\star^0} \left(\frac{V_C}{V_0} \right)^{-\alpha_\star} \quad (1.77)$$

in this recipe τ_\star^0 and α_\star are free parameters and V_0 is an arbitrary normalization factor. If we assume in eq. 1.76 that the disc radius proportional to the virial radius of the host DMH, the dynamical time at a given redshift is independent of the circular velocity. On the other hand the star formation efficiency increases at higher redshift. On the contrary eq. 1.77 has no explicit dependence on redshift but it depends strongly on circular velocity (Cole et al., 2000 proposed $\alpha_\star = -1.5$). Star formation is then less efficient in halos with small V_C .

Stellar Feedback

The cooling mechanisms we describe in 1.4.1 are expected to be very efficient at high-redshift in turning the shock-heated gas in cold material able to form stars. However, if we assume that every DM halo processes all of its gas into stars we run into several problems in explaining the observed galaxy properties, both in terms of stellar mass content and stellar populations (“overcooling” problem, see, i.e. White & Rees, 1978). At larger halo masses and lower redshifts this scenario also predicts large cooling flows at the center of galaxy clusters (see i.e. Fabian, 1994), whereas observations show no emission line due to warm or cold material in these regions, as expected in this scenario (Peterson et al., 2001). Therefore we have to arrange for some process able to limit cooling and to prevent too much gas turning into stars. One process that has been advocated in the literature envisions stellar feedback from supernovae (SNe) and evolving stars as the main mechanism able to reheat galactic gas. The total energy released by SNe is enough to unbind the baryons from galaxy halos, especially from the potential wells of low-mass systems (see, i.e., Dekel & Silk, 1986).

Stellar feedback is the result of two processes. The first mechanism is related to the strong radiation provided by massive young hot stars, while the second process is linked to the energy injection by SNe explosions. The ability of the energy from SNe to emerge from the star-forming cloud is strongly related to the physical conditions of the gas the cloud itself.

We can describe the mass distribution of a single generation of stars in terms of the *Initial Mass Function* $\phi(m)$ (hereafter IMF). Typical analytical approximations are based on observations in the solar neighborhood and are well described in the mass range $0.1M_{\odot} < m < 100M_{\odot}$ by the following equation:

$$\phi(m) \propto m^{-(1+x)} \quad (1.78)$$

Salpeter (1955) proposed a value $x = 1.35$. Alternative prescription for the IMF were proposed by Kennicutt (1983, 1998), Scalo (1986, 1998), Arimoto & Yoshii (1987) and Kroupa et al. (1990). Nowadays there is evidence that the IMF slope at low masses is flatter than a Salpeter form. The high mass tail of the IMF contains a limited number of objects, however the ionizing flux of these massive stars is enough to destroy the molecular cloud they are formed from before to onset of the first supernovae (Monaco 2004b, Matzner, 2002).

Models of galaxy formation and evolution typically assume that the mass of the gas reheated by stellar feedback \dot{m}_{reh} is proportional to the energy injected by supernovae E_{SN} , to the star formation rate \dot{m}_{\star} and either to the circular velocity of the halo V_C or to the escape velocity v_{esc} :

$$\dot{m}_{reh} = \epsilon_0 \frac{\eta_{SN} E_{SN}}{V_C^2} \dot{m}_{\star} \quad (1.79)$$

where ϵ_0 is a free parameter and η_{SN} is the number of supernovae per solar mass. An alternative formulation is the following (Cole et al., 2000):

$$\dot{m}_{reh} = \epsilon_0 (V_0/V_C)^{-\alpha_{reh}} \dot{m}_{\star} \quad (1.80)$$

where V_0 is a scaling parameter chosen so that ϵ_0 is of order unity.

Recently Monaco (2004a) proposed an improved formulation for stellar feedback, based on a detailed treatment of the physical conditions of the gas. In this model the explosion of SNe leads to the destruction of the star-forming cloud in $\sim 3Myr$: SN remnants percolate very soon, creating a single Super-Bubble (SB) for each forming cloud. The fate of SBs depends on the density and vertical scale-length of the system they belong to. Monaco (2004a) distinguished between thin systems, like spiral discs, where SBs blow out, and thick systems, like bulges, where SBs are confined by the pressure of the hot phase. Both blow-out and pressure confinement take place either in the adiabatic expansion phase, or after that part of the internal gas has cooled down and collapsed to a cold shell, pushed by the pressure of the remaining hot gas. This shell is called pressure-driven snowplough (PDS). The combination of different conditions lead to the definition of four feedback regimes, depending on whether SBs blow out or are confined before or after the onset of PDSs: Monaco (2004a) provided analytical formulations for all of them.

Hot gas is usually kept confined in galaxies by gravity and external pressure. However energy injection due to star formation and feedback processes can increase the energy of the gas up to a point at which the gas can escape the potential well. The relevance of these processes is related to the amount of gas involved. When only a small fraction of gas gains enough energy to escape we deal with single escaping clouds, on the other hand, when the process involves the galaxy as a whole we are in presence of a *galactic wind* (see i.e. Strickland 2004,2002).

1.4.2 Gravitational Processes

Infall

The evolving dark halos provide the framework for galaxy formation: the properties of galaxies depend on the amount of cool dense gas which accumulates into halo cores, on the efficiency of star formation from such gas, and on the interactions between galaxies.

It is possible to define a cooling radius r_{cool} as the radius within which the gas has had time to cool within the timescale τ_{cool} . The cooled material falls towards the galaxy at the center of the halo on a dynamical timescale. The amount of infalling material is limited by the longer between this two timescales, so it is straightforward to distinguish between two different cooling regimes. In the first one, we call *infall limited regime*, the gas cooling time is shorter than the dynamical timescale throughout the halo. We can approximate the rate of accumulation of cold gas with:

$$\dot{M}_{inf} \propto fV_c/G \quad (1.81)$$

where we indicate with f the fraction of material in the form of gas. It is worth noting that this estimate is independent of time. We can also define a *cooling limited regime* in which the cooling time in the outer halo is long compared to the dynamical time. We can estimate the rate at which cold gas accumulates as:

$$\begin{aligned} \dot{M}_{cool} &= 4\pi\rho(r_{cool})r_{cool}^2\frac{dr_{cool}}{dt} \\ &= fH_0(1+z)^{3/2}\frac{3V_c^2r_{cool}(V_c,z)}{4G} \\ &\propto f^{3/2}(1+z)^{3/4} \end{aligned} \quad (1.82)$$

The dependence on V_c is more complex than in eq. 1.81.

Comparing this two formulations we can see that for a given V_c cooling is more efficient at higher redshifts and for larger gas fractions. \dot{M}_{cool} can not be larger than \dot{M}_{inf} because gas has to be accreted before flowing to center. Then the supply of cold gas to the central region is approximated by:

$$\dot{M}(V_c, z) = \min(\dot{M}_{cool}, \dot{M}_{inf}) \quad (1.83)$$

Disc Formation

We saw in the previous sections that the baryonic gas in DMHs is subject to cooling processes that lead to the formation of cold clouds and subsequent star formation. In particular, the cooled gas collects at the center of each dark matter halo where it forms a self-gravitating structure. In this structure star formation and feedback processes occur.

The acquisition of angular momentum J of DMHs, due to tidal torques by the large scale structure, is described, i.e. in Catelan & Theuns, (1996). In the following we will assume that the baryonic matter acquires the same specific J . For an isolated system the mass M , energy E , and angular momentum J are all conserved under gravitational evolution. It is useful to define a dimensionless quantity known as *spin parameter*:

$$\lambda_{sp} = \frac{|E|^{1/2}|J|}{GM^{5/2}} \quad (1.84)$$

The spin parameter measures the relative importance of angular momentum and does not vary during collapse.

For an equilibrium system we can use the virial theorem to get:

$$\lambda_{sp} \sim 0.4V_{rot}/\sigma \quad (1.85)$$

where V_{rot} is the mean rotation velocity. N -body simulations produce value of λ_{sp} in the range $0.01 < \lambda_{sp} < 0.1$, with a median value of 0.05. Fall & Efstathiou (1980) showed that if galactic spin is related to tidal torques acting on DMHs, then extended halos are required to explain discs as large as these observed at present day. They also found that plausible initial angular momentum distributions for the gas could lead to near-exponential density profiles for the final disc. They proposed a log-normal approximation for the λ_{sp} distribution:

$$p(\lambda_{sp})d\lambda_{sp} = \frac{1}{\sqrt{2\pi}\sigma_{\lambda_{sp}}} \exp\left[-\frac{\ln^2(\lambda_{sp}/\bar{\lambda}_{sp})}{2\sigma_{\lambda_{sp}}^2}\right] \frac{d\lambda_{sp}}{\lambda_{sp}} \quad (1.86)$$

where $\bar{\lambda}_{sp} = 0.05$ and $\sigma_{\lambda_{sp}} = 0.5$. This function is a good fit to the N -body simulations results (i.e. Warren et al. 1992).

Following Mo, Mao & White (1998) we will focus on the predicted disc properties under the hypothesis that both mass and angular momentum of gas are proportional to the related quantities of host DMH. If we assume that DMHs are singular isothermal spheres, we can then express the density profile $\rho(r)$ as:

$$\rho(r) = \frac{V_c^2}{4\pi Gr^2} \quad (1.87)$$

where the circular velocity V_c is independent of radius r . Based on the result of section 1.3.3 we define the limiting radius of a DMH the radius r_{200} within which the mean mass is equal to $200\rho_{crit}$. We can define radius and mass at a given redshift z as:

$$r_{200} = \frac{V_c}{10H(z)} \quad (1.88)$$

$$M = \frac{V_c^2 r_{200}}{G} = \frac{V_c^3}{10GH(z)} \quad (1.89)$$

If the mass M_d settling into a disc is a fixed fraction m_d of the DMH mass then:

$$M_d = \frac{m_d V_c^3}{10GH(z)} \quad (1.90)$$

We now assume that disc are thin systems in centrifugal balance and with an exponential surface density profile:

$$\Sigma(R) = \Sigma_0 \exp(-R/R_d) \quad (1.91)$$

where R_d and Σ_0 are the disc scalelength and central surface density and:

$$M_d = 2\pi \Sigma_0 R_d^2 \quad (1.92)$$

Neglecting the gravitational effect of the disc, the rotation curves are flat at the level V_c and the angular momentum can be expressed as:

$$J_d = 2\pi \int V_c \Sigma(R) R^2 dR = 2M_d R_d V_c \quad (1.93)$$

Assuming $J_d = j_d J$ we get:

$$R_d = \frac{\lambda_{sp} j_d G M^{3/2}}{2m_d V_c |E|^{1/2}} \quad (1.94)$$

If we calculate the total energy E of a truncated isothermal sphere and we use definitions 1.88, 1.89, 1.92:

$$R_d = \frac{\lambda_{sp} j_d r_{200}}{\sqrt{2} m_d} \quad (1.95)$$

The previous equations describe the scaling of disc properties with respect to physical parameters. Since $H(z)$ increases with redshift, disc of fixed V_c are less massive, smaller and have higher surface densities with increasing redshift.

Disc Instabilities and Bulge Formation

The description of the previous section leads to a wide range of possible disc configurations. It is easy to prove that not all of them are stable. In fact, when the self-gravity becomes dominant, the disc is dynamically unstable to the formation of a bar. In this work we will refer to the results of Efstathiou, Lake & Negroponte (1982). They use N-body simulations to investigate global instabilities of exponential discs. According to their findings the onset of the bar instability can be described by the following criterion:

$$\epsilon = \frac{V_{max}}{(GM_d/R_d)^{1/2}} < \epsilon_{lim} \quad (1.96)$$

where V_{max} is the maximum rotation velocity of the disc. The critical value is $\epsilon_{lim} \sim 1$. Efstathiou, Lake & Negroponte (1982) proposed $\epsilon_{lim} \leq 1.1$ for a stellar disc, while Christodoulou et al. (1995) showed that $\epsilon_{lim} \leq 0.9$ is the preferred value in the case of a gaseous disc.

Disc instability results in the stellar disc evolving into a bar and then into a spheroidal bulge. Bulge formation is also due to interaction of the galaxy with the environment and with other objects, both through processes of disc instability and merging.

Dynamical Friction

Let us consider a massive body surrounded by a sea of less massive particles. If the massive body is at rest, it will induce an enhancement of the density around itself. The situation changes if the body is in relative motion with respect to the sea of particles. In this case the massive body creates a swarm of particles with a density greater than the mean density. This swarm slows the motion of the massive body. This process is called *Dynamical Friction*. The effect of gravitational force on a point-like body with mass M and velocity \mathbf{v} in motion in a homogeneous medium of non-collisional particles with density ρ_{part} and isotropic velocities can be analytically solved. The resulting expression (Chandrasekar 1949) is:

$$\frac{d\mathbf{v}}{dt} = -4\pi G^2 \frac{\mathbf{v} M \rho_{part} A(v) \ln(A)}{v^3} \quad (1.97)$$

The function $A(v)$ depends both on the velocity of the body and on the velocity distribution σ_{vp} of the particles. It behaves as $A(v) \propto -v$ for $v \ll \sigma_{vp}$ and $A(v) \propto -1/v^2$ for $v \gg \sigma_{vp}$. This implies that $d\mathbf{v}/dt \propto M$ (the force is proportional to M^2) for low velocities and $d\mathbf{v}/dt \propto \rho_{part}$ for high velocities.

In cases of interest the massive body is a galaxy and the particles represent DM particles of a cluster. The energy is transferred to the DM particles from galaxies and the net result is that galaxies tend to fall toward the center of the cluster. We can define a timescale for the process:

$$\tau_{DF} = \frac{v}{dv/dt} \quad (1.98)$$

At the end the galaxy merges with the one at the center of the cluster.

Tidal Stripping

When a galaxy has a close encounter, it feels the tidal field of the interacting body. A fraction of the orbital energy is then redistributed to external regions: these regions start to lose their mass (*collisional tidal stripping*). The effect is greater for close and slow encounters. This phenomenon has also a consequence on the maximum dimensions of galaxies in groups and clusters

(*tidal truncation*). Let us consider a spherical mass m with radius r lying at a distance d from a point-like object of mass M . We can write an equilibrium equation for the particles on the surface:

$$\frac{GM}{d^2} \left(\frac{d^2}{(d-r)^2} - 1 \right) = \frac{Gm}{r^2} \quad (1.99)$$

We can easily derive an expression for the *tidal radius* r_t :

$$r_t = \left(\frac{m}{2M} \right)^{1/3} d \quad (1.100)$$

This result holds for a free falling mass. If we consider an orbiting spherical mass, we get:

$$r_t = \left(\frac{m}{3M} \right)^{1/3} d \quad (1.101)$$

It implies that elongated orbits correspond to smaller truncations.

As the geometry gets more and more complicated (as in the case of a galaxy orbiting into a cluster) the dependence of the tidal radius on the orbit increases. However we can write the following useful approximation (σ_v^{gal} and $\sigma_v^{cluster}$ are the velocity dispersions in galaxy and cluster, d_b is the distance from the cluster barycenter):

$$r_t = \frac{\sigma_v^{gal}}{\sigma_v^{clu}} d_b \quad (1.102)$$

Moreover the interaction of galaxies at velocity v with the hot intragalactic medium of density ρ_{IGM} gives rise to a process known as *ram pressure stripping*. It is possible to demonstrate that the pressure is:

$$p_{ram} \sim \rho_{IGM} v^2 \quad (1.103)$$

The interstellar medium of the galaxy is removed when pressure overcomes gravitational attraction. The process is more efficient at the center of clusters and for galaxies with less ISM.

Galaxy Mergers

During hierarchical clustering DMHs merge continually, increasing their mass. Thus collisions and mergers of galaxies are also frequent. Satellite galaxies lose their angular momentum due to dynamical friction and merge with the central galaxy, but they can also merge with others satellites in case of binary encounters. The result of the merging event depends on the masses of the progenitors. The case of a small object being captured by the gravitational field of a massive galaxy is called a minor merger. On the other hand the case of two galaxies with similar masses is called a major merging event. Moreover The properties of the resulting objects depend on the ratio between masses and on orbital parameters. If a disk galaxy accretes an object of mass greater than 20 – 30% of its own mass, both theoretical arguments and numerical

experiments suggest that the stellar disk will be disturbed and may no longer resemble a “typical” spiral disk. Detailed N-body simulations show that the result of such an event has the kinematical properties of an elliptical galaxy.

1.5 Models of galaxy formation and evolution

In the previous section we analyzed the most important non-gravitational processes that influence galactic structure. It is worth noting that we have only a limited knowledge of the interplay between these processes that determine the mass assembly sequence of the different galaxy populations. Moreover, these processes are often modeled using local observation (as an example, models of star formation are based on observations on nearby objects). This introduces even more uncertainties. In order to give strong constraints about the relative importance of the various processes, models of galaxy formation must be compared to local and high redshift observations. The use of multiwavelength observations is a fundamental tool: as we pointed out in sec. 1.2.1 different electromagnetic bands sample different emission mechanisms and different properties of the same object. For this reason if we require that a model correctly predicts the observed properties of galaxies at different wavelength at the same time, we are able to understand both the present-day properties of the objects and their assembly history. The properties of galaxy populations that a model should predict are the distribution of stellar masses (*Stellar Mass Function*), luminosity in different bands (*Luminosity Functions*), sizes, morphologies, Tully-Fisher relation for spiral galaxies and the fundamental plane of elliptical galaxies. A relevant issue is the relationship between morphology and environment of a galaxy, but also the photometric properties of galaxies (color distributions, color bimodality) play a key role in constraining models. In order to give constraints on the processes responsible for the evolution of galaxies, models have to deal with the distribution of sources in the Universe, in particular the prediction of *Number Counts* in various bands and the *Redshift Distribution* of sources.

Several techniques are nowadays available for modeling galaxy formation and evolution. Among these we will focus our attention on Smoothed Particle Hydrodynamics (SPH) and Semi-Analytical Modeling.

In a cosmological volume the dynamics of the DM is determined by gravitational forces alone, and is accurately recovered by N -body simulations (sec. 1.3.3), which provide a description of the evolution of structures into the highly non-linear regime where DMHs form. On the other hand, gas is subject to pressure forces and radiative effects. SPH is a Lagrangian numerical method which follows the motion of a set of gas particles. The thermal energy, velocity and position of each particle are known at any given time by solving the hydro- and thermo-dynamic equations of motion. Estimates of gas properties at each particle position are derived by smoothing over the nearest neighborhood particles (see i.e. Monaghan, 1992). These gas properties are then used to calculate the forces acting on each particle in order to update their thermal

energies, velocities and positions. The situation is complicated by the fact that thermal processes such as star formation and stellar feedback involve length and mass scales orders of magnitude smaller than those addressed by typical cosmological boxes: this evidence forces the use of phenomenological recipes and prescriptions to address these processes (Katz, Weinberg & Hernquist, 1996; Springel & Hernquist, 2003).

In semi-analytical models (see i.e. Kauffmann et al. 1993, Cole et al. 2000, Somerville & Primack, 1999, Menci et al., 2003, Hatton et al., 2004) the processes involved in galaxy formation (i.e. DMHs assembly through mergers), are followed using analytic solutions and/or Monte-Carlo techniques. Other processes (i.e. star formation rate) are modeled by means of simple and physically motivated recipes. A set of parameters describes the various processes and their interplay. These parameters are usually fixed by comparing model predictions to observations. In these models the dynamics of the gas is strongly coupled with the evolution of DMHs.

Both techniques require a number of simplifying assumptions in order to model the evolution of the baryonic gas. However, these assumptions are very different between the two approaches, consequently SPH and semi-analytical models have complementary strengths and weaknesses and are both useful for studying different aspects of galaxy formation and evolution (see i.e. Benson et al., 2001 and Helly et al. 2003 for a comparison between the results of SPH and semi-analytical models). The key assumption of the SPH requires that the evolution of gas is well approximated by the evolution of a set of particles, carrying the information about the thermodynamical properties of the system. However, due to the smoothing, the description of the regions where the gas properties vary discontinuously (or at a scale much smaller than the smoothing scale) is poor. Semi-analytical models make several assumptions in the treatment of gas in order to obtain simple, analytic solutions to the complex hydrodynamic processes. They assume that DMHs are spherically symmetric and that infalling gas is shock-heated to the virial temperature of the halo and then settles with an universal density profile. On the contrary, SPH does not impose any restriction on the halo geometry and solves directly the equations for the evolution of both DM and gas particles leading to accurate representation of resolved objects. However limited resolution restricts the accessible dynamical range and the computational requirements of cosmological simulations limit the parameter space explorations. On the other hand semi-analytical models are computationally cheaper and reach extremely high mass resolutions in the halo merger trees. This features allow for a deeper investigation of the effect of varying both the parameter space or the treatment of processes.

1.5.1 Semi-analytical models

In this section we will describe the semi-analytic models that have been proposed in the literature. The semi-analytic approach was first formulated by White & Frenk (1991); we refer to the models presented in Kauffmann,

Guiderdoni & White (1993), Cole et al. (2000), Somerville & Primack (1999), Menci et al. (2004), Hatton et al. (2003), Granato et al. (2004). The number of parameters involved is large, and it is important to adopt a strategy for fixing the value of as many parameters as possible, in order to analyze the dependence of the results on the most interesting ones. A common technique adopts a small subset of local galactic observations. The request of a correct prediction of this dataset is used to constrain the parameter space of the models. In particular the most important local constraints are given by the luminosity function in B -band and K -band; the relative fraction of morphological types; the slope of the Tully-Fisher relation at faint magnitudes; the gas fraction in discs as a function of B -band luminosity; the distribution of disc sizes and the metallicity of ellipticals. Once the parameters have been set, the model predictions are then tested against a wide range of other observations such as the color distribution, the color-morphology relations, the elliptical color-magnitude relation, the cosmic star formation history, the redshift distribution of galaxies. In order to predict galactic SEDs semi-analytical models are interfaced with spectrophotometric codes. We will describe spectrophotometric codes as well as the role of dust absorption with great detail in 7.1.

In the following paragraphs we will describe some semi-analytical models with great detail. For each model we listed the most important assumptions, namely the computation of merger histories of DMHs; the assumed DM and gas distribution in DMHs; the assumed gas cooling function; the model for the disc formation; the recipes for star formation and feedback; the model for dynamical friction and orbital decay; the description of merging events; the model for chemical enrichment and the interface with the spectrophotometric code. A summary of the following paragraphs is given in table 1.1.

Kauffmann, Guiderdoni & White, (1993)

The original model has been proposed in Kauffmann, Guiderdoni & White (1993) and related papers (Kauffmann, 1996; Kauffmann & Charlot, 1998). Improvements have been presented in Kauffmann, et al. (1999) and Kauffmann & Haehnelt (2000) with the inclusion of a treatment for the growth and evolution of SMBH at the center of model galaxies.

- Merger histories of DMHs are computed following the extended Press & Schechter formalism, using the halo merger rate derived by Kauffmann & White (1993). In other versions they use merger histories extracted from N -body simulations.
- DMHs are modeled as truncated isothermal spheres.
- Gas distribution follows DM distribution.
- Gas cooling is described following White & Frenk (1991).
- Disc formation follows the modeling proposed by Mo, Mao & White (1998).

- Star formation within discs occur at a rate proportional to the mass of cold gas m_{cold} and with an efficiency proportional to the dynamical time τ_{dyn} of the disc ($\dot{m}_* = m_{cold}/(\tau_*^0 \tau_{dyn})$).
- Stellar feedback is modeled using 3 parameters ($\dot{m}_{reh} = \epsilon 4 \dot{m}_* \eta_{SN} E_{SN} / (3V_C^2)$). All the reheated gas is retained in the halo.
- When a new halo form each satellite galaxy enters the halo on a random orbit.
- Satellites merge on central galaxy on a dynamical friction timescale (Binney & Tremaine, 1987). Spheroids form trough mergers between galaxies of comparable mass. Mergers are classified according to the mass ratio between the satellite and the central galaxy. The discriminant value is 0.3.
- Instantaneous Recycling Approximation (Tinsley, 1980) is assumed for metal enrichment.
- Galaxy SEDs are computed using Bruzual & Charlot 2003 with a Kennicutt (1998) IMF.

This model is able to reproduce the local B -band and K -band luminosity function, the Tully-Fisher relation, the evolution of the star formation rate as a function of redshift, the evolution of the total mass density in cold gas, the variations of galaxy clustering with luminosity, morphology and reshift.

On the other hand this model does not reproduce the the correlation between the abundance of α elements (C, O, Si, Mg) relative to Iron and the velocity dispersion of elliptical galaxies (Thomas et al., 2002; Trager et al., 2000a,b). The predicted number density of elliptical galaxies decrease with redshift at variance with K -band observation which reveal a substantial population of passive galaxies already in place at $z \sim 1$ (Cimatti et al., 2002). The assumed cooling model predicts substantial cooling flows at the center of more massive halos, leading to the formation of galaxies that are too massive, too bright and too blue, with respect to the observations. In order to overcome this problem it is usually assumed that gas cooling in halos with circular velocity greater than some fixed value does not form stars.

Kauffmann & Haehnelt (2000) include in this framework a treatment for the growth and evolution of SMBH at the center of galaxies. Using their recipes they compute the cosmological evolution of the quasar sources powered by these objects during their accretion phases. They assume that SMBHs grow by merging and accretion of gas during major mergers of galaxies: in fact, according to N -body simulations results, galaxy mergers drive gas towards central galactic regions. When a merger between two galaxies takes place, they assume that the two pre-existing BHs at the center of progenitors coalesce instantaneously. In major merger events a fraction of the cold gas in progenitors is also accreted onto the new BH. A key assumption in this model is that the fraction of available cold gas accreted by BHs is smaller for low mass galaxies. Other physical processes able to accrete gas onto SMBHs,

such as gas accretion during minor mergers and accretion from gas halo, are neglected. This model reproduces the observed local relation between the velocity dispersion of spheroids (spiral bulges and ellipticals) and the mass of SMBH they host, the redshift evolution of bright quasars ($M_B < -24$) space density. It is worth noting that this last prediction is related to the assumption that in merging events star formation rate in spheroids and SMBH accretion are proportional and that the star formation efficiency $1/\tau_\star^0 \propto (1+z)^{-2}$.

Cole, Lacey, Baugh & Frenk, (2000)

Here we refer to the model of Cole et al. (2000). However several improvements have been proposed in Benson et al. (2003) Baugh et al. (2005) and Bower et al. (2005).

- Merger histories of DMHs are computed following the extended Press & Schechter formalism, using the analytic expression for halo merger rates derived by Lacey & Cole (1993). In Bower et al. (2005) they adopt the DMH merging trees extracted from the Millennium Simulation (Springel et al., 2005).
- A Navarro, Frenk & White (1996) profile for the DM distribution inside the halo is assumed.
- Diffuse gas in the halo is shock-heated at the virial temperature and its distribution follows a β -model profile (Cavaliere & Fusco-Fermiano, 1976)
- Cooling is described following the cooling function proposed by Sutherland & Dopita (1993) and the cooling radius approach of Frenk & White (1991).
- Disc formation follows the modeling proposed by Mo, Mao & White (1998).
- Star formation occurs within discs at a rate proportional to the mass of cold gas and with an efficiency which is function of the circular velocity of the disc ($\dot{m}_\star = m_{cold}/(\tau_\star^0 (V_{disc}/V_0)^{\alpha_{star}})$).
- Feedback efficiency is specified in terms of the circular velocity of the disc and it is modeled as follows: $\dot{m}_{reh} = \epsilon_{SN} (V_{disc}/V_0)^{-\alpha} \dot{m}_\star$. In early models all the reheated gas is ejected from the halo and returned after the mass of the halo has doubled, later models (Benson et al., 2003) compute the fraction of the reheated gas that is either ejected or retained.
- When a new halo forms each satellite galaxy enters the halo on a random orbit; orbit distribution follows Tormen (1997).
- Orbital decay of satellites due to dynamical friction is modeled following Lacey & Cole (1993). The outcome of each merger depends on the mass ratio between the satellite and the central galaxy. The discriminant value is 0.3. Elliptical galaxies are the outcome of major mergers. Disc instability is modeled but not taken into account in their reference model.

- Instantaneous Recycling Approximation is assumed for metal enrichment. Yields are computed following Renzini & Voli (1981) and Woosley & Weaver (1995).
- Galaxy SEDs are computed using Bruzual & Charlot 2003 with a Kennicutt (1983) IMF. In Baugh et al. (2005) they use the GRASIL spectrophotometric code with a top-heavy IMF.

This model is able to reproduce the B -band and K -band luminosity functions, the distribution of colors for the galaxy population as a whole, the ratio between morphological types, the distribution of disc sizes and the current cold gas content of discs. An interesting discrepancy between Cole et al. (2000) and Kauffmann et al. (1993) models is the fact that these models are not able to reproduce the B -band luminosity function and the normalization of the Tully-Fisher relation *at the same time*. This evidence is of fundamental importance because of the different weight the two groups assign to observables in order to fix the parameter space. Moreover this model predicts a shallow color-magnitude relation for bright elliptical galaxies, galactic circular velocities about 30% larger than observed and that over half the stars in the Universe form at a redshift lower than 1.5, at variance with $sub - mm$ (Chapman et al., 2003) and K -band observations (Cimatti et al., 2002). Besides central galaxies are too massive, too luminous and too blue, with respect to observations, because of strong cooling flows at the center of massive DMHs. Baugh et al. (2005) showed that in order to adequately predict SCUBA sources in this framework, they needed to assume a top-heavy IMF, in star-bursts. In a recent paper Bower et al. (2005) proposed that the problem of strong cooling flows in massive halos can be solved considering the effect of the feedback from QSO. In particular they demonstrate that the energy injected from AGNs in form of radio jets is able to regulate the cooling flows. If the AGN energy injection is greater than the cooling luminosity, they assume that the cooling flow is quenched.

Somerville & Primack, (1999)

The original formulation of the model has been presented in Somerville & Primack (1999). This paper focused on the prediction of the properties of local galaxies. The properties of high redshift objects have been shown in the companion paper Somerville, Primack & Faber (2001).

- Merger histories of DMHs are computed following the extended Press & Schechter formalism, using the halo merger rate derived by Somerville & Kolatt (1998)
- A Navarro, Frenk & White (1996) profile for the DM distribution inside the halo is assumed.
- Diffuse gas in the halo is shock-heated at the virial temperature and is distributed as an isothermal profile.

- Cooling is described following the cooling function proposed by Sutherland & Dopita (1993) and the cooling radius approach of Frenk & White (1991).
- Disc formation follows the model of by Mo, Mao & White (1998).
- Star formation is taken proportional to the cold gas mass and with an efficiency modeled as a free parameter ($\dot{m}_* = m_{cold}/\tau_*$). Mergers and interactions between galaxies trigger enhanced star formation episodes ($\dot{m}_* = e_{burst}m_{cold}/\tau_{dyn}$).
- Stellar feedback is modeled using: $\dot{m}_{reh} = \epsilon_0 E_{SN} \eta_{SN} \dot{m}_* / v_{esc}^2$. The rate at which the reheated gas can escape the disc and/or the halo is computed following the general arguments of Dekel & Silk (1986). v_{esc} is the average escape velocity of disc or halo; the reheating rate and ejected gas mass are calculated separately for each component.
- When DMHs merge the satellites of the largest progenitor remain undisturbed, central galaxies of other progenitors are placed at a radial distance, set as a free parameter, and their satellites are randomly distributed around them.
- Orbital decay of satellites due to dynamical friction is modeled following Binney & Tremaine (1987). Mergers between nearly equal-mass galaxies result in the formation of a spheroid. The mass ratio 0.25 is taken to discriminate between major and minor mergers. Satellite-satellite mergers are computed following Makino & Hut (1997).
- Instantaneous Recycling Approximation is assumed for metal enrichment. The total effective yield for chemical enrichment is a free parameter.
- Galaxy SEDs are computed using Bruzual & Charlot (2003) with a Scalo (1986) IMF.

This model is able to reproduce the B -band, K -band luminosity functions and the Tully-Fisher relation, but it faces difficulties in explaining other galactic properties: the colors of bright ellipticals are too blue, the bulk of star formation takes place at relatively low redshift, the space density of massive galaxies at $z > 1.5$ is not reproduced, cooling flows in massive halos have to be stopped in order to avoid the formation of very massive and luminous central galaxies, the metallicity-luminosity relation is not correctly reproduced, the relationship between circular velocity and exponential scale radius is poorly recovered.

Menci, Cavaliere, Fontana, Giallongo, Poli & Vittorini (2004)

The model presented in Menci et al. (2004) represents the synthesis of several papers (Cavaliere & Vittorini 2002; Menci et al., 2002, 2003).

- Merger histories of DMHs are computed following the extended Press & Schechter formalism, using the analytic expression for halo merger rates derived by Lacey & Cole (1993)

- A Navarro, Frenk & White (1996) profile for the DM distribution inside the halo is assumed.
- Diffuse gas in the halo is assumed to follow an isothermal profile.
- Cooling is described following the cooling function proposed by Sutherland & Dopita (1993) and the cooling radius approach of Frenk & White (1991).
- Disc formation follows the modeling proposed by Mo, Mao & White (1998).
- The efficiency of star formation in a disc of radius r_d and circular velocity v_d is taken $\dot{m}_* = m_{cold}/(\tau_*^0 r_d/v_d)$. Galaxy encounters are expected to destabilize part of the cold gas by causing it to lose angular momentum (following Cavaliere & Vittorini, 2000). One fourth of infalling material is supposed to feed a central BH, while the remaining gas is assumed to kindle a circumnuclear starburst. The star formation rate in starbursts depends on the fraction of destabilized gas and on the duration of the interaction.
- Stellar feedback is modeled using the following formulation: $\dot{m}_{reh} = \epsilon_0 E_{SN} \eta_{SN} \dot{m}_*/v_c^2$
- The dynamical evolution of galaxies inside DMHs is computed taking into account both orbital decay (following Lacey & Cole, 1993) and binary aggregations of satellite galaxies (following Cavaliere, Colafrancesco & Menci, 1992).
- AGN activity is modeled assuming the Cavaliere & Vittorini (2000) model. Galaxy encounters (computed following Cavaliere & Menci, 1993) are expected to destabilize part of the cold gas by causing it to lose angular momentum and to fall towards the center of the halo.
- Instantaneous Recycling Approximation is assumed for metal enrichment. The total effective yield for chemical enrichment is a free parameter.
- Galaxy SEDs are computed using Bruzual & Charlot 2003 with a Salpeter (1955) IMF.

The Menci et al. (2004) model is able to reproduce the basic set of local galaxy data. Moreover, it is able to reproduce the local color bimodality in agreement with Baldry et al. (2004). However when the model is tuned in order to reproduce Balogh et al. (2004) distributions, the agreement with local K -band and B -band worsens with respect to the best fit model. The model is also able to predict a larger stellar density at $z > 1$ and as a consequence a larger space density of massive galaxies at $z \sim 1.5$, in agreement with K -band observations. Some discrepancies with observations still hold, among which the most interesting is the overprediction of faint galaxies at all redshifts. Menci et al. (2003) show that this model is able also to predict the $z > 3$ rise and $z < 2.5$ decline of the quasar population.

The model has been proposed in Hatton et al. (2004). Improvements have been presented in Lanzoni et al. (2005).

- Merger histories of DMHs are computed directly from N -body simulations.
- The DM distribution inside halos is described by a tri-axial distribution. Axis lengths are computed from N -body simulations
- Diffuse gas in the halo is shock-heated at the virial temperature and its distribution follows β -model profile (Cavaliere & Fusco-Fermiano, 1976)
- Cooling is described following the cooling function proposed by Sutherland & Dopita (1993)
- Disc formation follows the modeling proposed by Mo, Mao & White (1998), with the spin parameter computed from N -body simulations.
- Star formation is modeled following Kauffmann, Guiderdoni & White 1993 ($\dot{m}_\star = m_{cold}/(\tau_\star^0 \tau_{dyn})$). In merger events a starburst component is taken into account. The rate of star formation in starburst is computed using the same formulation with a shorter timescale.
- Stellar feedback is modeled following Silk (2003) ($\dot{m}_{reh} = 2\epsilon_0 E_{SN} \eta_{SN} \dot{m}_\star / v_{esc}^2$). The fraction of reheated gas that is ejected from the disc in the intra halo medium (that is ejected from the halo) is computed using the escape velocity v_{esc} of the disc (halo). The gas ejected from the halo accumulates into a halo reservoir. Part of this material is allowed to infall back onto the parent DMHs with the accreted matter.
- When DMHs merge the properties of the new halo are computed directly from the N -body simulation. Galaxies are distributed in the new halo according to the mass and virial radius of their progenitor DMHs.
- Orbital decay is computed following the formulation of dynamical friction proposed by Binney & Tremaine (1987). Mergers between satellites are modeled following the results of Makino & Hut (1997). When two galaxies merge, the morphology of the resulting object is not a sharp function of the ratio between the masses of the progenitors, but it is smoother function of their properties. Spiral bulges and ellipticals form as the result of merging events.
- Chemical enrichment is computed taking into account the different lifetimes of stars of different mass. Stellar yields are computed according to Devriendt, Guiderdoni & Sadat (1999).
- Spectrophotometric properties of simulated galaxies are computed using the STARDUST code (Devriendt, Guiderdoni & Sadat, 1999) and a Kennicutt (1983) IMF.

This model correctly reproduce the observed B -band, K -band and IR -band luminosity functions and the optical versus infrared luminosity budget in $z = 0$ galaxies. The dependence of galaxy colors on the morphological type is qualitatively recovered. Also for this model substantial cooling flows at the center of more massive halos are predicted. In order to overcome this problem gas is prevented to cool down when the mass locked in spheroids becomes greater than $10^{11}M_{\odot}$. The Faber-Jackson relation and the Fundamental Plane of elliptical galaxies are recovered, even if early-type galaxies result too blue with a large scatter. The size of high surface-brightness discs are in the same range as the observational data, but the model predicts slightly too many large discs than observed. Moreover, massive galaxies rotate too fast and are too blue, with a lot of ellipticals still having discs.

Granato, de Zotti, Silva, Bressan & Danese, (2004)

Granato et al., (2004) presented a physically motivated model for the coevolution of massive galaxies and AGNs at their centers. This model uses a number of recipes analogous to semi-analytical models. It follows the evolution of the baryonic content of protospheroidal galaxies within massive DMHs at $z \geq 1.5$, but no attempt to model the subsequent evolution at low redshift is made. We summarize the most important assumptions in this model in terms of the list we use for semi-analytical models.

- The formation rate of massive halos (defined as halos more massive than $2.5 \times 10^{11}M_{\odot}$) is computed according to the positive part of the time derivative of the halo mass function (Haehnelt & Rees, 1993).
- The DMH density profile follows Navarro, Frenk & White (1997) and Bullock et al. (2001)
- The cold gas distribution is assumed to follow DM distribution.
- Sutherland & Dopita (1993) cooling function is assumed.
- Star formation occurs at a rate

$$\dot{m}_{\star} = \int_0^r \frac{1}{\max[\tau_{cool}(r), \tau_{dyn}(r)]} \frac{dm_{cold}}{dr} dr \quad (1.104)$$

Since both τ_{dyn} and τ_{cool} are weakly depend on the halo mass, the authors conclude that stars form faster within larger and more massive DMH.

- Stellar feedback is modeled using $\dot{m}_{reh} = 2/3\epsilon_0 E_{SN}\eta_{SN}\dot{m}_{\star}/\sigma^2$, where σ^2 represents the line-of-sight velocity dispersion.
- The gas loses angular momentum due to radiation drag as proposed by Umemura (2001):

$$\frac{dlnJ}{dt} \sim \frac{L_{sph}}{cm_{gas}}(1 - e^{-\tau}) \quad (1.105)$$

(where L_{sph} is the global stellar luminosity and τ represents the effective optical depth) The gas then flows towards the center feeding a mass

reservoir at a rate (Kawakatu et al. 2003):

$$\dot{m}_{infall} \sim \frac{L_{sph}}{c^2}(1 - e^{-\tau}) \quad (1.106)$$

The material can then flow towards the central BH on a timescale depending on the viscous drag $\tau_{visc} \sim r_a^2/\nu$ (where ν is the viscosity, r_a is the accretion radius of the black hole) The mass of the reservoir m_{res} evolves as $\dot{m}_{res} = \dot{m}_{inflow} - \dot{m}_{BH}$.

- QSO activity affects the interstellar medium of the host galaxy, through both the radiative output and the injection of kinetic energy producing gas outflows. Quasar feedback heats the ISM to a temperature $\sim 1KeV$, thus unbinding it and making it flow into the intergalactic medium (IGM). Quasar feedback prevents subsequent star formation; stellar populations undergo a phase of passive evolution.
- Chemical evolution of the gas is followed by using classical equations and stellar nucleosynthesis prescriptions, as for instance reported in Romano et al. (2002).
- Spectrophotometric properties of simulated galaxies are computed using GRASIL code (Silva et al., 1998). The IMF is chosen according to Romano et al. 2002

The prediction of this model are in good agreement with a number of observables which proved to be extremely challenging for the semi-analytical models (Silva et al., 2005), including the *sub - mm* and EROs number counts, the evolution of the *K*-band luminosity function and the redshift distribution of $K < 20$ sources. Also, the black hole mass function and the relationship between the black hole mass and the velocity dispersion in spheroids are nicely reproduced. This result is due to the fact that star formation and BH accretion are proportional. This model is tuned to the properties of $z > 1.5$ spheroids. There is no attempt in modeling spiral galaxies and $z < 1.5$ objects.

Backward Models

All the semi-analytic models described in the previous paragraphs follow the cosmological assembly of DMHs and galaxies from high-redshift objects to the local populations. Another possible approach to the problem of galaxy formation and evolution relies in starting from observational data and trying to reconstruct the possible star formation histories compatible with the observed galactic properties. In this framework the chemical abundances are considered a key tool: using chemical evolution models it is possible to constrain the timescale on which a stellar population reaches the observed metal abundances. In particular one of the most important tracers of the past star formation history is the ratio between the abundance of α -elements with respect to iron. It is common practice to indicate the ratio between the abundance of an element X and Fe in units of the solar value:

$$[X/Fe] = \log(X/H) - \log(X/H)_{\odot} \quad (1.107)$$

The value of $[\alpha/Fe]$ with respect to $[Fe/H]$ is particularly sensible to the relative frequency of Type Ia and II SNe, due to the time delay between the two classes of supernovae. In fact Type II supernovae (SNeII, whose progenitors are young massive blue stars) enrich the ISM of α -elements on a short timescale ($10^7 yr$), while iron is mainly produced by Type Ia supernovae (SNeIa, whose progenitors are evolved binary system) on a longer timescale ($> 10^9 yr$). Thus the $[Fe/H]$ can be considered as a clock because the iron abundance in galaxies increases with time as soon as Type Ia supernovae start to explode.

Matteucci (1994, 1996) proposed a model able to explain at the same time the level of α enhancement, the abundance ratios and the metallicity gradients observed in elliptical galaxies. In this model (also called *inverse wind model*) the efficiency of star formation is an increasing function of galactic mass. This implies a shorter period of star formation in massive ellipticals. In fact the efficiency of star formation is chosen in such a way that massive ellipticals develop the wind phase before less massive ones. This produces the observed increase of the $[Mg/Fe]$ ratio as a function of galactic mass. The strong wind phase is able to expel the ISM from the object, thus stopping subsequent star formation. This monolithic models assume that the galactic wind occurs when the energy injected by SNe into the ISM equals the potential energy of the gas. Quasar events can be connected to the winds episode (Matteucci & Padovani 1993). In the inverse wind model a very massive elliptical ($M = 10^{12} M_{\odot}$) starts developing a wind before $10^9 yr$ from the beginning of star formation, whereas a small elliptical forms stars for a longer period. As a result the average $\langle [Mg/Fe] \rangle$ is larger in massive than in small ellipticals.

Table 1.1: Comparison between different models of Galaxy formation and evolution

| | Kauffmann et al., (1993) | Cole et al., (2000) | Somerville & Primack, (1999) |
|--------------------|--|--|--|
| DM Merger Trees | Kauffmann & White (1993) | Lacey & Cole (1993) | Somerville & Kolatt (1998) |
| DMH profile | Truncated Isothermal Sphere | Navarro, Frenk & White (1995) | Navarro, Frenk & White (1995) |
| Gas profile | Truncated Isothermal Sphere | β -model | Isothermal Sphere |
| Gas Cooling | White & Frenk (1991) | Sutherland & Dopita (1993) | Sutherland & Dopita (1993) |
| Disc Formation | Mo, Mao & White (1998) | Mo, Mao & White (1998) | Mo, Mao & White (1998) |
| Star Formation | $\dot{m}_\star = m_{cold}/(\tau_\star^0 \tau_{dyn})$ | $\dot{m}_\star = m_{cold}/(\tau_\star^0 (V_{disc}/V_0)^{\alpha_\star})$ | $\dot{m}_\star = m_{cold}/\tau_\star$ |
| Enhanced SF | — | — | $\dot{m}_\star = e_{burst} m_{cold}/\tau_{dyn}$ |
| Stellar Feedback | $\dot{m}_{reh} = \epsilon 4 \dot{m}_\star \eta_{SN} E_{SN} / (3V_C^2)$ | $\dot{m}_{reh} = \epsilon_{SN} (V_{disc}/V_0)^{-\alpha} \dot{m}_\star$ | $\dot{m}_{reh} = \epsilon_0 E_{SN} \eta_{SN} \dot{m}_\star / v_{esc}^2$ |
| Orbital Decay | Binney & Tremaine (1987) | Lacey & Cole (1993) | Binney & Tremaine (1987) |
| Galaxy Mergers | Satellite-Central | Satellite-Central | Satellites-Central Satellite collisions (Makino & Hut, 1997) |
| QSO activity | (Kauffmann & Haehnelt 2000) | (Bower et al., 2005) | — |
| Spectrophoto. Code | Bruzual & Charlot (2003) | Bruzual & Charlot (2003) Silva et al. (1998) | Bruzual & Charlot (2003) |
| IMF | Kennicutt (1983) | Kennicutt (1983) Top-Heavy in starburst | Scalo (1986) |
| | Menci et al., (2004) | Hatton et al., (2003) | Granato et al. (2004) |
| DM Merger Trees | Lacey & Cole (1993) | N -body simulations | Haehnelt & Rees, (1993) |
| DMH profile | Navarro, Frenk & White (1995) | N -body simulations | Navarro, Frenk & White (1997) |
| Gas profile | Isothermal Sphere | β -model | Follow DM distribution |
| Gas Cooling | Sutherland & Dopita (1993) | Sutherland & Dopita (1993) | Sutherland & Dopita (1993) |
| Disc Formation | Mo, Mao & White (1998) | Mo, Mao & White (1998) + N -body | — |
| Star Formation | $\dot{m}_\star = m_{cold}/(\tau_\star^0 r_d/v_d)$ | $\dot{m}_\star = m_{cold}/(\tau_\star^0 \tau_{dyn})$ | $\dot{m}_\star = \int_0^r \frac{1}{\max[\tau_{cool}(r), \tau_{dyn}(r)]} \frac{dm_{cold}}{dr} dr$ |
| Enhanced SF | Starburst Model | Starburst component | — |
| Stellar Feedback | $\dot{m}_{reh} = \epsilon_0 E_{SN} \eta_{SN} \dot{m}_\star / v_c^2$ | $\dot{m}_{reh} = 2\epsilon_0 E_{SN} \eta_{SN} \dot{m}_\star / v_{esc}^2$ | $\dot{m}_{reh} = 2/3 \epsilon_0 E_{SN} \eta_{SN} \dot{m}_\star / \sigma^2$ |
| Orbital Decay | Lacey & Cole (1993) | Binney & Tremaine (1987) | — |
| Galaxy Mergers | Satellites-Central Binary Aggregations | Satellites-Central Satellite collisions (Makino & Hut, 1997) | — |
| QSO activity | Cavaliere & Vittorini (2000) | — | Granato et al. (2001) |
| Spectrophoto. Code | Bruzual & Charlot (2003) | Devriendt, Guiderdoni & Sadat, (1999) | Silva et al. (1998) |
| IMF | Salpeter (1955) | Kennicutt (1983) | Romano et al. (2002) |

Chapter 2

Active Galactic Nuclei and Quasars

Many galaxies show a very intense central emission. High resolution images of this region reveal a point-like highly luminous source. In extreme cases the central source is so bright that its emission supersedes the emission of the whole galaxy. Optical spectra of these objects show strong emission lines superimposed on a power-law continuum. These spectra are not compatible with the hypothesis of a stellar origin (i.e., an intense burst of star formation). This class of objects is named of *Active Galactic Nuclei* (AGNs).

Several different classifications of this phenomenon are in use. AGNs are divided into two categories on the basis of their radio luminosity (*Radio Loud* and *Radio Quiet* AGNs). It is worth noting that radio emission in Radio Quiet AGNs is already higher than radio emission from normal galaxies. Observations at radio wavelength of Radio Loud AGNs typically show a central point-like luminous source and one or two jets and lobes starting from the central source. Jets are able to reach distances from the central source up to $\sim 1Mpc$. It is possible to classify these object on the basis of their optical magnitude in the *V*-band. Objects with a magnitude fainter than -23 are classified as *Seyfert galaxies*, while their brighter counterparts are known as *Quasi stellar objects* or QSOs. This classification dates back to the first observations of these objects when the sensitivity of the instruments was low and distant and/or bright AGNs were seen essentially as point-like sources with spectral properties different from stars, while Seyferts appeared as galaxies with a bright central nucleus. At those times the nature of QSOs was unclear, so they were called quasi-stellar objects. Nowadays the extra-galactic nature of QSOs is well established, and the resolving power of modern instruments is sufficient to prove the fact that QSOs are hosted in galaxies. We refer to Radio-Loud AGNs with a point-like optical counterpart as *Quasi-stellar Radio Sources* or Quasars, while Radio-Loud AGNs with a faint optical counterpart are named Radiogalaxies.

An alternative classification is based on spectral features (see for reference fig.2.1). Typical optical spectra of AGN are characterized by a power-law continuum emission with superimposed emission line. There are two main

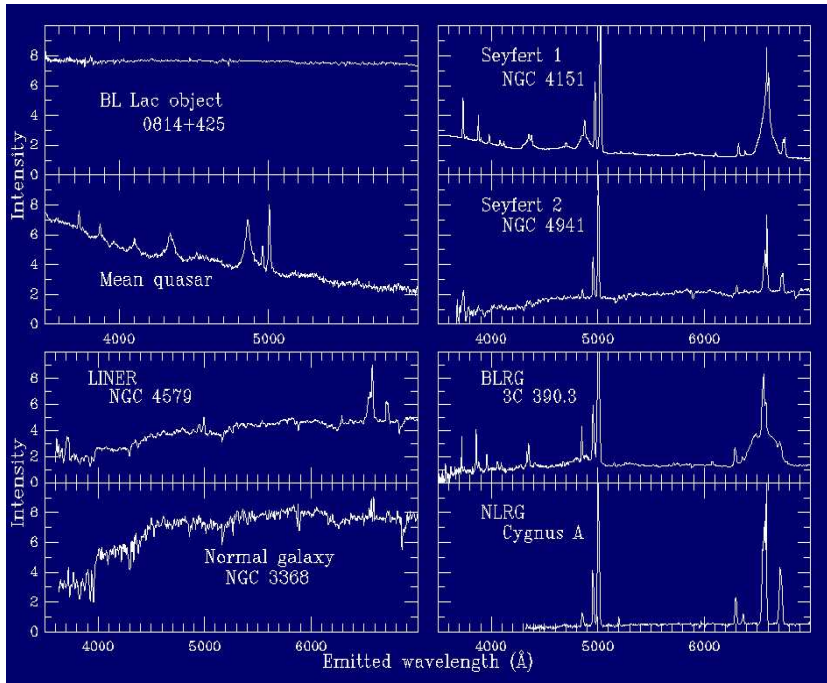


Figure 2.1: Examples of AGN spectra (image taken from B. Keel, lecture notes, <http://www.astr.ua.edu/keel/>)

classes according to the width (broad or narrow) of the observed emission lines. Broad lines correspond to permitted emission lines of high and low ionization. The broadening of the lines is interpreted as due to high velocity dispersion $\sim 10^4 Kms^{-1}$, while the absence of prohibited lines is interpreted as a signature of high densities. On the other hand narrow lines correspond to allowed and prohibited lines with high and low ionization: the width of the lines indicates velocity dispersions of the order of $\sim 1000 Kms^{-1}$, and the evidence of prohibited lines points towards low density environments. AGNs can be classified according to the presence of these lines into three main categories: Type I AGNs have both broad and narrow lines overimposed on a continuum emission, Type II AGNs have only narrow lines, LINER (*Low-ionization Narrow Emission Region*) have only narrow lines coming from low ionization regions.

The AGN luminosities are extremely high, reaching $10^{48} erg/s$. AGNs are typically transient phenomena, with an estimated mean lifetime of about $4 \times 10^7 yr$. It is very difficult to find a stellar process able to sustain AGNs, nowadays the most widely accepted explanation for AGN and QSO phenomena is based on the presence of a *Super-Massive Black Hole* (SMBH) in the center of the host galaxies.

2.1 Unified Model for AGNs

The hypothesis of SMBHs ($10^6 - 10^{10} M_\odot$) as the engine of the AGNs can solve many problems. First of all Black Holes (BHs) are able to convert the mass of infalling gas into radiative energy with high efficiency. Precise calculations involving General Relativity give the expected value of the efficiency η of the order of 0.1. We can estimate for instance the mass of a SMBH radiating $\sim 4 \times 10^{46} \text{ erg/s}$ in a time interval of about $4 \times 10^7 \text{ yr}$ with an efficiency of $\eta = 0.1$ as $\sim 3 \times 10^8 M_\odot$. The expected *Schwarzschild Radius* ($R_{sch} = GM_{BH}/c^2$) of such an object is of about $3 \times 10^{-5} \text{ pc}$. It means that BHs are very compact objects and are suitable candidates for the point-like appearance of AGN sources. Moreover the mass of AGN sources can be estimated by analyzing the dynamics of central gas clouds (i.e. via the Doppler broadening of emission lines), and it gives values of the central mass of the order of $10^6 - 10^{10} M_\odot$, again in agreement with the BH hypothesis.

The accretion rate of a BH is limited by the angular momentum of the infalling gas. The problem of the loss of the angular momentum is fundamental for modeling the evolution of AGNs. We will discuss it in great detail in following chapters. The infalling gas (that has already lost most of its angular momentum) forms an accretion disc around the SMBH. The resulting viscosity causes the loss of the residual angular momentum. The accretion disc heats up and emits thermal radiation. The inner regions are hotter and emit at shorter wavelengths.

It is possible to reconcile the variety of AGN properties into a unified model. This model postulates the presence of a central engine consisting in a SMBH surrounded by an accretion disc; a toroidal region consisting mainly in dust particles; two gas cloud regions with different radii and velocity dispersions. Radio-loud AGNs are characterized also by the presence of jets. Fig. 2.2 summarize the different typologies of AGNs justified by the unified model.

The toroidal structure around the central engine absorbs the radiation coming from the SMBH over a large solid angle. The central engine emits a bolometric luminosity of about $10^{42} - 10^{48} \text{ erg/s}$. The continuum emission comes from the central source and part of this radiation photoionizes the surrounding clouds. Broad lines are generated inside a small region (from 10^{-2} pc up to 10 pc): the *Broad Line Region* (BLR). In the BLR clouds the strong emission lines form. As we already introduce in last paragraph, the broadening of the lines is interpreted as the effect of the high velocity dispersion in clouds (temperature $\sim 10^5 \text{ K}$), where the absence of prohibited lines indicates densities of the order of $10^9 - 10^{10} \text{ cm}^{-3}$. The presence of high ionization lines in a warm medium is the signature of photoionization of the clouds (the system is not in local thermodynamical equilibrium). Those clouds are optically thick at UV wavelengths, so the fact that we are able to see the continuum emission from the central source indicates that their *covering angle* (i.e. the fraction of the solid angle covered by clouds as seen from the central source) is not very high (~ 0.1). The confinement of clouds in the BLR is under debate. It is possible that they are pressure confined by a surrounding intra-cloud hot medium or by their own magnetic fields, or it is also possible that

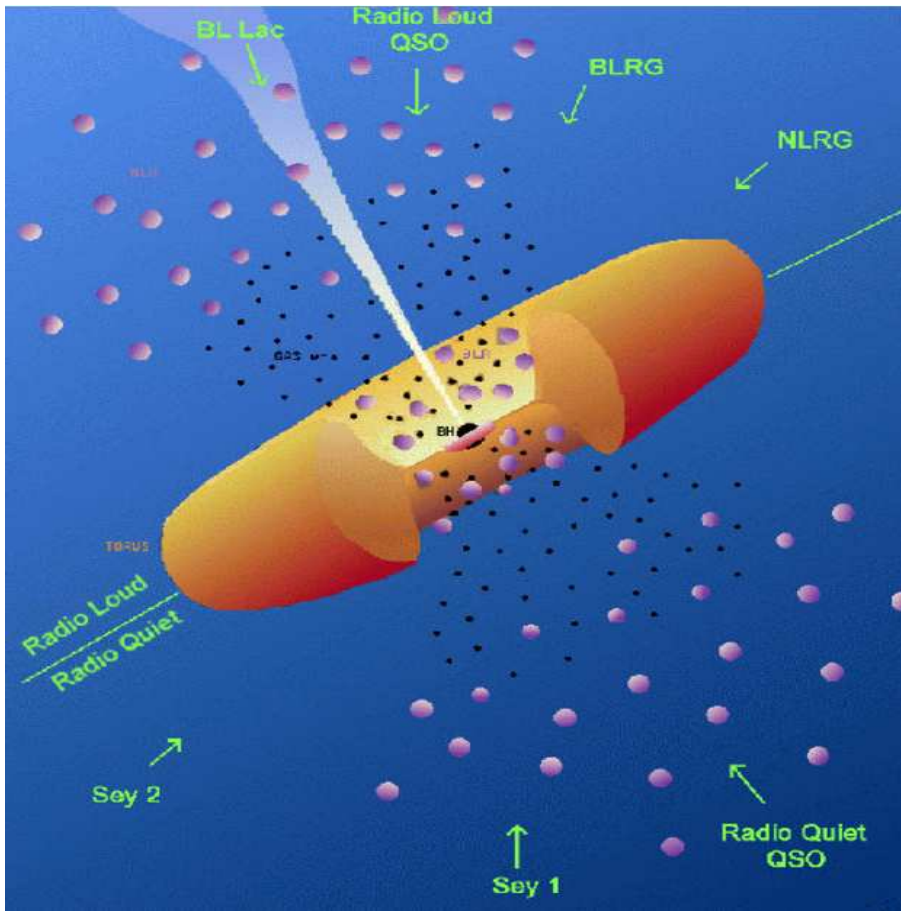


Figure 2.2: Unified model for AGNs (Image taken from Urry & Padovani (1995), modified by J. Wilms
(<http://astro.uni-tuebingen.de/wilms/teach/xray2/xray2233.html>)

clouds are short living systems continuously created and destroyed during the AGN shining. Narrow lines in AGN spectra are on the contrary generated in a region extending from $\sim 10 pc$ up to $1 kpc$ from the central source: the *Narrow Line Region* (NLR). The width of lines generating in this region is interpreted as the effect of a velocity dispersion lower than BLR clouds ($\sim 1000 km/s$, temperature $\sim 10^4 K$), while the observation of prohibited lines indicates a lower density ($10^2 - 10^6 cm^{-3}$) with respect to BLR. The estimate covering factor is ~ 0.2 .

In this framework we can easily understand the observed properties of AGNs. At polar observing angles we observe the inner regions and BLR clouds, so we will recognized a type I AGNs (continuum emission, broad and narrow lines); if we look trough the toroidal structure all BLR emission is completely obscured and we see only the emission from the outer NLR clouds and the resulting object is a type II AGN (narrow emission lines). The difference between AGN and QSO is due only to the bolometric luminosity of the source,

so as QSOs are only the brighter part of the AGN population. On the other hand the properties and the shining mechanism of AGN and QSO are exactly the same. For this reason in the following chapters we will refer to AGNs and QSOs as a unique class of sources, with no differences between faint QSOs and bright AGNs.

It is interesting to notice that compact and massive dark objects (MDOs) are often detected at the center of local galaxies (and also at the center of the Milky Way corresponding to the Sagittarius region). MDOs are commonly interpreted as quiescent (maybe slowly accreting) SMBH, the relics of the past AGN activity of their host galaxies. In the framework of the Unified Model a SMBH should be present at the center of each galaxy. When the SMBH accretes mass it gives rise to an AGN, whereas when it is in a quiescent phase it can be only seen as a MDO. Multiple accretion events are possible.

2.2 Multiwavelength AGN observations

The emission of AGNs spans the whole electromagnetic spectrum. The radio emission contributes a negligible fraction of the bolometric luminosity; it is due essentially to synchrotron emission from ultra-relativistic electrons spinning into a magnetic field. Radio-loud AGNs show a compact central radio source at the center of the host galaxy, eventually corresponding to the optical counterpart. This *core* corresponds also to the starting point of the radio jets. Radio jets extends on *kpc* up to *Mpc* scale. The spectra of the two structures are very different: the central source shows a flat spectrum, while jets are characterized by steep spectra.

The integrated infrared emission ($2 - 200\mu\text{m}$) of AGNs gives, on average, $\sim 30\%$ of the bolometric luminosity. In MIR and NIR bands we see the AGN radiation reprocessed by hot dust located in the obscuring torus. This dust is heated by the BH up to a temperature of 500-1000 K. The typical AGN SED peaks in the MIR (*IR bump*) and decreases towards the NIR.

The optical to soft X-ray emission of AGNs is characterized by the *big blue bump*, where the peak of quasar emission is usually found: it can be explained as thermal emission from the accretion disc. The resulting SED is the sum of the several Planckians related to the different temperatures. The typical optical spectrum of a bright type I AGN (see i.e. fig. 2.3) is characterized by a power-law continuum dominated by emission lines, in particular by the Lyman alpha (Ly_α) line (corresponding to the ionization energy of neutral hydrogen) and by several metal lines. Hundreds of emission lines are present in quasar spectra. In addition to these lines, another major feature in the optical/UV spectra of quasars is the *small blue bump* between $\sim 2200 \text{ \AA}$ and $\sim 4000 \text{ \AA}$. This is not a true continuum feature but is due to a forest of emission lines from the ion FeII and the Balmer recombination continuum. The redshift of the object is usually computed from the Ly_α line. The region blueward of Ly_α presents typical absorbing feature due to the intervening intergalactic medium between the source and the observer. The systematic description of these systems is beyond the purposes of this thesis.

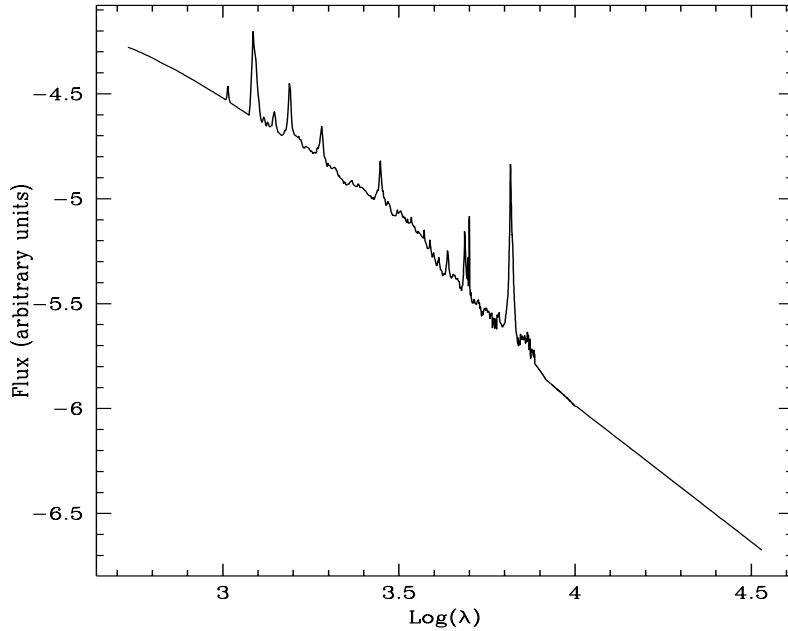


Figure 2.3: Cristiani & Vio (1990) composite spectrum of Type I QSO in the optical region.

Elvis et al. (1994) computed the mean spectrum of type I QSOs using a sample of observed spectra and used this result to estimate the *bolometric correction* in various electromagnetic bands. The bolometric correction c_{λ}^{bol} is defined as the ratio between the bolometric flux L_{bol} of an AGN and the monochromatic flux at a wavelength $\lambda = c/\nu$:

$$\nu f_{\nu} = \frac{L_{bol}}{c_{\nu}^{bol}} \quad (2.1)$$

The Elvis value for the Johnson B -band (corresponding to $\lambda \sim 4400\text{\AA}$) is $c_{4400}^{bol} \sim 10.4$.

The AGN rest-frame emission in FAR-Ultraviolet bands is very difficult to observe due to the presence of several interposing absorbers, both at galactic and extra-galactic distances. However because of the soft-X SED is lower than the optical-UV SED, we can argue that AGNs have their maximum emission at UV wavelengths.

AGNs are the most important extragalactic X-ray emitters. Almost 90% of the X-ray background (XRB) is due to point-like AGNs (Moretti et al., 2003). X-ray emission from AGNs is due to several mechanisms: at lower energies the emission is thermal from the inner regions of the accretion disc; going to higher energies the emission is due to optical photons comptonized by high-energy electrons. At even higher energies the emission can be understood in terms of two components: a direct one from inverse Compton scattering of

high energy electron and a reflected one from the gas surrounding the central engine and reprocessing its radiation. The typical spectrum of AGNs drops from the UV to the X-ray band, then it starts again to rise as a power-law. The X-ray emission extends from the Galactic absorption cut-off at ~ 0.1 keV up to ~ 300 keV. The intrinsic continuum X-ray emission of quasars is to first order a power law. Differently from optical wavelengths, X-ray astronomers tend to use the *photon index* Γ , where $N(E) \propto E^{-\Gamma}$. Emission and absorption features have been found that mask a direct view of the spectrum over virtually the whole X-ray band. Absorption in AGN X-ray spectra is particular relevant in the soft-X band, while the hard-X band is virtually unextincted in most cases. Type II AGNs show the higher intrinsic absorption as expected from the unified model.

The contribution of X-ray luminosity to the total luminosity of AGN can vary strongly with the bolometric luminosity of the object; as a consequence, X-ray bolometric corrections depend on the AGN bolometric luminosity (Marconi et al., 2004).

2.2.1 Building up a QSO template spectra library

In the following chapters we will compare the results of our model of galaxy formation and evolution with a set of multiwavelength AGN observations. In order to predict the properties of our simulated AGN population, we need a library of template AGN spectral energy distributions (SEDs). We built this as follows.

In the optical region we consider the QSO template spectrum of Cristiani & Vio (1990) down to 538\AA , extrapolated to 300\AA using the power-law slope proposed by Risaliti & Elvis (2004) $f_\nu \propto \nu^{-1.76}$. At shorter wavelengths (between 0.01 and 30\AA) we use a power-law SED with a photon index of $\Gamma = -1.8$ with an exponential cutoff $\exp(-E/200\text{KeV})$ (see i.e. La Franca et al., 2005). The relative normalization between the optical-UV and the X-ray branches of the spectrum is constrained through the quantity α_{ox} (Zamorani et al., 1981):

$$\alpha_{ox} = \frac{\log(L_{\nu_{2500\text{\AA}}}/L_{\nu_{1\text{ keV}}})}{\log(\nu_{2500\text{\AA}}/\nu_{1\text{ keV}})} \quad (2.2)$$

We use for α_{ox} the bolometric luminosity-dependent of α_{ox} value proposed by Vignali, Brandt & Schneider (2003):

$$\alpha_{ox} = -0.11 \log(L_{\nu(2500\text{\AA})}) + 1.85 \quad (2.3)$$

The interpolation between 30 and 300\AA follows Kriss et al. (1999). At infrared wavelength we use an approximation of the IR bump proposed by Shang et al. (2004).

We then produce a library of template spectra for $\text{Log}(L_{\text{bolo}}) = [42.0, 47.5]$ (in bins of 0.1 dex in luminosity). In fig. 2.4 we show a set of QSO template

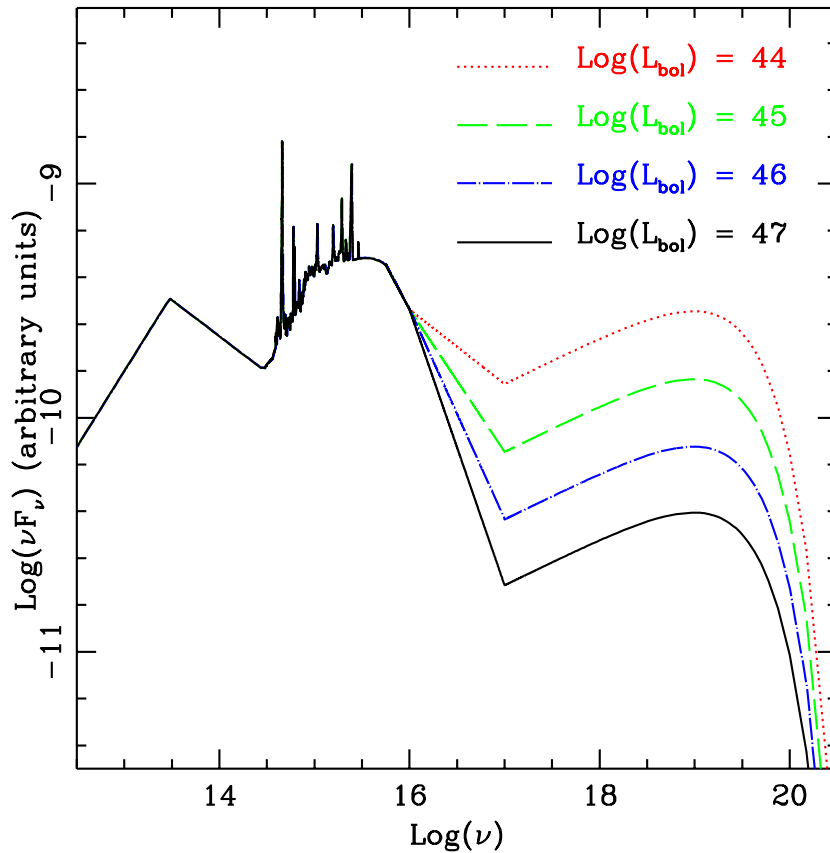


Figure 2.4: Four template spectra with different bolometric luminosity, selected from our library of template QSO spectra.

spectra taken from our library. The dependence of the bolometric correction on the bolometric luminosity of the object is evident.

2.3 AGN–Galaxy connection

In the last years evidence has grown on the importance of the interaction between AGNs and their host galaxies. This interaction is now deemed to be of fundamental relevance for understanding not only the assembly of the SMBHs responsible for the AGN activity, but also of the galaxies, in particular the spheroidal components (ellipticals or spiral bulges). Observations of nearby galaxies show the existence of a well defined correlation between the mass or central velocity dispersion of bulges and the mass of the BH they host (Kormedy & Richstone, 1995; Magorrian et al., 1998; more recent determinations are found in Marconi & Hunt, 2003 and Häring & Rix, 2004; see fig. 2.5). Moreover, the observed mass function of these BHs is consistent

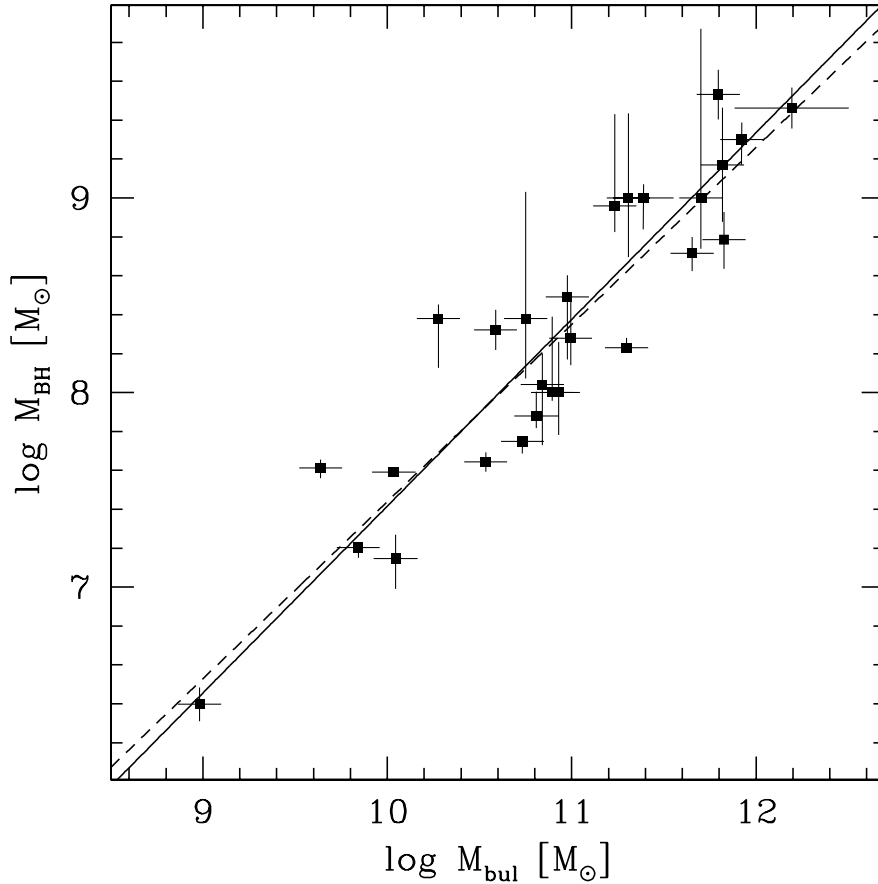


Figure 2.5: Observative M_{bul} vs M_{BH} relation: figure taken from Marconi & Hunt (2003)

with that inferred from quasars luminosities, under simple assumptions for the radiative efficiency and accretion rate (Salucci et al. 1999; Yu & Tremaine 2002; Shankar et al. 2004; see also Haiman, Ciotti & Ostriker 2004). On the other hand, observations at high redshift highlight that quasars and radio-loud AGNs are hosted in elliptical galaxies (see i.e. Dunlop 2003). Finally, jets from radio galaxies are now one of the most promising candidates for quenching cooling flows in galaxy clusters (Quilis, Bower, & Balogh 2001; Dalla Vecchia et al. 2004; Ruszkowski, Brüggén & Begelman 2004; Zanni et al., 2005; see also chapter 1.3.2 for a definition of the overcooling problem).

The discovery of the BH – bulge relation has stimulated a large number of theoretical papers aimed at reproducing it. Several authors proposed that the feedback from the AGN is able to self-limit the masses of both spheroids and BHs, (see, e.g., Ciotti & Ostriker 1997; Silk & Rees 1998; Haehnelt, Natarajan & Rees 1998; Fabian 1999; Granato et al. 2001, 2004; Murray, Quataert & Thompson 2005). However, other authors successfully reproduced the BH – bulge relation simply assuming a proportionality between star formation

(in bulges) and accretion rates, implicitly determined by the mechanism responsible for the almost complete loss of angular momentum of the gas accreting on the BH (see i.e. Kauffmann & Haehnelt 2000; Cattaneo 2001; Cavaliere & Vittorini 2002; Hatziminaoglou et al. 2003; Mahmood, Devriendt & Silk 2004; Bromley, Somerville & Fabian 2004). This point will be developed in chapter 5.

2.4 Redshift evolution of AGNs

The evolution of the luminosity function of AGNs in the soft (Hasinger et al., 2005) and hard X-ray bands (Barger et al., 2003; Ueda et al., 2003; La Franca et al. 2005; see i.e. fig. 2.6) reveals that the number density of fainter objects peaks at a lower redshift with respect to brighter ones. In particular the redshift of the peak in number density of AGNs increases with the hard X-ray luminosity L_X , from $z \sim 0.5 - 0.7$ at $L_X \sim 10^{42} - 10^{43}$, up to $z \sim 2.5$ at $L_X \sim 10^{46}$. The same conclusion holds for the analysis of the accretion history of SMBH. Shankar et al. (2004) showed that the most massive BHs (associated with bright QSOs) accreted their mass faster and at higher redshifts $z > 1.5$, while the lower mass BHs have mostly grown at $z < 1.5$. As already stressed in the overview and in sec. 1.2.4 this behavior is often referred to it as “anti-hierarchical” scenario of black-hole growth, or “downsizing”. This is confirmed by the analysis of Merloni (2004), based on the fundamental plane of AGN (Merloni, Heinz & di Matteo, 2003), and by Marconi et al. (2004).

This behavior is not easy to reproduce in the hierarchical cosmogonic scenario, where larger DMHs form on average later by the merging of less massive halos. As we already discussed in sec. 1.2.4, a similar trend has longly been claimed to be present in elliptical galaxies. As we already introduced in sec. 1.5.1, this points to a formation scenario characterized by a quick burst of star formation rapidly followed by a strong wind which expels the residual Inter-Stellar Medium (ISM); this wind should take place earlier in more massive galaxies (Matteucci 1994). In this framework it is also possible to explain the high metallicity of quasar hosts (Matteucci & Padovani, 1993; Hamann & Ferland, 1999; d’Odorico et al., 2004; Granato et al., 2004).

Recently, the GOODS collaboration determined the number density of faint quasars at $z \sim 4$ (Cristiani et al. 2004), revealing a dearth of objects with respect to naive extrapolations of Pure Luminosity Evolution (PLE) models anchored to the SDSS bright quasars (Fan et al. 2003). This evidence, confirmed by the COMBO17 survey at higher luminosities (Wolf et al. 2003) and consistent with the older data of Kennefick, Djorgovski and Meylan (1996), is again in line with the “anti-hierarchical” trend mentioned above. In following chapter 3 we will discuss how it is possible to use the Cristiani et al. (2004) results combined with SDSS observations in order to determine the LF of QSOs and its evolution in the range $3.5 < z < 5.2$. This determination result in great importance in order to constrain different model of galaxy formation and evolution as we will show in chapter 6.

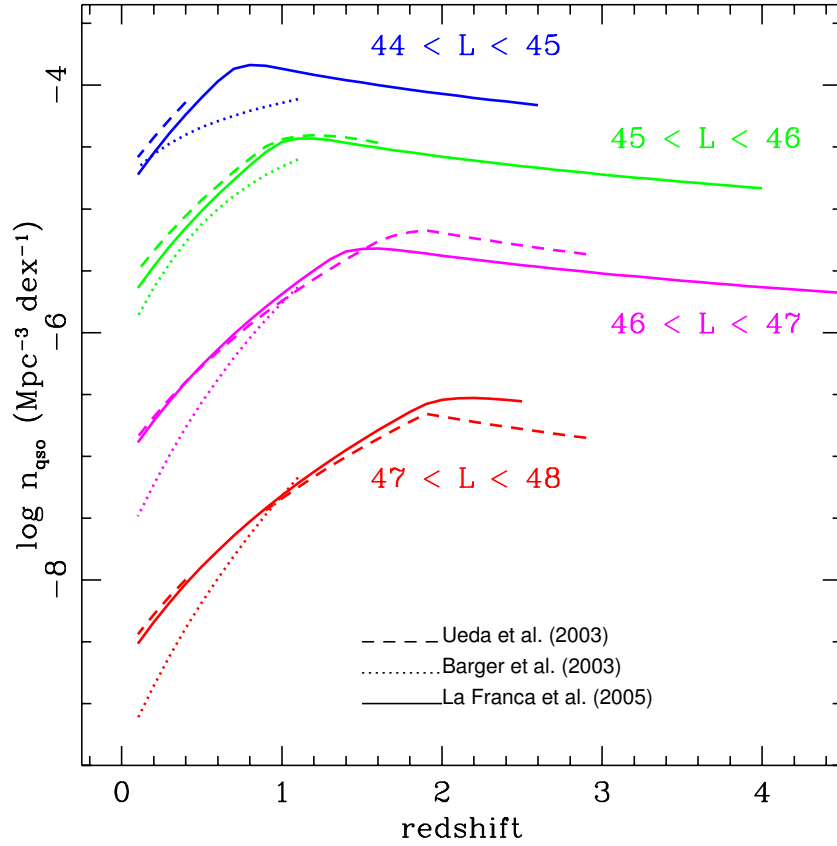


Figure 2.6: The effect of Downsizing as seen in Hard X-ray band. Comparison between the QSO number densities predicted by integrating the analytical fits of the luminosity functions of La Franca et al. (2005, solid line), Barger et al. (2003, dotted line), Ueda et al. (2003, dashed line).

Chapter 3

High Redshift QSOs in the GOODS

¹Once considered peculiar and exotic objects, quasars (QSOs) have been recognized in recent years to be an important and possibly a necessary phase of galactic evolution, at least for spheroids (Danese et al. 2003). In particular, models for the joint evolution of galaxies and QSOs (e.g. Granato et al 2001, 2004) reproduce the properties of present-day elliptical galaxies assuming that their vigorous star formation at high redshift is quenched by feedback (i.e. galactic winds) triggered by the QSO activity (see also chapter 5), fed by the matter accretion onto a SMBH at the center of the galaxy itself. In this way the properties of high redshift QSOs, in particular their luminosity function are fundamental to understand the phenomena that are driving galaxy formation, and have been hypothesized to invert the Dark Matter Halo (DMH) hierarchical sequence for the collapse of baryonic matter: the so called *downsizing* (Cowie et al., 2004, see also 1.2.4 and 2.4). The depth of the potential wells in different DMH is a key factor in determining the timescale for star formation, accretion and eventually the effects of feedback, setting the pace for AGN activity along the cosmic history.

Great progress has been recently achieved thanks to the large amount of data coming from major observational programs such as the *Two Degree Field QSO Redshift Sources* (2dF-QRS, Croom et al., 2004, www.2dFquasar.org) and the third edition of the *Sloan Digital Sky Survey Quasar Catalog* (DR3QSO, Schneider et al., 2005). The 2dF-QRS contains more than 23000 QSOs typically at redshift below $z \leq 2.10$, while the DR3QSO lists 46420 QSOs up to $z \sim 6.4$. However at high redshift the SDSS is sensitive only to the most luminous QSOs ($M_{145} \leq -26.5^2$). The faint end of the high- z QSO Luminosity Function (LF) is left almost unconstrained due to the challenging magnitude limit. However, the determination of the faint end slope plays a key role for comparing different predictions on galaxy formation and evolution, a field where the properties of QSOs encounter puzzling problems.

¹The results presented in this chapter will be submitted for publication in Fontanot, Cristiani, Monaco, et al. (2006)

²Absolute AB magnitude at a wavelength of 145 nanometers

The recent *Great Observatories Origins Deep Survey* (GOODS) provides an important database for studying QSOs with $M_{145} \leq -21$, thanks to the deepness of its optical observations and its multiwavelength nature. GOODS is a deep survey, not a wide one, but it is much larger than most previous deep HST/WFPC2 surveys, covering 320 arcmin^2 , 32 times the combined solid angles of the Hubble Deep Field-North and South, and four times larger than their combined flanking fields. The GOODS-ACS optical data have been analyzed in a previous paper (Cristiani et al. 2004) in order to select reliable QSO candidates and try a first estimate of their space density in the redshift interval $3.5 < z < 5.2$. The selection was carried out by defining suitable optical selection criteria based on magnitude limits and colors, and then by matching the optical candidates with x-ray Chandra Surveys (Alexander et al., 2003; Giacconi et al., 2002).

We take advantage of the SDSS 3rd Data Release, of a new analysis and a more complete spectroscopic follow up of the GOODS data in order to determine the QSO space density at $3.5 < z < 5.2$, down to the faint end of the LF. We adopt a definition of QSO encompassing all objects with strong, high-ionization emission lines and $M_{145} \leq -21$, including both conventional, broad-lined (type-1) QSOs and narrow-lined, obscured (type-2) QSOs. We adopt a flat universe with cosmological parameters $\Omega_m = 0.3$, $\Omega_\Lambda = 0.7$ and Hubble Constant $H_0 = 70 \text{ Km s}^{-1} \text{ Mpc}^{-1}$. Magnitudes are in the AB system.

3.1 The Database

3.1.1 Bright QSOs from the SDSS

The bright quasar sample we use in this work is extracted from the DR3QSO. The main SDSS catalogue covers an area of about 5282 deg^2 in photometry and 4188 deg^2 in spectroscopy. Photometric catalogues were compiled with observations in g , r , i , z bands (Fukugita et al., 1996). Several selection criteria were applied in order to select suitable candidates for spectroscopy. In a recent paper Richards et al., (2002) presented the definitive version of selection criteria. In particular we are interested in the high- z QSO selection. Due to the nature of SDSS observations, the DR3QSO is not a complete sample and consists of objects found in several spectroscopic campaigns. Richards et al., (2002) selection criteria are thought as useful tool in order to select a complete sample of high- z QSOs. However only part of the photometric selected QSOs candidates have been observed up to now. Comparing the SDSS photometric and spectroscopic catalogues, we estimate that only $\sim 21\%$ of photometric object satisfying the Richards et al., (2002) criteria had a spectrum. Fan et al. (2003) compiled a complete sample of high- z QSOs out of the SDSS commissioning data. However we decided to use DR3QSO, in order to have a larger sample of objects taken out from a larger area of the sky. The price of this choice consists in the fact that we were compelled to a more complex analysis in order to take into account the incompleteness of the DR3QSO with respect to our purposes. There are 581 QSOs in DR3QSO with a redshift between $3.5 < z < 5.2$ and satisfying the Richards et al., (2002) criteria.

Table 3.1: Parameters for the new field definition in the GOODS

| HDF-N | | CDF-S | |
|-------|-----------|-------|-----------|
| a | $b + 62.$ | a | $b - 27.$ |
| -0.46 | +4.67 | -2.46 | +18.93 |
| +0.47 | -3.96 | +0.34 | -3.70 |
| -0.47 | +4.38 | +0.34 | -3.40 |
| +0.47 | -4.18 | -2.45 | +19.32 |

3.1.2 Faint QSOs from the GOODS

The Great Observatories Deep Survey covers an area of 320 arcmin², subdivided in two 160 arcmin² sub-fields centered on the *Chandra* Deep Field-South (CDF-S) and Hubble Deep Field-North (HDF-N). The optical data have been obtained with the Advanced Camera for Surveys (ACS) onboard *HST* in the framework of the GOODS/ACS survey described in Giavalisco et al. (2004a). The catalogs used in this work, prepared using the SExtractor package (Bertin & Arnouts, 1996), are based on the version *v1.0* of the reduced, calibrated, stacked and mosaiced images acquired with HST and ACS as part of the GOODS ACS Treasury program³. Source detection has been made using the z-band images. The magnitude limits in the four bands are respectively 27.50, 27.25, 27.00 and 26.5.

The HDF-N and CDF-S fields have been observed in the X-rays with *Chandra* for 2 Ms and 1 Ms, respectively (Alexander et al. 2003; Giacconi et al. 2002), providing the deepest views of the Universe in the 0.5–8.0 keV band. The X-ray completeness limits over $\approx 90\%$ of the area of the GOODS fields are similar, with flux limits (S/N= 5) of $\approx 1.7 \times 10^{-16}$ erg cm⁻² s⁻¹ (0.5–2.0 keV) and $\approx 1.2 \times 10^{-15}$ erg cm⁻² s⁻¹ (2–8 keV) in the HDF-N field, and $\approx 2.2 \times 10^{-16}$ erg cm⁻² s⁻¹ (0.5–2.0 keV) and $\approx 1.5 \times 10^{-15}$ erg cm⁻² s⁻¹ (2–8 keV) in the CDF-S field (Alexander et al. 2003). The sensitivity at the aim point is about 2 and 4 times better for the CDF-S and HDF-N, respectively. As an example, assuming an X-ray spectral slope of $\Gamma = 2.0$, a source detected with a flux of 1.0×10^{-16} erg cm⁻² s⁻¹ would have both observed and rest-frame luminosities of 8×10^{42} erg s⁻¹, and 3×10^{43} erg s⁻¹ at $z = 3$, and $z = 5$, respectively (assuming no Galactic absorption). Alexander et al. (2003) produced point-source catalogs for the HDF-N and CDF-S and Giacconi et al. (2002) for the CDF-S.

The color selection

The selection of the QSO candidates has been carried out in the magnitude interval $22.25 < z_{850} < 25.25$. In order to avoid the lower quality zones of the ACS mosaics at the borders of the GOODS fields, we have carried out the selection in a slightly reduced area of 157.1 arcmin² in the HDF-N and 156.4 arcmin² in the CDF-S.

QSO expected colors in the ACS bands have been estimated as a function

³see, for details <http://www.stsci.edu/science/goods/>

of redshift using the template of Cristiani & Vio (1990, fig 2.3) of the QSO spectral energy distribution (SED) convolved with the Madau, Haardt & Rees (1999) model of the intergalactic medium (IGM) absorption. The same scheme will be adopted in the following for the estimate of expected colors in the different SDSS passbands, unless otherwise specified.

In Cristiani et al. (2004) four optical criteria had been tailored in order to select QSOs at progressively higher redshift in the interval $3.5 \leq z \leq 5.2$:

$$i - z < 0.35 \text{ AND } 1.1 < B - V < 3.0 \text{ AND } V - i < 1.0 \quad (3.1)$$

$$i - z < 0.35 \text{ AND } B - V > 3.0 \quad (3.2)$$

$$i - z < 0.5 \text{ AND } B - V > 2.0 \text{ AND } V - i > 0.8 \quad (3.3)$$

$$i - z < 1.0 \text{ AND } V - i > 1.9 \quad (3.4)$$

These color selection criteria are expected to be most complete and reliable at $z > 4$ (corresponding to criteria 3.2–3.4). They select a broad range of high- z AGN, not limited to broad-lined (type-1) QSOs, and are less stringent than these typically used to identify high- z galaxies (e.g., Giavalisco et al., 2004b). Below $z \simeq 3.5$ the typical QSO colors in the ACS bands move close to the locus of stars and low-redshift galaxies. Beyond $z \simeq 5.2$ the $i - z$ color starts increasing and infrared bands are needed to efficiently identify QSOs with an “ i -dropout” technique. The full set of color criteria select objects in the redshift range ($3.5 < z < 5.2$), while the subset (3.2–3.4) is able to select objects with $z > 4$.

Matching the color selection with X-ray catalogues

The optical candidates selected with the criteria (3.1–3.4) have been matched with X-ray sources detected by *Chandra* (Alexander et al. 2003; Giacconi et al. 2002) within an error radius corresponding to the 3σ X-ray positional uncertainty. With this tolerance the expected number of false matches is five and indeed two misidentifications, i.e. cases in which a brighter optical source lies closer to the X-ray position, have been rejected (both in the CDF-S). We expect that Type-1 QSOs with $M_{145} < -21$, given the measured dispersion in their optical-to-X-ray flux ratio (Vignali et al., 2003), should be detectable in our X-ray observation up to $z \sim 5.2$. Conversely, any $z > 3.5$ source in the GOODS region detected in the X-rays must harbor an AGN ($L_x(0.5 - 2 \text{ keV}) \geq 10^{43} \text{ erg s}^{-1}$).

The resulting sample consists of 16 candidates, 10 in CDF-S and 6 in HDF-N (Tab. 3.2). With respect to the candidates in Cristiani et al. (2004) we have found some differences: in HDF-N (CDF-S) three (one) candidates selected in Cristiani et al. (2004) disappear from the selection, while three (one) new candidates enter the selection. These differences are due first of all to the improved photometry of the adopted catalogue. In fact Cristiani et al. (2004) was based on a earlier version of the GOODS/ACS catalogue which modifies the estimated colors of the objects. Besides, we take advantage of the improved astrometry in the upgraded version of the optical ACS catalogues, by means of

which a better matching is possible between the optical and the X-ray sources. We discuss in more detail the implication of these changes in the next section.

Spectroscopic follow-up

The QSO candidates have been observed and their spectra reduced during in the GOODS spectroscopic survey (Vanzella et al., 2005; Szokoly et al., 2004 and Vanzella et al. 2006 in CDF-S; Cowie et al., 2004 and Wirth et al., 2004). Some objects have been observed in previous surveys (Barger et al. 2001, 2002, 2003) . The spectroscopic redshifts and the spectroscopic identifications of our candidates are listed in table 3.2.

Among them, 13 (5 in the HDF-N and 8 in CDF-S) turn out to be *AGN*, with 11 QSOs at $z > 3.5$ (4 and 7) of which 2 (0 and 2) are identified as Type-II. In particular one object (*CDF* – *S033229.29* – *275619.5*) turns out to be a QSO with a redshift $z = 4.759$. This object was observed and its spectrum (one hour exposure with *FORS2* at *ESO-VLT*) is show in fig. 3.1(a). This object, in addition to the already observed object *HDF* – *N123647.97* + *620941.7* at $z = 5.189$ (Barger et al., 2002), brings to two the total number of objects in the redshift range $4 < z < 5.2$, where our selection criteria are expected to be most complete and reliable.

Checking the completeness of the X-ray criterion

In table 3.2 the information about the morphology of the candidates in the optical catalogue is also listed. The SExtractor software provides a set of parameters quantifying the radius (in pixels) inside which a given percentage of the source flux is concentrated. In the following we fix this percentage at 10% and we consider the related parameter (we will refer to it as *FLUX_RADIUS*). The analysis of the distribution of *FLUX_RADIUS* values in our sample of QSOs candidates leads to interesting conclusions about the appearance of the sources. The candidates with greater *FLUX_RADIUS* values turn out to be either lower redshift contaminant galaxies or Type-2 QSOs. In particular this parameter is typically lower than 2 for Type-1 QSOs, while Type-2 QSOs show *FLUX_RADIUS* < 2.5 . Values greater than 2.5 usually correspond to low redshift galaxies and misidentifications.

If we consider the changes in the selected candidates between Cristiani et al. (2004) and the present work, we can also draw some interesting conclusion. As shown in the previous section, 3 objects selected in Cristiani et al. (2004) are not recovered in the present work. Two of these objects turn out to be lower redshift galaxies, and both have *FLUX_RADIUS* > 2.5 . The third object is a confirmed QSO candidate with a redshift $z = 2.573$. Our analysis shows that its new colors don't satisfy our criteria anymore. On the contrary, if we consider objects present in both in the first and in the present selection, those are confirmed QSOs. Finally, 3 new objects are selected with the last version of ACS-catalogue: all are confirmed QSOs. Among them we found an additional candidate (*CDF* – *S033240.82* – *275041.4*) which is a low redshift type-2 *AGN*.

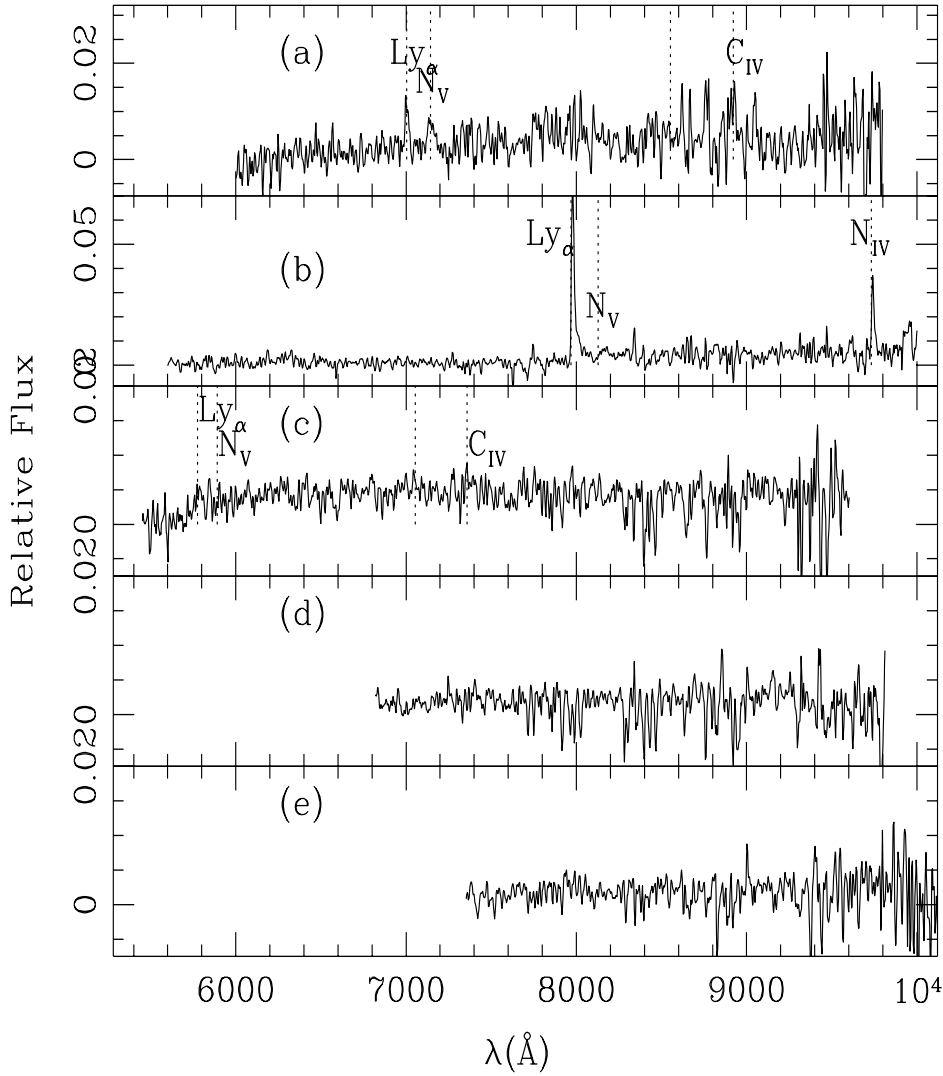


Figure 3.1: Spectroscopic follow-up results. Spectrum of $CDF - S033201.28 - 274432.2$ (upper panel) and of $CDF - S033229.29 - 275619.5$ (lower panel) with the features used in the determination of spectroscopic redshift. Spectra are the result of one hour exposure with *FORS2* at *ESO - VLT*.

Among our candidates we focus our attention of the confirmed $z = 4.76$ QSO ($CDF - S033229.29 - 275619.5$): it is a faint X-ray source and it was selected by matching our optical candidates with the supplementary X-ray catalogue by Giacconi et al. (2002). This brings up the possibility of the presence of an AGN population with faint X-ray fluxes, due to the heavy obscuration of the AGN, or to intrinsic faintness of the emission. This faint sources would be not present in the X-ray catalogues, we match the optical candidates with. We then decide to try to select new candidates without

applying the X-ray brightness hypothesis.

We start constraining our selection only to point-like sources and so we apply an additional criterion based on FLUX_RADIUS at the whole sample. By analyzing the distribution of the values of this parameter with respect to the allowed z_{850} magnitude limits it is possible to define an adequate criterion by means of which we are able to distinguish between point-like and extended sources.

$$\text{FLUX_RADIUS} < 2.0 \tag{3.5}$$

We decide to use the more stringent version of this criteria to reduce the number of selected objects to the more interesting ones. Applying the criteria (3.1–3.5) to the GOODS catalogues we recover 111 candidates in HDF-N and 108 in CDF-S. The candidates $z > 4$ QSO are 30 in HDF-N and 30 in CDF-S.

The resulting sample includes candidates in the redshift range $3.5 < z < 5.2$. However for $3.5 < z < 4$ the locus of expected QSO colors falls so near the locus of stellar colors that the photometric errors give us only a small chance to distinguish between stars and AGNs only on the basis of optical colors. The situation improves if we consider $z > 4$ candidates, in spite of the relevant difference between stellar and QSO expected colors; moreover this is also the redshift bin where we expect our selection criteria to be most complete and reliable. We then decide to focus our attention of this redshift interval in order to get better insight on the reliability of our morphological selection. We try to define a small sample including the most promising candidates in order to propose a spectroscopic follow-up of these objects. This subsample has been defined using color space sections as a diagnostic tool. We show an example of these sections in figure 3.2 for the $v - i$ vs $i - z$ space.

In fig. 3.2 we plot as crosses the colors of our $z > 4$ candidates. The solid line is the locus of expected QSO colors for $z > 2.7$; we indicate with asterisks the colors at a redshift of 3.5, 4 and 5.2. First of all we identify the candidates with no B_{445} counterpart as B -dropouts: we select these objects as good candidates at the redshift of interest. Among our morphological selected candidates we find 3 B -dropouts in CDF-S and 4 in HDF-N. A second criterion consists in the analysis of $V_{660} - i_{774}$ vs $i_{774} - z_{850}$ plane. Some of our candidates have colors very similar to QSO colors and different from star colors at the same time. Intriguingly, some of these objects correspond to B -dropouts. Among the others we select these with $V_{660} - i_{774}$ vs $i_{774} - z_{850}$ colors similar to the expected QSO colors. The resulting additional sample is listed in table 3.3 and consists of 5 candidates in the northern field and 5 candidates in the southern one. Among these additional candidates we are able to pick up the 2 already observed $z > 4$ QSOs. They are indicated as squares in figure 3.2. Their colors lie in the expected position and their recovery is a confirmation that our assumptions are reliable in selecting QSOs only on the basis of their optical color. The final subsample of 10 morphologically selected candidates is presented in tab. 3.3 and has been proposed for spectroscopic observation as a part of the GOODS program. A substantial fraction of these objects had been already observed during GOODS spectroscopic surveys. The spectra of some of these objects are collected in fig. 3.1. Two objects in the

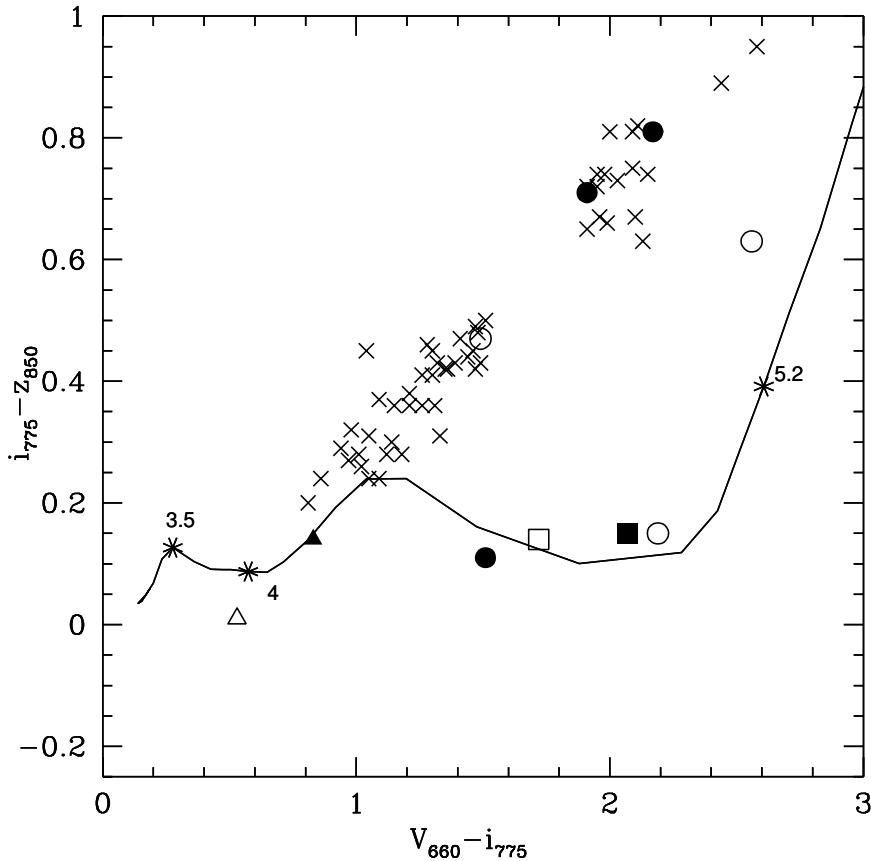


Figure 3.2: The $V_{660} - i_{775}$ versus $i_{775} - z_{850}$ color in HDF-N and CDF-S. The colors of the $z > 4$ morphological selected candidates are indicated with crosses. The filled (empty) symbols mark the position of our 5 final candidates in HDF-N (CDF-S). The squares represent the position of the confirmed $z > 4$ QSOs. The circles represent the position of the $B - V$ dropouts. The solid line shows the locus of expected QSO colors at $3.5 < z < 5.2$; we have marked with asterisks the positions corresponding to redshift 3.5, 4 and 5.2.

CDF-S result to be high redshift galaxies, but they lack any clear signal of AGN activity. The spectrum of one of them is shown in figure 3.1(b). This object is not a QSO, due to the lack of the typical features in the spectrum. However its extremely luminous Ly_{α} line makes its colors similar to our criteria and from this feature we are able to estimate that this object has a redshift $z = 5.554$. The four proposed objects in HDF-N have been observed. The resulting spectra are somehow inconclusive but no sign of AGN activity has been revealed. We can then conclude that the probability of finding additional QSOs with extremely faint X-ray fluxes in GOODS fields is low. The sample proposed in tab. 3.2 is therefore a reliable estimate of the total QSO space density in the redshift of interest.

After this analysis we can safely conclude that there are no more than 3–4 QSOs in the two combined GOODS fields with $z > 4$; at the moment only 2

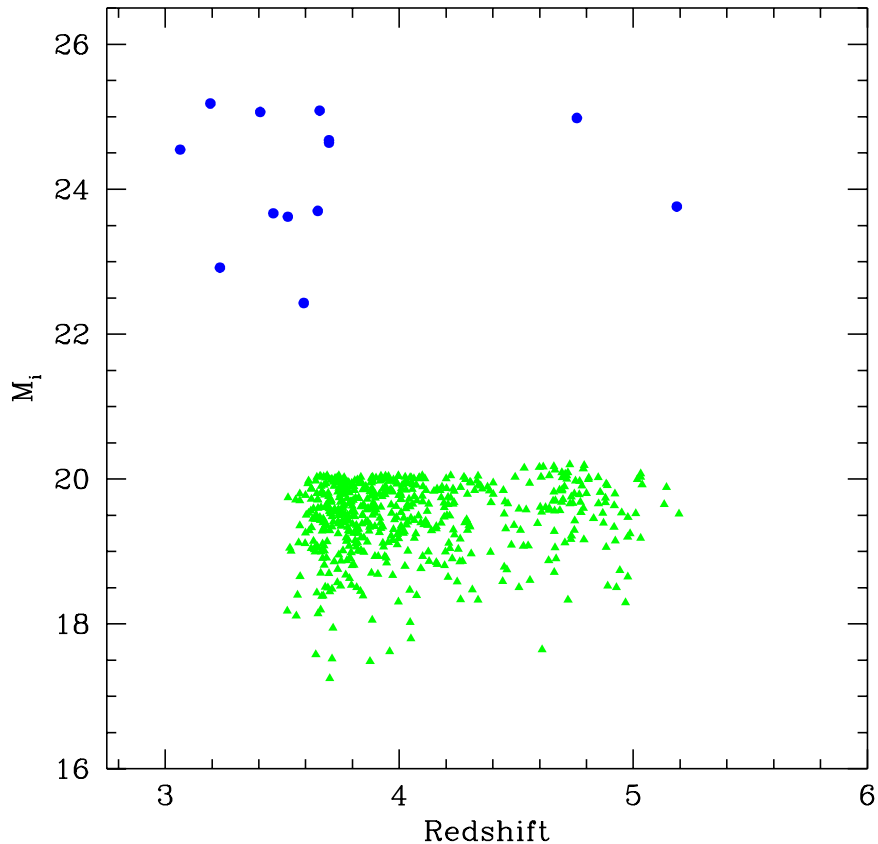


Figure 3.3: Distribution of DR3QSO (filled triangles) and GOODS (filled circles) quasars in the Redshift versus M_i space.

on them are confirmed.

3.2 Computing the Luminosity Function of high- z QSOs

In this section we describe the procedure we adopt in order to build up the high- z QSO LF from the joint analysis of GOODS and SDSS observations. The two samples are complementary in terms of the surveyed area and the brightness limit and are characterized by different photometric systems, selection criteria and spectroscopic completeness. In fig. 3.3 we show the position of the observed SDSS and GOODS QSOs in the z - M_i space. It is evident from the figure that the two survey cover two non-overlapping regions of this space. In order to have all these features under control we decide to build a QSO template library. Using this library we can analyze statistically the properties of QSO colors in the redshift interval of our interest and reconstruct separately the properties of the two surveys.

3.2.1 QSO template library

In order to build a QSO template library we decide to use the high quality SDSS QSO spectra at lower redshift. First of all we need a redshift interval for which the SDSS sample has a high level of completeness. We select the interval $2.2 < z < 2.25$ because at lower redshifts, owing to the dynamical range of the Sloan spectrograph, the Ly_α emission line is not completely sampled, while at $z > 2.25$ QSO colors start to be too close to the stellar locus. Among the object in DR3QSO with $2.2 < z < 2.25$, we select the higher quality spectra. Our final sample consists in 215 objects. We then compute the restframe spectrum of each object. We complete the spectra blueward the Ly_α using a continuum fitting technique similar to Natali et al. (1998): we define several “continuum windows” along the spectrum and fit the observed fluxes with a power law. We use the resulting parameters to complete the spectrum blueward the Ly_α .

We use each spectrum in our library to compute the theoretical QSOs colors at increasing redshift in the SDSS and ACS photometric systems. In order to simulate the QSO spectra at different cosmic epochs we redshift our spectra up to the redshift of interest, then use the Madau, Haardt & Rees (1999) model for the IGM to simulate the IGM absorption.

In order to test the IGM model at the redshift of our interest we compare its predictions with the observations of Songaila (2004). We apply the IGM model to the Cristiani & Vio (1990) template spectrum and we compute the absorption τ following the same procedure used by Songaila (2004) on real spectra. The result is shown in fig. 3.4. Green crosses refer to the observed values of Songaila (2004), while the magenta dashed line represents the prediction of Madau, Haardt & Rees (1999) model. It is evident from the figure that this model overpredicts the Ly_α transmitted fraction at redshift larger than 4, and underpredicts the Ly_β and Ly_γ at redshift larger than 3. We use the ratio between observations and predictions to compute an empirical correction to the Madau, Haardt & Rees (1999) model at the corresponding wavelengths. The red solid line in fig. 3.4 represents the result when we apply our modified IGM absorption model to the Cristiani & Vio (1990) template spectrum.

3.2.2 QSOs color prediction

We then compute the expected mean QSO colors using our template library. The statistical analysis of the whole sample provides a distribution of colors due to the different continuum slopes and strength of the emission lines in the observed spectra.

In figure 3.5 we show our results for the SDSS photometric system compared to real colors in DR3QSO. The points refer to the color of observed QSOs at different redshift (see caption for more details). In the left panel the dashed line refers to the Richards et al., (2002) SDSS selection criteria for $z > 3.5$ QSOs. Our predictions of QSO colors are represented with solid lines (dotted lines are 5% and 95% percentiles). The agreement with the observed colors is quite good.

We also accurately predict the redshift evolution of QSO colors. In fig. 3.6

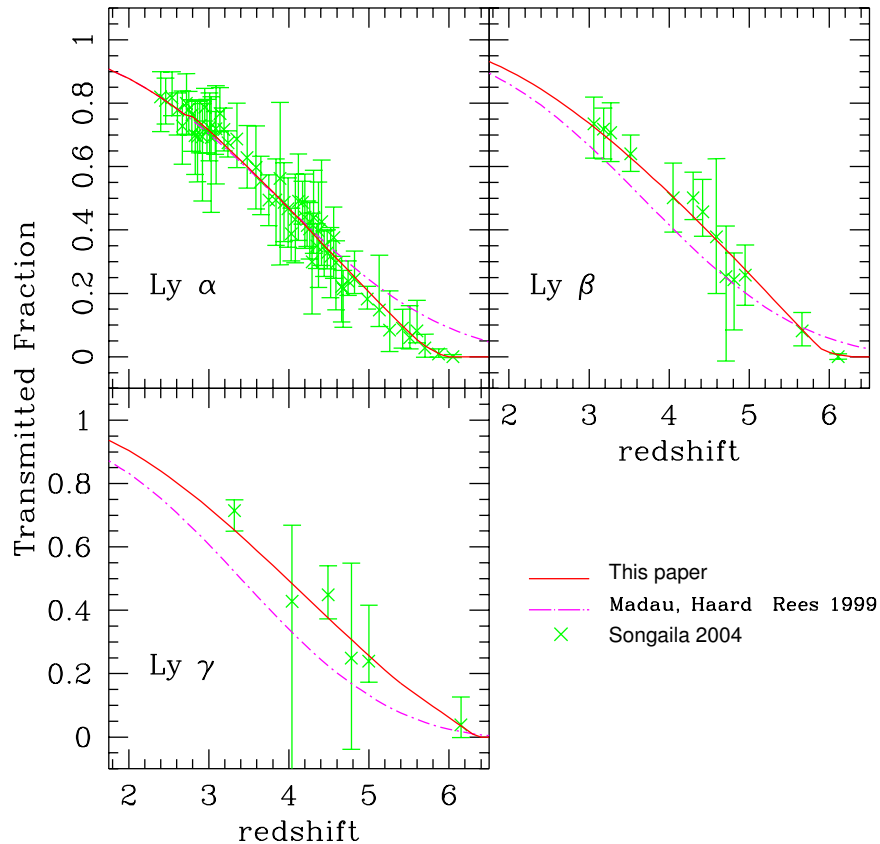


Figure 3.4: Comparison between different estimates of IGM absorption. Green crosses refer to Songaila (2004) observations; magenta dashed lines refers to the prediction of Madau, Haardt & Rees (1999) model (applied to the QSO template spectrum of Cristiani & Vio 1990), while red solid line shows the applied IGM absorption.

we show our prediction for the $g-r$, $r-i$, $i-z$ color in the SDSS photometric system compared with observed QSO colors. We are able to recover both the trend of colors with redshift, and the scatter around the mean colors (as in fig. 3.5 dotted lines refer to 5% and 95% percentiles). Similar results hold for the GOODS survey.

3.2.3 Completeness against selection criteria

It is evident from fig. 3.5 and fig. 3.6 that we are able to predict the expected colors with accuracy. We can then safely use our template library in order to estimate the properties of the two independent samples. In particular we focus our attention on the completeness of the samples selected using the GOODS and DR3QSO criteria. In order to obtain a robust estimate of this quantity we apply the selection criteria to our template library and analyse the fraction

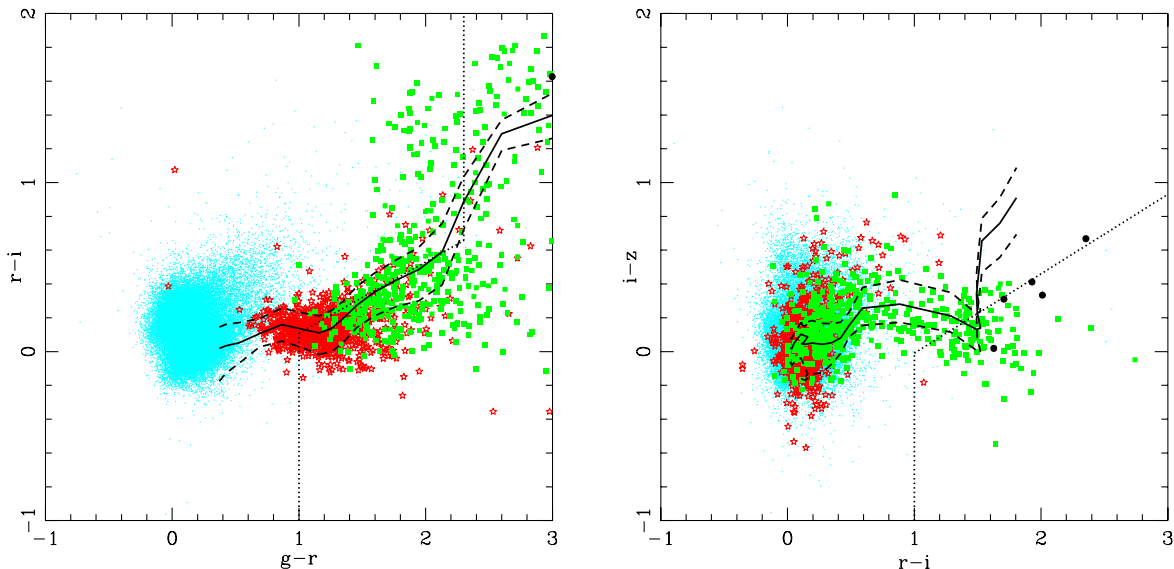


Figure 3.5: Color diagrams for the confirmed QSOs in DR3QSO. Red stars refer to objects with $3.5 < z < 4.0$; green squares refer to objects with $4.0 < z < 5.2$; filled circles refer to objects with $z > 5.2$; cyan dots refer to objects with $z < 3.5$. The solid line refer to our prediction of QSOs colors in the SDSS photometric system. Dotted lines are the 5% and 95% percentiles. Dashed line refers to the selection criteria of Richards et al. (2002) for $z > 3.5$ QSOs.

of QSOs which survive the selection at various redshifts. The result is shown in figure 3.7 (left panel). The SDSS selection criteria seems to be inefficient in selecting objects at $z \sim 4.4 - 4.5$. We try to confirm this result using the DR3QSO. We consider the redshift distribution of all objects, and we compare it with the redshift distribution of DR3QSO objects satisfying the Richards et al., (2002) selection criteria. The result is shown in figure 3.7 (right panel). We find an evident lack of $z \sim 4.4 - 4.5$ objects satisfying the selection criteria with respect to the total sample. We analyse also the same distribution for the Fan et al. (2003) sample and we find analogous results.

3.2.4 Simulated catalogues

We assume a luminosity function of the form of a double power-law:

$$\Phi(L_{145}, z) = \frac{\Phi^*(L^*)}{(L_{145}/L^*)^{-\alpha} + (L_{145}/L^*)^{\alpha}}$$

or, expressed in magnitudes:

$$\Phi(M_{145}, z) = \frac{\Phi^*(M^*)}{10^{0.4(\alpha+1)(M_{145}-M^*)} + 10^{0.4(\beta+1)(M_{145}-M^*)}}$$

We model also a pure luminosity evolution (PLE)

$$L^* = L_{(z=2.1)}^* (1+z)^k$$

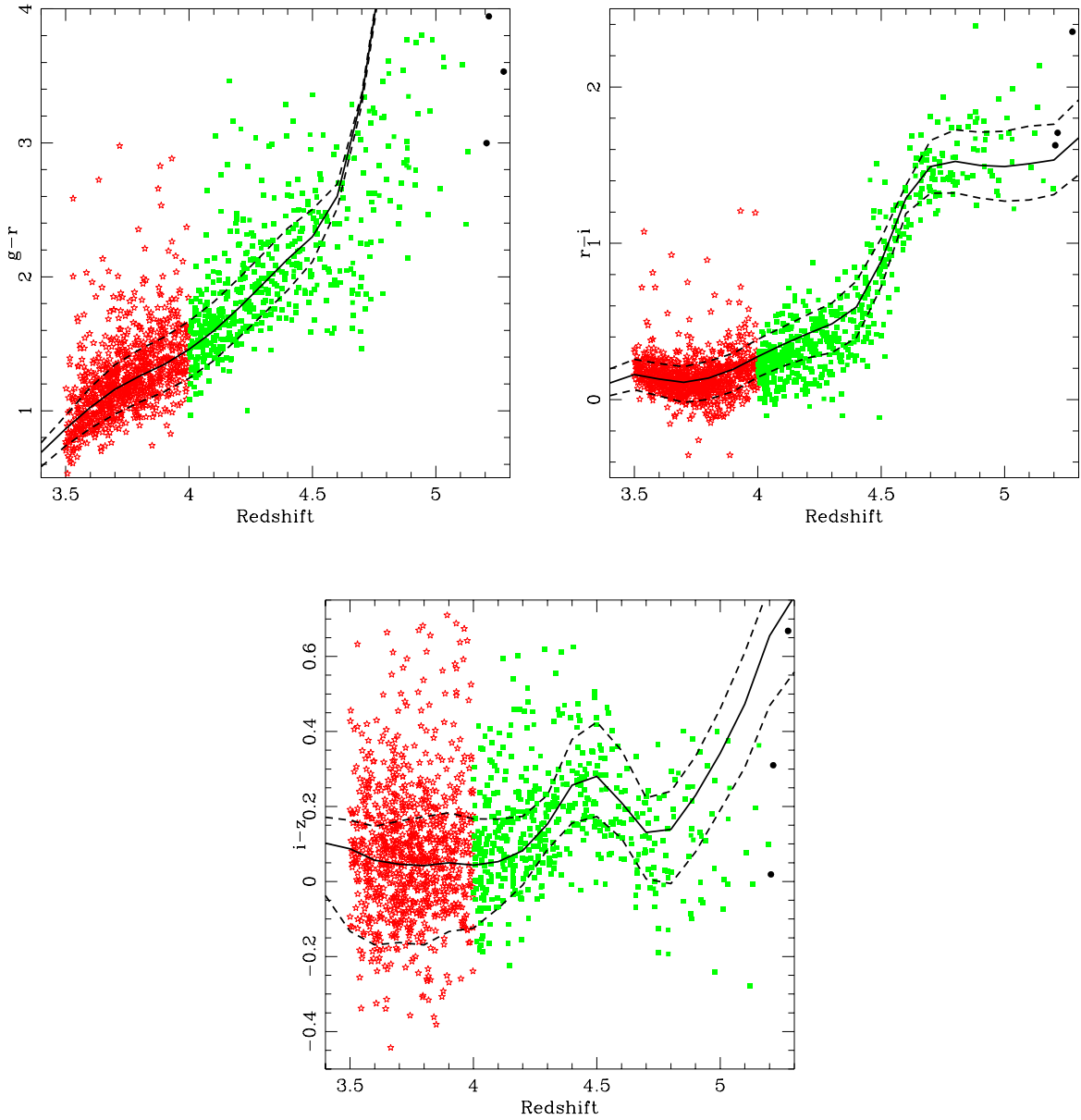


Figure 3.6: Evolution of QSO colors with redshift in the SDSS photometric system. Symbols are the same of figure 3.5.

or in magnitudes:

$$M^* = M_{(z=2.1)}^* - 2.5 k \log(1 + z)$$

and a pure density evolution (PDE)

$$\Phi^* = \Phi_{(z=2.1)}^* (1 + z)^k$$

Given a value for the break luminosity (L^* or M^*), for the slopes of the double power-law α and β , for the normalization $\Phi_{(z=2.1)}^*$ and for the redshift evolution parameter k , we are able to calculate from the LF the

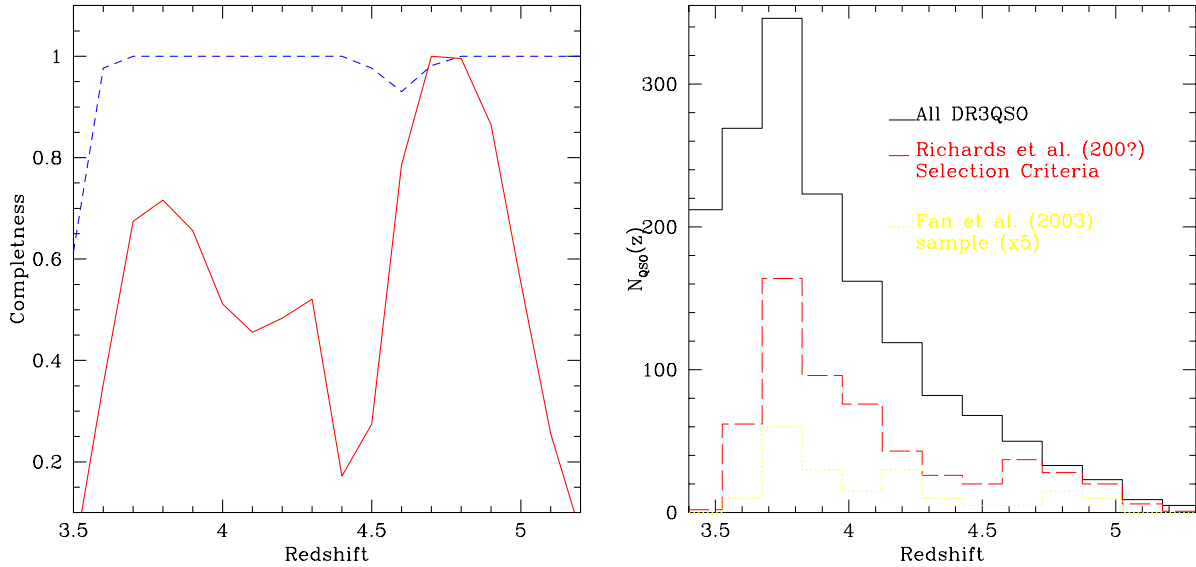


Figure 3.7: Left panel: Completeness of selection criteria at various redshifts. The solid line refers to Richards et al., (2002) selection criteria for SDSS sources. The dashed line refer to Croom et al. (2004) selection criteria in the GOODS fields. Right panel: Redshift distribution of DR3QSO sources (solid line). The dashed line represents the redshift distribution of DR3QSO sources satisfying the Richards et al., (2002) selection criteria. The dotted line represents the redshift distribution of Fan et al. (2003) sample (multiplied by a factor 5 for graphical reasons) taken out of the SDSS commissioning data.

expected number of objects up to a given magnitude in a given area of the sky. We then extract for each object a suitable value of absolute M_{145} and redshift, according to the assumed LF. This way we construct a simulated sample. We then associate to each simulated object a template spectrum, randomly chosen from our library. Using the template K-correction and colors at the corresponding redshift, we simulate the apparent magnitudes in the SDSS and ACS photometric systems. We also compute an estimate of the photometric errors in each band by analyzing the magnitude errors in DR3QSO and GOODS. This way we end up with mock SDSS+GOODS catalogues and apply to them the selection criteria of real catalogues, thus ending up with a simulated sample of QSOs.

3.2.5 Computing the QSO LF

The advantage of such an approach is related to the fact that we are able to generate and analyze a set of simulated SDSS+GOODS samples with the same properties of the real ones in terms of selection criteria, completeness, color and redshift distribution. We can associate simulated catalogues to each starting set of LF parameters. Using multiple realization for each parameter set, we are also able to limit the statistical error in these simulations and use them to

estimate the goodness of the agreement of a given LF to the observed sample, directly comparing observed and simulated objects. We divide the $z - M_i$ space into bins according to the distribution of observed objects and define a χ^2 statistics by comparing the simulated and observed objects in each bin. By using a minimization technique we then compute the best fit parameters of the Luminosity Function.

Our test LF has 5 free parameters. In order to compare our results to previous studies, we have decided to fix some of these using the analytical fit of the 2dF-QRS LF Croom et al. (2004). In Croom et al. (2004) they fit the 2dF-QSR with an analytical form similar to ours. They find that the LF is well approximated by a PLE in the redshift range between $0.4 < z < 2.1$. We use their estimate of parameters at $z = 2.1$ as a starting point for our PDE and PLE models. We try different models, that differ in the number of parameters fitted and in the kind of evolution. First of all we fit only against the evolutionary parameter k_{slope} with PDE and PLE models (models PDECr1p and PLECr1p); then we fit against two parameters k_{slope} and M_\star (models PDECr2p and PLECr2p); finally we fit against the three parameters k_{slope} , M_\star and α (models PDE-3p and PLE-3p). In a recent paper Richards et al. (2005) compiled a sample of quasars using imaging data from the SDSS and spectra taken by the 2dF facility at the Anglo-Australian Telescope. Their data are in good agreement with the 2QZ results of Croom et al. (2004) at the bright end, but they require a steeper faint end slope. We decide to consider models with the faint end slope taken from Richards et al. (2005), and the others parameters from Croom et al. (2004). In some cases we fit only the parameter k_{slope} (models PDERi1p and PLERi1p), while in other cases we fit k_{slope} and M_\star (models PDERi2p and PLERi2p). Fan et al. (2001) found a shallower slope for the bright end of LF using SDSS commissioning data. We define models fixing β to their value, and fitting the other parameters (respectively PLEF3p, PDEF3p).

We also try a different redshift evolution for the PDE model parameterized as follows:

$$\Phi^\star = \Phi^\star_{(z=2)} e^{k((1+z)-3.)}$$

The corresponding models are labeled according to the previous notation PDECK1p (Croom et al., 2004, parameters, fit against k_{slope}), PDECK2p (Croom et al., 2004, parameters, fit against k_{slope} and M_\star), PDERk1p (Croom et al., 2004, parameters and Richards et al., 2005, faint end slope, fit against k_{slope}), PDERk2p (Croom et al., 2004, parameters and Richards et al., 2005, faint end slope, fit against k_{slope} and M_\star), PDEk3p (Croom et al., 2004, parameters, fit against k_{slope} , M_\star and α), PDEFk3p (as PDEk3p but adopting the bright end slope of Fan et al. 2001). Finally, we perform an additional statistical check on the results by comparing the simulated and observed QSO distribution with a Kolmogorov–Smirnov bidimensional test.

In table 3.4 we collect the results for all models. For each model we indicate the fixed parameters, the fitted parameters, the corresponding value of the reduced χ^2 and the Kolmogorov–Smirnov probability P_{KS} . We compare our best fit models in fig. 3.8. We multiply the best fit model (PDE-3p) by the ratio

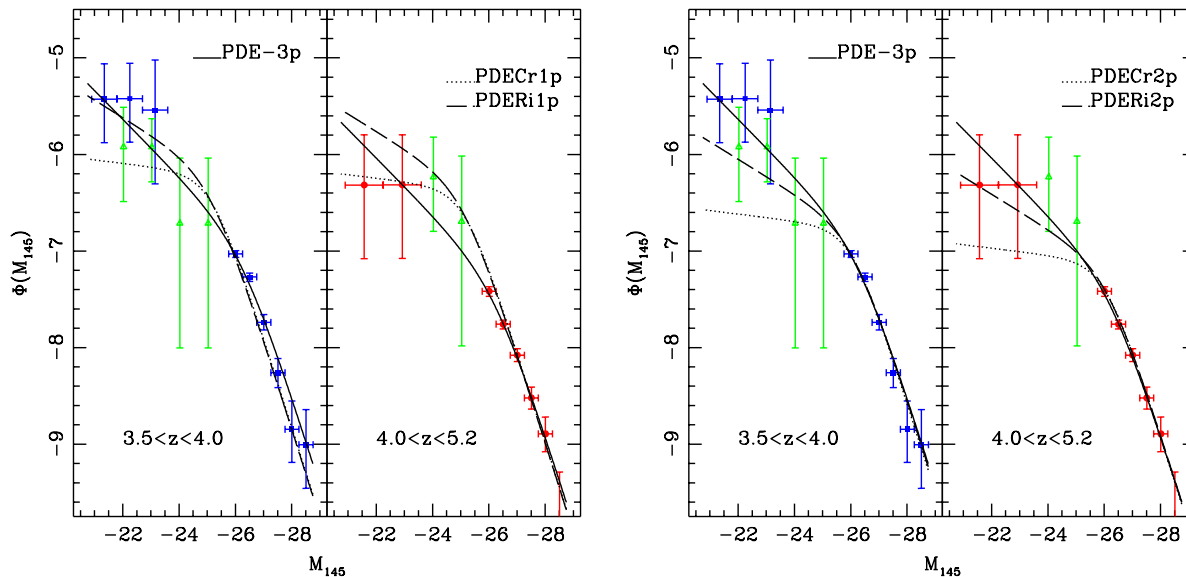


Figure 3.8: Analytical fits to the high- z QSO LF. See text for more details on various models. Blue and Red squares refer to the estimate of the QSO LF following La Franca & Cristiani (1997). Green empty triangles refer to the results of the the COMBO17 survey (Wolf et al., 2003).

between the number of observed sources and the number of simulated sources in a single simulated catalogue. La Franca & Cristiani (1997) demonstrated that this technique is less affected by possible bias effects with respect to the conventional $1/V_{max}$ technique.

It is very difficult to reproduce the observed distribution of objects with PLE models. On the contrary PDE models show a different level of agreement according to the number of fixed parameters. Models with one free parameter (PDECr1p and PDERi1p) are not able to reproduce real surveys in both redshift intervals. The problem is related to the adopted value of the M_* parameter. In models (PDECr2p and PDERi2p) we fit both k_{slope} and M_* and the agreement improves considerably. We interpret this result as a sign of an M_* evolution from $z \sim 2.1$ to $z \sim 3.5$. We also notice that models with a steeper slope of the faint end show a better agreement with observations. This finding is confirmed by the model PDE-3p, which shows the higher probability for a faint-end slope as steep as -1.76 . Similar results hold for PDE models with exponential evolution. Models with a shallower slope of the bright end of the LF (as suggested by Fan et al., 2003) are not able to reproduce the observed distribution of bright objects. A bright end slope as steep as Croom et al. (2004) is required.

We use our best estimate of the LF (PDE-3p) to compute the QSO contribution to the UV background at these redshift. Following the method proposed by Barger et al. (2003), we calculate the number of ionizing photons per baryon produced in the redshift interval by the observed AGN LF and we convert the rest frame 1450 \AA light to the number density of ionizing photons

using the form of the near-ultraviolet spectrum given in Madau, Haardt & Rees (1999). We find a ratio between ionizing photons and baryons of order of ~ 0.05 ; this result is similar to what Barger et al. (2003) found for $5 < z < 6.5$ QSOs. Both these results are an evidence that the QSO contribution to the UV background is insufficient to ionize the IGM at these redshifts.

3.3 Conclusions on the QSO LF

In this chapter we use the SDSS and GOODS databases in order to build a LF in the magnitude interval $-21.0 < M_{145} < 28.5$ and in the redshift interval $3.5 < z < 5.2$. We complete the analysis of Cristiani et al. (2004) on QSOs candidate selection in GOODS fields. We repeat the original analysis using the improved version of optical and X-ray catalogues, and we discuss the results of the spectroscopic follow-up of targets. The main conclusions of Cristiani et al. (2004) are confirmed by spectroscopy. We also explore the possible presence of faint X-ray AGNs, not detected in the Alexander et al. (2003) and Giacconi et al. (2002) catalogues. This additional analysis is mainly based on the morphology of the ACS optical images. The resulting additional candidates are selected through a direct comparison with the expected QSO colors. We observe spectroscopically the most interesting candidates and we find no additional QSO among them. We can then conclude that there is no relevant population of faint X-ray high- z AGNs with magnitude $M_{145} < -21$ in our fields.

We compute the high-redshift AGN luminosity function by combining the GOODS QSO sample with the DR3QSO one. In order to understand the systematics affecting the two different samples we develop a robust method for simulating the combined survey and estimating the completeness of the adopted selection criteria. This method is based on the definition of a library of QSO template spectra, starting from SDSS QSO observed spectra at lower redshift. Using this library we are able to predict the color of observed high- z QSO in the SDSS and the GOODS photometric systems. Assuming a parameterization of the QSO LF and its redshift evolution we simulate the expected number of objects in bin of redshift and apparent magnitude. Computing the agreement between real and simulated samples we are able to quantitatively evaluate the agreement of the fitting LF with data.

We assume several LF models, calibrated on low-redshift observations; our results show that PDE models agree with observations better than PLE models, even if a luminosity evolution of M_{145} from $z \sim 2.1$ to $z \sim 3.5$ is required to obtain a good match. The most interesting result is related to the faint end slope of the LF: models assuming a steep faint end slope (e.g. Richard et al., 2005) score a higher probability with respect to models assuming a flat faint end slope (e.g. Croom et al, 2004). If we try to fit also the faint end slope we obtain an even higher best fit value. Our result is in agreement with the conclusion of Hao et al. (2005): they analysed the emission line luminosity function of AGNs in the SDSS sample in the redshift interval $0.0 < z < 1.5$ and found a steeper value for the faint end slope with respect to Croom et

al. (2004) estimate. Finally, we do not find any evidence for a flattening of the bright end of the luminosity function with respect to Croom et al. (2004) value, at variance with the result of Fan et al. (2003).

We use our best estimate for the LF to compute the QSO contribution to the UV background at these redshift: we conclude that the QSO contribution to the UV background is insufficient to ionize the IGM at these redshifts. The present results on the high- z LF will be used in chapter 6 to give constraints to this model and to estimate the relevance of the joint feedback from Supernovae and AGN in shaping the redshift evolution of AGNs.

Table 3.2: QSO candidates.

| High-redshift QSO candidates in the CDF-S. | | | | | | | | | | | | | |
|--|--------------------|-----------------|--------------|-----------|---------|---------|---------|---|-----------|-------------|-----------------------|-----------------|---------------------------------------|
| Optical | Optical | Optical - X-ray | | z_{850} | $B - V$ | $i - z$ | $V - i$ | F_x^4 | | Flux | spectr. | spectroscopic | |
| RA | DEC | Δ RA | Δ DEC | AB | AB | AB | AB | 0.5 - 2 keV | 2 - 8 keV | Radius | redshift ⁵ | identification | |
| $3^h + m s$ | $-27^\circ + ' ''$ | (arcsec) | (arcsec) | (mag) | (mag) | (mag) | (mag) | (10^{-16} erg s $^{-1}$ cm $^{-2}$) | | (pixels) | | | |
| 32 04.93 ⁶ | 44 31.7 | +1.7 | -0.5 | 23.668 | 1.41 | 0.05 | 0.20 | < 0.74 | 4.10 | 1.75 | 3.462 | QSO | Cristiani et al. (2000) |
| 32 14.44 | 44 56.6 | +0.0 | +0.0 | 23.094 | 2.77 | 0.43 | 1.42 | 0.41 | < 4.3 | 3.58 | 0.738 | Galaxy | Szokoly et al. (2004) |
| 32 18.83 | 51 35.4 | +0.0 | +0.0 | 25.085 | 2.26 | 0.16 | 0.49 | 0.74 | 14.0 | 2.58 | 3.660 | Type-2 QSO | Szokoly et al. (2004) |
| 32 19.40 ⁷ | 47 28.3 | +0.8 | -0.7 | 24.676 | 1.29 | 0.05 | 0.42 | < 0.31 | 1.17 | 1.96 | 3.700 | Galaxy | Vanzella et al. (2005) |
| 32 29.29 ⁸ | 56 19.4 | -1.0 | +0.1 | 24.984 | > 3 | 0.14 | 1.72 | 0.50 | < 7.6 | 1.31 | 4.759 | QSO | Vanzella et al. (2005) |
| 32 29.84 | 51 05.8 | +0.0 | +0.0 | 24.642 | 2.36 | -0.04 | 0.55 | 3.06 | 31.8 | 1.97 | 3.700 | Type-2 QSO | Norman et al. 2002 |
| 32 39.66 | 48 50.6 | +0.0 | +0.0 | 24.547 | 3.20 | 0.21 | 0.95 | 7.48 | 70.6 | 2.46 | 3.064 | Type-2 QSO | Szokoly et al. (2004) |
| 32 40.83 | 55 46.7 | +0.0 | +0.0 | 25.183 | 1.77 | 0.09 | 0.79 | 5.42 | 93.4 | 2.72 | 0.625 | Type-2 AGN | Szokoly et al. (2004) |
| 32 41.85 | 52 02.5 | +0.0 | +0.0 | 22.430 | 1.46 | -0.02 | 0.48 | 16.7 | 38.2 | 1.25 | 3.592 | QSO | Szokoly et al. (2004) |
| 32 42.83 | 47 02.4 | +0.0 | +0.0 | 25.184 | 1.43 | 0.00 | -0.13 | 6.31 | 16.4 | 1.22 | 3.193 | QSO | Szokoly et al. (2004) |
| High-redshift QSO candidates in the HDF-N. | | | | | | | | | | | | | |
| $12^h + m s$ | $62^\circ + ' ''$ | | | | | | | | | | | | |
| 36 29.44 | 15 13.2 | +0.0 | +0.1 | 23.701 | 1.29 | 0.19 | 0.73 | 8.05 | 11.2 | 1.21 | 3.652 | QSO | Cowie et al. (2004) |
| 36 42.22 | 17 11.6 | +0.2 | +0.2 | 24.022 | 1.28 | 0.23 | 0.39 | 9.48 | 23.2 | 1.50 | 2.724 | QSO | Barger et al. (2001) |
| 36 43.09 | 11 08.8 | +0.2 | -0.6 | 22.918 | 1.11 | 0.06 | 0.48 | 0.75 | < 2.0 | 7.13 | 0.299/3.234 | Extended | Cohen et al. 2000/Cowie et al. (2004) |
| 36 47.96 | 09 41.6 | -0.3 | -0.1 | 23.761 | 4.81 | 0.15 | 2.07 | 2.72 | 4.89 | 1.27 | 5.186 | QSO | Barger et al. (2002) |
| 37 03.98 | 11 57.8 | -0.7 | -0.8 | 25.067 | 1.36 | 0.05 | 0.18 | 0.37 | 3.49 | 1.38 | 3.406 | QSO | Barger et al. (2003) |
| 37 23.71 | 21 13.3 | +0.2 | +0.7 | 23.621 | 1.21 | 0.02 | 0.32 | 5.07 | 11.6 | 1.37 | 3.524 | QSO | Cowie et al. (2004) |

Table 3.3: Additional QSO candidates

| High-redshift QSO candidates in the CDF-S. | | | | | | | | | | | |
|--|--------------------|-----------|---------|---------|---------|----------|-------|----------|-----------------------|----------------|------------------------|
| Optical | | z_{850} | $V - i$ | $i - z$ | $B - V$ | FWHM | Class | Flux | spectr. | spectroscopic | |
| RA | DEC | AB | AB | AB | AB | Image | star | Radius | redshift ^a | identification | |
| $3^h + m s$ | $-27^\circ + ' ''$ | (mag) | (mag) | (mag) | (mag) | (pixels) | | (pixels) | | | |
| 32 01.28 | 44 32.2 | 25.206 | 2.19 | 0.15 | > 3 | 6.81 | 0.75 | 1.97 | <i>4.750,4.850</i> | | Vanzella et al. (2005) |
| 32 18.91 | 53 02.7 | 24.561 | 2.56 | 0.63 | > 3 | 4.14 | 0.85 | 1.53 | 5.554 | EL-Galaxy | |
| 32 22.66 | 51 37.1 | 25.160 | 1.49 | 0.47 | > 3 | 3.19 | 0.98 | 1.21 | <i>0.600,4.450</i> | | Vanzella et al. (2005) |
| 32 29.29 | 56 19.4 | 24.984 | 1.72 | 0.14 | > 3 | 3.84 | 0.99 | 1.31 | 4.759 | QSO | Vanzella et al. (2005) |
| 32 40.38 | 44 31.0 | 25.223 | 0.53 | 0.01 | 3.10 | 5.70 | 0.78 | 1.65 | <i>4.000,3.950</i> | | |
| High-redshift QSO candidates in the HDF-N. | | | | | | | | | | | |
| $12^h + m s$ | $62^\circ + ' ''$ | | | | | | | | | | |
| 36 01.80 | 11 36.2 | 25.205 | 0.83 | 0.14 | 2.08 | 3.28 | 0.97 | 1.16 | <i>3.750,3.750</i> | | |
| 36 21.76 | 11 20.0 | 24.068 | 2.17 | 0.81 | > 3 | 3.41 | 0.99 | 1.29 | <i>5.350,5.350</i> | | |
| 36 47.96 | 09 41.6 | 23.761 | 2.07 | 0.15 | 4.81 | 3.28 | 0.99 | 1.27 | 5.186 | QSO | Barger et al. 2002 |
| 36 55.37 | 12 13.7 | 24.098 | 1.91 | 0.71 | > 3 | 3.15 | 0.99 | 1.26 | <i>0.800,4.650</i> | | |
| 37 11.81 | 11 33.5 | 25.141 | 1.51 | 0.11 | > 3 | 4.35 | 0.85 | 1.60 | <i>4.450,4.700</i> | | |

^aData in italics refer to photometric estimate of the redshift under the assumption of QSO spectrum.

Table 3.4: Best fit parameters of the Luminosity Function of high-redshift QSOs

| | M^* | $\Phi^*(Mpc^{-3})$ | α | β | k_{slope} | χ^2 | P_{KS} |
|---------|-------------------|-------------------------------|------------------|---------------|------------------|----------|----------|
| PDECr1p | -25.116 (fixed) | 1.67×10^{-6} (fixed) | -1.09 (fixed) | -3.31 (fixed) | -2.15 ± 0.34 | 1.9 | < 1% |
| PDERi1p | -25.116 (fixed) | 1.67×10^{-6} (fixed) | -1.45 (fixed) | -3.31 (fixed) | -2.01 ± 0.23 | 1.7 | < 1% |
| PDECr2p | -26.04 ± 0.39 | 1.67×10^{-6} (fixed) | -1.09 (fixed) | -3.31 (fixed) | -4.94 ± 1.27 | 0.68 | 1% |
| PDERi2p | -26.11 ± 0.11 | 1.67×10^{-6} (fixed) | -1.45 (fixed) | -3.31 (fixed) | -5.07 ± 0.62 | 0.46 | 5% |
| PDE-3p | -26.27 ± 0.20 | 1.67×10^{-6} (fixed) | -1.74 ± 0.27 | -3.31 (fixed) | -5.62 ± 0.63 | 0.38 | 26% |
| PDEF3p | -26.34 ± 0.15 | 1.67×10^{-6} (fixed) | -1.82 ± 0.10 | -2.58 (fixed) | -5.80 ± 0.74 | 1.0 | < 1% |
| PDECK1p | -25.116 (fixed) | 1.67×10^{-6} (fixed) | -1.09 (fixed) | -3.31 (fixed) | -0.49 ± 0.04 | 1.7 | < 1% |
| PDERk1p | -25.116 (fixed) | 1.67×10^{-6} (fixed) | -1.45 (fixed) | -3.31 (fixed) | -0.55 ± 0.07 | 1.4 | < 1% |
| PDECK2p | -25.90 ± 0.28 | 1.67×10^{-6} (fixed) | -1.09 (fixed) | -3.31 (fixed) | -1.13 ± 0.25 | 0.50 | 24% |
| PDERk2p | -26.11 ± 0.06 | 1.67×10^{-6} (fixed) | -1.45 (fixed) | -3.31 (fixed) | -1.30 ± 0.14 | 0.37 | 29% |
| PDEk3p | -26.08 ± 0.12 | 1.67×10^{-6} (fixed) | -1.42 ± 0.25 | -3.31 (fixed) | -1.26 ± 0.19 | 0.37 | 40% |
| PDEFkp | -26.09 ± 0.48 | 1.67×10^{-6} (fixed) | -1.74 ± 0.38 | -2.58 (fixed) | -1.34 ± 0.45 | 0.94 | < 1% |
| PLECr1p | -25.116 (fixed) | 1.67×10^{-6} (fixed) | -1.09 (fixed) | -3.31 (fixed) | -0.77 ± 0.10 | 1.5 | < 1% |
| PLERi1p | -25.116 (fixed) | 1.67×10^{-6} (fixed) | -1.45 (fixed) | -3.31 (fixed) | -0.82 ± 0.03 | 1.5 | < 1% |
| PLECr2p | -25.58 ± 0.18 | 1.67×10^{-6} (fixed) | -1.09 (fixed) | -3.31 (fixed) | -1.42 ± 0.37 | 1.2 | < 1% |
| PLERi2p | -25.52 ± 0.10 | 1.67×10^{-6} (fixed) | -1.45 (fixed) | -3.31 (fixed) | -1.40 ± 0.21 | 1.2 | < 1% |
| PLE-3p | -25.55 ± 0.10 | 1.67×10^{-6} (fixed) | -1.26 ± 0.06 | -3.31 (fixed) | -1.40 ± 0.24 | 1.2 | < 1% |
| PLEF3p | -25.66 ± 0.12 | 1.67×10^{-6} (fixed) | -1.20 ± 0.72 | -2.58 (fixed) | -2.61 ± 0.42 | 0.56 | 1% |

Chapter 4

GALRISE Model for the Joint Evolution of Galaxies and AGNs

4.1 Outline of the model

¹In this section we describe the structure of the code, system of equations for the mass flows, and briefly introduce the main physical ingredients included in the code.

The model is composed by many parts. Merger trees are constructed with the aid of the PINOCCHIO tool (Monaco et al. 2002a; Monaco, Theuns & Taffoni 2002b; Taffoni, Monaco & Theuns 2002). Merging times for substructure in DM halos (and thus merging times for galaxies) are computed following the recipes by Taffoni et al. (2003). The evolution of baryons within the DM halos takes into account the hydrostatic equilibrium of hot halo gas, its cooling and subsequent infall to the central galaxy, the formation of discs (due to the conservation of the angular momentum) and bulges (due to mergers or disc instabilities), star formation and feedback within the discs and bulges, the escape of gas from the galaxy to the halo (galactic wind) and from the halo to the IGM (galactic super-wind), the accretion of gas onto seed BHs and their feedback on the galactic ISM and the hot halo gas, the chemical evolution of the mean metallicity of gas and stars.

All the relevant pieces of physics will be described in detail in the following sections.

4.1.1 DM halos and galaxies

The merger trees of DM halos are obtained using the PINOCCHIO code (the details are given later in Section 4.2.1). The use of PINOCCHIO is motivated by its excellent performance obtainable even with modest computer resources (see also Zhao et al. 2003; Li, Mo & van der Bosh 2005). The PINOCCHIO code is not considered as an integrated part of the galaxy formation code; any

¹The results presented in this chapter will be submitted for publication in Monaco, Fontanot & Taffoni (2006)

other code for generating merger trees can be used in its place, provided that the output is given in the same way as PINOCCHIO.

Each DM halo that ever gets as massive as at least ten particles² constitutes an end branch of the tree; the time at which a halo gets as massive as ten particles is named *appearance time*. A galaxy is associated to each end branch. When a DM halo merges with a larger one, it disappears as an individual entity and becomes a substructure (or satellite) of the larger DM halo; while its external regions are tidally stripped, its core (which contains its associated galaxy) generally survives for some time. A galaxy that is associated with an existent DM halo is named *central*; in general the central galaxy is the largest in a DM halo, though this may not always be the case. Galaxies associated to substructures are named *satellites*. At each DM halo merging, the galaxies involved in the merging (the two central ones and their satellites, if any) continue to exist till they merge with other galaxies or are destroyed by tides (Section 4.3.3).

4.1.2 Baryons

The baryonic content of each galaxy is divided into three components, namely a halo, a bulge and a disc (Figure 4.1). Each component is made up by three phases, i.e., cold gas, hot gas and stars³. The halo component of central galaxies contains the virialized gas pervading the DM halo, cold gas associated with the cooling flow and halo stars. Non-central galaxies are in principle allowed to have some halo matter associated; this may be the case, for instance, of rather large galaxies in small, loose groups. In the present formulation, however, non-central galaxies do not retain mass in their halo baryonic component, though this assumption can be relaxed.

For each component the code follows the mass and metal content of the three phases (cold gas, hot gas, stars), plus the thermal energy of the hot gas (that determines its temperature) and the kinetic energy of the cold gas (that determines its velocity dispersion). In total, 8 variables are associated to each component.

Together with the 8×3 variables associated to the three components, other quantities are integrated by the code as variables. In the cooling model (Section 4.4.3) the cooling radius is treated as a dynamical variable. Hot or cold gas can flow out of a DM halo in a super-wind, and the code follows its mass, energy (thermal or kinetic) and metals. Finally, each galaxy contains a BH (starting from a low-mass seed) and a reservoir of low-angular momentum gas that can accrete onto it. Summing up, the following variables are integrated during the evolution of a galaxy:

²As shown in Monaco et al. (2002b), ten particles are not enough to reconstruct robustly a DM halo. On the other hand, this limit is not applied to select bona-fide DM halos, but to infer the appearance time of an object. The natural choice for this would be the collapse time of its first particle, corresponding to the creation of a 1-particle halo. We deem that 10 particles is a good compromise between the need for mass resolution and robustness.

³In most other galaxy formation models the hot gas of a galaxy is contained in the halo, while discs contain cold gas and stars; so these models are not truly multi-phase. GALRISE instead is designed to handle a two-phase gas in each component.

- cooling radius of the hot halo gas;
- mass, metals and kinetic energy of cold super-wind gas;
- mass, metals and thermal energy of hot super-wind gas;
- black hole mass;
- black hole reservoir.

In total, 33 variables describe each evolving galaxy. It is relatively simple to add new variables, so this number may increase in future versions. We plan also to allow the subdivision of discs into n_{rad} rings, in which case the number of variables would be $25 + 8 \times n_{\text{rad}}$.

4.1.3 Algorithm

The algorithm is composed by two main parts. In the first part the merger trees are extracted from the PINOCCHIO run (Section 4.2.1). Based on the merger histories, the dynamical friction and tidal destruction times for the satellite DM halos are estimated (Section 4.3.3) and the merger trees for the galaxies are constructed. In the second part of the code, the galaxy evolution subroutine is called for each branch of the DM halo tree. A branch is defined as the evolution of a DM halo between two subsequent mergings, be them major or minor; end branches start at the appearance time of the halo. The evolution code integrates all the variables defined above (Section 4.1.2), following the mass, metal and energy flows given below in Sections 4.1.4, 4.1.5, 4.1.6 and 4.1.7. For each branch all galaxies contained in the DM halo are evolved. Satellites are evolved first, so that the evolution of the hot halo gas (associated to the central galaxy) takes into account their energetic input. Of course, the integration of a single galaxy stops at its merger or destruction time (see Section 4.3.3) whenever these events occur.

Some critical events, like disc instabilities, mergers and quasar winds, are modeled outside the galaxy evolution code. The associated mass and energy flows are named here *external flows*.

The evolution of a galaxy system is performed with a Runge-Kutta integrator (Press et al. 1992). To improve the stability of the integration and to allow a regular time sampling, the integration of a galaxy in a branch is subdivided into time fragments, starting or ending at times $i_{\text{sample}}\Delta_t$, where i_{sample} is the sampling index and Δ_t is usually set to 0.1 Gyr. In general the branch ends are not integer multiples of Δ_t ; for instance, if a galaxy is to be integrated from $t_1 = 4.386$ to $t_2 = 4.728$ Gyr, the integration will be subdivided into the intervals $[4.386, 4.4]$, $[4.4, 4.5]$, $[4.5, 4.6]$, $[4.6, 4.7]$ and $[4.7, 4.728]$. The integration is also stopped whenever the system reaches some critical stage, like in disc instabilities or in quasar winds.

The values of the 24 variables relative to galaxy components, introduced in Section 4.1.2, are stored at times $i_{\text{sample}}\Delta_t$, together with bulge and disc radii and velocities, black hole masses, punctual values for the star formation rates of bulge and disc and the accretion rate onto the black hole. Cooling radii, outflowed masses and black-hole reservoirs are not sampled.

Table 4.1: Mass and energy flows in the integration (equations 4.1, 4.3 and 4.5).

| Flow | Comment | Equation/ Section |
|-----------------------------------|--------------------------------|-----------------------|
| Mass flows | | |
| $\dot{M}_{\text{co,H}}$ | cooling flow | eq. 4.26 |
| $\dot{M}_{\text{ev,H}}$ | evaporation in halo | zeroed |
| $\dot{M}_{\text{sf,H}}$ | star formation in halo | zeroed |
| $\dot{M}_{\text{rs,H}}$ | restoration in halo | zeroed |
| $\dot{M}_{\text{in,H}}$ | infall from halo | eq. 4.35 |
| \dot{M}_{csw} | cold super-wind | eq. 4.44 |
| $\dot{M}_{\text{cw,H}}$ | cold wind to halo | eq. 4.2 |
| \dot{M}_{csat} | cold wind from satellites | sect. 4.1.7 |
| \dot{M}_{cosm} | cosmological infall | eq. 4.21 |
| \dot{M}_{hsw} | hot super-wind | eq. 4.41 |
| $\dot{M}_{\text{hw,H}}$ | hot wind to halo | eq. 4.2 |
| \dot{M}_{hsat} | hot wind from satellites | sect. 4.1.7 |
| $\dot{M}_{\text{co,B}}$ | cooling in bulge | eq. 4.51 |
| $\dot{M}_{\text{ev,B}}$ | evaporation in bulge | eq. 4.51 |
| $\dot{M}_{\text{sf,B}}$ | star formation in bulge | eq. 4.62 |
| $\dot{M}_{\text{rs,B}}$ | restoration in bulge | eq. 4.62 |
| $\dot{M}_{\text{in,B}}$ | infall to bulge | sect. 4.35 |
| $\dot{M}_{\text{hw,B}}$ | hot wind from bulge | eqs. 4.64, 4.71 |
| $\dot{M}_{\text{cw,B}}$ | cold wind from bulge | eqs. 4.70, 4.71 |
| $\dot{M}_{\text{co,D}}$ | cooling in disc | eq. 4.51 |
| $\dot{M}_{\text{ev,D}}$ | evaporation in disc | eq. 4.51 |
| $\dot{M}_{\text{sf,D}}$ | star formation in disc | eq. 4.58 |
| $\dot{M}_{\text{rs,D}}$ | restoration in disc | eq. 4.58 |
| $\dot{M}_{\text{in,D}}$ | infall to disc | sect. 4.35 |
| $\dot{M}_{\text{hw,D}}$ | hot wind from disc | eq. 4.58 |
| $\dot{M}_{\text{cw,D}}$ | cold wind from disc | eq. 4.58 |
| Thermal energy of hot gas | | |
| $\dot{E}_{\text{ev,H}}$ | evaporation in halo | zeroed |
| $\dot{E}_{\text{co,H}}$ | cooling of hot gas | eq. 4.27 |
| $\dot{E}_{\text{SN,H}}$ | energy from SNe in halo | zeroed |
| \dot{E}_{cosm} | shock-heating of infalling IGM | eq. 4.22 |
| \dot{E}_{hsw} | energy lost by hot super-wind | eq. 4.41 |
| $\dot{E}_{\text{hw,H}}$ | hot wind to halo | eqs. 4.59, 4.65, 4.79 |
| \dot{E}_{hsat} | hot wind from satellites | sect. 4.1.7 |
| \dot{E}_{ad} | adiabatic expansion | eq. 4.41 |
| \dot{E}_{grav} | grav. collapse for low energy | eq. 4.34 |
| Kinetic energy of cold gas | | |
| $\dot{K}_{\text{co,H}}$ | energy of cooling flow | eq. 4.28 |
| $\dot{K}_{\text{ev,H}}$ | evaporation in halo | zeroed |
| $\dot{K}_{\text{sf,H}}$ | star formation in halo | zeroed |
| $\dot{K}_{\text{SN,H}}$ | energy from SNe in halo | zeroed |
| $\dot{K}_{\text{in,H}}$ | energy lost by infall | eq. 4.36 |
| \dot{K}_{csw} | energy lost by cold super-wind | eqs. 4.44 |
| $\dot{K}_{\text{w,H}}$ | energy acquired by winds | eq. 4.60, 4.66 |
| \dot{K}_{sat} | energy acquired by satellites | sect. 4.1.7 |
| \dot{K}_{ad} | adiabatic expansion 98 | eq. 4.44 |
| $\dot{K}_{\text{ds,H}}$ | turbulent dissipation | zeroed |

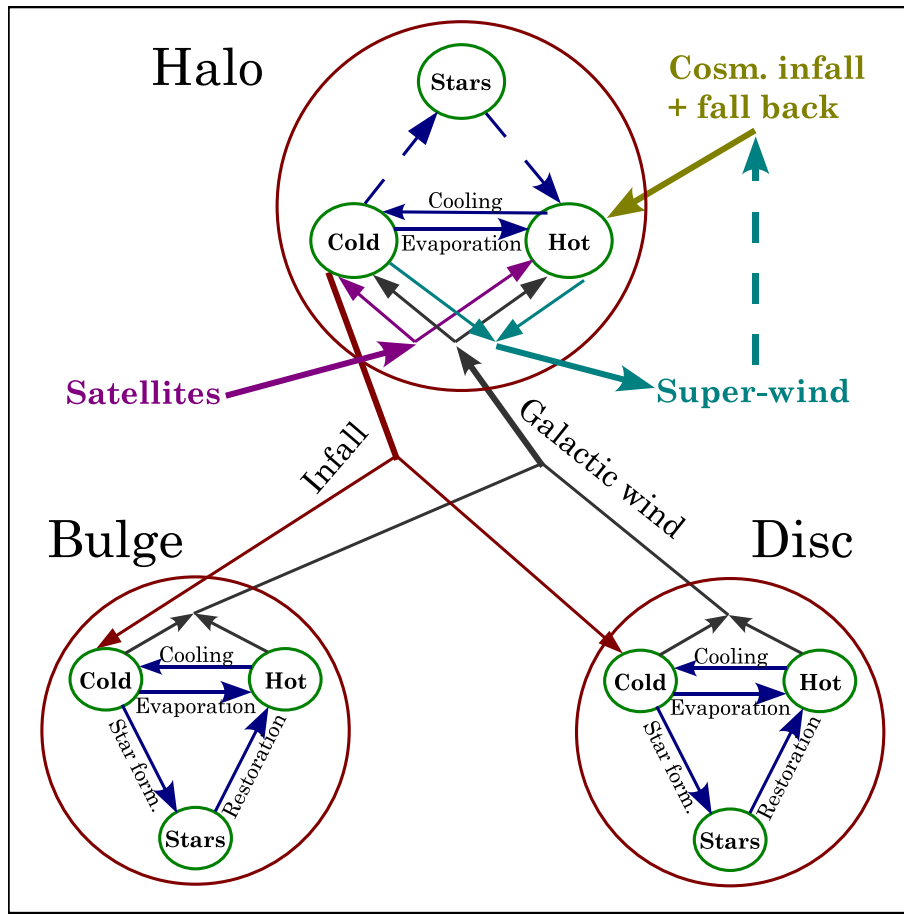


Figure 4.1: General scheme of mass flows in a model galaxy

4.1.4 Mass flows

Baryonic matter flows through the components and between the phases as illustrated in Figure 4.1. Within each component the three phases exchange mass through the following flow terms:

- evaporation (\dot{M}_{ev} – from cold to hot);
- cooling (\dot{M}_{co} – from hot to cold);
- star formation (\dot{M}_{sf} – from cold to star);
- restoration (\dot{M}_{rs} – from star to hot).

No mass is allowed to flow from hot gas to stars and from stars to cold gas. This scheme is rather general; for instance, a flow from the hot to the cold phase stimulated by pressure-driven snowploughs (see M04 for more details) can be modeled as an additive term to the cooling flow.

Matter flows among the components as follows:

- primordial gas flows to the halo together with the accreted DM mass (cosmological infall, \dot{M}_{cosm});

- cold gas infalls from the halo to the disc or bulge (\dot{M}_{in});
- cold and hot gas are expelled by the bulge or disc to the halo in a wind (\dot{M}_{cw} and \dot{M}_{hw});
- both hot and cold gas are allowed to leave the halo in a super-wind (\dot{M}_{hsw} and \dot{M}_{csw});
- this expelled material is allowed to get back to the halo together with the cosmological infall;
- winds from satellites are injected in the halo component of their central galaxy (\dot{M}_{cs} and \dot{M}_{hs}).

The resulting system of equations for the mass flows between phases and components is:

$$\begin{aligned}
\dot{M}_{\text{c,H}} &= \dot{M}_{\text{co,H}} - \dot{M}_{\text{ev,H}} - \dot{M}_{\text{sf,H}} - \dot{M}_{\text{in,H}} - \dot{M}_{\text{csw}} + \dot{M}_{\text{cw,H}} + \dot{M}_{\text{csat}} \\
\dot{M}_{\text{h,H}} &= \dot{M}_{\text{ev,H}} - \dot{M}_{\text{co,H}} + \dot{M}_{\text{rs,H}} + \dot{M}_{\text{cosm}} - \dot{M}_{\text{hsw}} + \dot{M}_{\text{hw,H}} + \dot{M}_{\text{hsat}} \\
\dot{M}_{\text{s,H}} &= \dot{M}_{\text{sf,H}} - \dot{M}_{\text{rs,H}} \\
\dot{M}_{\text{c,B}} &= \dot{M}_{\text{co,B}} - \dot{M}_{\text{ev,B}} - \dot{M}_{\text{sf,B}} - \dot{M}_{\text{cw,B}} + \dot{M}_{\text{in,B}} \\
\dot{M}_{\text{h,B}} &= \dot{M}_{\text{ev,B}} - \dot{M}_{\text{co,B}} + \dot{M}_{\text{rs,B}} - \dot{M}_{\text{hw,B}} \\
\dot{M}_{\text{s,B}} &= \dot{M}_{\text{sf,B}} - \dot{M}_{\text{rs,B}} \\
\dot{M}_{\text{c,D}} &= \dot{M}_{\text{co,D}} - \dot{M}_{\text{ev,D}} - \dot{M}_{\text{sf,D}} - \dot{M}_{\text{cw,D}} + \dot{M}_{\text{in,D}} \\
\dot{M}_{\text{h,D}} &= \dot{M}_{\text{ev,D}} - \dot{M}_{\text{co,D}} + \dot{M}_{\text{rs,D}} - \dot{M}_{\text{hw,D}} \\
\dot{M}_{\text{s,D}} &= \dot{M}_{\text{sf,D}} - \dot{M}_{\text{rs,D}}
\end{aligned} \tag{4.1}$$

In the right hand side, the suffixes c, h and s denote the cold, hot and star phases. In all cases the suffixes H, B and D following the comma denote the flows relative to the halo, bulge and disc components. Mass conservation implies that the following relations hold:

$$\begin{aligned}
\dot{M}_{\text{in,H}} &= \dot{M}_{\text{in,B}} + \dot{M}_{\text{in,D}} \\
\dot{M}_{\text{cw,H}} &= \dot{M}_{\text{cw,B}} + \dot{M}_{\text{cw,D}} \\
\dot{M}_{\text{hw,H}} &= \dot{M}_{\text{hw,B}} + \dot{M}_{\text{hw,D}}
\end{aligned} \tag{4.2}$$

Table 4.1 gives a list of all mass flows, with a quick explanation and a reference for their quantification. Some mass flows, like those related to star formation in the halo, are not used in the present version of the code; they are labeled as “zeroed” in the table.

4.1.5 Energy flows

Each mass flow from/to the hot or cold components corresponds to a flow of thermal or kinetic energy. Whenever energy is conserved, the energy flow will be equal to the thermal or kinetic energy associated to the corresponding mass

flow; energy losses (due for instance to cooling or dissipation of turbulence) or injections (due to gravitational collapse or feedback) will give further terms in the equations.

As far as the hot halo phase is concerned, the energy cooling flow $\dot{E}_{\text{co,H}}$ represent the energy radiated by the gas, and its connection to the mass cooling flow is explained in Section 4.4.3. Stellar feedback comes mainly from the hot wind flows of the central galaxy, $\dot{E}_{\text{hw,H}}$ (which takes contribution from the bulge, the disc and the AGN), and of the satellites, \dot{E}_{hsat} ; in this case no analogous of equations 4.2 holds as the energy of the hot wind does not come from the energy of the bulge and disc hot phases but is injected by SNe. Energy is gained also by gravitational collapse whenever the thermal energy is lower than that required by hydrostatic equilibrium, and this is modeled with the term \dot{E}_{grav} (Section 4.4.4). Hot super-winds carry thermal energy to the IGM, but the work done by the hot gas to expel these winds leads to a further energy loss, \dot{E}_{ad} , as explained in Section 4.4.5. Finally, star formation in the halo, if present, would imply energy injection by SNe; this is taken into account through the restoration term, which for sake of clarity is called $\dot{E}_{\text{SN,H}}$.

The equation for the evolution of the thermal energy of the halo hot phase is then:

$$\begin{aligned} \dot{E}_{\text{H}} = & \dot{E}_{\text{ev,H}} - \dot{E}_{\text{co,H}} + \dot{E}_{\text{SN,H}} + \dot{E}_{\text{cosm}} - \dot{E}_{\text{hsw}} \\ & + \dot{E}_{\text{hw,H}} + \dot{E}_{\text{hsat}} - \dot{E}_{\text{ad}} + \dot{E}_{\text{grav}} \end{aligned} \quad (4.3)$$

These terms are listed in Table 4.1. Analogous equations can be written for the thermal evolution of the hot phase in bulges and discs:

$$\begin{aligned} \dot{E}_{\text{B}} &= \dot{E}_{\text{ev,B}} - \dot{E}_{\text{co,B}} + \dot{E}_{\text{SN,B}} - \dot{E}_{\text{hw,B}} \\ \dot{E}_{\text{D}} &= \dot{E}_{\text{ev,D}} - \dot{E}_{\text{co,D}} + \dot{E}_{\text{SN,D}} - \dot{E}_{\text{hw,D}} \end{aligned} \quad (4.4)$$

In this case energy is injected by SNe and gained by evaporation of cold gas, and is lost by cooling and hot winds. In the present version of the model the thermal evolution of the hot phase of the ISM is not followed in detail, so that the equations 4.4 are included in the code but all the energy flows are set to zero. These mass flows are not reported in table 4.1. They can be activated whenever a more detailed modeling of the ISM is required.

The evolution of the kinetic energy of the cold halo phase follows a similar track. In the case of the cold halo gas, energy is injected by SNe connected to the halo star formation ($\dot{K}_{\text{SN,B}}$, which is inactive in this version of the code) and by winds. In this case, we take into account the possible role of cold winds, which inject cold gas with some kinetic energy, and hot winds, which exert pressure on the existing clouds accelerating them. Kinetic energy is then carried from central galaxies and satellites through the flows $\dot{K}_{\text{w,H}}$ and \dot{K}_{sat} . Cold super winds lead again to a loss of kinetic energy both connected to the ejected gas (\dot{K}_{csw}) and to the work done in ejecting it (\dot{K}_{ad}). Moreover, kinetic energy can be dissipated by clouds collisions or, more generally, by

turbulence ($\dot{K}_{\text{ds,H}}$). This last term is the one ultimately responsible for infall of gas into the central galaxy; however, to keep the physical description at a simpler level, we model infall as described in Section 4.4.4 and do not take dissipation explicitly into account here (so that this energy flow is set to zero). The resulting equation is:

$$\begin{aligned}\dot{K}_{\text{H}} &= \dot{K}_{\text{co,H}} - \dot{K}_{\text{ev,H}} - \dot{K}_{\text{sf,H}} + \dot{K}_{\text{SN,H}} - \dot{K}_{\text{in,H}} - \dot{K}_{\text{csw}} \\ &\quad + \dot{K}_{\text{w,H}} + \dot{K}_{\text{sat}} - \dot{K}_{\text{ad}} - \dot{K}_{\text{ds,H}}\end{aligned}\quad (4.5)$$

Again, the kinetic energy of the bulge and disc components is formally present in the code but all the flows are set to zero. The system of equations would be:

$$\begin{aligned}\dot{K}_{\text{B}} &= \dot{K}_{\text{co,B}} - \dot{K}_{\text{ev,B}} - \dot{K}_{\text{sf,B}} + \dot{K}_{\text{SN,B}} + \dot{K}_{\text{in,B}} - \dot{K}_{\text{cw,B}} - \dot{K}_{\text{ds,B}} \\ \dot{K}_{\text{D}} &= \dot{K}_{\text{co,D}} - \dot{K}_{\text{ev,D}} - \dot{K}_{\text{sf,D}} + \dot{K}_{\text{SN,D}} + \dot{K}_{\text{in,D}} - \dot{K}_{\text{cw,D}} - \dot{K}_{\text{ds,D}}\end{aligned}\quad (4.6)$$

4.1.6 Metal flows

Metal flows follow closely the mass flows, with the addition of source terms \dot{M}_{yi}^Z that model the creation of new metals by stars. The metals are always given to the hot phase.

$$\begin{aligned}\dot{M}_{\text{c,H}}^Z &= \dot{M}_{\text{co,H}}^Z - \dot{M}_{\text{ev,H}}^Z - \dot{M}_{\text{sf,H}}^Z - \dot{M}_{\text{in,H}}^Z - \dot{M}_{\text{csw}}^Z + \dot{M}_{\text{cw,H}}^Z + \dot{M}_{\text{csat}}^Z \\ \dot{M}_{\text{h,H}}^Z &= \dot{M}_{\text{ev,H}}^Z - \dot{M}_{\text{co,H}}^Z + \dot{M}_{\text{rs,H}}^Z + \dot{M}_{\text{cosm}}^Z - \dot{M}_{\text{hsw}}^Z + \dot{M}_{\text{hw,H}}^Z + \dot{M}_{\text{hsat}}^Z + \dot{M}_{\text{yi,H}}^Z \\ \dot{M}_{\text{s,H}}^Z &= \dot{M}_{\text{sf,H}}^Z - \dot{M}_{\text{rs,H}}^Z \\ \dot{M}_{\text{c,B}}^Z &= \dot{M}_{\text{co,B}}^Z - \dot{M}_{\text{ev,B}}^Z - \dot{M}_{\text{sf,B}}^Z - \dot{M}_{\text{cw,B}}^Z + \dot{M}_{\text{in,B}}^Z \\ \dot{M}_{\text{h,B}}^Z &= \dot{M}_{\text{ev,B}}^Z - \dot{M}_{\text{co,B}}^Z + \dot{M}_{\text{rs,B}}^Z - \dot{M}_{\text{hw,B}}^Z + \dot{M}_{\text{yi,B}}^Z \\ \dot{M}_{\text{s,B}}^Z &= \dot{M}_{\text{sf,B}}^Z - \dot{M}_{\text{rs,B}}^Z \\ \dot{M}_{\text{c,D}}^Z &= \dot{M}_{\text{co,D}}^Z - \dot{M}_{\text{ev,D}}^Z - \dot{M}_{\text{sf,D}}^Z - \dot{M}_{\text{cw,D}}^Z + \dot{M}_{\text{in,D}}^Z \\ \dot{M}_{\text{h,D}}^Z &= \dot{M}_{\text{ev,D}}^Z - \dot{M}_{\text{co,D}}^Z + \dot{M}_{\text{rs,D}}^Z - \dot{M}_{\text{hw,D}}^Z + \dot{M}_{\text{yi,D}}^Z \\ \dot{M}_{\text{s,D}}^Z &= \dot{M}_{\text{sf,D}}^Z - \dot{M}_{\text{rs,D}}^Z\end{aligned}\quad (4.7)$$

Because of the similarity of mass and metal flows, we do not give a separate table for the latter.

4.1.7 Other variables

The behaviour of galaxy winds and super-winds depends on whether the galaxy is central or satellite. In the case of central galaxies, galaxy winds go to the halo as described in Section 4.1.4, while galaxy super-winds are recorded by suitable variables (Section 4.1.2) and stored at the end of the integration in a vector, so as to fall back onto the DM halo at a later time (Section 4.4.5). In

this case the information on the thermal or kinetic energy of the expelled gas is not retained. In this version of the code, satellite galaxies do not retain their halo matter, so that the galactic winds are directly expelled by their DM halos. This is done by equating the wind and super-wind mass flows, $\dot{M}_{\text{csw}} = \dot{M}_{\text{cw}}$. These winds are stored in a dedicated vector. Mass, energy and metals are then extracted from this vector and deposited into the halo component of the main halo through the satellite flows (as satellite galaxies are orbiting in the main halo, the kinetic energy of the cold wind gas is recomputed using the velocity dispersion of the main halo). For sake of consistency and simplicity, gas from all satellite galaxies of a DM halo is stored in this vector and then injected into the halo component of the central galaxy at a rate averaged over the integration time-bin.

The mass flows connected to accretion onto a BH are described in Section 4.8.1, while the evolution of the cooling radius is given in Section 4.4.3.

4.1.8 External flows

In some critical cases baryons are transferred among phases, components and galaxies outside the integration code. The cases are described below in full detail, we give here only a list:

- disc instabilities (Section 4.5.1);
- merging of galaxies (Section 4.3.3);
- tidal disruption of galaxies (Section 4.3.3);
- tidal stripping of galaxies (Section 4.3.3);
- entrance into a cluster (Section 4.3.3);
- quasar winds (Section 4.8.1).

4.1.9 Initial conditions

At the appearance time all halos are assumed to be as large as 10 particles⁴. Typical appearance times of DM halos may be as early as $z \sim 10$ for the most massive objects at $z = 0$ and with a mass resolution of $\sim 10^9 M_{\odot}$. All the baryons present in these primordial DM halos are typically assumed to be in the hot halo phase, whose thermal energy, acquired by gravitational shocks, is computed with the model described in Section 4.4.2. An issue with this setting is the quick start of cooling in these initial halos. This overcooling is a numerical artifact due to the lack of sampling of the tree; if this were resolved at a smaller mass resolution, the DM halo would then already contain some heating source at that time. To limit this numerical overcooling, it is assumed that the halos have just suffered a major merger at their appearance time, so that the onset of cooling is delayed by a few sound-crossing times (see Section 4.4.1 for details).

⁴Some DM halos grow larger than 10 particles by a merger, but this detail is neglected.

Moreover, after reionization the ionizing background is likely to prevent the cooling of any halo whose circular velocity is smaller than $\sim 50 \text{ km s}^{-1}$ (e.g., Benson et al. 2001). This criterion is implemented in this code; however, a $\sim 10^{10} M_{\odot}$ halo at $z \geq 6$ has a circular velocity $\geq 67 \text{ km s}^{-1}$, so that radiative feedback is clearly not enough to prevent strong cooling in moderate-mass halos at high redshift.

To test the robustness of the initial conditions to numerical overcooling, we let a specified fraction f_{icdisc} of the gas be in a cold disc from the start. This is done to allow stellar feedback to contrast the first cooling flow. This test reveals that the final results are remarkably insensitive to the fraction of gas put in these “primordial” discs. We conclude that the building of bright galaxies does not depend strongly on the limit on mass resolution.

4.1.10 Cosmology and units

We use a “concordance” Λ CDM cosmology with parameters $\Omega_0 = 0.3$, $\Omega_{\Lambda} = 0.7$, $\Omega_b = 0.04$, $\sigma_8 = 0.9$, $H_0 = 70 \text{ km s}^{-1} \text{ Mpc}^{-1}$. All physical quantities are scaled to this H_0 value.

Masses are given in M_{\odot} , lengths in Mpc, times in Gyr, velocities in km s^{-1} , thermal energies in 10^{60} erg , kinetic energies in $M_{\odot}(\text{km s}^{-1})^2$. Flows are given in Gyr^{-1} (i.e., mass flows in $M_{\odot} \text{ Gyr}^{-1}$, thermal energy flows in $10^{60} \text{ erg Gyr}^{-1}$, kinetic energy flows in $M_{\odot} (\text{km s}^{-1})^2 \text{ Gyr}^{-1}$); however, mass flows will be reported here in the more conventional $M_{\odot} \text{ yr}^{-1}$ units.

4.2 DM halos

4.2.1 DM merger trees

As mentioned above, we use the PINOCCHIO code to generate the merger trees. This code, which uses a scheme based on Lagrangian Perturbation Theory (Bouchet et al. 1995; Buchert & Ehlers 1993), applies to the same type of initial conditions used by N-body simulations, and is able to predict which DM particles end up in halos, thus allowing a detailed reconstruction of the merger trees. The PINOCCHIO merger trees are equivalent to those given by N-body simulations, with a further advantage (shared with the less accurate Extended Press & Schechter approach; see Bond et al. 1991; Lacey & Cole 1993) of a very fine time sampling that allows to track the merging times without being restricted to a fixed grid in time (scale factor). Other notable differences with respect to N-body trees is the impossibility of PINOCCHIO DM halos to decrease in mass, a condition which is not strictly valid for the N-body simulations. At variance with EPS merger trees, PINOCCHIO allows for multiple mergers of DM halos.

The input ingredient of GALRISE is then a list of merger trees generated by a PINOCCHIO run. The format of PINOCCHIO outputs are such that only the output at the final redshift is needed to reconstruct the merger trees of a realization, and from them compute the galaxy properties at all times. In PINOCCHIO, each DM halo retains its identity even when it disappears by

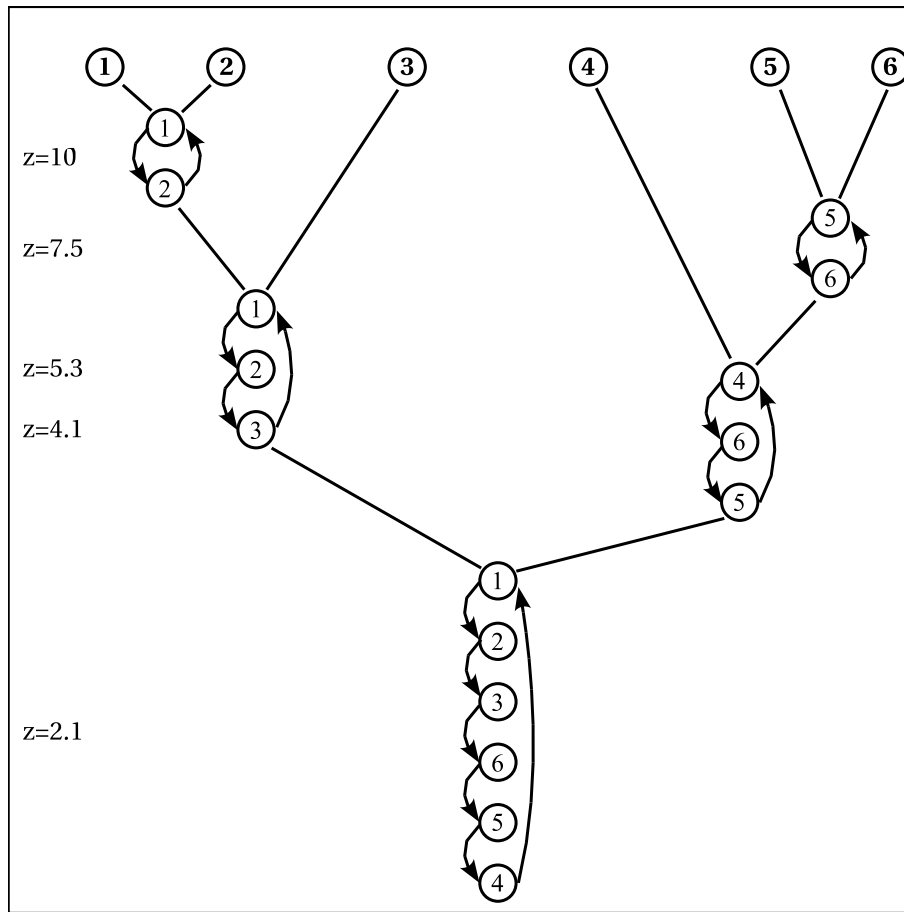


Figure 4.2: Example of ordering of the PINOCCHIO merger trees. In all the mergings shown in this picture, the halo coming from the left is more massive than that coming from the right.

merging with another larger halo. The input files contain, for each DM halo that has ever existed with at least 10 particles, the following information: (i) ID number, (ii) ID of the halo it belongs to at the final redshift, (iii) linking list of the halos, (iv) ID of the halo it has merged with, (v) mass of the halo at the merging time, (vi) mass of the halo it has merged with (before merging) (vii) merging redshift, (viii) redshift of appearance. Halos that exist at the final redshift have field (i) and (ii) equal, and merging redshift equal to -1; field (iv) is also set to -1, while field (v) contains the mass of the halo at the final redshift and field (vi) is 0.

Similarly to GALFORM (Cole et al. 2000), the linking list provided by the 2.1 version of PINOCCHIO (in preparation) is organized in such a way that merged halos are accessed so as to preserve chronological order. This is illustrated in the example of Figure 4.2. Each time a halo appears from a peak, its linking list points to itself. Suppose now that halo 1 merges with the smaller halo 2 at $z_{\text{merge}}=10$, and that both halos have no substructure. Then the linking list is updated so that halo 1 points to halo 2 and vice-versa. At $z_{\text{merge}}=5.3$ halo 1 (which contains halo 2 as a substructure) merges with halo 3, which

has no substructure. Then the last halo of the chain, halo 2, is linked to halo 3, and this back to halo 1. Halos 5 and 6 merge at $z_{\text{merge}}=7.5$, and their fate is similar to halos 1 and 2. Halo 5 then merges with the larger halo 4 at $z_{\text{merge}}=4.1$; in this case halo 4 does not link directly to halo 5, which is put at the end of the chain, but to halo 6. At $z_{\text{merge}}=2.1$ halos 1 and 4 merge. In this case, the last element of the chain of halo 1 (halo 3) is linked to the second of the chain of halo 4 (halo 6). The final sequence is then 1-2-3-6-5-4. In more general terms, the two groups are linked in the following order: first the chain of the surviving DM halo, then the chain of the disappearing one, with the first element (the main halo before merging) put as last. It is clear that, starting from the *second* element of the final chain, two subsequent events are always accessed in chronological order. This does not imply a strict chronological order of all the mergings: in our example halo 3 ($z_{\text{merge}}=5.3$) is accessed before halo 6 ($z_{\text{merge}}=7.5$), but the two events are on independent branches of the tree.

4.2.2 DM halo properties

The physical properties of the DM halos (which are not predicted by PINOCCHIO) are determined as follows. The density run of the DM halo is assumed to follow the NFW profile, according to which a halo with a virial radius r_H is characterized by a scale radius r_s and a concentration $c_{\text{nfw}} = r_H/r_s$. Defining the quantity $\delta_c \equiv 200c_{\text{nfw}}^3(1 + c_{\text{nfw}})/(3(1 + c_{\text{nfw}})\ln(1 + c_{\text{nfw}}) - c_{\text{nfw}})$, the NFW profile of a halo at redshift z is:

$$\rho_{\text{DM}}(r) = \rho_c(z) \frac{\delta_c}{c_{\text{nfw}} x (1 + c_{\text{nfw}} x)^2}, \quad (4.8)$$

where $\rho_c(z)$ is the critical density at the redshift z and $x \equiv r/r_s$. The virial radius r_H of a halo of circular velocity V_H is computed assuming that its average density is 200 times the critical density (see also eq. 1.88 and eq. 1.89):

$$\begin{aligned} V_H &= (10M_H G H(z))^{1/3} \\ r_H &= \frac{V_H}{10H(z)} \end{aligned} \quad (4.9)$$

where M_H is the halo mass and $H(z)$ is the Hubble constant at z .

The concentration c_{nfw} is computed, as a function of M_H and z , following Eke et al. (1998). Given the mass M_H , redshift z and concentration c_{nfw} we compute the gravitational binding energy of the halo ($U_H = \int \rho \Phi d^3r$) as:

$$U_H = \frac{GM_H^2}{r_H} \delta_c^2 \left(\ln^2(1 + c_{\text{nfw}}) - \frac{c_{\text{nfw}}^2}{1 + c_{\text{nfw}}} \right). \quad (4.10)$$

From it and the virial theorem the velocity dispersion of the halo (such that the total kinetic energy of halo particles is $M_H V_{\text{disp}}^2/2 = -U_H/2$) can be computed as:

$$V_{\text{disp}} = \sqrt{-U_H/M_H} \quad (4.11)$$

If λ is the spin parameter of the DM halo (eq. 1.84), its specific angular momentum computed as:

$$\frac{J_H}{M_H} = GM_H \lambda \sqrt{-0.5U_H/M_H}. \quad (4.12)$$

The DM halo parameters (M_H , c_{nfw} , r_h , V_H , U_H , J_H) are re-computed at each time-step along the integration.

The spin parameter λ of DM halos is in principle provided by PINOCCHIO, which is able to predicted the angular momenta of halos. Its predictions show some (modest) degree of correlation with the momenta of simulated halos (the spin directions tend to be loosely aligned within 60°), and the statistics of spin is reproduced at the cost of adding free parameters (Monaco et al. 2002b). While even a modest correlation with the N-body solution is an advantage with respect to drawing random numbers, the complications involved in reconstructing the spin history of halos weights more than any possible practical advantage. As a consequence, we prefer to randomly assign a λ value to each DM halo, drawing it from the log-normal distribution (eq. 1.86) where we use values $\bar{\lambda}_{sp} = 0.05$ and $\sigma_{\lambda_{sp}} = 0.3$ (Cole et al. 2000 use the slightly lower value of 0.23 for $\sigma_{\lambda_{sp}}$; we follow Monaco, Salucci and Danese 2000 using 0.3, which is a better fit to many spin distributions available in the literature and cited in that paper). As explained in Section 4.5.1, a variation of λ with time (for instance at major mergers) creates problems with the model of disc structure. To avoid these problems, the λ parameters are held constant during the evolution of each halo. This of course does not imply a constant specific angular momentum for the halos, as both M_H and U_H in equation 4.12 change with time.

As for DM satellites, it is assumed that their properties (mass, scale radius, concentration) remain constant after their merger. Satellites are however subject to tidal stripping, as explained in Section 4.3.1. Tidal stripping is only taken into account in two cases: to strip mass from discs and bulges, in case of extreme stripping, and to compute the merging time for substructure after a merger. In all the other cases the unstripped mass of the satellite is used.

4.3 Galaxy mergers, destruction and stripping

4.3.1 Dynamical friction on satellites

The computation of merging times for satellites follows the model of Taffoni et al. (2003). In the simplest case, two DM halos without substructure merge, so that the smaller halo becomes a satellite of the larger one. The properties of the two halos at the merging time are computed as explained in section 4.2.2, and the subsequent evolution of the main halo is neglected (up to the next major merger). The orbital parameters are extracted at random from suitable distributions, in particular the ellipticity e of the orbit (defined as $e = (r_{\text{apo}} - r_{\text{peri}})/(r_{\text{apo}} + r_{\text{peri}})$, where r_{apo} and r_{peri} are the apoastron and periastron distances of the orbit) is extracted from a Gaussian with mean 0.7

and variance 0.2 (Tormen et al., 1997). Regarding the energy of the orbit, parameterized with x_c (defined as $x_c = r_c/r_H$, where r_c is the radius of a circular orbit with the same energy and r_H the halo radius), we prefer to assign to it the average value 0.5, as this quantity is not strongly constrained by simulations.

Together with the angular momentum of DM halos, PINOCCHIO is able to estimate the orbital parameters of merging halos. We have verified that the statistics of the quantities e and x_c obtained from PINOCCHIO under reasonable assumptions is compatible with that found in simulation. However, as for the angular momentum and for analogous reasons, we prefer to extract these parameters from the known distributions.

Galaxy mergings are due to the decay of the orbit of their host DM satellite by dynamical friction; in this scheme galaxy satellites can only merge with their central galaxy. Tidal shocks can lead to a complete disruption of satellites; in these rather unlikely events all the matter of the satellite is dispersed into the halo of the central galaxy. Taffoni et al. (2003) give fitting formulae, accurate to the 15% level, for the merging and destruction times for substructures that take into account dynamical friction, mass loss by tidal stripping and tidal shocks.

Though the merger and disruption times of Taffoni et al. (2003) include a rather sophisticated treatment of tidal stripping, we implement this effect at a very simple level. Tidal stripping is applied at the first periastron of the satellite. The tidal radius is computed as the radius at which the density of the un-perturbed satellite is equal to the density of the main DM halo at the periastron. All the mass external to the tidal radius is then considered as unbound from the satellite. However, while the stripping radius is recorded, the halo mass is not updated but kept fixed in the following evolution. Later, disc structure (see Section 4.5.1) is computed with the unperturbed halo mass, while for the recomputation of merging times after a major merger the stripped mass is used (see below).

Tidal stripping affects also the fraction of mass of (unperturbed) disc and bulge that lies beyond the tidal radius. Notice that, for simplicity, neither the DM halo nor the disc and bulge are assumed to be perturbed by this process.

In the more general case of two substructured halos that merge, we distinguish between major and minor mergers as follows:

$$\text{Major merger of DM halos : } M_{\text{sat}}/M_{\text{main}} > f_{\text{hmm}} \quad (4.13)$$

(we recall that the main DM halo includes the satellite). N-body simulations show that when this condition, with $f_{\text{hmm}} \simeq 0.2$, is satisfied the perturbation induced by the satellite leads to a reshuffling of all the orbits. At a major merger we then re-extract the orbital parameters and re-compute the merger and destruction times for all the satellites of the main DM halo, as if they just entered the halo. As a consequence, some galaxies near to their merging time can be moved to a different orbit that does not lead to merging, while some other galaxies can suffer tidal stripping more than once. Clearly the recomputation of the merging and destruction times for a substructure may not

be very accurate, especially for satellites that have suffered strong mass loss. In this case we keep the scale radius and concentration of the satellite fixed, but use (as mentioned above) the stripped mass to compute the merging and destruction times. As these times are rather long for small satellites, the final results is that the galaxies just don't merge and the accuracy of the prediction is not important.

Minor mergers do not influence the evolution of the satellites of the main DM halo, but do affect the satellites of the smaller DM halo (going itself to become a satellite), for which there is no difference between minor and major merger.

4.3.2 Galaxy merger trees

The galaxy merger trees are constructed, analogously to the DM halo merger trees, by specifying for each galaxy (i) the galaxy where its stars lie at the the final time, (ii) the merging redshift, (iii) the galaxy it has merged with, (iv) a linking list for the merged galaxies, (v) and (vi) the masses of each pair of merged galaxies. Destroyed galaxies are recorded by assigning a negative value to field (i). The construction of galaxy trees is performed as follows: at each halo merger the merging and destruction times for the galaxies are computed (Section 4.3.1), then the galaxies are merged or destroyed at that time if the DM halo they belong to has not been involved in a major merger or has become a satellite in the meantime.

While multiple mergers are allowed by PINOCCHIO, galaxy mergers are all binary.

4.3.3 Galaxy mergers

When two galaxies merge, their fate depends again on the ratio of their masses. Major mergers of galaxies are defined as:

$$\text{Major merger of galaxies : } M_{\text{sat}}/M_{\text{cen}} > f_{\text{gmm}} \quad (4.14)$$

where the parameter f_{gmm} is suggested by simulations to take a value of 0.3 (Kauffmann et al., 1999; Cole et al., 2000; see also sec. 1.5.1). In this specific case baryonic masses are used (i.e. the mass in hot, cold and star phases of the bulge and halo components), and the central galaxy does not include the satellite, so this condition is similar to that of equation 4.13 with a value of 0.25. While the condition on DM halos can be computed directly from the PINOCCHIO trees and without running the galaxy evolution code, the condition of equation 4.14 must be computed at the merger time, after the evolution code has determined the baryonic galaxy masses.

At minor mergers, the whole satellite is added to the bulge, while the disc remains unaffected. This is at variance with Cole et al. (2000), that give the stars to the bulge and the gas to the disc. Their choice is however questionable, as the dissipative matter is more likely to go to the bulge; this is why we prefer to give everything to the bulge. A more accurate solution of this problem will clearly depend on the orbit of the merger, but a more sophisticated treatment

is beyond the interest of this work; moreover, our tests have revealed no strong difference between the two cases (see Section 4.5.2 for more comments).

At major merger all the gas and stars of the two merging galaxies are given to the bulge of the central one. It is worth mentioning that in our modeling mergers are not directly associated to bursts of star formation. A starburst is immediately stimulated by the presence of gas in the bulge component.

Stripping and galaxy destruction (which is in some way an extreme event of stripping) bring gas to the halo of the central galaxy. As star formation in the halo switched off, this is the main way to bring stars to the halo. We anticipate that this mechanism is not very effective in galaxy clusters, where only a few per cent of the stellar mass is finally found in the halo, at variance with the 10-30 per cent found in observed clusters. Murante et al. (2004) have performed hydro simulations to address this problem, coming to the conclusion that the high fraction of cluster stars can be reproduced, but the main mechanism is not tidal stripping but violent relaxation in major mergers. To mimic such effect, we assume that a fraction f_{scatter} of the star mass of the merging galaxies is scattered to the halo at each major merging. With this simple rule we are able to reproduce the high fraction of cluster stars.

As we already saw in sec. 1.5.1, interactions between satellites, like binary mergers, flybys (that stimulate star formation) or galaxy harassment (Moore et al. 1996) are not included at the moment. We know that these events can have an impact on the evolution of galaxies (Menci et al. 2002) and AGN (Cavaliere & Vittorini 2000). We plan to introduce such events in the future.

4.4 Halo gas

4.4.1 Equilibrium model for the hot phase

The equilibrium configuration of the hot halo gas is computed at each time step, under the assumption that in the absence of major mergers the gas re-adjusts quasi-statically to the new equilibrium configuration.

The hot halo phase is assumed to be (i) in hydrostatic equilibrium in an NFW halo, (ii) filling the volume from a cooling radius r_{cool} to the virial radius r_{H} , (iii) described by a polytropic equation of state with index γ_{p} .

The equation of hydrostatic equilibrium:

$$\frac{dP_g}{dr} = -G \frac{\rho_g M_H(< r)}{r^2} \quad (4.15)$$

(where P is the gas pressure, r is the radius, $M_H(< r)$ is the DM halo mass⁵ within r and ρ_g the gas pressure) is easily solved in the case of an NFW density profile (equation 4.8). The solution is:

⁵Gravity is supposed to be dominated by DM, so as to use for $M_H(< r)$ the NFW mass profile, as if the baryons were distributed as the DM. The error induced in this assumption is not likely to be relevant; a more sophisticated treatment would not allow to obtain an analytic solution for the profile.

$$\begin{aligned}
\rho_g(r) &= \rho_{g0} \left(1 - a \left(1 - \frac{\ln(1 + c_{\text{nfw}}x)}{c_{\text{nfw}}} \right) \right)^{1/(\gamma_p-1)} \\
P_g(r) &= P_{g0} \left(1 - a \left(1 - \frac{\ln(1 + c_{\text{nfw}}x)}{c_{\text{nfw}}} \right) \right)^{\gamma_p/(\gamma_p-1)} \\
T_g(r) &= T_{g0} \left(1 - a \left(1 - \frac{\ln(1 + c_{\text{nfw}}x)}{c_{\text{nfw}}} \right) \right)
\end{aligned} \tag{4.16}$$

Defining the virial temperature of the halo as $T_{\text{vir}} = \mu_{\text{hot}} m_p V_c^2 / 3k$ (where $\mu_{\text{hot}} m_p$ is the metallicity-dependent mean molecular weight of the hot gas) and calling η the ratio $T_g(r)/T_{\text{vir}}$ and η_0 its value at $r = 0$, the constant a is defined as:

$$a = \frac{\gamma_p - 1}{\gamma_p} \frac{3}{\eta_0} \frac{c_{\text{nfw}}(1 + c_{\text{nfw}})}{(1 + c_{\text{nfw}}) \ln(1 + c_{\text{nfw}}) - c_{\text{nfw}}} \tag{4.17}$$

The constants T_{g0} , ρ_{g0} and P_{g0} are defined as the extrapolation of the density and temperature profiles to $r = 0$, even though the gas is assumed to be present only beyond r_{cool} . They are fixed by requiring that the total mass and energy of the gas corresponds to M_g and E_g . It is worth noting that the energy is not constrained to be equal to its virial value. The first condition can be solved explicitly if the energy is specified:

$$\rho_{g0} = \frac{M_g}{4\pi r_s^3} \left[\int_{r_{\text{cool}}/r_s}^{c_{\text{nfw}}} t^2 \left(1 - a \left(1 - \frac{\ln(1 + t)}{t} \right) \right)^{1/(\gamma_p-1)} dt \right]^{-1} \tag{4.18}$$

The second condition is:

$$E_g = \frac{6\pi k T_{g0} \rho_{g0} r_s^3}{\mu_{\text{hot}} m_p} \int_{r_{\text{cool}}/r_s}^{c_{\text{nfw}}} t^2 \left(1 - a \left(1 - \frac{\ln(1 + t)}{t} \right) \right)^{\gamma_p/(\gamma_p-1)} dt \tag{4.19}$$

This equation cannot be solved explicitly, as the coefficient a depends on the energy itself through η_0 . To find a solution to these two equations it is necessary to use an iterative algorithm. As a consequence, the computation of the two integrals contained in equations 4.18 and 4.19 is the most time-consuming computation of the whole code. A dramatic speed-up (at the cost of a negligible error) is obtained by computing the integrals in a grid of values of a , r and γ_p ; the solution is then found by linearly interpolating the table.

The function $1 - a(1 - \ln(1 + c_{\text{nfw}}x)/c_{\text{nfw}})$ in equations 4.16 becomes negative at large radii. In this case density, pressure and temperature are not defined. Usually this happens beyond the virial radius r_{H} , unless the central temperature is lower than the following limit:

$$\eta_0 < 3 \frac{\gamma_p - 1}{\gamma_p} \frac{c_{\text{nfw}} - \ln(1 + c_{\text{nfw}})}{\ln(1 + c_{\text{nfw}}) - c_{\text{nfw}}/(1 + c_{\text{nfw}})} \tag{4.20}$$

This condition can be met at high redshift, when c_{nfw} -values are high. In this case no gas is assumed to be present beyond the point of zero density, so that the gas is bound to the inner part of the halo and its pressure at the virial radius is null.

When most hot halo gas in high-redshift halos has cooled, the cooling radius r_{cool} may not be much smaller than the virial radius, and the thermal energy of the uncooled gas may be rather low. In these cases it may be difficult to find an equilibrium solution, as when equation 4.20 is obeyed the external parts are devoided of gas. Since most of the hot gas has already cooled, a precise modeling of these cases is not of great interest, so to avoid computational problems the equilibrium solution is found by assuming an energy not smaller than 90 per cent of the virial energy. This value is used only to compute the equilibrium solution, the actual energy is allowed to assume low values.

A low level of thermal energy for the hot gas is however unphysical, as this quantity is regulated to the virial level by hot super-winds, that expel gas when the energy is too high, and gravitational collapse, that heats the gas when the energy is too low. Super-winds are described in Section 4.4.5, while the heating of the hot, quasi-hydrostatic gas by gravitational collapse is modeled in a very simple way in Section 4.4.4.

4.4.2 Shock heating

The equilibrium model does not specify the amount of thermal energy of the hot gas; this is acquired by the infalling gas through shocks. The cosmological infall mass-flow is computed by linearly interpolating the DM halo mass between the branch ends (whose distance in time is Δt) and assuming that a fraction Ω_b/Ω_0 of that mass is in IGM:

$$\dot{M}_{\text{cosm}} = \frac{\Omega_b}{\Omega_0} \frac{\Delta M_H}{\Delta t} \quad (4.21)$$

We then assume that this gas acquires an energy equal to f_{shock} times that suggested by the virial theorem:

$$\dot{E}_{\text{cosm}} = f_{\text{shock}}(-0.5 U_H) \dot{M}_{\text{cosm}}/M_H \quad (4.22)$$

where the binding energy of the halo U_H is given by equation 4.10. The parameter f_{shock} is suggested by hydro simulations to be slightly higher than 1 (Wu, Nulsen & Fabian 2000). We adopt a value of 1.2.

A similar heating is applied in the following cases: (i) the hot gas contained in the DM halos at the appearance time (see section 4.1.9), (ii) the hot halo gas of satellite DM halos at their merging time (before their halo component is given to the main DM halo), (iii) the hot halo gas at major mergers. In all these cases heating is applied not to a mass flow but to the whole hot halo gas phase:

$$E_H = f_{\text{shock}}(-0.5 U_H) M_{\text{h,H}}/M_H \quad (4.23)$$

Hydro simulations suggest that any cold gas present in the halo is re-heated by shocks during a major merger. Accordingly, we allow shock-heating to affect also the cold halo phase at major mergers. This option can be switched on on request.

Cases (ii) and (iii) refer to gravitational heating due to merging events. This heating is of course not instantaneous; the energy is redistributed to the whole halo gas in a few crossing times. This behaviour is implemented by quenching cooling for a number n_{quench} of crossing times r_H/V_H ; after the quenching (which ends at some time t_q), the cooling flow is allowed to start gradually as $\exp\{-[r_H/V_H(t-t_q)]^2\}$. The parameter n_{quench} is very important to control the cooling of gas, especially at high redshift. The same quenching is applied to DM halos at their appearance time (case (i) above). This is done to avoid overcooling due to the lack of sampling of the merger history of the halo below the mass resolution, and amounts to assuming that the appearing halos have just formed by a major merger.

4.4.3 Cooling

The cooling radius is defined as the radius within which the hot halo gas has cooled down (sec. 1.4.2). In most semi-analytic models the hot gas profile is computed at a major merger; the time-dependent cooling radius is then computed as the radius at which the cooling time of a gas shell is equal to the time since the merger. In the present model the cooling radius is instead treated as a dynamical variable. This allows to re-compute the gas profile at each time-step, and to incorporate the heating effect of the hot wind coming from the central galaxy.

The cooling rate of a shell of gas of width Δr at a radius r is computed as:

$$\Delta \dot{M}_{\text{cool}}(r) = \frac{\Delta M_g(r)}{t_{\text{cool}}(r)}, \quad (4.24)$$

where $\Delta M_g = 4\pi r^2 \rho_g(r) \Delta r$ is the shell mass and $t_{\text{cool}}(r) = \Lambda_{\text{cool}}(T_g(r))$ is the cooling time at radius r . For the cooling function Λ_{cool} , we use the metallicity-dependent function tabulated by Sutherland & Dopita (1993, see sec. 1.4.1 and in particular fig. 1.10). The cooling time depends on density and temperature, but the density dependence is by far stronger, both intrinsically and because the temperature profile is much shallower than the gradient profile. So the integration in r can be performed by assuming $T_g(r) \simeq T_g(r_{\text{cool}})$. Calling \mathcal{I} the integral:

$$\mathcal{I}(r_{\text{cool}}/r_s, c_{\text{nfw}}, a, \gamma_p) = \int_{r_{\text{cool}}/r_s}^{c_{\text{nfw}}} \left(1 - a \left(1 - \frac{\ln(1+t)}{t} \right) \right)^{2/(\gamma_p-1)} t^2 dt \quad (4.25)$$

the resulting cooling flow is:

$$\dot{M}_{\text{cool}} = \frac{4\pi r_s^3 \rho_{g0}}{t_{\text{cool},0}} \mathcal{I}(r_{\text{cool}}/r_s, c_{\text{nfw}}, a, \gamma_p) \quad (4.26)$$

In this equation the cooling time $t_{\text{cool},0}$ is computed using ρ_{g0} for the density (the dependence of density on radius is taken into account by the integrand), and $T_g(r_{\text{cool}})$ for the temperature, as explained above. Analogously to the integrals of equations 4.18 and 4.19, the integral in equation 4.26 is computed on a grid of parameter values and then estimated by linear interpolation on the table. The rate of energy loss by cooling is computed analogously:

$$\dot{E}_{\text{cool}} = \frac{3kT_g(r_{\text{cool}})}{2\mu_{\text{hot}}m_p} \frac{4\pi r_s^3 \rho_{g0}}{t_{\text{cool},0}} \mathcal{I}(r_{\text{cool}}/r_s, c_{\text{nfw}}, a, \gamma_p) \quad (4.27)$$

The cooled gas carries with it a kinetic energy:

$$\dot{K}_{\text{co,H}} = \frac{1}{2} \dot{M}_{\text{co,H}} V_{\text{disp}}^2 \quad (4.28)$$

where V_{disp} is the velocity dispersion of the DM halo defined in equation 4.11.

When a heating source is present, these two terms behave differently. While the energy radiated away by the hot gas at a given density and temperature does not change, the amount of cooled mass depends on how much of this energy is replaced by the heating source. We then compute the cooling time as:

$$t_{\text{cool},0} = \frac{3kT_g(r_{\text{cool}})\mu_{\text{hot}}m_p}{2\rho_{g0}(\Lambda_{\text{cool}} - \Gamma_{\text{heat}})} \quad (4.29)$$

This cooling time is used in equation 4.26 to compute the mass cooling flow. A negative value implies a net heating of the source, in which case the cooling flow is put to zero.

The source of heating is the central galaxy, which hampers cooling through the hot wind energy flow, $\dot{E}_{\text{hw,H}}$. This flow carries the energy produced by SNe both in the bulge and in the disc; any AGN contribution is added to it. Satellites instead are assumed to orbit on average in the external regions, so that the energy contributed by their winds is injected beyond the cooling radius and does not interact with the cooling flow. To compute the heating term it is necessary to specify how this heating is distributed. For simplicity we assume that heating and cooling affect the same gas mass $4\pi r_s^3 \rho_{g0} \mathcal{I}$, i.e. the inner shell at r_{cool} that is effectively cooling. The heating term is then computed as:

$$\Gamma_{\text{heat}} = \frac{\dot{E}_{\text{hw,H}}}{4\pi r_s^3 \mathcal{I}} \left(\frac{\mu_{\text{hot}} m_p}{\rho_{g0}} \right)^2 \quad (4.30)$$

Once the cooling and heating sources are fixed, the evolution of the cooling radius is computed by inverting the usual relation, $\dot{M}_{\text{cool}} = -4\pi \rho_g r_{\text{cool}}^2 dr_{\text{cool}}/dt$, taking into account that the hot wind mass flow $\dot{M}_{\text{hw,H}}$ is adding to the hot halo phase at the cooling radius:

$$\dot{r}_{\text{cool}} = \frac{\dot{M}_{\text{cool}} - \dot{M}_{\text{hw,H}}}{4\pi \rho_g(r_{\text{cool}}) r_{\text{cool}}^2}. \quad (4.31)$$

In this way, the cooling radius decreases if the hot wind term overtakes the cooling term.

Equation 4.31 shows that the cooling radius cannot vanish, Moreover, in the case of very strong cooling flows the Runge-Kutta integrator may try some calls with $r_{\text{cool}} > r_{\text{H}}$, giving rise to numerical problems. The cooling radius is then forced to lie between a small value (taken to be 0.01 times the scale radius r_s) and 90 per cent of the virial radius r_{H} . This is done by gradually setting \dot{r}_{cool} to zero when the limits are approached. The presence of a small lower limit for r_{cool} does not influence the results, because of the flat density profile in the central regions. The upper limit can instead influence significantly the behaviour of cooling, but this happens when most of the hot gas has already cooled, a situation in which a precise modeling is not very important and the validity of the model itself is more doubtful (see the discussion in Section 4.4.1).

The existence of a cooling radius implies a central region in the DM halo devoid of hot gas. The gas in the surrounding regions would then be pushed toward the centre by pressure. This can be modeled very simply by adding to the equation for r_{cool} a negative term that closes the cooling hole at the sound speed c_s :

$$\dot{r}'_{\text{cool}} = \dot{r}_{\text{cool}} - c_s \quad (4.32)$$

This term is inserted only on request.

4.4.4 Infall

The dynamical time of the halo at a radius r is defined as the time required by a mass particle to free-fall to the centre:

$$t_{\text{dyn}}(r) = \frac{1}{\sqrt{2}V_c} \left(\frac{3\delta_c}{200c_{\text{nfw}}^2} \right)^{-1/2} r_s \int_0^{r/r_s} \left[\frac{\ln(1+y)}{y} - \frac{\ln(1+r/r_s)}{r/r_s} \right]^{-1/2} dy \quad (4.33)$$

Infall affects the hot and cold phases in very different ways. The hot phase is in hydrostatic equilibrium; however, if its energy is lower than the virial energy it will gain the missing energy by gravitational collapse, though this infall will not perturb significantly the quasi-equilibrium configuration of the gas. We model this process as follows: whenever the thermal energy of the hot gas $E_{\text{h,H}}$ is lower than the virial energy $(-0.5U_{\text{H}})M_{\text{h,H}}/M_{\text{H}}$ we add the missing energy on a dynamical time scale, computed at the cooling radius r_{cool} where most gas mass is located:

$$\dot{E}_{\text{grav}} = \frac{(-0.5U_{\text{H}})M_{\text{h,H}}/M_{\text{H}} - E_{\text{h,H}}}{t_{\text{dyn}}} \quad (4.34)$$

The cold phase is unstable for collapse and flows to the central galaxy. Most semi-analytic codes, at variance with GALRISE, unify the processes of cooling and infall by computing an infall radius for the gas as the radius at which the infall time of a gas shell is equal to the time since last major merger, then using the smallest between the cooling and infall radii to compute the

cooling flow. This choice implies an assumption of no difference between the hot halo gas and the cooled gas that is infalling toward the central galaxy. The hot wind ejected by a galaxy acts preferentially on the most pervasive hot phase, affecting in a much weaker way the cold infalling gas, which naturally fragments into clouds with a low covering factor. So, we deem that treating the infalling gas as belonging to a different phase is a step forward in the physical description of galaxy formation.

The cold gas is let infall to the central galaxy on a number n_{dyn} of dynamical times computed at the cooling radius r_{cool} :

$$\dot{M}_{\text{in,H}} = \frac{M_{\text{c,H}}}{n_{\text{dyn}} t_{\text{dyn}}(r_{\text{cool}})} \quad (4.35)$$

The corresponding loss of kinetic energy and metals is:

$$\dot{K}_{\text{in,H}} = \frac{K_{\text{H}}}{n_{\text{dyn}} t_{\text{dyn}}(r_{\text{cool}})} \quad (4.36)$$

$$\dot{M}_{\text{in,H}}^Z = \frac{M_{\text{c,H}}^Z}{n_{\text{dyn}} t_{\text{dyn}}(r_{\text{cool}})} \quad (4.37)$$

Infalling gas loses energy mainly by unelastic collisions, dissipation of turbulence, dynamical friction. All these events could be modeled in a much more careful (and uncertain) way through the kinetic dissipation term \dot{K}_{ds} . However, equation 4.35 takes implicitly all these events into account through the parameter n_{dyn} . This simple setting then allows us to neglect the kinetic dissipation term \dot{K}_{dis} .

The infalling cold gas is divided between the disc and the bulge as follows. As a first option, all the infalling gas is given to the disc, under the assumption that it has the same specific angular momentum as the DM halo. In presence of a significant or dominant bulge the formation of such a disc by infall implies that the bulge has no influence on it, even when a large fraction of it is embedded in the bulge. This is a rather strong assumption, as the hot pressurized phase pervading the bulge (Section 4.6.3) can lead to significant loss of angular momentum of the gas by ram pressure. Then, as a second option we let gas infall on the bulge by a fraction equal to the mass of the disc contained within the half-mass radius of the bulge:

$$\dot{M}_{\text{in,B}} = \dot{M}_{\text{in,H}} \left[1 - \exp\left(-\frac{R_b}{2R_d}\right) \left(1 + \frac{R_b}{2R_d}\right) \right] \quad (4.38)$$

Here and in the following, R_b denotes the half-mass radius of the bulge, while R_d is the scale radius of the disc.

This option has a significant effect on the ability of quenching the cooling at low redshift by AGN jets (Section 4.8.2): if the infalling gas has to wait for an external trigger (like a merger) to get into the bulge component, and from there to accrete onto the central BH, the feedback from the AGN will be activated with a significant delay with respect to the start of the cooling flow, while the activation will be much quicker if the infalling gas is allowed to flow directly into the bulge.

4.4.5 Galaxy super-winds and cosmological fall-back

Whenever the gas phases of the halo component are too energetic to be bound to the halo, they are allowed to escape as a galactic super-wind.

The hot phase is kept confined not only by gravity but also by the external pressure term that balances thermal pressure at the virial radius. This external pressure can be computed as the thermal pressure of the hot gas at the virial radius. However, as explained in Section 4.4.1, there are a number of numerical features that make the prediction of the gas properties in the external regions of the halo rather delicate. We then prefer to resort to a simpler physical description of winds. The hot gas is let flow away whenever its energy overtakes the virial one by a factor f_{wind} :

$$\text{hot wind condition : } E_{\text{hot,H}} > f_{\text{wind}} E_{\text{vir}}, \quad (4.39)$$

where $E_{\text{vir}} = (-0.5)U_H M_g / M_H$ (see Section 4.4.2). The parameter f_{wind} is inserted to avoid the excessive escape of gas that we have noticed when it is set to unity; the results are rather stable when $f_{\text{wind}} \sim 2$, so we adopt this value. Clearly this parameter should be fixed by a careful comparison to hydro simulations. Calling $t_{\text{sound}} = r_h / c_s$ the sound-crossing time of the halo, the hot wind mass and energy flows are then computed as:

$$\begin{aligned} \dot{M}_{\text{hsw}} &= \left(1 - \frac{f_{\text{wind}} E_{\text{vir}}}{E_{\text{hot,H}}}\right) \frac{M_{\text{hot,H}}}{t_{\text{sound}}} \\ \dot{E}_{\text{hsw}} &= \frac{3kT_g}{\mu_{\text{hot}} m_p} \dot{M}_{\text{hsw}} \\ \dot{M}_{\text{hsw}}^Z &= \dot{M}_{\text{hsw}} \frac{M_{\text{h,H}}^Z}{M_{\text{h,H}}} \end{aligned} \quad (4.40)$$

A quick computation can show that the loss of thermal energy by adiabatic expansion of the hot gas due to the mass loss should be equal to 2/3 of the energy loss: if $P = \rho kT / \mu_{\text{hot}} m_p$ and $dV = \rho dM$ then $PdV = kTdM / \mu_{\text{hot}} m_p$. So we set:

$$\dot{E}_{\text{ad}} = \frac{2}{3} \dot{E}_{\text{hsw}} \quad (4.41)$$

A similar model is applied to the cold wind (with $\sigma_H = 2K_H / M_{\text{c,H}}$ the velocity dispersion of cold halo clouds and $t_{\text{kin}} = r_h / \sigma_H$):

$$\text{cold wind condition : } K_H > f_{\text{wind}} \frac{1}{2} M_{\text{c,H}} V_{\text{disp}}^2. \quad (4.42)$$

$$\begin{aligned} \dot{M}_{\text{csw}} &= \left(1 - \frac{f_{\text{wind}} V_{\text{disp}}^2}{\sigma_H^2}\right) \frac{M_{\text{c,H}}}{t_{\text{kin}}} \\ \dot{K}_{\text{csw}} &= \left(1 - \frac{f_{\text{wind}} V_{\text{disp}}^2}{\sigma_H^2}\right) \frac{K_H}{t_{\text{kin}}} \end{aligned} \quad (4.43)$$

$$\dot{M}_{\text{csw}}^Z = \dot{M}_{\text{csw}} \frac{M_{\text{c,H}}^Z}{M_{\text{c,H}}}$$

$$\dot{K}_{\text{ad}} = \frac{2}{3} \dot{K}_{\text{csw}} \quad (4.44)$$

The mass ejected by the DM halo is then re-acquired back by it at a later time. We estimate the fall-back time as follows. The cold and hot gas phases escape because their typical velocity (kinetic or thermal) is larger than the escape velocity of the halo they belong to. At the end of an integration, we then scroll the merger tree forward in time and compute the time at which the parent DM halo has a larger escape velocity than the typical velocity of the ejected gas. We then let this gas fall back to the DM halo together with the infalling IGM (equation 4.21). However, while the large-scale structure outside a DM halo is clustered, galactic super-winds are emitted in a much more isotropic way. As a consequence, much mass could be ejected into voids and never fall back to the DM halo. We take this into account by letting only a fraction f_{back} of the ejected gas fall back to the DM halo. Our results are remarkably insensitive of the value of this parameter; we use 0.5 in the following.

4.5 Bulge and Disc structure

For each exponential disc we record its scale radius R_D and its velocity V_D at the optical radius, defined as $3.2R_D$ (Persic, Salucci & Stel 1996). The half-mass radius of the disc is then equal to $1.6783R_D$. For each bulge we record its half-mass radius R_B (equal to 1.35 effective radii) and its circular velocity defined as $V_B^2 = GM_B/R_B$. These quantities are sampled in the time grid defined in Section 4.1.3.

4.5.1 Discs

The size of galaxy discs is computed following an extension of the model by Mo, Mao & White (1998, see sec. 1.4.2) that takes into account the presence of a bulge. It is assumed that the hot gas has the same specific angular momentum as the DM halo, and that this angular momentum is conserved during the infall. Moreover, it is assumed that the disc is exponential. The angular momentum of the disc is:

$$J_D = 2\pi \int_0^\infty V_{\text{rot}}(r) \Sigma(r) r^2 dr. \quad (4.45)$$

where $\Sigma(r) = M_D \exp(-r/R_D)/2\pi R_D^2$ is the exponential profile of surface density. The rotational velocity given in this formula contains contributions from the DM halo, bulge and disc: $V_{\text{rot}}^2 = V_H^2 + V_B^2 + V_D^2$. The halo contribution is simply $V_H^2(r) = GM_H(r)/r \times (1 - \Omega_b/\Omega_0)^6$ and an analogous expression

⁶In this case the density profiles of DM and baryons are so different that they need to be treated differently, so that, at variance with the computation of the hot halo gas profile (Section 4.4.1) and

is valid for the bulge, for which we assume a Young density profile (whose projection gives the observed de Vaucouleurs profile). The disc contribution is as usual:

$$V_D^2 = \frac{GM_D}{R_D} y^2 (I_0(y)K_0(y) - I_1(y)K_1(y)), \quad (4.46)$$

where $y = r/2R_D$ and the functions contained in the equation are the standard Bessel functions. The specific angular momentum must be equal to that of the DM halo, $J_D/M_D = J_H/M_H$. This translates into an equation for R_D that must be solved iteratively, starting from the approximate solution $R_D \sim 0.71\lambda r_H$ (from eq. 1.95). This computation is a bottleneck for the whole code, especially if the disc structure is updated at each time-step as the profile of the hot halo gas is. To speed up the code, disc structure is updated each time the disc grows in mass by some fraction, set to 1 per cent. We have verified that this approximation reproduces with fair accuracy a disc which is growing in mass by continuous infall. Because of feedback, a disc that receives no infalling gas decreases in mass by ejecting gas to the halo. This mass ejection presumably leads to a decrease of surface density with no change in the radius. We then decide to re-compute the radius only when the disc mass increases with respect to the value at the last update.

Adiabatic contraction of the DM halo as the baryons settle in the centre of the halo is introduced (again following Mo, Mao & White 1998) by assuming that the adiabatic invariant $GM(r)r$ is constant. This implies that the DM mass within a radius r comes from a larger radius r_i such that:

$$M_{\text{DM}}(r_i) + M_D(r) + M_B(r) = \frac{r_i}{r} M_{\text{DM}}(r_i) \quad (4.47)$$

(here M_{DM} is the unperturbed mass density profile of the DM halo, and only the non-baryonic DM is considered). Equation 4.47, which must be solved together with equations 4.45 and 4.46, introduces a second iteration in the computation, and then a further slow-down of the code. A solution for this would be to solve the equation in a 4D grid of values of the parameters λ , c_{nfw} , M_D/M_H and M_B/M_H , then interpolating the solution on the table. This improvement is in project. In the meantime, the computation of adiabatic contraction is switched on only on request. We find that its introduction does not influence strongly the results of the code.

The specific angular momentum of DM halos changes during their evolution, both in modulus and in direction. The change in the latter quantity, for instance, drives those precessions of discs that are commonly found in N-body simulations. As mentioned above, PINOCCHIO can in principle provide information on the evolution of the angular momentum of DM halos; another simple choice would be that of re-drawing λ from its distribution (equation 1.86) at each major merger of DM halos. However, major changes in J_H are not handled easily by the Mo, Mao & White model if a disc is already formed. In fact, as the DM halo grows in mass the main contribution

in agreement with Mo, Mao & White (1998), we exclude baryons from the computation of the DM density profile.

to its angular momentum is given by the most recently accreted mass shells, while the model does not take into account the internal distribution of angular momentum, so that the change induced by last accreted and not yet cooled shell would force a recomputation of the whole disc structure. This can lead to unphysical events like sudden bursts of star formation due to a sudden decrease of λ after a major merger. Such events can be avoided either by simply keeping fixed the value of λ for each DM halo, which is our choice, or by using a more sophisticated algorithm for disc structure, able to consider the contribution to the angular momentum of the disc by accreting shells of gas.

A connected sophistication lies in taking into account the internal distribution of angular momentum, which behaves like $J_a(r) \propto M(r)^\alpha$ (Warren et al. 1992; Bullock et al. 2001), with the exponent α ranging from 1 to 1.3. This has important implications in the modeling of discs, as it implies that the first cooled gas has a low angular momentum, and then settles into a more compact, higher density disc. However, a straightforward implementation of this criterion is not easy, as it leads to a coupling of J_H and J_D to the amount of cooled gas and then to the disc mass, which is determined by the combined action of cooling and feedback, which in turn depends on the surface density of cold gas and then on R_D and J_D . This leads to nasty oscillations or numerical instabilities in the integration.

This illustrates an extreme case of another issue which is not addressed by this code, namely that the re-heated gas of galaxy winds is assumed to have the same specific angular momentum as the halo, something that may be unrealistic in many cases. Clearly the distribution of angular momentum of gas is a topic that needs much attention. Hydro simulations are the right tool to address this issue, and yet the distribution of angular momentum is only recently showing some hints of numerical convergence in the biggest simulations (see, e.g., Governato et al. 2004). From this point of view, it is remarkable that the simplest assumptions on the distribution of angular momentum give discs whose properties are not so different from reality.

4.5.2 Bulges

If discs contain the baryons that have retained their angular momentum, bulges contain the baryons that have lost most of it. In GALRISE there are four ways to let gas lose angular momentum and flow to the bulge. The first is direct infall from the halo. Indeed, as suggested by Granato et al. (2004) and mentioned above, the first fraction of gas that collapses is likely to have a low angular momentum, and is then doomed to become a spheroid. We do not implement this idea directly, to avoid the numerical problems mentioned above. However, as explained in Section 4.4.4, we allow gas to infall in an existing bulge by a fraction equal to the fraction of disc mass embedded in a bulge.

The second mechanism is bar instability. Whenever a disc embedded in a DM halo has a sufficiently high surface density, it becomes unstable to bar formation. The bar brings a fair fraction of the disc mass into the bulge; we assume this fraction to be $f_{\text{bar}} = 0.5$. For the condition for disc stability we use eq. 1.96 (Efstathiou, Lake & Negroponte 1982; Christodoulou, Shlosman &

Tohline 1995; Mo, Mao & White 1998): The value for ϵ_{lim} ranges from 1.1 for stellar discs to 0.9 for gaseous disc; as this effect is mostly important at high redshift, when discs are mostly gaseous, we use the lower value. This condition is checked at each integration time-step, and whenever it is not satisfied the integration is interrupted. At this point a fraction f_{bar} of the disc mass is given to the bulge, and the integration is started again. No starburst is explicitly connected with this event, but the presence of gas in the bulge gives rise to a stronger star formation event (see Section 4.6.3).

The third mechanism is of course the merging of galaxies. The implementation of mergers has already been described in Section 4.3.3. It is worth noticing here that the uncertainty in the fate of gas in minor mergers (we put the whole satellite in the bulge, other authors make different choices) does not influence much the results, because most mass in ellipticals comes from major mergers (and disc instabilities at $z > 5$), while most mass in discs comes from cooling flows.

In both cases of disc instability and mergers the radius of the bulge R_{new} formed by the merger of objects 1 and 2 is computed as suggested by Cole et al. (2000):

$$\frac{(M_1 + M_2)^2}{R_{\text{new}}} = \frac{M_1^2}{R_1} + \frac{M_2^2}{R_2} + \frac{f}{c} \frac{M_1 M_2}{R_1 + R_2}. \quad (4.48)$$

Here R_1 and R_2 are the half-mass radii of the merging galaxies, computed taking into account both bulges and discs. For the parameter f/c we use the values of 2 for the mergers and 4 for disc instabilities, as suggested by Cole et al. (2000).

The fourth mechanism to form a bulge is through feedback. A necessary condition for a gaseous disc not to transfer angular momentum outwards is that the dissipative cold gas has a low enough velocity dispersion, a condition which is satisfied in observed nearby discs. However, the kinetic energy of the cold phase is determined by feedback from SNe. We anticipate (see Section 4.6.1) that for discs with a high enough surface density of cold gas (present mainly at high redshift) the velocity dispersion of cold clouds can be much higher. This implies a loss of angular momentum and a corresponding thickening of the disc into a bulge object. We model this event simply by forcing a bar instability (i.e. transferring a fraction f_{bar} of mass to the bulge) whenever the surface density of cold gas Σ_{gas} overtakes a limiting value:

$$\Sigma_{\text{gas}} > \Sigma_{\text{limit}} \quad (4.49)$$

This fourth mechanism is important to have bright quasars at high redshift. Clearly the triggering of a bar instability is only a numerical trick to obtain the wanted result of moving mass to the bulge. A more sophisticated treatment would require to divide the disc into an inner, high density part, that is transformed to a bulge, and an outer disk part. Such sophistications will be considered in future work.

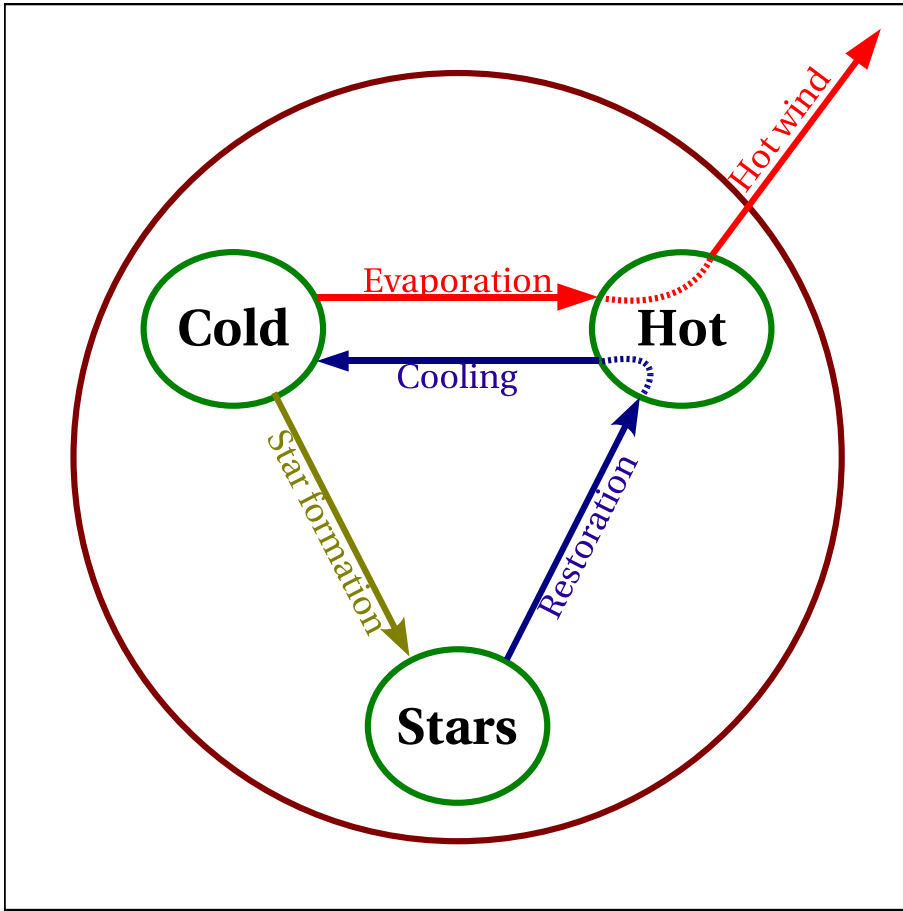


Figure 4.3: Mass flows for the one-phase version

4.6 Feedback

GALRISE allows a two-phase treatment of the star-forming ISM analogous to that described in Monaco (2004a). However, this feature is not fully exploited in this version of the code. For sake of simplicity, we prefer here to insert simpler feedback rules motivated by the results of Monaco (2004a), leaving a true multi-phase treatment to the future.

The single-phase dynamics is obtained by forcing the hot phase of disc and bulge components to be void (it usually contains only a small fraction of the mass). This is done by equating the restoration and cooling terms on the one hand, and the evaporation and hot wind terms on the other hand (figure 4.3):

$$\begin{aligned} \dot{M}_{\text{co}} &= \dot{M}_{\text{rs}} \\ \dot{M}_{\text{ev}} &= \dot{M}_{\text{hw}} \end{aligned} \quad (4.50)$$

Monaco (2004a) studied the evolution of the ISM under the following assumptions (see also sec. 1.3.2): (i) the ISM is composed by two phases, a hot and a cold one, in thermal pressure equilibrium; (ii) collapsing and star-forming clouds arise from the cold clouds by kinetic aggregations; (iii)

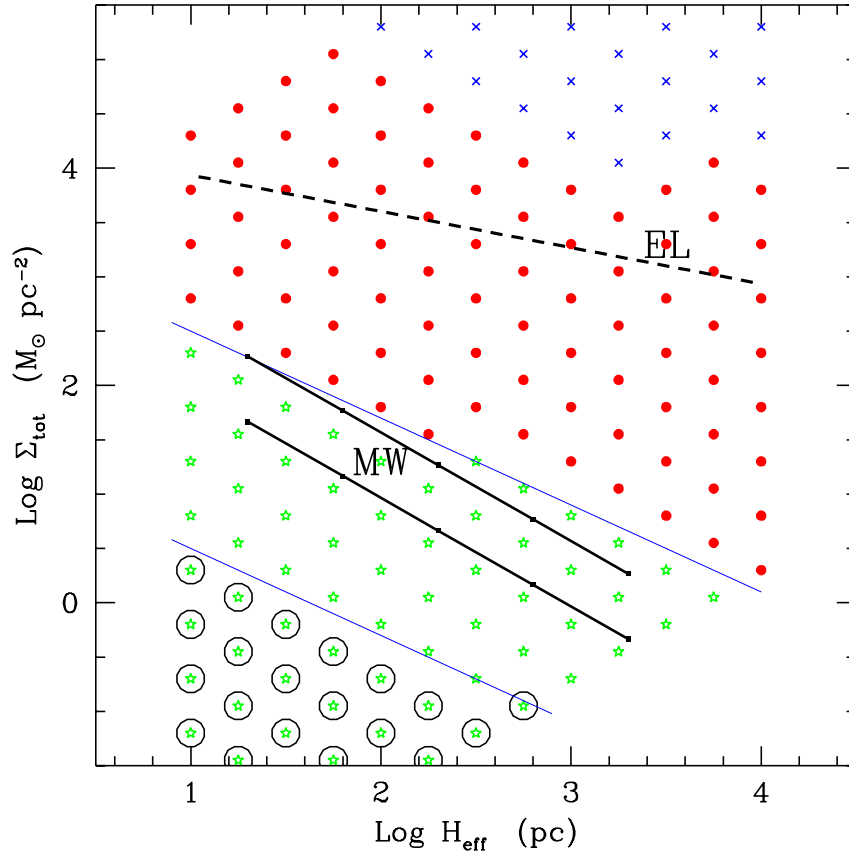


Figure 4.4: Feedback regimes as a function of surface mass density and vertical scale-length.

type II SNe exploding within a star-forming cloud give rise to a single super-bubble; (iv) the super-bubble propagates in the most pervasive hot phase; (v) the super-bubble expands until either it is stopped by the external pressure or it blows out of the structure. Four possible self-regulated feedback regimes follow naturally from this setting, depending on whether the super-bubbles stop by pressure confinement or blow-out, before or after the internal hot gas has started cooling (so as to form a pressure-driven snowplough, hereafter PDS).

In that paper it was shown that the dynamics of feedback depends mainly on density (we will use the total surface density of the disc Σ in the following) and vertical scale-height H_{eff} of the system. In realistic systems feedback can take place in the regimes where super-bubbles blow-out or are confined in the adiabatic stage. Figure 3a of Monaco (2004a), which is reported here for sake of clarity (Figure 4.4), shows that the adiabatic blow-out and confinement regimes take place in two different regions of the Σ - H_{eff} space, separated by the relation:

$$\Sigma = 8 \left(\frac{H_{\text{eff}}}{1000 \text{ pc}} \right)^{-0.8} \text{ M}_{\odot} \text{ pc}^{-2} \quad (4.51)$$

The numerical constants in this relation depend on the (uncertain) values of the parameters used in the model, so they are to be considered as indicative.

Galaxy discs and bulges tend to stay respectively in the adiabatic blow-out and confinement regimes, so at a first look there is no much doubt on how to apply the feedback regimes within a galaxy formation code: discs are in the adiabatic blow-out regime, bulges are in the adiabatic confinement regime. However, the central region of a disc can be in the adiabatic confinement regime for at least two reasons: (i) it is embedded in a bulge, so that its ISM is pressurized by the bulge hot phase; (ii) its surface density is high enough to cross the limit of equation 4.51 for adiabatic confinement. This happens at a typical surface density of $\Sigma \sim 300 \text{ M}_{\odot} \text{ pc}^{-2}$. Point (i) has been used to justify the direct infall of gas from the halo to the bulge (Section 4.4.4). Point (ii) has been mentioned in Section 4.5.2 to argue for feedback-induced loss of angular momentum, and the effects of such feedback have been modeled by forcing bar formation when the surface density of cold gas is high (equation 4.49).

To fully implement the Monaco (2004a) feedback recipes in GALRISE it is necessary to assess the role of the velocity dispersion of cold clouds, a quantity which is left as a free parameter in that paper. This is done in the following subsection. After that we explain how we implement feedback in the case of thin or thick systems. In addition to this treatment, we have implemented also the feedback rules described by Cole et al. (2000, sec. 1.5.1), so as to be able to compare the two approaches. However, this comparison will not be presented here.

4.6.1 Kinetic feedback and the velocity dispersion of cold clouds

We do not include here a full self-consistent treatment of the kinetic energy of cold clouds, but try to take into account its effect as follows. The velocity dispersion $\sigma_{\text{cold}} = \sqrt{2K/M_{\text{cold}}}$ of cold clouds is determined as a first approximation by the equilibrium between the injection of kinetic energy by SNe and the dissipation by turbulence. The injection of kinetic energy is:

$$\dot{K}_{\text{SN}} = \epsilon_k \frac{\dot{M}_{\text{sf}}}{M_{\star, \text{SN}}} E_{\text{SN}} \quad (4.52)$$

where E_{SN} is the energy of a SN, $M_{\star, \text{SN}}$ is the mass of newly formed stars per SN and ϵ_k is its fraction given to the cold phase as kinetic energy. The rate of energy dissipation is observed in hydro simulation to be of the order (Mac Low 2002):

$$\dot{K}_{\text{ds}} = -\frac{1}{2} \frac{M_{\text{cold}} \sigma_{\text{cold}}^3}{L_{\text{drive}}} \quad (4.53)$$

where L_{drive} is the scale at which turbulence is driven, suggested to be twice the diameter of the typical size of the superbubble. To determine σ_{cold} we

assume that an equilibrium configuration is quickly reached and neglect all mass flows, so that (equation 4.6) $\dot{K}_{\text{SN}} + \dot{K}_{\text{ds}} = 0$. We then obtain:

$$\sigma_{\text{cold}} = \sigma_0 t_{\star}^{-1/3} \quad (4.54)$$

(t_{\star} is given in Gyr, so as to have σ_0 in km s^{-1}) where $\sigma_0 = (2L_{\text{drive}}\epsilon_k E_{\text{SN}}/M_{\star,\text{SN}})^{1/3}$ and its numerical value is:

$$\sigma_0 = 9.3 \left(\frac{L_{\text{drive}}}{100 \text{ pc}} \right)^{1/3} \left(\frac{\epsilon_k}{0.01} \right)^{1/3} E_{51}^{1/3} \left(\frac{M_{\star,\text{SN}}}{120 M_{\odot}} \right)^{-1/3} \text{ km s}^{-1} \quad (4.55)$$

In a thin system the fraction of (thermal and kinetic) energy injected into the ISM is predicted by Monaco (2004a) to be about 5 per cent, so ϵ_k will be of order of 0.01, while the driving scale should be of order of the vertical scale-length of the system, ~ 100 pc. The predicted value for σ_{cold} in a Milky Way-like galaxy (with $t_{\star} \sim 2$ Gyr) is then $\sim 7 \text{ km s}^{-1}$, in remarkable agreement with the observed value which ranges between 6 and 9 km s^{-1} . Much higher values of the velocity dispersion are expected in thick systems, where ϵ_k is much higher (all the SN energy is retained by the system) and t_{\star} much lower. As a consequence, we neglect kinetic feedback in discs but take it into account in bulges. Given the great uncertainty in the driving scale of turbulence in mergers, the normalization constant σ_0 will be left as a free parameter.

We stress that equation 4.55 is valid under the assumption that turbulence is driven by SNe and not by gravitationally induced motions like differential rotation or tidal disturbances in mergers. In the case of our Galaxy, Mac Low (2002) argues that SNe are the most likely drivers of turbulence, and the good agreement of the predicted value of σ_{cold} given above with the observed one suggests that SNe are at least a significant contributor. In thick systems, like gas-rich spheroids or mergers, gravitationally-induced turbulence will be very important. However, the most relevant consequence of a high value of σ_{cold} for our purposes is the massive removal of cold gas during episodes of strong star formation. It is clear that if a condition $\sigma_{\text{cold}} > V_B$ is reached in a gas-rich bulge, then the driver of turbulence must be star formation and not gravity, while in the case of a low value of σ_{cold} no mass is removed. So, in this case the assumption will work in the range where its results are most influential.

4.6.2 Thin systems

In thin systems super-bubbles blow out of the disc soon after they form and while they still are in the adiabatic stage, and their porosity remains low. The fraction of the SN energy that is injected into the ISM is limited to a few per cent of the total budget, while most energy is directly injected into the halo through a tenuous, metal-rich hot wind. The ISM self-regulates to a configuration that is very similar to that of the Milky Way (Monaco, 2004a). The star formation regulates to a level similar to that found in nearby galaxies by Schmidt (1969) and quantified more recently by Kennicutt (1998).

In Monaco (2004a) the resulting star-formation timescales were incorrectly scaled with the infall time and the total surface density Σ of the system. A more careful analysis reveals that, for a fixed set of parameters and at fixed H_{eff} , t_{\star} depends only on the cold gas surface density Σ_{cold} . This is expected, as the star-formation timescale is determined by the intrinsic properties of the ISM, not by the rate at which mass is acquired by it or by the amount of stars present. A better fit of the results of Monaco (2004a) in the adiabatic blow-out regime (for the standard set of parameters defined in that paper) gives:

$$t_{\star} = 6 \Sigma_{\text{cold}}^{-0.4} \left(\frac{H_{\text{eff}}}{100 \text{ pc}} \right)^{0.65} \text{ Gyr} \quad (4.56)$$

Here Σ_{cold} is in $M_{\odot} \text{ pc}^{-2}$.

In the simple case of a constant value of H_{eff} for all galaxies, the Schmidt-Kennicutt law is recovered with a very similar normalization (however, observations refer to integrated quantities, this prediction refers to a section of the disc). But the assumption of a constant H_{eff} is rather artificial, as the vertical scale-length of the cold gas is determined by the vertical gravitational equilibrium as $H_{\text{eff}} = \sigma_{\text{cold}}^2 / \pi G \Sigma_{\text{tot}}$, so a constant value would imply a tuned variation of Σ and σ_{cold} . The other simple possibility is to assume a constant value for σ_{cold} . This leads to the prediction $t_{\star} \propto \Sigma_{\text{cold}}^{-1.05} f_{\text{cold}}^{0.65}$, where f_{cold} is the fraction of cold gas in the disc. This relation is apparently steeper than the observed Schmidt law; however, Σ_{cold} and f_{cold} are correlated, in that lower Σ_{cold} discs, having lower star-formation rates, retain a greater fraction of their gas. So the outcoming relation between t_{\star} and Σ_{cold} is shallower.

If the dependence of the velocity dispersion on the star-formation timescale, equation 4.54, is taken into account, then (normalizing the relation to the Schmidt-Kennicutt value at $\Sigma_{\text{cold}} = 13 M_{\odot} \text{ pc}^{-2}$, the gas density of the Milky Way), the predicted relation for the star-formation timescale in discs is⁷:

$$t_{\star,D} = 9.1 \Sigma_{\text{cold},D}^{-0.73} \left(\frac{f_{\text{cold}}}{0.1} \right)^{0.45} \text{ Gyr} \quad (4.57)$$

This relation is again apparently steeper than the Schmidt-Kennicutt one, but when the correlation between Σ_{cold} and f_{cold} is taken into account it comes out with a slope consistent with the observation. This will be shown in Section 4.11.

Other complications can be introduced in this picture: if the driving length L_{drive} is equal to twice the diameter of the blowing-out super-bubbles, it will scale with H_{eff} . Moreover, the efficiency of feedback is known in Monaco (2004a) to increase slightly with Σ (and then with Σ_{cold}). Introducing these dependences we obtain a scaling of t_{\star} with Σ_{cold} and f_{cold} similar to equation 4.57, with slightly different exponents. We have verified that these

⁷To obtain equation 4.56 a constant σ_{cold} was assumed, so this equation is not used consistently. However, the σ_{cold} parameter in Monaco (2004a, there called σ_V) influences only the rate of kinetic aggregation of clouds, and the results have been shown to be insensitive of its actual value, so equation 4.56 can be safely used even in the case of a varying σ .

somewhat different descriptions of feedback do not give significantly different results, so we keep equation 4.57 as a reference.

In the adiabatic blow-out regime, the amount of cold mass ejected by the super-bubbles is modest, while the amount of hot gas that is ejected out to the halo is very similar to the star-formation rate. Moreover, a fraction f_{rest} of the mass of newly formed stars is quickly restored to the hot phase of the ISM. As a consequence, the star-formation and wind mass flows are:

$$\begin{aligned}
 \dot{M}_{\text{sf,D}} &= \dot{M}_{\text{cold,D}}/t_{\star,\text{D}} \\
 \dot{M}_{\text{rs,D}} &= f_{\text{rest}} \dot{M}_{\text{sf,D}} \\
 \dot{M}_{\text{hw,D}} &= \dot{M}_{\text{sf,D}} \\
 \dot{M}_{\text{cw,D}} &= 0
 \end{aligned}
 \tag{4.58}$$

As shown in Section 4.6.1, the low velocity dispersion of the cold gas guarantees that there is no cold wind due to the high level of turbulence.

The hot wind mass flow carries the energy of SNe blown out by the super-bubbles. We assume that a fraction $f_{\text{th,D}}$ of a 10^{51} erg SN is carried by the hot wind gas. For thin systems this fraction is estimated to be ~ 0.8 by Monaco (2004b). However, this number is highly uncertain because (i) the loss of SN energy within the star-forming cloud could be higher, as many authors working on the physics of ISM have often claimed, (ii) the SN energy could be well in excess of 10^{51} erg, (iii) some energy could be lost in the interaction with the hot halo gas. Moreover, there is a degeneracy between this parameter and $M_{\star,\text{SN}}$, which depends on the IMF. It is then wise to leave $f_{\text{th,D}}$ as a free parameter.

To the energy of type II SNe we add a contribution from type Ia SNe as one per year per $10^{12} M_{\odot}$ of stars. This is done in order to test the energetic effect of these SNe. In the case of thin systems with a continuous star formation, and given the uncertainty on $f_{\text{th,D}}$, the contribution from type Ia SNe is almost irrelevant. As suggested for instance by Recchi, Matteucci & D’Ercole (2001), type Ia SNe may have a higher efficiency of energy injection, as they don’t explode in the dense molecular clouds. As a consequence, one might want to have a different efficiency $f_{\text{th,Ia}}$ for the two SN types. Given the modest importance of these we prefer not to add a further parameter.

The contribution of the disc to the hot wind energy term is then:

$$\dot{E}_{\text{hw,H}}|_{\text{disc}} = f_{\text{th,D}} E_{\text{SN}} \left(\frac{\dot{M}_{\text{sf,D}}}{M_{\star,\text{SN}}} + 1 \text{ SN yr}^{-1} \frac{M_{\text{star,D}}}{10^{12} M_{\odot}} \right)
 \tag{4.59}$$

The outflowing hot gas will interact with the halo cold phase in a way that is difficult to model. In order to be able to constrain the effect of this process, we allow for a fraction of the thermal energy to be given to the halo cold phase:

$$\dot{K}_{\text{w,H}}|_{\text{disc}} = f_{\text{kin}} \dot{E}_{\text{hw,H}}|_{\text{disc}}
 \tag{4.60}$$

For simplicity we do not subtract this energy from the hot wind budget. We stress that this term is not due to a contribution of cold wind but to the interaction of the hot wind with the cold halo phase.

4.6.3 Thick systems

In the model by Monaco (2004a) the gravitational perturbations to the ISM are neglected. This assumption is questionable for spiral discs, but the coincidental similarity between the timescale for kinetic aggregations and the disc timescale, that drives the sweeping by spiral arms, makes the kinetic aggregation mechanism a good substitute for spiral arms in creating massive clouds, at least at an order-of-magnitude level. Things change in the case of thick systems, where most energy is efficiently pumped into the hot phase so that the ISM is much more pressurized, the star-forming clouds are much smaller and denser, and kinetic aggregations are disfavoured. This leads to the prediction of a lower level of star formation compared to the Schmidt-Kennicutt law (figure 7 of Monaco, 2004a). However, tidal disturbances will be much stronger in a bulgy object, at least when it is formed through a disc instability or a merger, so that the formation of collapsing clouds will not be determined by kinetic aggregations. Moreover, in a major merger the pressurization due to the onset of the adiabatic confinement regime will cause a quick drop of the Jeans mass, and this will make most clouds present in the merging discs collapse and form stars in a short time. These transient effects have not been properly modeled by Monaco (2004a), so we prefer to determine the star-formation timescale directly from the Schmidt law:

$$t_{\star,B} = 4 \Sigma_{\text{cold},B}^{-0.4} \text{ Gyr} \quad (4.61)$$

The resulting star-formation and restoration rates are:

$$\begin{aligned} \dot{M}_{\text{sf},B} &= M_{c,B}/t_{\star,B} \\ \dot{M}_{\text{rs},B} &= f_{\text{rest}} \dot{M}_{\text{sf},B} \end{aligned} \quad (4.62)$$

As for the thin system case, the rate at which hot gas flows to the halo is similar to the star formation rate, so that we retain this prediction. While in thin systems the energy is injected to the halo mainly by blowing-out superbubbles, in thick systems the energy is ejected through this hot wind. In the Monaco (2004a) model the typical temperature of the hot phase is found to be of $\sim 10^7$ K. In this case it is easy to compute that, for $M_{\star,\text{SN}} = 120 M_{\odot}$ and 10^{51} erg per SN the fraction of SN energy carried away by SNe is $f_{\text{th},B} \simeq 0.5$, slightly lower than the thin system case. Moreover, while a disc is unable to confine a gas phase with a temperature as high as $\sim 10^6$ K, a massive bulge can gravitationally confine its hot phase, whose temperature corresponds roughly to the virial temperature of a bulge with $V_B \sim V_{\text{hot}} = 300 \text{ km s}^{-1}$. We then limit the hot wind as follows:

$$\beta = \frac{\sqrt{V_{\text{hot}}^2 - V_B^2}}{V_{\text{hot}}} \quad (4.63)$$

where of course $\beta = 0$ if $V_B > V_{\text{hot}}$. The resulting hot wind rate is:

$$\dot{M}_{\text{hw},B} \Big|_{\text{therm}} = \beta \dot{M}_{\text{sf},B} \quad (4.64)$$

while the hot wind energy is:

$$\dot{E}_{\text{hw,H}}|_{\text{bulge}} = f_{\text{th,B}} E_{\text{SN}} \beta \left(\frac{\dot{M}_{\text{sf,B}}}{M_{\star,\text{SN}}} + 1 \text{ SN yr}^{-1} \frac{M_{\text{star,B}}}{10^{12} M_{\odot}} \right) \quad (4.65)$$

As for the thin systems, we allow some energy to accelerate the cold halo phase:

$$\dot{K}_{\text{w,H}}|_{\text{bulge,hw}} = f_{\text{kin}} \dot{E}_{\text{hw,H}}|_{\text{bulge}} \quad (4.66)$$

Because in thick systems all the energy of SNe is injected to the ISM and star-formation timescales are much shorter (in virtue of the increased surface density), the injection of kinetic energy leads to velocity dispersions of the cold phase much larger than the $\sim 7 \text{ km s}^{-1}$ found in discs. In this case some cold clouds may get enough kinetic energy to be able to leave the potential well of the bulge. This process is commonly called kinetic feedback. The probability that a cold cloud is unbound, i.e. it has a velocity larger than the escape velocity of the bulge, $\sqrt{2}V_B$, is computed under the hypothesis of a Maxwellian distribution of velocities with rms σ_{cold} :

$$P_{\text{unb}} = \text{erfc} \left(\frac{V_B}{\sigma_{\text{cold}}} \right) + \frac{2}{\sqrt{\pi}} \frac{V_B}{\sigma_{\text{cold}}} \exp \left(-\frac{V_B^2}{\sigma_{\text{cold}}^2} \right) \quad (4.67)$$

The average velocity of the unbound clouds is:

$$v_{\text{unb}} = \sigma_{\text{cold}} \frac{4}{\sqrt{2\pi}} \frac{\left(1 + \left(\frac{V_B}{\sigma_{\text{cold}}} \right)^2 \right) \exp \left(-\frac{V_B^2}{\sigma_{\text{cold}}^2} \right)}{P_{\text{unb}}} \quad (4.68)$$

The velocity of the clouds after being ejected out of the bulge will be:

$$v_{\text{out}} = \sqrt{v_{\text{unb}}^2 - 2V_B^2} \quad (4.69)$$

This process will generate a wind flux roughly equal to the unbound mass, $P_{\text{unb}} M_{\text{c,B}}$, divided by the crossing time R_B/v_{unb} . This outflow is naturally identified with a cold wind, adding mass to the cold halo phase. The cold wind mass flow is:

$$\begin{aligned} \dot{M}_{\text{cw,B}} &= M_{\text{c,B}} P_{\text{unb}} \frac{v_{\text{unb}}}{R_b} \\ \dot{K}_{\text{w,H}}|_{\text{bulge,cw}} &= \frac{1}{2} \dot{M}_{\text{cw,B}} v_{\text{out}}^2 \end{aligned} \quad (4.70)$$

However, the fate of the cold clouds ejected by a bulge may be different. The exit from the pressurized bulge to the halo would make those clouds expand, and then be much more sensitive to the bow shock generated by their interaction with the hot halo gas and to thermal evaporation. As a results, the cold clouds ejected by the bulge could be heated and mix with the hot phase. A similar thing takes place in SPH hydro simulations of galaxy formation, where (typically cold) particles neighbouring newly formed stars are given some kinetic energy; this energy is quickly thermalized and the outflowing

particle is quickly heated to a high temperature. If this is the case, the cold and hot wind flows should be given as follows:

$$\begin{aligned}
\dot{M}_{\text{hw,B}}\Big|_{\text{kin}} &= M_{\text{c,B}} P_{\text{unb}} \frac{v_{\text{unb}}}{R_b} \\
\dot{M}_{\text{hw,B}} &= \dot{M}_{\text{hw,B}}\Big|_{\text{therm}} + \dot{M}_{\text{hw,B}}\Big|_{\text{kin}} \\
\dot{M}_{\text{cw,B}} &= 0
\end{aligned}
\tag{4.71}$$

From the energetic point of view, the kinetic energy of this outflow will be typically not enough to heat the gas to a high temperature, so the heating will be done with the same energy budget of equation 4.65; in other words, no energy is added to the $\dot{E}_{\text{hw,H}}$ term. We have implemented both possibilities, and the choice between the two has been left free.

4.7 Metals

The evolution of metals is given by the equations 4.7. In this set of equations most metal flows are obtained from their related mass flow as follows:

$$\dot{M}_{\text{flow}}^Z = \frac{M_{\text{source}}^Z}{M_{\text{source}}} \dot{M}_{\text{flow}}
\tag{4.72}$$

where M_{source} and M_{source}^Z are the gas and metal masses of the source phase. The cosmological infalling gas is assumed to have a metallicity $Z_{\text{pre}} \sim 10^{-4} Z_{\odot}$ due to pre-enrichment by sources that are below the mass resolution limit (from popIII stars to very small primeval galaxies). These flows take into account the transfer of metals among phases and components, but not their production.

Metals are produced by newly formed stars in an Instantaneous Recycling Approximation (IRA), i.e. their production follows promptly star formation and the new metals are immediately mixed with the ISM. Newly metals are spread into the ISM mainly by SNe, so analogously to the energy they are likely to be selectively ejected to the halo. This is clearly true in the blowing-out thin systems, but even in thick systems metals are first mixed with the hot gas that escapes the halo at a rate equal to the star-formation rate. To model this effect, a fraction f_{Zej} of the new metals is ejected directly to the halo through hot winds:

$$\dot{M}_{\text{hw,H}}^Z\Big|_{\text{ej}} = f_{\text{Zej}} Y (\dot{M}_{\text{sf,B}} + \dot{M}_{\text{sf,D}})
\tag{4.73}$$

where Y is the fraction of mass in newly produced metals per generation of stars. This term is added to the $\dot{M}_{\text{hw,H}}^Z$ metal flow; satellite galaxies will inject their metals to the halo component of the main DM halo they belong to through the satellite metal flows. The other metals will be given to the hot phase of the component they belong to:

$$\dot{M}_{\text{yi}}^Z = (1 - f_{\text{Zej}}) Y \dot{M}_{\text{sf}},
\tag{4.74}$$

In the present formulation, these metal flows are added also to the corresponding cooling metal flows to assure that the metals go to the cold phase.

The same parameter $f_{Z_{ej}}$ is for simplicity used both for disc and bulge, even though one might want to use different values for the two components. A value of 0.5 will be used in the following.

Finally, if the star formation in halos is switched on, all the metals are obviously injected to the hot halo phase.

4.8 AGN activity

4.8.1 Accretion onto black holes

A seed black hole of mass M_{seed} is put at the centre of each DM halo. These black holes may be generated by the collapse of the first stars (e.g., Volonteri, Haardt & Madau, 2003). Seed masses should be of order of tens to hundreds M_{\odot} ; however, they start growing very soon during the early evolution of baryons in DM halos. This happens at times and for DM halo masses that are not sampled in the typical runs used in galaxy formation. We then use a higher value for the seed mass, $M_{\text{seed}} = 1000 M_{\odot}$; the results are quite stable for reasonable variations of this parameter.

The accretion of gas onto the black holes is possible only if this gas has lost nearly all of its angular momentum. The first step in this loss is the same that leads to the formation of bulges; we then base our computation of black hole accretion on the cold bulge gas. As the amount of accreted gas is small, we do not remove the accreted mass from the matter budget. In other words, the mass in black holes does not obey a mass conservation constraint as the mass of all the other components.

The gas is assumed to lose angular momentum at a rate proportional to the star-formation rate. This is justified by the radiation drag mechanism proposed by Umemura (2001) and used by Granato et al. (2004). However, a connection between loss of angular momentum and star formation likely has a more general validity, as many mechanisms able to cause a loss of angular momentum (turbulence, kinetic aggregations etc.) are directly or indirectly driven by massive stars and SNe. A more general relation between \dot{M}_{lowJ} and $\dot{M}_{\text{sf,B}}$ is obtained assuming a power-law dependence with exponent α_{lowJ} between the two quantities:

$$\dot{M}_{\text{lowJ}} = f_{\text{lowJ}} \dot{M}_{\text{sf,B}} \left(\frac{\dot{M}_{\text{sf,B}}}{100 M_{\odot} \text{ yr}^{-1}} \right)^{\alpha_{\text{lowJ}} - 1} \quad (4.75)$$

For $\alpha_{\text{lowJ}} = 1$ this relation is equivalent to that of Granato et al. (2004, sec. 1.5.1), while for $\alpha_{\text{lowJ}} \neq 1$ the f_{lowJ} parameter is scaled to a star formation rate of $100 M_{\odot} \text{ yr}^{-1}$.

We follow Granato et al. (2004) by assuming that this gas does not flow directly onto the black hole but settles on a reservoir of low-angular momentum gas, whose mass is M_{resv} . From this reservoir the gas accretes onto the black

hole at a rate regulated by the viscous time-scale of the accretion disc, modeled by Granato et al. (2004) as:

$$\dot{M}_{\text{visc}} = k_{\text{accr}} \frac{\sigma_B^3}{G} \left(\frac{M_{\text{res}}}{M_{\text{BH}}} \right)^{3/2} \left(1 + \frac{M_{\text{BH}}}{M_{\text{resv}}} \right)^{1/2} \quad (4.76)$$

where the constant k_{accr} is suggested by the authors to take a value $\sim 0.001^8$, $\sigma_B \simeq 0.65V_B$ is the 1D velocity dispersion of the bulge and M_{BH} is of course the BH mass.

Accretion is always limited by the Eddington-Salpeter rate, whose time-scale (for a radiation efficiency of 0.1) is $t_{\text{Ed}} = 0.04$ Gyr. The evolution of the black hole-reservoir system is then:

$$\begin{aligned} \dot{M}_{\text{BH}} &= \min \left(\dot{M}_{\text{visc}}, \frac{M_{\text{BH}}}{t_{\text{Ed}}} \right) \\ \dot{M}_{\text{resv}} &= \dot{M}_{\text{lowJ}} - \dot{M}_{\text{BH}} \end{aligned} \quad (4.77)$$

In chapter 5, the accretion rate onto the black hole will be modeled as $M_{\text{serv}}/t_{\text{Ed}}$. We prefer equation 4.76 in virtue of its sounder physical motivation; however, the two choices give similar results.

4.8.2 Feedback from jets

Jets coming from radio-loud AGN are though to be one of the most promising mechanisms to stop the cooling flows in galaxy clusters (sec. 2.3). Besides, a successful reproduction of the high-luminosity cutoff of the luminosity function of galaxies requires a proper modeling of this kind of feedback (Benson et al. 2003; Bower et al., 2005). The efficiency of radiation of AGNs is known to decrease when the accretion rate in units of the Eddington rate $\dot{m} = \dot{M}_{\text{BH}} t_{\text{Ed}} / M_{\text{BH}}$ is lower than $\sim 10^{-2}$. Slowly accreting black holes however radiate very efficiently in the radio (see, e.g., Merloni et al. 2003). It is then reasonable to assume that the efficiency of energy emission in jets is 0.1 if \dot{m} is small, and lower for higher accretion rates. As ~ 10 per cent of bright QSOs are radio-loud, we estimate the efficiency of jet emission as 0.01 in the case of $\dot{m} > 0.01$.

The efficiency with which this energy heats the hot halo gas component depends on the hot gas temperature to the power 3/2. In order to keep the expression simple and avoid possible unwanted numerical instabilities in the integration, we scale the efficiency with the circular velocity of the halo:

$$f_{\text{jet}} = f_{\text{jet},0} \left(\frac{V_c}{1000 \text{ km s}^{-1}} \right)^3 \quad (4.78)$$

The efficiency f_{jet} is never allowed to be higher than unity.

The energy injected into the halo hot gas is then:

⁸Because of a misprint, the value is indicated to be 10^{-4} in their paper, while the correct value is an order of magnitude larger.

$$\begin{aligned} \dot{E}_{\text{hw,H}}|_{\text{jets}} &= f_{\text{jet}} 0.1 \dot{M}_{\text{BH}} c^2 && \text{if } \dot{m} < 0.01 \\ &f_{\text{jet}} 0.01 \dot{M}_{\text{BH}} c^2 && \text{if } \dot{m} < 0.01 \end{aligned} \quad (4.79)$$

We find that this implementation of jet feedback is not very effective in avoiding strong cooling flows at low redshift, and then the formation of too massive giant ellipticals. The reason for this lies in the timescales for the loss of angular momentum: the gas that accretes onto the black holes comes from the same cooling flow that must be quenched, but in the time required by this gas to lose angular momentum (i.e. to flow to the bulge, form a significant amount of stars, accrete on a viscous accretion timescale) a lot of gas has had time to cool, and jets cannot re-heat this cooled gas.

As a second option, we implement a much simpler recipe for jet feedback. Whenever a cooling flow is present ($\dot{M}_{\text{co,H}}$), it is assumed that a fraction f_{BH} of the cooled gas is immediately accreted onto the black hole, provided the mass of the black hole is large enough so that the accretion rate is lower than the Eddington rate. The cooling flow is then explicitly quenched whenever the predicted accretion rate is not higher than the Eddington rate of the accreting black hole; this procedure then applies only at low redshift, when massive black holes have already assembled. Following Bower et al. (2005), this quenching is applied only to DM halos more massive than $10^{13} M_{\odot}$, as hydro simulations show that the efficiency of jet heating drops dramatically for such small halos. Notably, the mass that is deemed to accrete onto the black hole is not given to the black hole; however, this should amount to a negligible amount of mass.

This procedure is not affected by the problem explained above, and is very effective in quenching cooling flows and avoiding the formation of too massive galaxies. However, neglecting the timescales for the triggering of this kind of feedback is just a way to hide important and poorly understood pieces of physics. We will then use this procedure only to produce acceptable galaxy samples, but we do not claim that this is a way to give a full and self-consistent solution of the physical problem.

4.8.3 Quasar winds

A bright quasar shining into a star-forming bulge can inject a great amount of energy into the ISM, leading to a massive removal of cold gas. This mechanism will be described in detail in chapter 5 and 6. These winds have a modest effect on the formation of a galaxy, but influence the formation and evolution of AGN.

4.9 Parameters

Table 4.2 gives a complete list of the parameters of the model, with the value used to compute the results. To these the cosmological parameters (Ω_0 , Ω_{Λ} , Ω_b , H_0 and σ_8 ; see Section 4.1.10) should be added; these are now fixed with a good accuracy, with the exception of σ_8 whose value influences strongly the

number of DM halos at high redshift. The number of parameters is high, and this reflects both the number of physical processes that are included in the galaxy formation code and the level of uncertainty in many of these processes. Anyway, galaxy formation is a problem of complexity, and there is no way to reduce the number of parameters other than hiding them by fixing them to some value. On the other hand, the number of observables that can be used to constrain these parameters is very high, so that it is possible in principle to constrain most of them, apart from degeneracies. The most obvious one in this context is the degeneracy between the energy of a SN, the star mass per SN $M_{\text{star,SN}}$ and the thermal feedback efficiencies $f_{\text{th,B}}$ and $f_{\text{th,D}}$. For this reason we only vary the efficiencies, leaving $M_{\star,\text{SN}}$ fixed and not even including the SN energy as a parameter.

In practice, many of these parameters are fixed independently by the results of N-body simulations or by observations, and their variation within the known uncertainties does not influence the results strongly. We fix these parameters to the values given in the table. The other parameters are then of primary importance, and are labeled with a mark in the table.

4.10 Post Processing

For each tree that is analysed, all the variables introduced in section 4.1.2, together with the disc and bulge radii and velocities, star formation rates and accretion rate onto black holes (at the sampling time, not averaged on the time bin), are sampled in intervals of time Δ_t and at the final time. All these quantities are output at the end, together with the merger histories of galaxies, constructed as specified in section 4.2.1.

For each time bin this information is issued for all the existing galaxies of a tree. However, this is not sufficient to reconstruct the star-formation history of a galaxy component, because disc instabilities, mergers, tidal stripping and destruction events move stars among galaxies and components; as a consequence, the sampled star formation history of stars that are formed in a galaxy component does not coincide with the star formation history of the stars eventually found in that galaxy component. To reconstruct this last quantity, all the events that transfer star mass from a component or a galaxy to another are recorded and output at the end. Star formation histories are then reconstructed at the post-processing stage by scrolling the sampled history of galaxies and moving star mass among the components. This is a very quick process, that can be done at the reading time. Moreover, the process can be done up to any time in the sampling grid.

The star formation rates are then reconstructed in time bins of width Δ_t , which is set to 0.1 Gyr. This sampling is fine but for the last bin considered, as the last formed stars, that dominate the UV, B and FIR spectra, live for less than the sampling bin. Then the last time bin is divided into two parts, a first one of width 0.01 Gyr, for which the punctual star formation is assumed, and a second one, where the remaining stars are assumed to form at a constant rate. The integral of this two-step star formation rate is obviously constrained

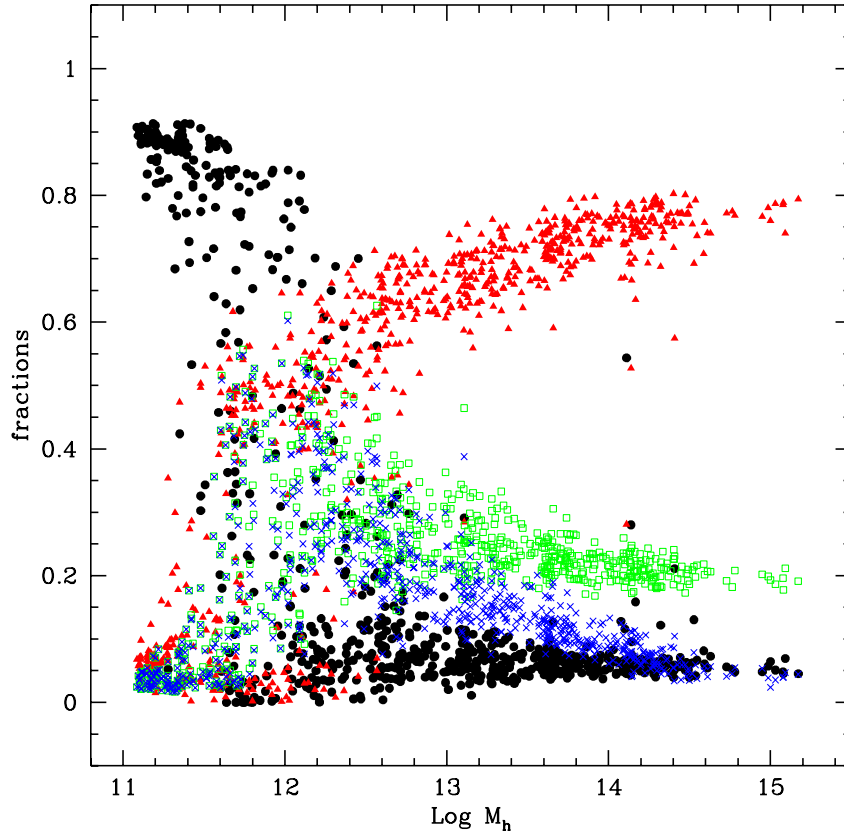


Figure 4.5: DM halos at $z = 0$: fraction of baryons in hot halo gas, stars in all galaxies, stars in the central galaxy and expelled by winds.

to give the total amount of stars formed in the bin.

4.11 Results

In this section we present the main results of the code, obtained with the set of parameters given in Table 4.2. These allow to obtain a good fit for many observational datasets, so they will be used also in next chapters as a reference set. However, we do not present here a true best-fitting model, as there are issues of galaxy formation that still need to be understood or properly addressed. As a consequence, we do not exclude further tuning to optimize the predictions when comparing with specific datasets. Moreover, for sake of simplicity here we restrict ourselves to predictions that do not require the use of a spectrophotometric code. In this way all the uncertainties involved in the generation of SEDs for the model galaxies are bypassed.

All the results are based on a single 512^3 PINOCCHIO run of a 200 Mpc box ($h = 0.7$) with the standard cosmology given in Section 4.1.10. The mass resolution is $2.4 \times 10^9 M_\odot$; then the smallest halo considered contains 50

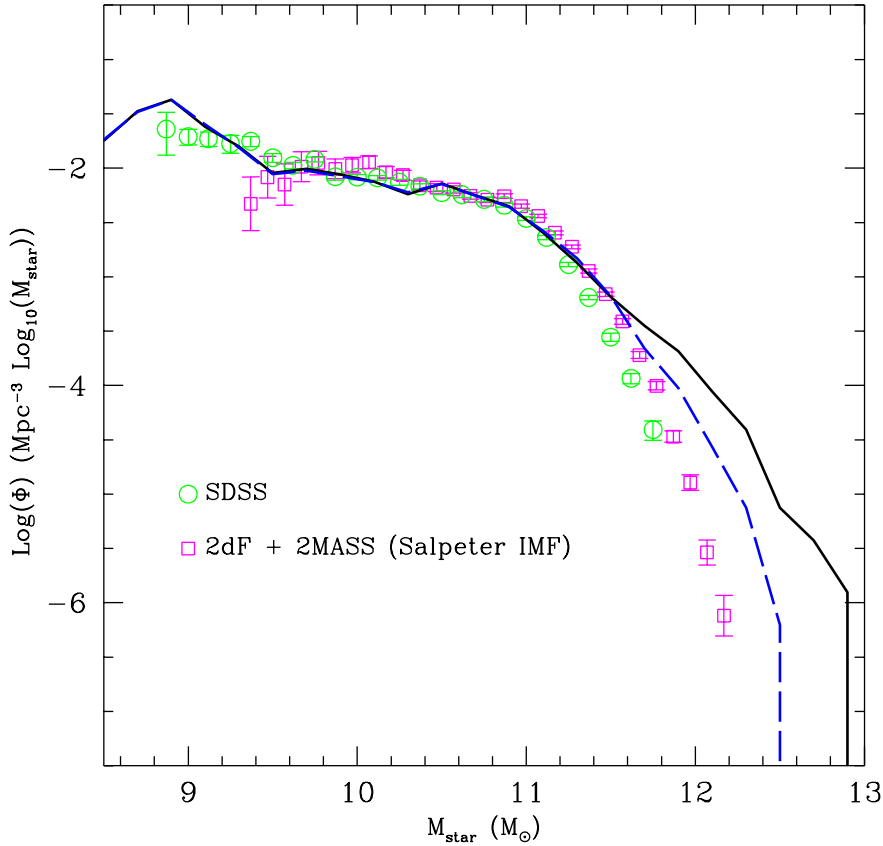


Figure 4.6: Star mass function of galaxies at $z = 0$, compared with the results of SDSS (Bell et al., 2003) and 2dF+2MASS (Cole et al., 2001).

particles, for a mass of $1.2 \times 10^{11} M_{\odot}$, while the branch ends of the merger trees start at a mass of $2.1 \times 10^{10} M_{\odot}$. We find that the stellar mass of the typical galaxy contained in the smallest DM halos at $z = 0$ is $\sim 10^9 M_{\odot}$, so the star mass function is severely incomplete at smaller masses. To limit the size of the output and the computing time, the mass function of DM halos is sampled by picking no more than 100 halos per mass bin of 0.5 dex (or all halos in the bin if they are less than 100). The statistical distributions of galaxies are then computed by weighting each galaxy by the inverse of the fraction of the corresponding DM halos picked up in the mass bin. For each DM halo all galaxies and satellites are computed, so that for a given star mass the satellites of large DM halos are oversampled with respect to the central galaxies, which are numerically dominant at each bin. This feature is corrected for by the weighting scheme (satellites that belong to rarer and well-sampled halos are weighted much less than central galaxies of similar stellar mass, that belong to smaller and more sparsely sampled DM halos) but shows up when galaxy properties are reported in a scatterplot, like in the Tully-Fisher relation. In such cases we further sparse-sample the satellites according to the relative weights of the DM halo they belong to and the DM halo that gives a central

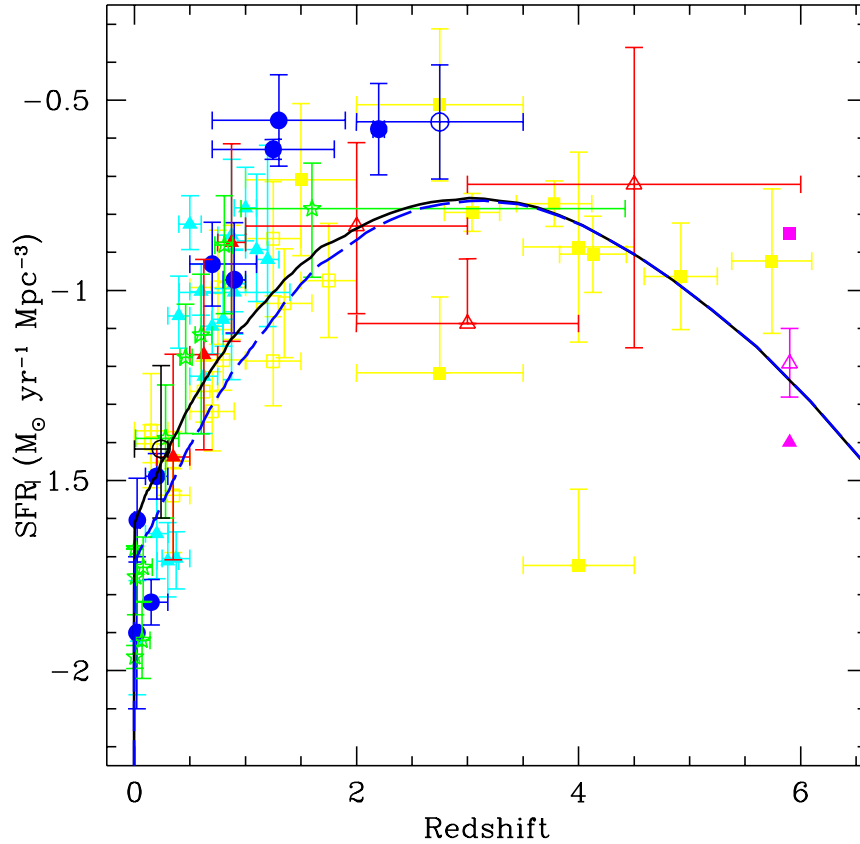


Figure 4.7: Star formation rate density as a function of redshift, compared with the data compiled and homogenized by Hopkins (2004).

galaxy of similar stellar mass. In this way we have a roughly constant number of galaxies per logarithmic interval of stellar mass; this will be explained in chapter 7.

Figure 4.5 gives, for each DM halo at $z = 0$, the fraction of baryons that are found in hot halo gas, in stars of all galaxies (but not in the halo), in stars of the central galaxy, and the fraction of baryons ejected by winds and not fallen back. These components clearly do not exhaust the list of baryonic components (halo stars and cold gas components are excluded here), so these fractions do not add up to one. However, this figure helps in showing a number of important features. There is a clear transition at a DM halo mass range of $10^{12} - 10^{13} M_{\odot}$: smaller halos lose most of their baryons by ejecting them to the IGM and their stellar content is dominated by the central galaxy, while larger halos retain most of their baryons as hot gas and have a small fraction of stars (~ 20 per cent) in the central galaxy. In both cases the fraction of stars (both total and in the central galaxy) declines quickly with increasing or decreasing mass, while a clear maximum is reached at $10^{12} M_{\odot}$. All these features reproduce nicely the trends suggested in the seminal papers of galaxy formation (see, for instance, White & Rees 1978 or Dekel & Silk 1984): small

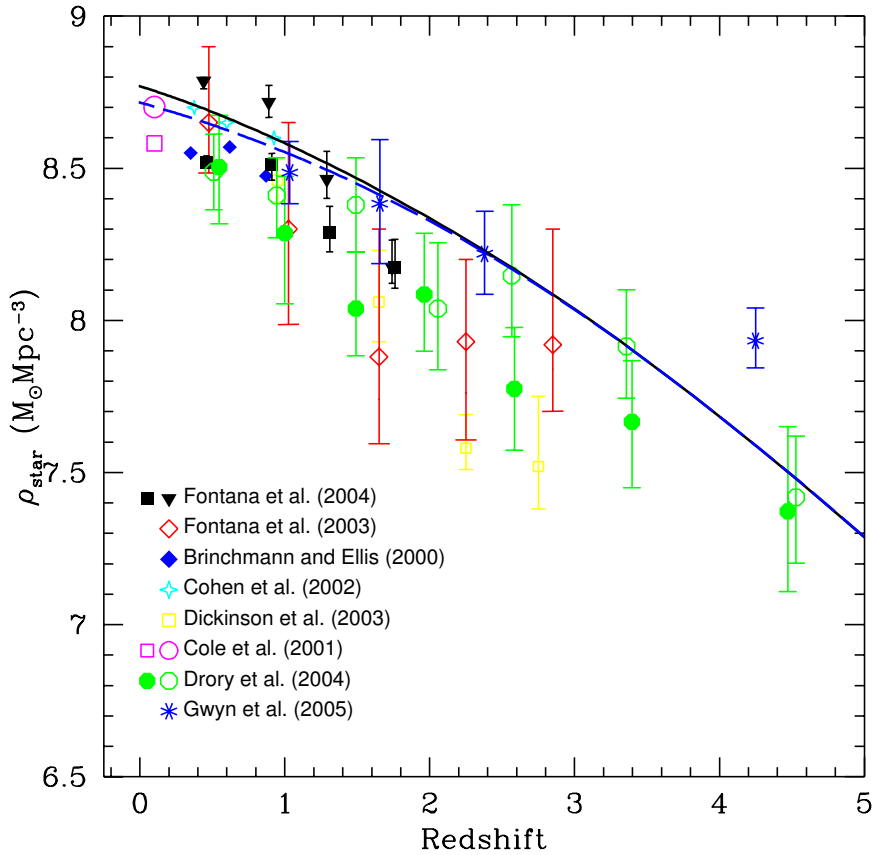


Figure 4.8: Star mass density as a function of redshift. Data are taken from Fontana et al. (2003, 2004), Brinchmann & Ellis (2000), Cohen et al. (2002), Dickinson et al. (2003), Cole et al. (2001), Drory et al. (2004), Gwyn et al. (2005).

halos are evacuated by winds driven by SNe, while in large halos the large cooling time (aided by AGN feedback) prevents most gas from cooling. As a further element, the presence of many Milky Way-sized halos with almost no hot gas, in nice agreement with the lack of X-ray emitting around our Galaxy, is worth noticing.

The trends of decreasing efficiency of star formation in smaller and larger halos than $10^{12} M_{\odot}$ are needed to produce the observed low-luminosity slope and high-luminosity cutoff of the galaxy LFs. Figure 4.6 shows the predicted star mass function of galaxies, compared with the data by SDSS (Bell et al., 2003) and 2dF (Cole et al., 2001; 2dF data are combined with 2MASS observations) surveys. The low-mass slope is nicely reproduced, even in the slight steepening below $10^{10} M_{\odot}$. However, the high-mass cutoff is not strong enough, and the biggest ellipticals are too massive. AGN feedback helps in decreasing the mass of the most massive ellipticals by roughly a factor of two, but this is not enough to solve the problem. The “forced quenching” procedure mutated from Bower et al. (2005) and explained in Section 4.8.2 can lead to a much more drastic quenching of the cooling flow; the resulting stellar mass

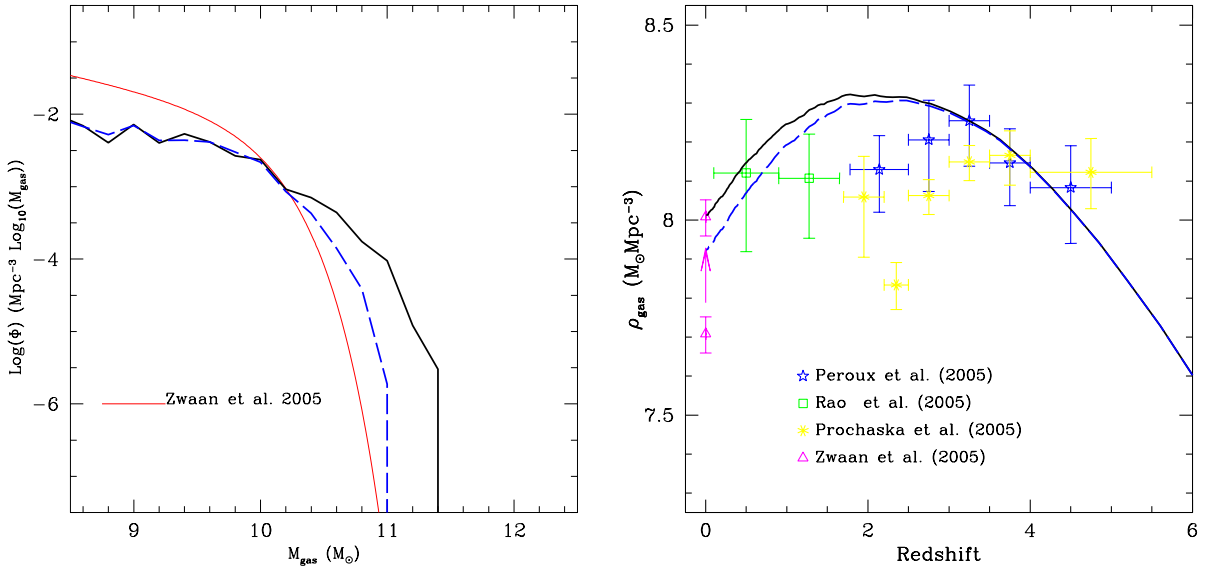


Figure 4.9: Left panel: mass function of cold gas, compared to the HIPASS data by Zwaan et al. (2005). Right panel: evolution of the cold gas density, compared to the HIPASS point and to estimates from DLAs (Prochaska et al. 2004; Peroux et al. 2005; Rao et al., 2005). The ratio between HI and total cold gas mass is assumed to be 1/2 (see the text for details).

function is shown in the figure as a dashed line. Figure 4.6 shows also the stellar mass function of discs and bulges. A very similar result is obtained by dividing the sample in disc- and bulge-dominated galaxies (where domination refers to stellar mass). In line with what is observed, bulges dominate at large masses, while discs are more abundant at small masses.

Figure 4.7 shows the prediction of the star formation rate density as a function of redshift. The data have been collected and homogenized by Hopkins (2004). The prediction fits well the data, with some underestimate at $z \sim 1$, epoch in which the contribution of small galaxies is significant. In particular, the peak of star formation is predicted to be at $z \sim 3$, in agreement with the estimates based on sub-mm counts. The level of star formation is still high at $z \sim 6$, only a factor of 2.5 lower than the peak value. In the redshift range $0 < z < 1$ the decline is shallower than the data suggest, and this is connected with the incomplete quenching of cooling flows. Most of this star formation takes place in discs, triggered by the strong cooling flows at high redshift more than to mergings (we will deepen this point in sec. 7.3.2, fig. 7.8). Figure 4.8 shows the density of stellar mass as a function of redshift. Though this quantity is related to the cosmic star formation rate (it is simply its integral in time), it is compared with a completely different set of data (see e.g. Fontana et al., 2004 and the caption of fig. 4.8). The agreement is again good from $z \sim 4$ to 0, with some overestimate at small redshift due to the mass excess of massive ellipticals.

Figure 4.9 shows the prediction of the mass function of HI at $z = 0$,

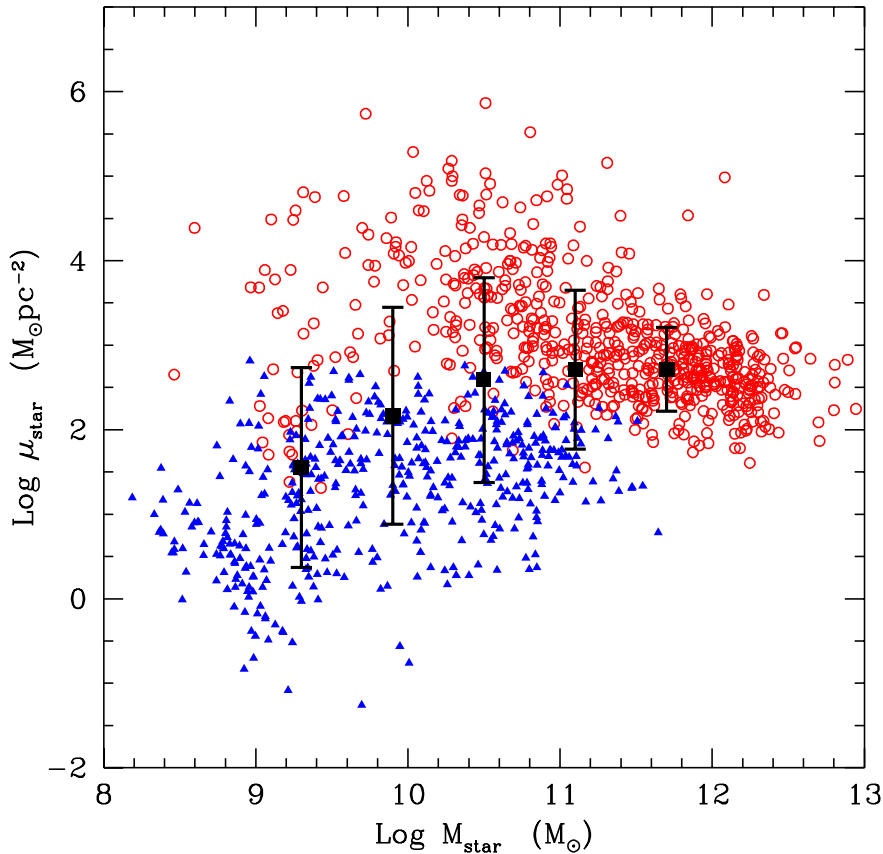


Figure 4.10: Mass versus surface density for disc- and bulge-dominated galaxies.

compared to the HIPASS data (Zwaan et al., 2005), and the evolution of the cold gas density, compared to the data from DLA systems (Prochaska et al. 2004; Peroux et al. 2005; Rao et al., 2005). Following the suggestion of Fukugita & Peebles (2004), to the $(3.5 \pm 0.8) \times 10^{-4}$ value of Ω_{HI} we add a contribution $(1.6 \pm 0.4) \times 10^{-4}$ of H_2 , and multiply the result by 1.38 to take helium into account. This amounts to multiplying the HI values by a factor of two or, equivalently, to divide the cold gas mass by a factor of two to predict the HI mass. Both from the $z = 0$ gas mass function and from the DLA data there is an indication of a lack of cold gas in the model, which is however related to gas masses lower than $10^{10} M_{\odot}$, where the mass resolution is important. Moreover, the slight overestimate of the large-mass cutoff is clearly related to the lack of proper quenching of the cooling flow.

Figure 4.10 shows the galaxies in the stellar mass–surface density plane. Spiral discs and bulges tend to occupy different regions of the plane; the scatter is however so strong that, as observed, no clear bimodality emerges from the distribution of these galaxies. A decrease of the surface brightness at masses $< 10^{10} M_{\odot}$ is obtained, in agreement with the SDSS data of Kauffmann et al. (2003).

Figure 4.11 shows the surface densities of cold gas versus star formation rate

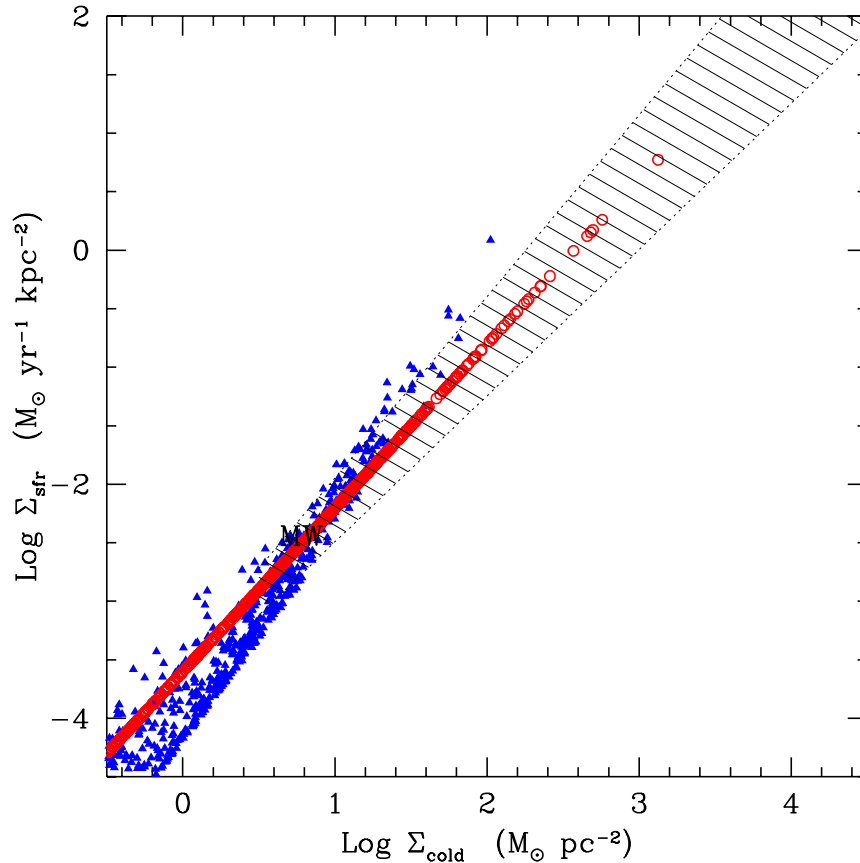


Figure 4.11: Schmidt-Kennicutt law for the model disc components. The shaded area gives the average relation obtained by Kennicutt (1998); the error refers to the mean, not to the observed scatter.

for disc and bulge galaxies, compared to the Schmidt-Kennicutt law (Kennicutt 1998). Discs show a slightly steeper relation (at the $2-\sigma$ level), which however is observationally determined by adding the starbursts at higher Σ_{cold} values. Also, the showed model galaxies over-sample the population of bright objects with lower gas fractions, and this bias steepens the predicted relation. Given the observational errors quoted by Kennicutt (1989), we conclude that there is a very good agreement between data and prediction, even in terms of the scatter of the discs around the average relation.

Figure 4.12 shows the predicted Tully-Fisher relation of disc-dominated galaxies. There is a tail of compact and rapidly spinning outliers that correspond to rather compact discs whose DM halos merge with a much larger one. These discs burn their gas slowly and are found as compact, old, gas poor galaxies in groups or clusters at $z = 0$. These objects are unlikely to be recognized as spirals. When we remove objects with a gas fraction lower than 0.1 per cent, most of these outliers are removed. Notably, galaxies follow the same Tully-Fisher relation independently of their surface brightness.

Figure 4.13 shows the elliptical galaxies in the stellar mass- R_B plane,

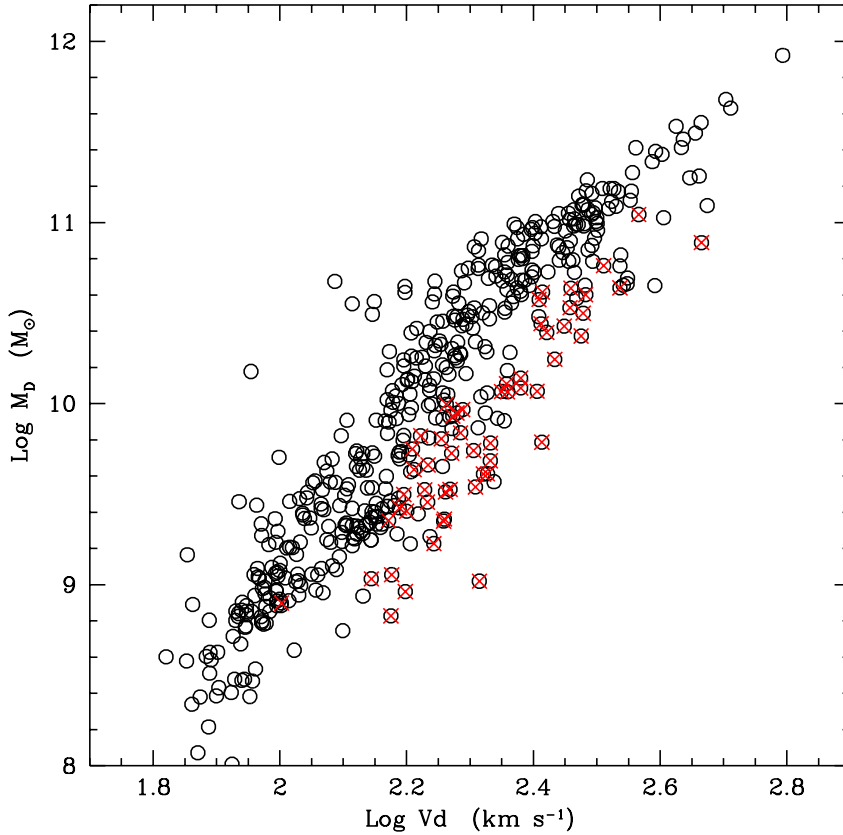


Figure 4.12: Baryonic Tully-Fisher relation for central, disc-dominated galaxies at $z = 0$.

compared to the observed relation obtained from the data of Marconi & Hunt (2004, see also Chapter 5). The data lie nicely within the observed range, with some overestimate at large masses which is again connected to the lack of quenching of cooling flows. We do not show a prediction of the fundamental plane, because the virial theorem is implicit in our relation between mass, radius and velocity dispersion, and the computation of \mathcal{M}/\mathcal{L} ratios need a spectro-photometric code to be computed.

Figure 4.14 shows the predicted metallicity of discs, bulges and hot halo gas. Elliptical galaxies show a mass-metallicity relation that steepens considerably at masses smaller than $11^{10} M_{\odot}$. Spirals show a similar though weaker trend. The hot halo gas of galaxy clusters is enriched to a level of roughly $Z_{\odot}/3$, raising to solar values for groups; this is in agreement with the observed trends (see e.g., Baumgartner et al. 2005). Galactic-sized halos are devoided of hot gas, whose metallicity is dominated by scatter.

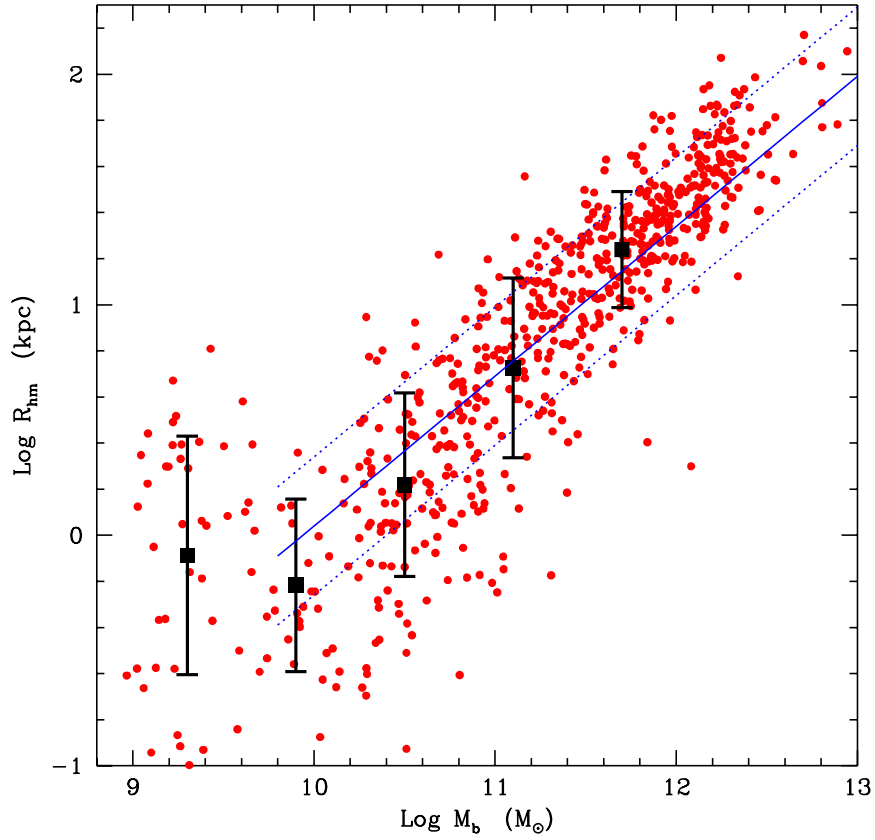


Figure 4.13: Structure of elliptical galaxies; data are obtained from Marconi & Hunt (2004).

4.12 Conclusions

In this chapter we have presented and described in detail the code GALRISE for the formation and evolution of galaxies and AGN. The main differences between GALRISE and the other models mentioned above are the following: (i) the evolution of the various components and phases of a galaxy is followed by integrating a differential system of equations along each branch of a merger tree, thus allowing for the most general (and non-linear) set of equations for mass and energy flows; (ii) in each galaxy component (halo, bulge, disc) the gas is modeled as two-phase; (iii) the evolution of the thermal and kinetic energies of the hot and cold phases is taken into account; (iv) the halo gas components (hot gas, cooling flow, halo stars) are described by a simple model that treats cooling and infall as separated processes, takes into account the mass and energy injection by galaxy winds and allows for galactic superwinds; (v) feedback and star formation are inserted following the results of the model by Monaco (2004a,b), plus an additional prescription for kinetic feedback; (vi) accretion onto BHs and its feedback onto the galaxy are built-in. This increased level of sophistication allows to move from a phenomenological

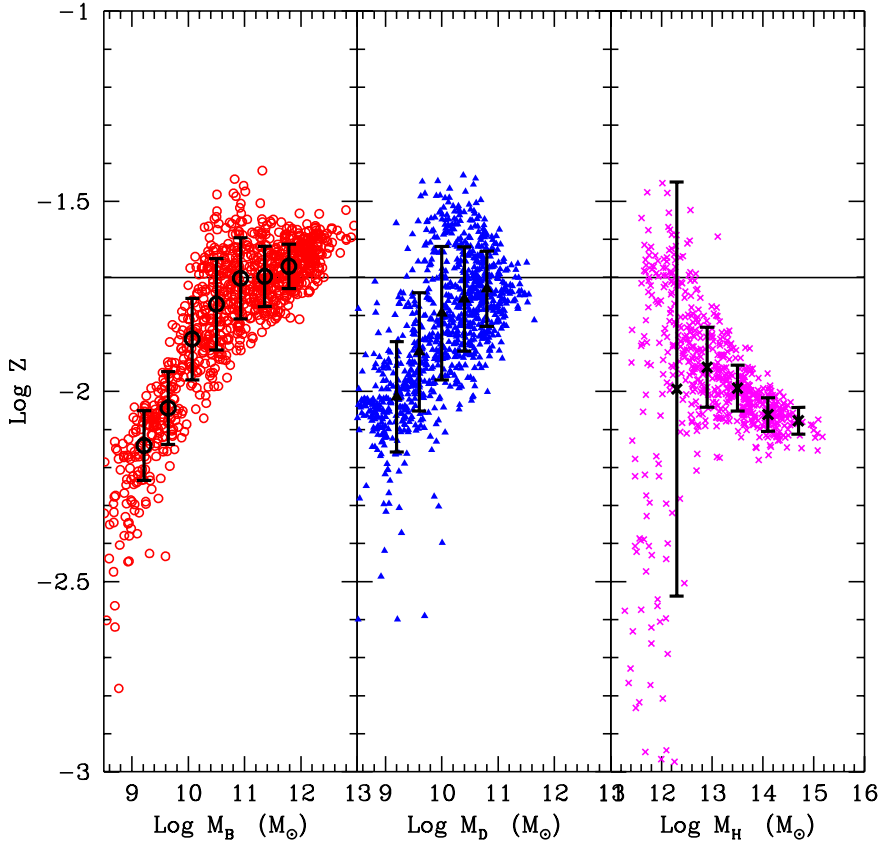


Figure 4.14: Metal content of discs, bulges and hot halo gas.

description of gas physics (especially of feedback), based on simple scalings with the depth of the DM halo potential, toward a physically motivated one. The numerical integration of the mass and energy flows allows a much wider set of physical processes to be implemented, but implies a significant slow-down of the code, which however is still so quick that the computation of the SEDs is the real bottleneck of the computation. Another drawback is the arising of numerical instabilities in the integration, so that much care is needed in including the recipes.

The multi-phase nature of GALRISE is exploited only partially. However, the ability of disentangling the hot halo gas from the cooling flow is to our understanding one of the reasons for the success in predicting the early assembly of massive galaxies. Indeed, the cold halo gas, having a much lower covering factor, will intercept only a small fraction of the feedback energy coming from the hot galactic wind; it will be reheated only after falling onto the galaxy and taking part to the star formation process. With respect to treating this gas as still hot (and then subject to feedback), this gives much stronger cooling flows in high-redshift, infall-dominated halos.

The model for the hot gas components, as well as the model for feedback and star formation (based on the results of the physical model of Monaco 2004),

are not based on completely phenomenological recipes, like power-law scalings with the circular velocity of the halo, but on a more detailed description of the multi-phase ISM and ICM. Then, GALRISE can be seen as an attempt to go from a “phenomenological” to a “simplified” description of the physics of galaxy formation. As an example of the advantage of a more physical picture of feedback, we mention the role of kinetic feedback in star-forming bulges, which we propose in chapter 6 as the base to understand the observed downsizing of the AGN population. However, the attempt to go beyond a phenomenological level is still incomplete; for instance, the time-scale for star formation in bulges is taken from the observed Schmidt law.

Despite the significant technical differences with the competitor models, the predictions of GALRISE at $z = 0$ are very well in line with the others. For instance, before the long procedure of optimization and refinement of the model was concluded, the resulting stellar mass function was a bit too steep, low at the knee, and with a weak cutoff, very similar to most competitor models. Similarly, most of the figures shown in Section 4.11, which will be no surprise-predictive power still to come even at a qualitative level for most cosmologists. A qualitative comparison of our results with the N-body ones of Borgani et al. (2004), obtained with a GADGET2 code (Springel et al. 2001), has shown in many cases the same qualitative trends, as for instance the formation of too massive ellipticals in clusters and the inability of stripping to produce a sufficient number of halo stars. This implies that the field is reaching an interesting level of maturity, so that an increase in the level of sophistication in these models is justified.

We do not regard this model as a “theory of everything” for galaxies, but simply as a powerful tool to understand the complex nature of galaxies and to bridge in a realistic way the physical processes in play with the observations that can constrain them. It is then important to focus on the discrepancies with observations, and to the insights on the physical processes that they provide. It is very hard for us to reproduce the exponential cut of the luminosity function, even when AGN feedback is included, and this relates to the poor level of understanding of why cooling flows are quenched. This is in line with Benson et al. (2003) etc. When we apply a forced quenching procedure to quench the cooling flow, as the one proposed by Bower et al. (2005), we almost recover the exponential cut without compromising our predictions on many other observables. This implies that the discrepancy between model and data is recognized and isolated, but a complete self-consistent solution is still to be found.

Another discrepancy arises in the mass function of cold gas; our small galaxies have the right amount of stars but a smaller amount of gas. This is also connected to the mass resolution of the DM halo merger trees. In any case, the fraction of cold gas in such small galaxies depends on many details, the most important of which is the effect of the external UV field, that can prevent the outer regions of low surface brightness galaxies to form stars (Efstathiou 1992; Babul & Rees 1992; Schaye 2004). A modeling of this effect is probably necessary to reproduce the properties of small galaxies.

The formation of galaxy discs is based on the (reasonable but still not demonstrated) assumptions of conservation of angular momentum and exponential discs, neglecting important problems as the distribution of angular momentum within the DM halos, Another issue concerns the shape of the DM halo, which we assume to be NFW, which is at variance with what observers suggest (see, e.g., Gentile et al., 2004). Clearly much more detailed modeling is desired. Given the complexity of this topic, it is very remarkable that the observed Tully-Fisher relation is roughly reproduced under the simplest assumptions.

Table 4.2: Model parameters, with their reference value, brief description, kind of constraint available for the parameter and reference in the text. Parameters marked by a “!” are of primary importance. Cosmological parameters are not included.

| Name | ref. value | Comment | Constraint | Equation/Section |
|------------------------------------|-----------------------------|--|-----------------|------------------|
| mergers | | | | |
| f_{hmm} | 0.2 | major merger condition for DM halos | N-body | eq. 4.13 |
| f_{gmm} | 0.3 | major merger condition for galaxies | N-body | eq. 4.14 |
| f/c | 2.0 | bulge formation in mergers/disc instabilities | N-body | eq. 4.48 |
| ! f_{scatter} | 0.1 | fraction of stars scattered at a galaxy major merger | N-body | sect. 4.3.3 |
| halo component | | | | |
| ! γ_p | 1.1 | polytropic index of the hot gas | free | eq. 4.16 |
| ! f_{shock} | 1.2 | shock heating factor | N-body | eqs. 4.22, 4.23 |
| ! heat cold gas | YES | switch for heating cold halo gas at major mergers | N-body | sect. 4.4.2 |
| ! n_{quench} | 1 | no. of crossing times for quenching cooling | free | sect. 4.4.3 |
| ! close hole | NO | switch for closing the cooling hole | free | eq. 4.32 |
| ! infall on bulge | YES | switch for allowing infall on the bulge | free | eq. 4.38 |
| ! n_{dyn} | 1.5 | no. of dynamical times for infall | free | eq. 4.33 |
| f_{wind} | 2 | energy factor to trigger a super-wind | eqs. 4.39, 4.42 | |
| f_{back} | 0.5 | fraction of super-wind mass that falls back | free | sect. 4.4.5 |
| disc structure | | | | |
| ϵ_{lim} | 0.9 | limit for bar instability | N-body | eq. 1.96 |
| f_{bar} | 0.5 | fraction of disc that goes to bulge | free | sect. 4.5.2 |
| stars and metals | | | | |
| $M_{\star, \text{SN}}$ | 120 M_{\odot} | star mass per SN | IMF | eq. 4.52 etc. |
| ! f_{rest} | 0.4 | fraction of restored mass | IMF | eqs. 4.58, 4.62 |
| ! Y | 0.03 | Yield per generation | (free) | eqs. 4.73, 4.74 |
| Z_{pre} | 10^{-6} | pre-enrichment | free | sect. 4.7 |
| ! f_{Zej} | 0.5 | fraction of metals ejected to halo | free | eq. 4.73 |
| star formation and feedback | | | | |
| ! $f_{\text{th,D}}$ | 0.6 | thermal efficiency of feedback in thin systems | free | eq. 4.59 |
| ! $f_{\text{th,B}}$ | 0.5 | thermal efficiency of feedback in thick systems | free | eq. 4.65 |
| ! f_{kin} | 0 | kinetic energy from hot winds | free | eqs. 4.60, 4.66 |
| ! σ_0 | 80 km s^{-1} | turbulent velocity of clouds | free | eq. 4.54 |
| ! Σ_{limit} | ∞ | critical gas surface density for discs | free | eq. 4.49 |
| ! hot kin. fb | YES | switch for giving kinetic feedback to the hot wind | free | eqs. 4.70, 4.71 |
| AGN | | | | |
| M_{seed} | 1000 M_{\odot} | seed black hole mass | theory | sect. 4.8.1 |
| ! f_{lowJ} | 0.003 | rate of loss of angular momentum | free | eq. 4.75 |
| ! $f_{\text{jet},0}$ | 1 | efficiency of jet feedback for a 1000 km s^{-1} halo | N-body | eq. 4.78 |
| numerical parameters | | | | |
| ! M_{part} | $2.4 \times 10^9 M_{\odot}$ | particle mass | — | — |
| f_{cdisc} | 0 | fraction of gas in disc in the ICs | free | sect. 4.1.9 |
| Δ_t | 0.1 Gyr | numerical interval for the integration | free | sect. 4.1.3 |

Chapter 5

Feedback from Quasars in Star-forming Galaxies and the triggering of Massive Galactic Winds

¹We saw in the previous sections that AGNs are intimately connected to the spheroidal components of galaxies. There are several pieces of evidence pointing to a connection between the formation of the two classes of objects. Among them we consider (i) the well defined correlation between the mass of the dormant black holes hosted in ellipticals and spiral bulges and their mass or central velocity dispersion (sec. 2.3 and fig. 2.5), (ii) the fact that the mass function of these black holes is found to be consistent with that inferred from the accretion history of quasars (sec. 2.3) and (iii) the observational evidence that at higher redshift, quasars and radio galaxies are systematically found to be hosted at the centers of elliptical galaxies (see, e.g., Dunlop et al. 2003).

Many authors have proposed that feedback from the quasar could self-limit the bulge and black hole masses, forcing them to be proportional (see, e.g., Ciotti & Ostriker 1997; Silk & Rees 1998; Haehnelt, Natarajan & Rees 1998; Fabian 1999; Murray, Quataert & Thompson, 2005). The dynamical importance of feedback is confirmed by N-body hydro simulations (see, e.g., Springel, Di Matteo & Hernquist 2004). As we pointed out in 1.5.1 many galaxy formation models based on hierarchical clustering are also successful in predicting the quasar–bulge connection, even in absence of an explicit self-limiting mechanism, by assuming simply that some fraction of cold bulge gas is accreted onto the black hole (Kauffmann & Haehnelt 2000; Cattaneo 2001; Cavaliere & Vittorini 2002; Hatziminaoglou et al. 2003; Mahmood, Devriendt & Silk 2004; Bromley, Somerville & Fabian 2004). However, the level of alpha-enhancement of stars in ellipticals is difficult to obtain in this framework (Thomas, 1999). On the other hand elliptical galaxies, a homogeneous class of old, metal-rich, alpha-enhanced stellar populations with little ISM, have

¹The results presented in this chapter have been published in Monaco & Fontanot (2005).

longly been supposed to form through a quick burst of star formation followed by a strong wind, able to wipe the galaxy out of its ISM and to expel metals (especially iron) to the inter-cluster medium (ICM) (see, e.g., Renzini 2004). To reproduce the correlation between stellar mass and the level of alpha enhancement, this wind must halt star formation earlier in more massive galaxies (sec. 1.5.1 and 1.5.1).

The energy budget of an accreting black hole radiating with an efficiency $\eta = 0.1$ amounts to $\eta M_{\bullet} c^2 \simeq 1.8 \times 10^{61} (M_{\bullet}/10^8 M_{\odot})$ erg. A $M_{\bullet} \simeq 1.6 \times 10^8 M_{\odot}$ black hole, which radiates 2.9×10^{61} erg during his life, is typically hosted by a $M_{\text{bul}} \simeq 10^{11} M_{\odot}$ bulge (see, e.g., Shankar et al. 2004). The binding energy of such a bulge (with velocity dispersion $\sigma \simeq 200 \text{ km s}^{-1}$) is of order $M_{\text{bul}} \sigma^2 \simeq 8.0 \times 10^{58} M_{\text{bul},11} \sigma_{200}^2$ erg (here $M_{\text{bul},11} = M_{\text{bul}}/10^{11} M_{\odot}$ and $\sigma_{200} = \sigma/200 \text{ km s}^{-1}$). It suffices then to inject ~ 0.3 per cent of the energy budget into the ISM of a forming galaxy to influence it strongly, e.g. to trigger a strong wind able to remove most ISM from the galaxy.

The mechanism responsible for this injection of energy is however unclear. In fact, a great part of the energy is emitted as UV-X radiation. Following Begelman (2004), a relatively hard UV-X source can affect the ISM by two main processes. The first is radiation pressure, exerted especially on dust grains, that can push matter in the radial direction. However, its efficiency in accelerating matter is of order v/c , where v is the bulk velocity of the gas in the radial direction. Its effectiveness in creating bulk motions of gas is then restricted to the neighborhood of the central engine, where the r^{-2} dependence makes it very strong, thus compensating for the very low initial v/c . Recently, Murray et al. (2005) proposed that radiation pressure alone can drive a rather robust wind, able to remove some 10 per cent of the matter out of a bulge. This is true if the whole ISM is optically thick to radiation; we will come back to this point in Section 3.

Radiation pressure is also a good candidate for causing the strong outflows seen in Broad Absorption Line (BAL) quasars. These objects, relatively rare at the peak of quasar activity but rather common at high redshift (see, e.g., Maiolino et al. 2003), show outflows along the line of sight with velocity up to $\sim 0.1c$. The kinetic energy associated to these outflows is likely high; however, energy budget and effectiveness in triggering a galaxy-wide wind depend sensitively on the covering factor of the expelled gas. BAL quasars could correspond to a particular stage in which the quasar emits a very strong wind with a high covering factor; this stage should last much less than an Eddington time ($t_{\text{ed}} \simeq 4 \times 10^7$ yr for $\eta = 0.1$). Such an outflow would be effective in removing most ISM from the host galaxy (see, e.g., Granato et al. 2004). If instead BAL quasars correspond to rather common, low covering factor events, their ejection will most likely trigger star formation (similarly to what happens in radio galaxies, where radio jets are aligned with star-forming regions) more than quenching it by removing all the ISM.

Radiative heating is the second mechanism. Quasars emit UV-X light with a relatively hard spectrum, corresponding to inverse Compton temperatures of order $T_{\text{IC}} \simeq 2 \times 10^7$ K (see Sazonov, Ostriker & Sunyaev 2004b). Assuming

thermal equilibrium in presence of this heating source, cold gas will be partially or totally heated to a temperature $\sim T_{\text{IC}}$ if radiation pressure is important with respect to the thermal one of the ISM (Krolik, McKee & Tarter 1981; Begelman, McKee & Shields 1983). Begelman (1985) estimated that such ablation could evacuate the inner region of Seyfert galaxies. Moreover, radiation pressure can accelerate cold clouds to some 100 km s^{-1} . In a typical star-forming spheroid, whose ISM is likely characterized by a high thermal pressure, radiative heating will perturb the ISM in the inner region of the galaxy, but taken alone it will not be able to cause a massive wind. Sazonov et al. (2004a) computed the effect of such heating on the ISM of a forming spheroid; in their calculation a wind is triggered when the fraction of old gas to total baryons is ≤ 1 per cent, and star formation is almost over. As a result, the amount of ejected matter is modest.

The radiation pressure of a black hole accreting at a rate \dot{M}_\bullet at a distance r is (assuming an efficiency $\eta = 0.1$ as above and expressing the pressure in terms of P/k , where k is the Boltzmann constant):

$$\frac{P_{\text{rad}}}{k} = \frac{L}{4\pi r^2 ck} \simeq 4.4 \times 10^7 \left(\frac{\dot{M}_\bullet}{4 M_\odot \text{ yr}^{-1}} \right) \left(\frac{r}{1 \text{ kpc}} \right)^{-2} \text{ K cm}^{-3}. \quad (5.1)$$

This relation is calibrated on the Eddington accretion rate ($4 M_\odot \text{ yr}^{-1}$) of a $1.6 \times 10^8 M_\odot$ black hole hosted in a $10^{11} M_\odot$ bulge. For a star-forming spheroid the thermal pressure P_{th}/k can be as high as $10^5 - 10^6 \text{ K cm}^{-3}$ (see Section 2). The limit for the existence of a hot phase subject to runaway heating is $P_{\text{rad}}/P_{\text{th}} \geq 7 - 27$ (Begelman et al. 1983). This is valid for plain inverse-Compton heating; heating by metal line absorption is very likely to contribute significantly (Ostriker & Ciotti 2004). Taking a condition $P_{\text{rad}} \geq 10P_{\text{th}}$, runaway heating will be effective within a radius:

$$R_{\text{th}} = 2.1 \left(\frac{\dot{M}_\bullet}{4 M_\odot \text{ yr}^{-1}} \right)^{1/2} \left(\frac{P_{\text{th}}/k}{10^6 \text{ K cm}^{-3}} \right)^{-1/2} \text{ kpc}. \quad (5.2)$$

This radius is of the same order of magnitude as the limiting radii reported by Sazonov et al. (2004a).

An element that has not been considered in the literature is that the perturbation induced by radiative heating will influence the way in which feedback from SNe works. In particular, radiation pressure can be very efficient in driving a massive wind if some other mechanism is able to generate a reasonably fast, optically thick outflow with a high covering factor. This can be provided by the percolation of many SN remnants in the so-called Pressure-Driven Snowplough (PDS) phase, that takes place after part of the internal hot gas of the remnant has cooled and collapsed into a dense, cold shell (called “snowplough”, see, e.g., Ostriker & McKee 1988). In a recent work Monaco (2004a) presented a model for feedback in galaxy formation. We introduce this model in 1.3.2. We show in this chapter that the insertion of a physically motivated evaporation term induced by the quasar leads very naturally (and without any tuning of the parameters) to a critical change of the feedback

regime that causes, through the percolation of snowploughs, the creation of an optically thick super-shell that expands out of the galaxy at a speed of $\sim 200 \text{ km s}^{-1}$. Such a shell, pushed by radiation pressure, can be ejected out of a large spheroid, quenching star formation and leaving behind a hot rarefied bubble. This mechanism can lead to a self-regulated black hole–bulge relation very similar to the observed one.

As mentioned above, the black hole–bulge relation can be generated simply by the mechanism responsible for the nearly complete loss of angular momentum, necessary to the gas to be able to accrete onto the black hole. A good fit is obtained if the accumulation of a reservoir of low-angular momentum gas proceeds at a rate proportional to the star formation rate in the bulge, or equivalently if a fraction of the cold bulge gas is systematically put into this reservoir. To assess the actual importance of winds in hierarchical galaxy formation, we insert a motivated wind criterion into a new galaxy formation model (that follow loosely the steps of commonly used “semi-analytic” models), and show with an example under which conditions the black hole mass is self-limited by winds more that determined by the reservoir mechanism.

In this chapter we will present a new model taking into account the effect the introduction of a physically motivated QSO evaporation term and we will discuss under which physical conditions such model leads to the triggering of a galactic wind. Then we will introduce quasar-triggered winds in our galaxy formation model.

5.1 The model for feedback

We give here a more detailed description (with respect to 1.3.2) of the model for feedback presented in Monaco (2004a); please refer to that paper for all details, and for a complete discussion of all the hypotheses.

Consider a volume V filled with a two-phase ISM, made up by a pervasive hot phase, of density and temperature n_h and T_h , and a distribution of cold clouds, of density and temperature n_c and T_c . Pressure equilibrium is assumed, so that $n_h T_h = n_c T_c$. Fixing the cold phase temperature to $T_c = 100 \text{ K}$, it is very easy to express the filling factors of the two phases in terms of their temperatures and mass fraction (equation 2 of Monaco, 2004a).

Cold clouds are assumed to have a power-law mass function, $n(m_{\text{cl}}) dm_{\text{cl}} \propto m_{\text{cl}}^{-\alpha_{\text{cl}}} dm_{\text{cl}}$. The parameter α_{cl} is set here for simplicity to -2 , the expected value for a typical fractal distribution (Elmegreen 2002). The range of allowed masses is bounded below by a mass $m_l = 0.1 M_\odot$, and above by a mass m_u . The upper bound is fixed as follows: all clouds more massive than the Jeans mass m_J (that takes into account the non-sphericity of clouds, see Lombardi & Bertin 2001) collapse in a dynamical time t_{dyn} , form stars and are finally destroyed within another t_{dyn} . During the $\sim 2t_{\text{dyn}}$ period they acquire mass through unelastic collisions with smaller clouds, up to a mass m_u , computed with the aid of the Smoluchowski equation of kinetic aggregations. The fraction f_{coll} of cold gas involved in the star formation process is then equal to the fraction of mass in clouds with $m_J \leq m_{\text{cl}} \leq m_u$.

A fraction $f_\star=0.1$ of the collapsing cloud is transformed into stars. Monaco (2004b) showed that, due to the multi-phase nature of the ISM, the explosion of SNe leads to the destruction of the star-forming cloud in ~ 3 Myr, leading to a modest loss of ~ 5 per cent of the energy budget. SN remnants percolate very soon, creating a single SB for each forming cloud. The SBs expand according to the solution of Weaver et al (1977); they propagate into the hot pervasive phase, their (modest) interaction with the cold clouds is neglected. As we already said in 1.3.2 the fate of SBs depends on the vertical scale-length of the system they belong to: four different self-regulated feedback regimes can arise, depending on whether the SBs end by blow-out or pressure confinement, before or after the PDS stage starts. While blow-out in the PDS stage is not common, blow-out in the adiabatic stage is the typical feedback regime in galaxy discs.

In the following we concentrate on thick systems. In the adiabatic confinement regime, the details of the SB evolution are not important, as all the energy that manages to escape the star-forming cloud is given to the hot phase.

The system considered in Monaco (2004a) is composed by cold and hot gas phases, stars and an external halo (a passive reservoir of gas). Cold gas flows into the volume from the external halo on some specified infall time t_{inf} :

$$\dot{M}_{\text{inf}} = \frac{M_{\text{halo}}}{t_{\text{inf}}}. \quad (5.3)$$

Star formation proceeds at a rate:

$$\dot{M}_{\text{sf}} = f_\star f_{\text{coll}} \frac{M_{\text{cold}}}{t_{\text{dyn}}}, \quad (5.4)$$

and enriched gas is restored from dying stars (in an instantaneous recycling approximation) at a rate:

$$\dot{M}_{\text{rest}} = f_{\text{rest}} \dot{M}_{\text{sf}}, \quad (5.5)$$

where f_{rest} is the fraction of restored mass (assumed here to be 0.2). Besides, a fraction $f_{\text{evap}}=0.1$ of the star-forming cloud is evaporated by HII regions and SNe (see Monaco 2004b), giving origin to an evaporation flow:

$$\dot{M}_{\text{evap}} = f_{\text{evap}} f_{\text{coll}} \frac{M_{\text{cold}}}{t_{\text{dyn}}}. \quad (5.6)$$

The hot phase cools at a rate:

$$\dot{M}_{\text{cool}} = f_{\text{cool}} \frac{M_{\text{hot}}}{t_{\text{cool}}}, \quad (5.7)$$

where the cooling time t_{cool} is computed using the simple approximation proposed by Cioffi, McKee & Bertschinger (1988) and $f_{\text{cool}}=0.1$ is a parameter that regulates the passage from the hot to the cold phase (whose value depends on the complex density structure of the cooling gas). Finally, the hot phase

typically is not confined within the star-forming region (the volume V that contains the ISM), so it leaks out at a rate:

$$\dot{M}_{\text{leak}} = \frac{\dot{M}_{\text{hot}}}{t_{\text{leak}}}, \quad (5.8)$$

where the leaking time t_{leak} is the sound-crossing time of the structure.

The mass of the four components evolves according to this set of equations:

$$\begin{cases} \dot{M}_{\text{cold}} &= \dot{M}_{\text{inf}} + \dot{M}_{\text{cool}} - \dot{M}_{\text{sf}} - \dot{M}_{\text{evap}} \\ \dot{M}_{\text{hot}} &= -\dot{M}_{\text{cool}} - \dot{M}_{\text{leak}} + \dot{M}_{\text{evap}} + \dot{M}_{\text{rest}} \\ \dot{M}_{\star} &= \dot{M}_{\text{sf}} - \dot{M}_{\text{rest}} \\ \dot{M}_{\text{halo}} &= -\dot{M}_{\text{inf}} + \dot{M}_{\text{leak}} \end{cases} \quad (5.9)$$

An analogous system can be easily written for the metal flows.

The hot phase gains thermal energy from SNe (both through blasts and through the evaporated gas) at a rate:

$$\dot{E}_{\text{sn}} = E_{51} \frac{\dot{M}_{\text{sf}}}{M_{\star, \text{sn}}}, \quad (5.10)$$

where E_{51} is the energy of the single SN in units of 10^{51} erg (for simplicity we subtract from it any eventual loss due to the destruction of the star-forming cloud) and one SN progenitor is formed each $M_{\star, \text{sn}}$ of stars (we take $M_{\star, \text{sn}}=120 M_{\odot}$). Cooling and leak-out lead to energy losses at rates:

$$\dot{E}_{\text{cool}} = \frac{E_{\text{hot}}}{t_{\text{cool}}}, \quad (5.11)$$

$$\dot{E}_{\text{leak}} = \frac{E_{\text{hot}}}{t_{\text{leak}}}. \quad (5.12)$$

The evolution of the energy of the hot phase is then:

$$\dot{E}_{\text{hot}} = -\dot{E}_{\text{cool}} - \dot{E}_{\text{leak}} + \dot{E}_{\text{sn}}. \quad (5.13)$$

In case of PDS confinement, the \dot{E}_{sn} term must take into account the energy radiated away by the SB, while snowploughs generate a further mass flow \dot{M}_{snpl} from the hot to the cold phase, with the corresponding loss of thermal energy \dot{E}_{snpl} (see Monaco, 2004a, for details).

As an illustrative example we show the evolution of a “monolithic” spheroid of mass $10^{11} M_{\odot}$ and half-mass radius (used as vertical scale-length) $R_{\text{hm}} = 4.9 \text{ kpc}$. Its circular velocity at R_{rmhm} is 209 km s^{-1} , and its average density at the same radius is $0.1 M_{\odot} \text{ pc}^{-3}$. The infall time is assumed to be equal the dynamical time, $t_{\text{inf}}=2.5 \times 10^7 \text{ yr}$. Figure 5.1 shows the evolution of the four mass components, the main mass flows and the state of the ISM as a function of time. The cold gas accumulates quickly, but the efficient feedback prevents stars from forming as quickly. The ISM self-regulates to $P/k \sim 10^6 \text{ K cm}^{-3}$, $T_{\text{h}} \sim 2.5 \times 10^7 \text{ K}$, $n_{\text{h}} \sim 4 \times 10^{-2} \text{ cm}^{-3}$ and $n_{\text{c}} \sim 10^4$. Star formation regulates to a value of $\sim 50 M_{\odot} \text{ yr}^{-1}$, while infall and leak-out assume very similar values. Cooling is always negligible. Most importantly, the porosity

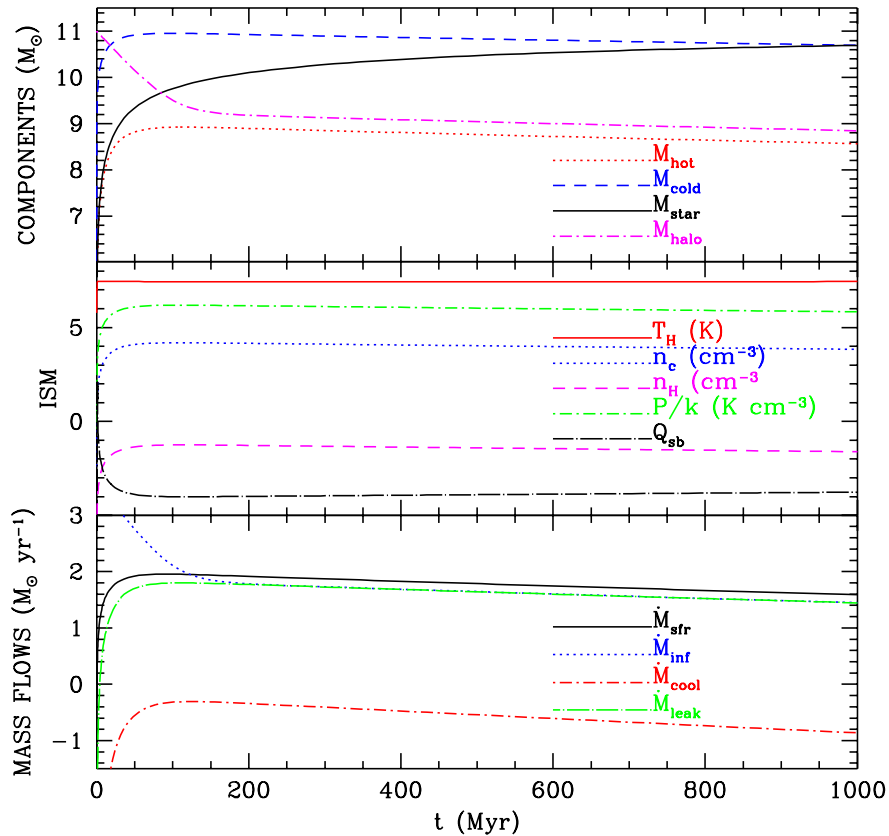


Figure 5.1: Evolution of a toy spheroid with the feedback model of Monaco (2004a). $10^{11} M_{\odot}$ are first put into the external halo and then let infall on the “galaxy”. The upper panel shows the evolution of the mass in the four components (see the labels) as a function of time. The mid panel shows the evolution of the ISM (pressure, density of the two phases, temperature of the hot phase, porosity of SBs). The lower panel shows the main mass flows. All quantities in the y-axes are logarithmic.

Q_{sb} of the expanding SBs is always very low, as the blasts are very quickly halted by the high pressure of the external gas.

The feedback regime described above applies to the case when the cold gas infalls smoothly to the galaxy in small chunks, so that the creation of collapsing clouds is left to the coagulation mechanism introduced above. This is not the case in major mergers of disc galaxies; tidal disturbances in the last phases of the merger increase the thickness of the system, that switches then from adiabatic blow-out to adiabatic confinement. The sudden decrease of the Jeans mass, due to the increased pressure, adds then to the tidal disturbances in causing a diffuse burst of star formation on a dynamical timescale. However, only a fraction f_{\star} of each cloud is transformed into stars, so this burst will contribute to the increase of pressure but will not consume a very large amount

of stars. Tidal disturbances, besides helping the triggering of star formation in clouds, will also stretch and fragment them in small pieces, helping the system to get into the new regime. Most gas will then be transformed into stars when the new feedback regime has taken place.

A more thorough description of this process and a more careful comparison to observations is left to next chapter. Here we notice only that the adiabatic confinement regime implies the presence of significant amounts of molecular gas (with such a high n_c molecular hydrogen should be present even in non-collapsing clouds) in conjunction with a relatively modest star formation activity. This is nicely consistent with the observation of cold gas in elliptical galaxies at the center of massive cooling-flow clusters (see, e.g., Edge & Frayer 2003).

5.2 Feedback from the quasar

5.2.1 The effect of radiative heating

We assume for the moment that the whole galaxy is affected by radiative heating in the same way. To model the perturbation induced by this heating we add to the system described above a seed black hole of $1000 M_\odot$, accreting mass at the Eddington rate for the whole period. We model radiative heating as an evaporation term \dot{M}_{rh} , proportional to the accretion rate onto the black hole \dot{M}_\bullet , that moves mass from the cold to the hot phase:

$$\dot{M}_{\text{rh}} = k_{\text{rh}} \dot{M}_\bullet. \quad (5.14)$$

This term gives a positive contribution to the \dot{M}_{hot} equation and a negative one to the \dot{M}_{cold} equation in the system 5.9. The corresponding energy flow term, \dot{E}_{rh} , is obtained assuming that the gas is heated to the inverse Compton temperature of the AGN, $T_{\text{IC}} = 2 \times 10^7$ K:

$$\dot{E}_{\text{rh}} = \frac{3}{2} k T_{\text{IC}} \frac{\dot{M}_{\text{rh}}}{\mu m_p} \quad (5.15)$$

(here μ is the mean molecular weight of the hot phase, and is self-consistently computed in the model). The global heating rate of the quasar is $6.7 \times 10^{44} \tau T_{\text{IC}8} L_{46} \text{ erg s}^{-1}$ (Begelman 1985), where τ is the electron scattering optical depth of the cold phase, $T_{\text{IC}8} = T_{\text{IC}}/10^8$ K and L_{46} is the ionizing radiation of a quasar in units of 10^{46} erg. The optical depth can be written as that of a single cloud, τ_{cl} , times the covering factor \mathcal{C} of the cold phase. For a typical AGN spectrum a fraction $f_{\text{ion}} \simeq 37$ per cent of the radiated energy is above the Lyman limit². In this case $L_{\text{ion}} = 2.0 \times 10^{45} \dot{M}_\bullet \text{ erg s}^{-1}$, where \dot{M}_\bullet is in units of $M_\odot \text{ yr}^{-1}$. The constant k_{rh} of equation 5.14 is then estimated by equating

²This is computed using the quasar template spectrum of Cristiani & Vio (1990) down to 538 Å, extrapolated to 300 Å with the recipe of Risaliti & Elvis (2004). At shorter wavelength (between 0.01 and 30 Å) we use a power-law with a photon index of $\Gamma = -1.8$ (see Comastri et al., 1995). The relative normalization is fixed by assuming $\alpha_{\text{ox}} = -1.63$ (Vignali et al. 2003). The interpolation between 30 and 300 Å follows Kriss et al. (1999).

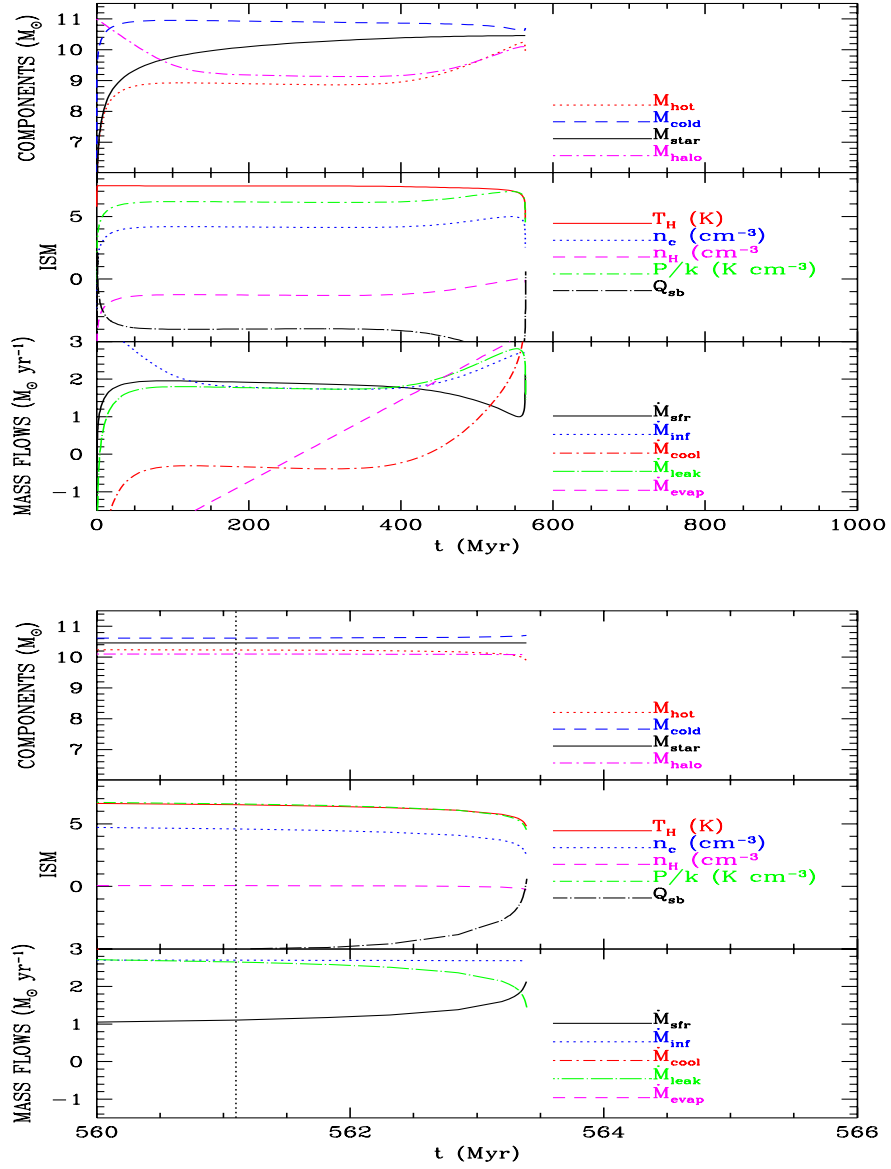


Figure 5.2: As in Figure 5.1 for the evolution of the toy spheroid in case of runaway radiative heating. The right panel shows a detail of the critical change of regime; the dotted vertical line denotes the starting time of the PDS confinement regime.

the heating rate to the thermal energy gained by the evaporated mass. We obtain:

$$k_{\text{rh}} = 104\tau_{\text{cl}}\mathcal{C}. \quad (5.16)$$

This is likely to be a lower limit, due to the neglected metal line heating. The cold phase of a highly pressurized ISM like that of Figure 5.1, with the mass

subdivided into many small clouds, presents a rather high covering factor³, $\mathcal{C} \sim 0.3$. The value of τ_{cl} could be low for these very high density clouds. However, in a more realistic setting a significant fraction of the cold phase would be in a warm intermediate phase, with $T \sim 10^4$. While a modeling of the dynamical role of this warm phase is beyond the interest of this work, it is clear that this phase would present significant values of τ_{cl} and \mathcal{C} . Heating by metal lines would obviously strengthen this conclusion. On the other hand, attenuation by diffuse dust would give lower evaporation rates. As a conclusion, we reckon that a value of ~ 20 - 50 for k_{rh} is reasonable. Begelman (1985, 2004) quotes an evaporation rate of $20 - 200 \mathcal{C} (L_{\text{ion}}/10^{46} \text{ erg}) M_{\odot} \text{ yr}^{-1}$ for a spiral-like ISM. This would correspond to $k_{\text{rh}} = 4 - 40 \mathcal{C}$, lower than the value quoted above. But Begelman’s calculation refers to the rather different case of a wind generated in a spiral galaxy by a central AGN. In our case the geometry of the system is rather different, and we do not require that the gas is ejected out of the galaxy in a wind. This justifies the higher evaporation rate.

Figure 5.2 shows the effect of this heating term on the system. As soon as the radiative heating mass flow becomes comparable to the other ones (\dot{M}_{sf} , \dot{M}_{leak} and \dot{M}_{inf}), ~ 400 Myr after the beginning, the density of the hot phase starts increasing. The pressure grows, while the temperature of the hot phase starts to decrease, due to the enhanced cooling. SBs are confined by the enhanced pressure earlier and earlier, and Q_{sb} decreases considerably. When n_h grows large enough, the system switches to the PDS confinement feedback regime. In this case a significant amount of energy from SNe is radiated away before the blast is pressure-confined by the hot phase. The resulting snowploughs move mass from the hot to the cold phase, causing a sudden decrease of the density and temperature of the hot phase. This leads to a drop in thermal pressure, with a consequent increase of the Jeans mass of cold clouds and of the star formation rate.

Most importantly, just after the change to the PDS confinement regime has taken place, the porosity of the SBs jumps suddenly from very low to > 1 values. This means that the SBs percolate into a unique super-SB, a cold super-shell that sweeps the galaxy, cleaning it very efficiently from all of its ISM. The final velocity of SBs at the formation time of the super-shell will not be much higher than the thermal velocity of the hot phase, $\sim 200 \text{ km s}^{-1}$. This means that the outgoing mass will be accelerated by radiation pressure with an initial efficiency of ~ 0.06 per cent. This efficiency will grow as the shell is accelerated to a higher speed.

The percolation of a diffuse distribution of blasts will produce not only an outgoing supersonic super-shell. A significant fraction of the mass will be compressed to the center of the galaxy by the same blasts. This is well illustrated, for instance, by the simulation of Mori, Ferrara & Madau (2002) of a blow-out in a primordial galaxy. Though the physical scales and the energetic

³We have $\mathcal{C} = 3f_c R/4a_{\text{cl}}$, where f_c is the filling factor of the cold phase, R the size of the structure and a_{cl} the typical size of the cold clouds. For the model in Figure 5.1, $f_c \sim 2 \times 10^{-4}$ and $a_{\text{cl}} \sim 1$ pc, so that for $R \sim 2$ kpc (the size at which a typical $10^{11} M_{\odot}$ bulge with an Eddington-accreting black hole is heated) $\mathcal{C} \sim 0.3$.

budget involved are quite different, the geometry and the astrophysics of the problem are similar. In their simulations a fraction of order of 10 per cent of the gas (the precise number depending on the distribution of the star-forming clouds) is compressed to the center of the halo, while the rest is blown away. In our case, the gas compressed to the center will give rise to a secondary burst of star formation and to further accretion onto the black hole. This will eventually give more energy to the super-shell, both in terms of new SNe giving thermal energy to the rarefied hot gas and in terms of new radiation pressure from the accreting black hole. Moreover, if the ISM is dusty in the starburst phase, the dust will be destroyed by the quasar or removed by the wind just after the percolation phase. The main unobscured shining phase of the quasar could then correspond to the accretion of the matter compressed to the center by the blasts.

The super-shell will form mainly by the sweeping of the hot phase, which at the onset of PDS confinement amounts to ~ 20 per cent of the mass, while the very dense cold clouds (~ 50 per cent of the mass) will be affected less strongly. So, the super-shell may leave some cold mass behind. However, it is likely that this mass will be promptly consumed into stars, for the following reasons. Radiative heating acts preferentially on cold clouds, so the matter left will be in relatively large clouds, where star formation is easier to trigger. At the super-shell formation, sweeping by the supersonic shells will trigger star formation in many of the remaining clouds. After the formation of the super-shell, the galaxy will be filled with hot, pressurized gas, able to thermo-evaporate the leftovers of the star formation process (which amount to ~ 90 per cent of the mass involved in star formation). Moreover, radiative heating and radiation pressure themselves can pressurize the clouds, stimulating star formation (Begelman 1985). As a conclusion, it is likely that the cold gas left behind by the shell will be promptly consumed into stars or evaporated.

From this toy model we learn that the galactic wind is triggered whenever the evaporation rate is roughly a factor of 10 larger than the (unperturbed) star formation rate. As this quantity scales with the initial gas mass, and as the Eddington accretion rate is proportional to the black hole mass, this “monolithic” toy model implies a correlation between stellar and black hole masses, due to the self-limiting feedback from the quasar. However, the black hole mass at the shining time is $\sim 2 \times 10^9 M_\odot$, much larger than what expected in this spheroid. Moreover, no mention is done here on how gas manages to lose angular momentum so as to be able to accrete onto the black hole.

5.2.2 Radiation pressure on the expanding super-shell

The mass that can be accumulated initially in the super-shell is limited by the kinetic energy that the shell can receive from SNe. Figure 5.2 shows that at the percolation time the star formation is as high as $\sim 100 M_\odot \text{ yr}^{-1}$. For $M_{\star, \text{sn}} = 120 M_\odot$, this corresponds to 0.83 SN per year. This level of star formation will be sustained for at least one shell-crossing time, which is the time required to the shell to form. For a fiducial initial velocity $v_i = 200 \text{ km s}^{-1}$, coincidentally very similar to the circular velocity of a $10^{11} M_\odot$ bulge at the half-mass radius

($R_{\text{hm}} = 4.9$ kpc), $V_c = 209$ km s $^{-1}$, the shell crossing time is very similar to the dynamical time of the bulge, 2.5×10^7 yr, and also to the time required to an $8\text{-}M_{\odot}$ star to explode. In this time about 2.2×10^7 SN progenitors are formed, for an energy budget of $\sim 2 \times 10^{58}$ erg. The kinetic energy of a $10^{10} M_{\odot}$ shell (amounting to 10 per cent of the total mass) traveling at 200 km s $^{-1}$ is $\sim 4 \times 10^{57}$; it will be accelerated by SNe if a reasonable 20 per cent efficiency is assumed. However, this is likely to be only a lower limit. Indeed, such a starburst consumes only $2.5 \times 10^9 M_{\odot}$ of stars. In other words, $\sim 4 M_{\odot}$ are accelerated for each M_{\odot} of stars formed. As commented above, the formation of the super-shell will likely trigger a burst of star formation, both by compressing cold gas to the center and by sweeping the most massive cold clouds. If for instance $10^{10} M_{\odot}$ of gas are transformed into stars during the formation of the super-shell, the fraction of mass that can be accelerated by SNe raises to 40 per cent. We conclude that the available energy from SNe does not put strong constraints on the amount of mass that can be accelerated.

The amount of mass that can be ejected in a wind is instead limited by the ability of radiation pressure to perform work on the shell. Due to its high pressure, the gas in the shell is not subject to runaway radiative heating until it becomes subsonic or is destroyed by Rayleigh-Taylor instabilities. While sweeping the hot gas phase and, later, the hot halo gas pervading the dark matter halo that surrounds the galaxy, the super-shell grows in mass. It is slowed down by gravity, pressure from the external hot gas and mass load.

The equation of motion of a super-shell of mass M_s , radius R_s and velocity v_s can be written as follows:

$$\frac{1}{2} M_s \frac{dv_s^2}{dR_s} = -v_s^2 \frac{dM_s}{dR_s} - G M_s \frac{M_{\text{tot}}(R_s)}{R_s^2} + (P_{\text{rad}} + P_{\text{int}} - P_{\text{ext}}) 4\pi R_s^2. \quad (5.17)$$

We will neglect the internal pressure term, P_{int} , and concentrate on radiation pressure (equation 5.1).

Let's first assume that a shell of constant mass is leaving an isolated bulge of mass M_{bul} ; no dark matter component is considered at the moment. Fitting the data of Marconi & Hunt (2003), we find that the half-mass radius ($R_{\text{hm}} = 1.35 R_e$, where R_e is the effective radius) of an elliptical galaxy scales with the bulge mass as follows:

$$R_{\text{hm}} = 4.9 M_{\text{bul},11}^{0.65} \text{ kpc}. \quad (5.18)$$

The scatter around this relation is ~ 0.3 dex. For the mass profile we assume for simplicity a roughly constant rotation curve, so that $M_{\text{bul}}(r) \propto r$. We then fix the value of $M_{\text{bul}}(r)/r$ to its value at the half-mass radius, $M_{\text{bul}}/2R_{\text{hm}}$.

The mechanical pressure exerted by radiation depends on the optical depth of the shell, $P_{\text{rad}}(1 - e^{-\tau_{\text{shell}}})$. The column density of a shell of mass $M_s = f_s M_{\text{bul}}$ at a radius R (in kpc) is $8.0 \times 10^{23} f_s M_{\text{bul},11} R^{-2}$ cm $^{-2}$. Following Begelman (2004), electron scattering gives only $\tau_{\text{shell}} \sim 0.7x f_s M_{\text{bul},11} R^{-2}$, where x is the ionization fraction. Photoionization gives $\tau_{\text{shell}} \sim 100 (P_{\text{th}}/P_{\text{rad}}) f_s M_{\text{bul},11} R^{-2}$. As long as the shell propagates supersonically, its pressure is very high, so

the value of τ_{shell} at $P_{\text{th}} = P_{\text{rad}}$ is a very conservative lower bound. The high pressure guarantees also that the shell is not affected by runaway radiative heating. Dust absorption on the other hand gives $\tau_{\text{shell}} \sim 10^5 f_s M_{\text{bul},11} R^{-2}$. Moreover, the ratio between the mean free path of the dust grains and the thickness of the shell results $\sim 4 \times 10^{-5} f_s^{-1} M_{\text{bul},11}^{-1} R^2$ (Murray et al. 2005), so that dust grains are hydrodynamically coupled to the fluid. As a conclusion, the shell absorbs most of the quasar light from ~ 4000 to $\sim 1 \text{ \AA}$, so that radiation pressure (equation 5.1) can be safely used in equation 5.17. This is valid until the shell is so diluted that $\tau_{\text{shell}} \sim 1$, which happens only at several half-mass radii.

Solving equation 5.17, we find that the kinetic energy of the shell, K_s , evolves like:

$$K_s = -f_s M_{\text{bul}} V_c^2 \ln \left(\frac{R_s}{R_i} \right) + \frac{L}{c} (R_s - R_i) + K_i. \quad (5.19)$$

Here V_c is the circular velocity of the bulge at R_{hm} , and the suffix i refers to the initial conditions, so that $K_i = f_s M_{\text{bul}} v_i^2 / 2$. Requiring that the minimum of K_s is positive, we obtain an upper limit on f_s which is given by the largest root of the algebraic equation $(a + \ln(b/f_s))f_s - b = 0$, where $a = 1 + v_i^2 R_{\text{hm}} / GM_{\text{bul}}$ and $b = 2R_{\text{hm}} L R_i / GM_{\text{bul}}^2 c$. Scaling the accretion rate to $4 M_{\odot} \text{ yr}^{-1}$ (the Eddington accretion rate of a $1.6 \times 10^8 M_{\odot}$ black hole hosted in a $10^{11} M_{\odot}$ bulge) and assuming that the initial radius of the shell is that at which radiation pressure equals the thermal one (equation 5.2), we obtain that the upper limit to f_s is fit (within ~ 15 per cent) by the following formula:

$$f_s < 0.21 \left(\frac{\dot{M}_{\bullet,4}}{M_{\text{bul},11}^{1.1}} \right)^{1.5}. \quad (5.20)$$

(here $\dot{M}_{\bullet,4} = \dot{M}_{\bullet} / 4 M_{\odot} \text{ yr}^{-1}$).

Radiation pressure is then able to expel up to 21 per cent of the mass of a star-forming spheroid if its black hole follows the known black hole–bulge relation and is accreting at the Eddington ratio. More active black holes can remove much larger amounts of mass (assuming that star formation is strong enough to create such massive super-shells). This provides a self-limiting mechanism able to generate a black hole–bulge correlation very similar to that observed⁴.

This result is valid for bulges with escape velocities larger than 200 km s^{-1} . Less massive bulges than $10^{10} M_{\odot}$ have escape velocities below this limit, so mass removal is efficient even in case of no accretion. This implies a much looser black hole–bulge correlation at such masses.

Once the super-shell has left the galaxy, it interacts with the hot gas pervading the dark matter halo. In this case the gravity term of equation 5.17 contains also the contribution of the halo, while the hot halo gas slows down the shell by mass load and thermal pressure. We have verified that for reasonable

⁴Equation 5.2 is used assuming a constant gas pressure for all bulges. Smaller bulges are however denser. From the model described in Section 2 we find that roughly $P_{\text{th}} \propto M_{\text{bul}}^{-0.5}$. Taking this into account, we obtain $f_s \leq 0.2 (\dot{M}_{\bullet,4} / M_{\text{bul},11}^{0.9})^{1.5}$.

values of the halo parameters (mass, concentration, gas distribution etc.) the shell will be promptly stopped as soon as it interacts with the gas. At this point it will fragment. At a speed of $\sim 200 \text{ km s}^{-1}$, a distance of a few tens of kpc is reached in several tens of Myr, i.e. $\sim 2\text{-}3$ Eddington times. If the accretion of the material compressed at the center started promptly at shell formation, and if the quasar were visible only after the shell is destroyed, then most accretion would be hidden by the dusty shell. However, the time necessary to the gas compressed to the center to lose its angular momentum is likely to be not negligible. For instance, Granato et al. (2004) suggest a timescale for viscous accretion of order $5 \times 10^7 \text{ yr}$ for a black hole of $10^8 M_\odot$ in a 200 km s^{-1} bulge, amounting to ~ 1.2 Eddington times. We suggest as a likely scenario that while the shell is pushed by accretion of the low-angular momentum gas accumulated during the stage of self-limited star formation (in the adiabatic confinement feedback regime), the accretion of the material compressed at the center at the super-shell formation takes place mostly after the shell has been destroyed.

The drop in pressure consequent to the shell destruction makes radiative heating effective again and, due to the very high covering factor of the shell gas, a part of it can be in principle heated back to T_{IC} . However, it is easy to verify that the heating time evolves like $t_{\text{heat}} \sim 1.2 \times 10^8 R^2 L_{46}^{-1} (T/T_{\text{IC}}) N_{H,24} \text{ yr}$, where T is the temperature of the heated gas and $N_{H,24}$ the column density of the layer that is affected by heating, in units of 10^{24} cm^{-2} (see Begelman 2004). Clearly, for distances significantly larger than one kpc, the heating time becomes too large for runaway heating to be effective. In this case the shell will be heated to a much lower temperature than T_{IC} .

During the expansion, radiation pressure performs a work LR_s/c on the super-shell. For $M_\bullet = 4 M_\odot \text{ yr}$ and $L = 2.3 \times 10^{46}$, at a fiducial distance of 20 kpc (roughly 5 half mass radii, at which the effects of the dark-matter and hot-gas halo should be important) the AGN has given $4.7 \times 10^{58} \text{ erg}$ to the shell. The efficiency of energy injection depends on the actual expansion velocity, which however does not exceed much the initial one if the shell is near its mass limit. Besides, for $k_{\text{rh}} = 50$ and $M_\bullet = 1.6 \times 10^8 M_\odot$, radiative heating injects $6.5 \times 10^{59} \text{ erg}$ into the ISM, amounting to 2 per cent of the energy budget. However, most of this energy is lost to radiation during the formation of the super-shell. This calculation confirms that the energetic efficiency of feedback from quasars is very likely smaller than 1 per cent. In this case, the 5 per cent efficiency used in the simulations of Springel et al. (2004) seems a rather extreme choice.

To understand the robustness of these conclusions, we have repeated the computation of the fraction of mass removed by the wind under several different assumptions on the mass profile, obtaining in most cases a fraction of order of 10 per cent times $(M_{\bullet,4}/M_{\text{bul},11})$ to the power 1.5–2 ($M_{\text{bul},11}$ may be raised to a power very similar to one).

As a conclusion, radiation pressure can remove about 20 per cent of the mass of a star-forming spheroid hosting an Eddington accreting black hole that follows the local black hole–bulge relation. However, it cannot remove this gas

from the massive dark-matter halo that hosts the bulge.

5.2.3 Feedback from AGN in presence of other stellar feedback regimes

The mechanism described above depends on the assumption that feedback is in the adiabatic confinement regime when the quasar shines. Here we show that the validity of the numbers given above is more general.

As shown in Monaco (2004b), small star-forming clouds are destroyed by a single SN. As the number of SNe per cloud is rather small, the fraction of energy lost in destroying the cloud could be rather high. This justifies a lower effective value for E_{51} in the case of adiabatic confinement. In Monaco (2004a) it was found that, for $E_{51}=0.3$, the system goes to the PDS confinement regime. This has the effect of lowering the pressure and increasing the porosity. The onset of the PDS confinement regime can be smooth (as the example given in Monaco 2004a) or critical; for the infall times used here the onset is critical, leading to the percolation of SBs. This will lead to critical, self-stimulated bursts of star formation, that will increase the pressure and make the solution bounce back to the adiabatic confinement one. In principle, this would lead to the creation of a galaxy-wide super-shell. However, in absence of a synchronized trigger as a shining quasar, this explosion will presumably interest different parts of the galaxy at different times; moreover, even in case a super-shell is formed, its velocity will be lower than the escape velocity of the cloud, so the cold gas will fall back soon if $M_{\text{bul}} > 10^{10} M_{\odot}$. As a conclusion, the system will spend most of its time in the adiabatic confinement regime, with possible (self-stimulated and quickly self-quenched) bursts of star formation; consequently, the effect of radiative heating will be similar to what described above.

Murray et al. (2005) estimated that radiation pressure by an Eddington accreting black hole can wipe out some 10 per cent of the mass of an optically thick spheroid simply by radiation pressure. Also this self-limiting mechanism induces a black-hole bulge relation compatible with observations. Repeating their calculation for our $10^{11} M_{\odot}$ case spheroid we obtain $f_s < 0.06\mathcal{C}$. Clearly, the presence of an outward-moving shell with $\mathcal{C} = 1$ makes the case for a massive wind driven by radiation pressure much more convincing.

5.3 Shining quasars in the hierarchical context

All the calculations given above assume that an Eddington-accreting black hole is present in a star-forming spheroid, and do not take into proper account two very important aspects of galaxy and quasar formation, namely the formation and evolution of galaxies driven by the hierarchical assembly of dark matter halos, and the nearly complete loss of angular momentum necessary to the gas to accrete onto the central black hole. We show in the following how the results of sec. 5.2 apply when inserted into GALRISE. In this section we will use a slightly simplified version of GALRISE: in particular (i) we fix $\alpha_{\text{lowJ}} = 1$, (so as the eq. 4.75 is equivalent to the formalism of Granato et al., 2004) (ii)

if the accretion rate induced by star formation is larger than the Eddington limit, the exceeding gas is put into a reservoir, that is later accreted onto an Eddington time:

$$\dot{M}_\bullet = \min\left(k_{\text{resv}}\dot{M}_{\text{sf}} + \frac{M_{\text{resv}}}{t_{\text{ed}}}, \frac{M_\bullet}{t_{\text{ed}}}\right) \quad (5.21)$$

$$\dot{M}_{\text{res}} = k_{\text{resv}}\dot{M}_{\text{sf}} - \dot{M}_\bullet \quad (5.22)$$

(iii) the feedback from jets is not taken into account.

The aim here is not to present a proper complete modeling of galaxies and quasars (which is left to chapters 6 and 7), but just to illustrate under simple hypothesis how the triggering of galaxy winds may behave in a more realistic situation than a “monolithic” spheroid.

5.3.1 Low-angular momentum gas and the triggering of the wind

As long as a significant fraction of the stars of a spheroid is formed within the spheroid itself (and not in self-regulated discs that later merge into spheroids), the relation between star formation rate and black hole accretion (equation 5.21) induces a black hole–bulge correlation similar to that observed for reasonable values of k_{resv} . Many authors (cited in the introduction) have used similar rules in conjunction with hierarchical galaxy formation models, correctly reproducing the black hole–bulge correlation with no need for self-regulation. With our galaxy formation model we find a good fit for the black hole–bulge correlation for $k_{\text{resv}}=0.003$. We demonstrate now that in this case galaxy winds are likely irrelevant.

According to Figure 5.2, the catastrophic switch from the adiabatic to the PDS confinement regime happens whenever the evaporation rate overtakes the (unperturbed) star-formation rate by a factor of ~ 10 . However, this is valid in the region affected by radiative heating, which for simplicity we assumed in Section 3 to coincide with the whole galaxy; in a realistic case the evaporation is limited to the inner region of the galaxy, $r < R_{\text{rh}}$, which contains only a fraction of the total cold gas and star formation rate (~ 20 per cent in our $10^{11} M_\odot$ spheroid case). Even within this region, the evaporation grows linearly with the radius r through the covering factor \mathcal{C} (equation 5.16), so if the gas distribution in this region is flatter than r^{-2} (and the mass of cold gas grows more rapidly than r) the triggering condition will first be reached in the inner regions and then propagate inside-out⁵. A reasonable and simple triggering criterion for a star-forming galaxy is then obtained when evaporation overtakes the *global* star-formation rate by a factor k_{trigger} of order unity:

$$\dot{M}_{\text{rh}} > k_{\text{trigger}}\dot{M}_{\text{sf}}. \quad (5.23)$$

Using equations 5.14, 5.21 (assuming that accretion is not Eddington limited) and 5.23, it is easy to see that winds will be triggered if $k_{\text{trigger}} < k_{\text{rh}} \times$

⁵Besides, the condition of adiabatic confinement requires that the gas distribution is flatter than r^{-2} up to the vertical scale-length of the system.

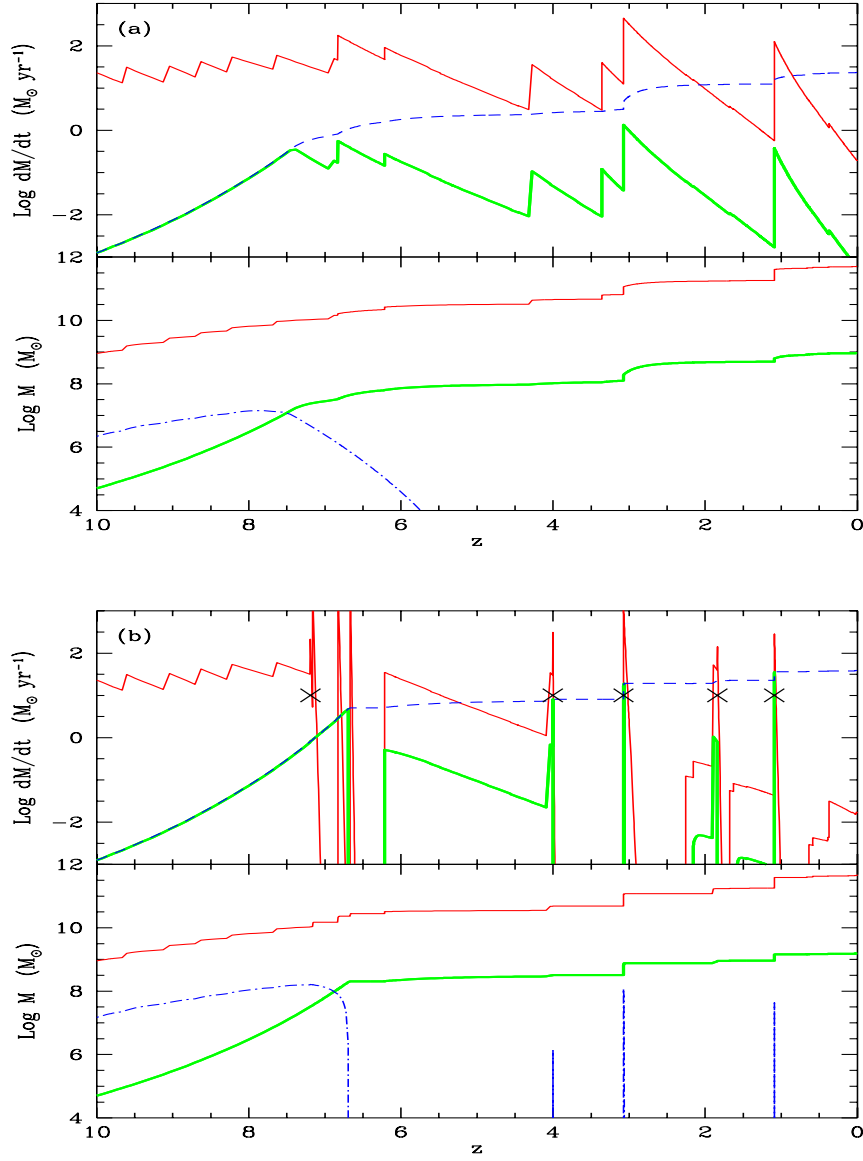


Figure 5.3: Evolution of the main progenitor of an elliptical galaxy contained in a $1.1 \times 10^{13} M_{\odot}$ dark matter halo. (a): no winds ($k_{\text{resv}}=0.003$). (b): with winds ($k_{\text{rh}}=50$, $k_{\text{resv}}=0.02$ and $k_{\text{trigger}}=1$). Upper panels: star formation rate in the bulge of the main progenitor (continuous lines), accretion rate on the black hole (heavy continuous lines), Eddington limit (dashed lines). The crosses in the right panel denote the shining events. Lower panels: stellar mass of the bulge of the main progenitor (continuous lines), black hole mass (heavy continuous lines), reservoir mass (dot-dashed lines).

k_{resv} . For $k_{\text{resv}}=0.003$ (the value with which the black hole–bulge correlation is reproduced with no winds) and $k_{\text{rh}}=50$, this implies $k_{\text{trigger}} < 0.15$. In other

words, winds will work only if radiative heating is concentrated on ~ 1.5 per cent of the star-forming region. The result of switching winds in this case is to limit black hole masses to lower values, with a resulting underestimate.

Alternatively, the mass deposition rate on the reservoir can be higher. In this case the black hole–bulge correlation is due to the self-limiting action of winds. Keeping $k_{\text{rh}}=50$ and assuming $k_{\text{trigger}}=1$, winds are triggered if $k_{\text{resv}} \geq 0.02$, nearly an order of magnitude higher than before.

To be more specific, a massive wind in the galaxy formation model is triggered whenever: (i) the triggering condition of equation 5.23 is satisfied; (ii) the accretion rate in Eddington units is larger than 0.01 (otherwise the system switches to a radiatively inefficient accretion mode, and the present model does not apply); (iii) the amount of cold mass present in the bulge is lower than equation 5.20. To implement the post-wind scenario described in Section 3, 10 per cent of the cold gas is not put into the shell but consumed by star formation on a bulge dynamical time, while a fraction k_{resv} of this gas is put in the reservoir to be accreted onto the black hole. The cold gas in the shell is then given to the cold halo component.

The main uncertainties and degrees of freedom in the modeling of the wind are the following: (i) the timescale of star formation in bulges is fixed in a phenomenological way, better modeling is needed. (ii) The modeling of the reservoir of low-angular momentum gas is reasonable but not unique. (iii) The parameter k_{rh} is fixed with no explicit reference to R_{rh} or to the covering factor of cold clouds. (iv) The parameter k_{resv} is very poorly constrained. (v) The constant in equation 5.20 depends on many uncertain details and may reasonably be considered as a free parameter (we will keep it fixed to the value given above). (vi) The parameter k_{trigger} is uncertain by at least a factor of ten. (vii) The fraction of mass compressed to the center after the wind is uncertain as well.

5.3.2 An example

In this subsection we show that there is a significant part of the parameter space that allows for quasar-triggered galaxy winds, and briefly outline the effect these would have on the galaxy population as a whole.

We have taken a $1.1 \times 10^{13} M_{\odot}$ dark matter halo from a 256^3 PINOCCHIO realization of size 93 Mpc. The particle mass for this box is 3×10^9 , corresponding to a mass resolution for the merger tree of $\sim 10^{11} M_{\odot}$. Due to its particular merger history, this halo hosts a spheroid at the final time ($z = 0$). The mass of the spheroid depends of course on the details of galaxy formation, and ranges from 10^{11} to $5 \times 10^{11} M_{\odot}$. We have run the model assuming first no winds ($k_{\text{rh}}=0$), so that the black hole–bulge correlation is set by angular momentum loss ($k_{\text{resv}}=0.003$). Figure 5.3a shows the resulting evolution of the main progenitor of the galaxy. In particular, we show accretion and star formation rates, bulge, black hole and reservoir masses. It is worth clarifying that all these quantities refer to the bulge of the main progenitor; accretion takes places also in the black holes of satellite galaxies, while stars form both in satellites and discs.

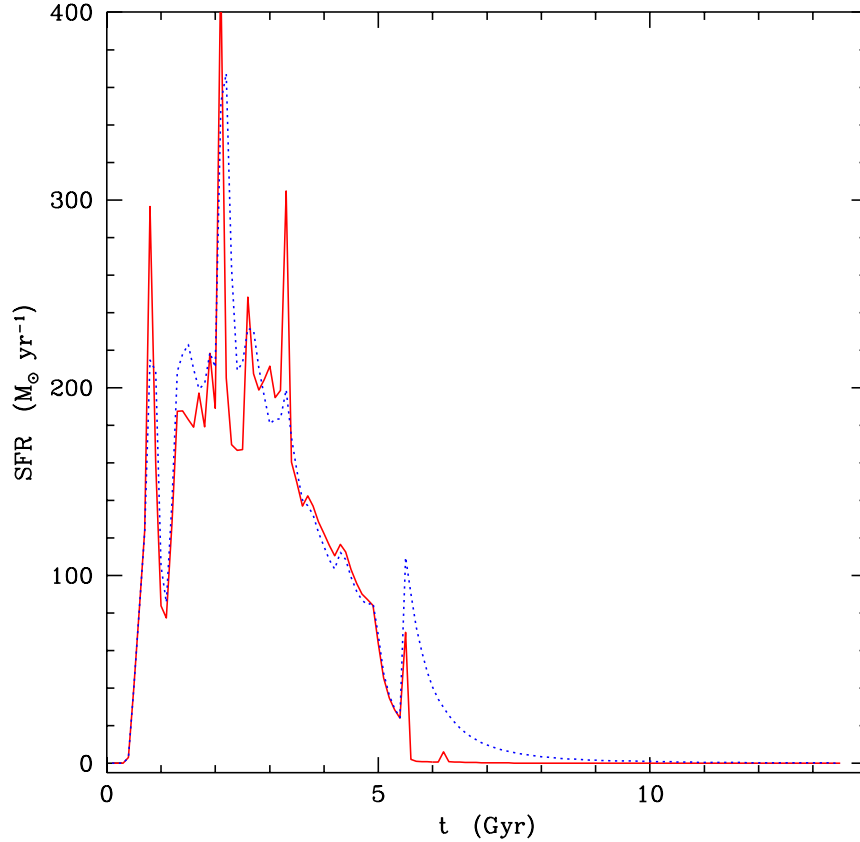


Figure 5.4: Star formation rates for the two examples shown in Figure 5.3. This time the star formation rate of all the stars contained in the galaxy at $z = 0$ is given. The dotted line refers to the example without winds (Figure 5.3a), the continuous line to the example with winds (Figure 5.3b).

In this case of no wind, the assembly of the galaxy proceeds gradually. The two main star-formation events are located at $z \sim 3$ and ~ 1 , while the sawtooth-like events at very high redshift are due to successive disc instabilities. The black hole starts accreting mass at very early times, and its accretion is Eddington limited till $z \sim 7.5$. By $z \sim 6$ a $\sim 10^8 M_\odot$ black hole is already present. The two main shining events closely follow the mergers, and are both sub-Eddington. Most black hole mass is acquired by accretion more than by black hole mergers. At the final time the bulge and black hole masses are 5.1×10^{11} and $9.4 \times 10^8 M_\odot$, compatible with the observational black hole–bulge relation.

Figure 5.3b shows the same example with $k_{\text{th}}=50$ and $k_{\text{resv}}=0.02$. The evolution at very high redshift is similar, but the Eddington accreting phase goes on for a longer time (due to the higher amount of low-angular momentum gas available), so that the resulting black hole is a factor of 3 more massive at redshift ~ 6 . The first shining event takes place at $z \sim 7$, and has the effect

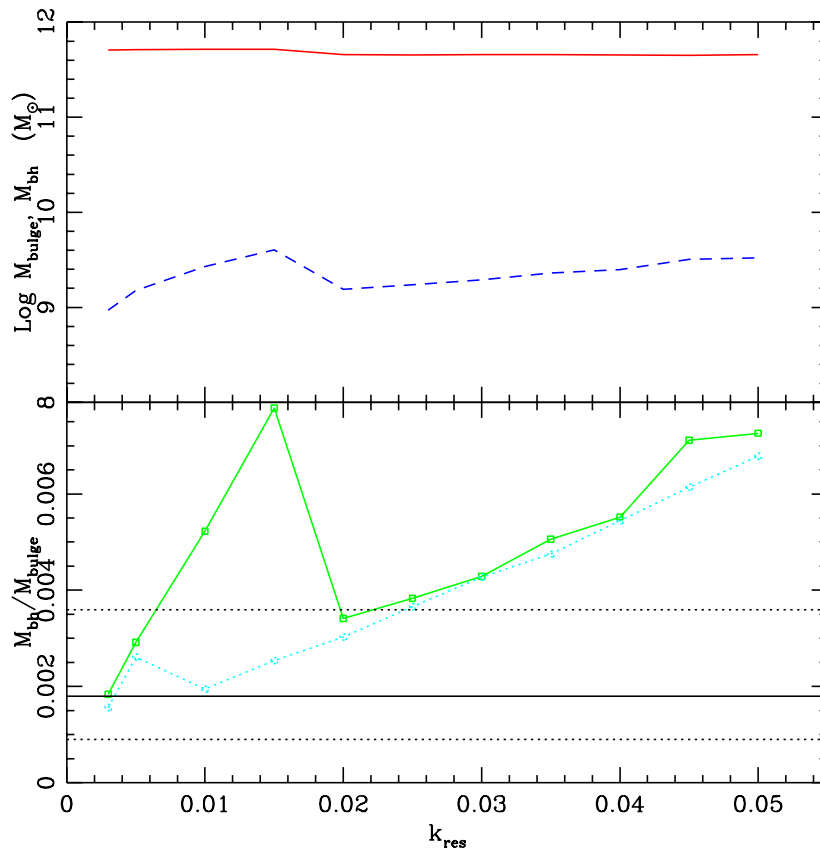


Figure 5.5: Upper panel: bulge (continuous line) and black hole (dashed line) masses as a function of k_{resv} for the example of Figure 5.3 ($k_{\text{trigger}}=1$). Lower panel: black hole–bulge ratio as a function of k_{resv} for the case $k_{\text{trigger}}=1$ (continuous line) and $k_{\text{trigger}}=0.3$ (dotted line). The horizontal continuous and dashed lines show the range allowed by observations (Shankar et al. 2004).

of quenching star formation in the spheroid. Further shinnings take place at redshifts $\sim 4, 3, 2$ and 1 . In each case we have a short quasar phase that however contributes significantly at the mass of the black hole only at redshift 3 (with a significant burst at $z \sim 1$). In the meantime, the episodes of star formation are quickly quenched. As a result, the final bulge and black hole masses are 4.6×10^{11} and $1.6 \times 10^9 M_{\odot}$. This galaxy lies a factor of 2 above the observational relation, just below the $1\text{-}\sigma$ 0.3 dex dispersion.

Figure 5.4 shows, as a function of cosmological time, the star formation rates of all the stars contained in the final spheroid for the two cases. This is different from the star formation rate of the bulge of the main progenitor, as it contains the contribution of stars formed in discs and satellites. The two star formation rates do not differ much; the most notable effect is the truncation of the low-redshift tail of star formation. This detail however can be very

important because minor episodes of star formation can influence strongly the luminosity-weighted colors of galaxies. Moreover, the chemical evolution of these object is also affected by late star formation events, that take place from iron-enriched material and decrease the α -enhancement (see, e.g., Matteucci 1996). The effect of winds will then be to increase the number of passive old galaxies at $z \sim 1-2$ and to allow a high level of α -enhancement.

Besides, the quasar population will be more deeply affected by winds, especially for $M_{\text{bul}} < 10^{10} M_{\odot}$, where SNe alone are able to generate a massive wind. In this case we expect an increase of bright quasars at very high redshift (because the Eddington limited phase lasts longer) and a decrease at low redshift (because the shining events are suppressed by winds), in agreement with the trends suggested by observations.

Figure 5.3.1 shows how the black hole and bulge masses and their ratio change when the k_{resv} parameter is increased; for $k_{\text{resv}} < 0.02$ both black hole mass and ratio grow linearly with k_{resv} , but as soon as winds come into play the fraction self-regulates to a value that remains relatively stable till $k_{\text{resv}} = 0.03$, then starts growing again. The upper panel shows that the main effect of wind triggering is on the black hole, though bulges tend to be slightly less massive. Finally, a good value for the black hole–bulge ratio is obtained with $k_{\text{trigger}} = 0.3$ and $k_{\text{resv}} = 0.01$ (dotted line)

5.4 Conclusions on QSO Feedback

Radiation pressure and radiative heating are two unavoidable processes during the shining of a quasar that strongly influence the ISM of a star-forming spheroid. However, taken alone they may not be able to trigger those massive winds that have often been assumed to take place during the formation of a spheroidal galaxy. Based on the GALRISE model for feedback in galaxy formation, we have proposed that a massive removal of ISM from a large star-forming spheroid can be triggered by the joint action of SNe and quasar light as follows: (i) stars form in a self-regulated way in a two-phase, highly pressurized ISM; (ii) through runaway radiative heating, the quasar evaporates part of the cold phase; (iii) when the evaporation rate is strong enough, the feedback regime changes: due to the higher density of the hot phase, SBs arising from the star-forming clouds get to the PDS stage before being halted by pressure confinement; (iv) the consequent drop in pressure leads to the percolation of cold shells and to the creation of an expanding super-shell; (v) some mass is compressed to the center, giving rise to a nuclear starburst and to further black hole accretion; (vi) the remaining cold gas (not included in the shell or in the nucleus) is most likely involved in diffuse star formation; (vii) radiation pressure pushes the shell out of the galaxy if it is not too massive; (viii) as soon as it interacts with the external hot halo gas, the shell halts and fragments; (ix) a part of it is finally evaporated by radiative heating, though to a much lower temperature than the inverse Compton one of the quasar.

We have demonstrated that this mechanism can lead to a self-limited black hole–bulge relation similar to the observed one. However, using a

galaxy formation model (presently under development) that takes into account black hole accretion, we have shown that the black hole–bulge relation is also reproduced assuming that the rate of deposition of low-angular momentum gas onto the black hole amounts 0.3 per cent of the star formation rate in the bulge. Including a motivated criterion for quasar-triggered winds, we have shown that the black hole–bulge relation is self-limited by winds whenever the deposition rate is at least ~ 1 per cent of the bulge star-formation rate. Compared to the no-wind case, this mechanism leads to more massive black holes at high redshift and to a quenching of low-redshift activity.

There are two main possible objections to this scenario. First, a massive removal of ISM can be caused by other mechanisms, like a kinetic ejection of matter from the AGN (Granato et al. 2004) or simply by radiative heating (Sazonov et al. 2004a) or radiation pressure (Murray et al. 2005) by the quasar light, so there is no real need for such a sophisticated and indirect mechanism. Ejection of matter at nearly relativistic speed is observed in action in extreme BAL quasars; however, this mechanism can work only if the covering angle of the outflow is large. On the other hand, the radiation of the quasar alone may be able to remove only a modest fraction of the mass of the ISM, not larger than a few per cent. The triggering mechanism suggested here has the merit of creating an outwardly expanding, optically thick super-shell (with unity covering factor), which is then easily pushed away by radiation pressure. An appreciable element is that the prediction comes out naturally from the model of Monaco (2004a) without any parameter tuning.

The second objection is that if a reservoir of low angular momentum gas is created at a rate proportional to the star-formation rate in bulges, then there is no need for a self-limiting mechanism responsible for the black hole–bulge relation. In this case the condition for wind triggering may never (or almost never) be reached in practice. Probably the strongest argument in favor of winds lies in the chemical enrichment patterns of bulges (stars, ISM and circum-quasar gas), but more work is needed for an assessment of this point.

It is not easy to devise critical observational tests to understand if a mechanism like the one described here is actual. Due to the number of processes involved and to the huge uncertainties in many of the parameters, many different configurations may lead to very similar predictions. To be more specific, all the evolution from the starburst to the ejection of the shell would be hidden by dust, so the quasar would be invisible. Shining quasars would correspond to the stage after the destruction of the shell, so the only clearly observable stage would correspond to the last phases of expulsion and evaporation of the shell. For $k_{\text{rh}}=50$ this takes a time $t \sim 5 \times 10^8 f_s M_{\text{bul},11} M_{\bullet,4}$ yr, so a massive shell would be visible for $\sim 12 \times f_s$ Eddington times as an absorber with a low expansion velocity. Such objects are seen for instance in absorption of optical quasar spectra (see, e.g., Srianand & Petitjean 2000; D’odorico et al. 2004). Their structure is generally very complex, and outflowing speeds range from hundreds to tens of thousands of km s^{-1} . A quick and dirty comparison with such data is then impossible, and more precise

predictions need a dedicated calculation and will be presented elsewhere.

Another way to probe the validity of the wind model is through its effects on the statistical properties of galaxies. In this case the problem is in the degeneracy with all the other (numerous and uncertain) parameters of galaxy formation. Anyway, the higher accretion rate connected with quasar triggered winds gives more massive black holes at $z \sim 6$ and a quenching of low- z activity, in line with the observational evidence, while the expulsion of the metals generated after the first burst of star formation is in line both with the high level of alpha enhancement of ellipticals and with the high abundance of iron in clusters. Moreover, the fact that no limit on the fraction of mass that can be removed is present for bulges less massive than $10^{10} M_{\odot}$ implies an increase in the scatter of the black hole–bulge relation at small masses; the observations for such small bulges are few, but the possible finding of outliers in the relation would be in line with this prediction. A more accurate analysis will be presented in next chapter.

Chapter 6

The Effect of Stellar Feedback and Quasar Winds on the AGN Population

¹In chapter 4 we described in full detail our model for the joint formation and evolution of galaxies and AGNs and we introduced the reader into our parameter space. Most parameters do influence the predictions on the AGN population in a rather predictable way, so we concentrate on varying only a few mostly relevant parameters, leaving the others fixed to their standard values. The first of these parameters is related to the amount of kinetic feedback in bulges. As shown in chapter 4, the velocity dispersion of cold clouds σ_{cold} in a star-forming ISM scales with the star-formation timescale t_* as:

$$\sigma_{\text{cold}} = \sigma_0 t_*^{-1/3}. \quad (6.1)$$

(t_* is given in Gyr, so as to have σ_0 in km s^{-1}). The normalization parameter σ_0 depends on many uncertain details, like the driving scale of turbulence. In thick systems, due to the high efficiency of (both thermal and kinetic) energy injection, σ_0 is likely to be higher than in thin systems like discs. In conjunction with the much lower star-formation time-scale, this can lead to significant values of σ_{cold} in bulges. We will show in the following that kinetic feedback in bulges plays a very important role in limiting faint AGNs at high redshift. We will test σ_0 values ranging from ~ 0 to $\sim 100 \text{ km s}^{-1}$.

The second parameter considered is Σ_{lim} . As a result of the strong cooling flows at high redshift, and of the assumption that the cooled gas settles on a discs, high-redshift discs may have very high surface densities of cold gas, sufficient to let them switch to the adiabatic confinement regime, typical of star-forming bulges and characterized by a higher velocity dispersion of clouds. In these conditions the transport of angular momentum within the gaseous disc is very efficient, so that these objects are very likely to become bulges. This mechanism is implemented in a very simple way by stimulating a bar instability

¹The results presented in this chapter will be submitted for publication in Fontanot, Monaco et al. (2006a).

(which amounts to moving half of the disc mass to the bulge) whenever the gas surface density of the disc overtakes a value Σ_{lim} . The reference value for this parameter is $300 M_{\odot} \text{pc}^{-2}$.

6.1 Modeling AGNs in GALRISE

6.1.1 Accretion onto BHs

As we already stated in sec. 4.8.1 a seed BH of $10^3 M_{\odot}$ is assigned to each DM halo (see, e.g., Volonteri, Haardt & Madau 2003 for a justification). Gas can accrete onto the BH only after having lost nearly all of its angular momentum J . The first step in this loss is connected to the same processes that lead to the formation of bulges. Further losses may be connected to turbulence, magnetic fields or radiation drag (Umemura 2001). In all these cases it is reasonable to assume that a low- J reservoir forms at a rate proportional to the star-formation rate in the bulge $\dot{M}_{\text{low}J} = f_{\text{low}J} \dot{M}_{\text{sf},B}$ ($f_{\text{low}J}$ is equivalent to k_{resv} in chap 5). We saw in sec. 4.8.1 that a more general relation between $\dot{M}_{\text{low}J}$ and $\dot{M}_{\text{sf},B}$ is obtained assuming a power-law dependence with exponent $\alpha_{\text{low}J}$ between the two quantities (eq. 4.75):

$$\dot{M}_{\text{low}J} = f_{\text{low}J} \dot{M}_{\text{sf},B} \left(\frac{\dot{M}_{\text{sf},B}}{100 M_{\odot} \text{yr}^{-1}} \right)^{\alpha_{\text{low}J}-1} \quad (6.2)$$

For $\alpha_{\text{low}J} = 1$ this relation is equivalent to that of Granato et al. (2004), while for $\alpha_{\text{low}J} \neq 1$ the $f_{\text{low}J}$ parameter is scaled to a star formation rate of $100 M_{\odot} \text{yr}^{-1}$. The gas flown in the low- J reservoir accretes onto the BH at a rate determined by the viscosity of the accretion disc; this accretion rate \dot{M}_{visc} is found in chapter 4 (eq. 4.76). Accretion is limited by the Eddington-Salpeter rate $\dot{M}_{\text{BH}}/t_{\text{Ed}}$, where $t_{\text{Ed}} \simeq 4 \times 10^7 \text{yr}$ is the Eddington-Salpeter timescale. The resulting system of equations for the BH and reservoir masses is also defined in 4 (eq. 4.77)

6.1.2 Quasar-triggered winds

We already saw in chapter 5 that AGN activity releases a huge amount of energy so that, although the mechanisms for transferring it into the ISM are not very clear, this energy may easily trigger a massive galactic wind, able to remove all ISM from the galaxy. This would mark the end of the star formation episode that stimulated the accretion onto the BH. The details of the onset of such winds are very unclear, so we decided to insert winds in the model in two ways.

In both cases we use the same criterion proposed in chapter 5 for triggering the wind: the UV-X radiation of the AGN is able to evaporate some $50 M_{\odot}$ of cold gas for each M_{\odot} of accreted mass. When this evaporation rate overtakes the star-formation rate by a factor of order unity, then the effect of the AGN radiation is sufficient to influence the ISM in a significant way. Removing

one parameter (the evaporation efficiency and the triggering parameter are degenerate), the triggering condition can be written as:

$$\dot{M}_{\text{BH}} > f_{\text{qw}} \dot{M}_{\text{sf,B}} \quad (6.3)$$

The parameter f_{qw} takes values of order of $10^{-2} - 10^{-3}$; in this work we use 0.006. Clearly, this criterion is very similar to equation 4.75 for $\alpha_{\text{lowJ}} = 1$, which however refers to the build-up of the reservoir, not to the accretion rate of the BH. A modeling of the delay between loss of angular momentum and accretion onto the BH, dictated by equation 4.76, is then necessary to use the criterion of equation 6.3.

A massive removal of cold gas can take place only if the AGN is powerful enough to perform the work. Such a self-regulating mechanism is able by itself to produce a black hole–bulge relation compatible with the one observed at $z = 0$; following the result of chapter 5 we put a second condition for the triggering of the wind, requiring that the mass of cold gas to be removed is not too large:

$$\frac{M_{\text{cold}}}{M_B} < 0.21 \left(\frac{\dot{M}_{\text{BH}}}{4 \text{ M}_{\odot} \text{ yr}^{-1}} \right)^{1.5} \left(\frac{M_B}{10^{11} \text{ M}_{\odot}} \right)^{-1.65} \quad (6.4)$$

A third condition is set by requiring the BH to accrete by more than 1 per cent of the Eddington rate:

$$\dot{M}_{\text{BH}} > 0.01 \frac{M_{\text{BH}}}{t_{\text{Ed}}} \quad (6.5)$$

This is motivated by the low radiative efficiency of the flow in such cases. These three triggering conditions are these proposed in chapter 5 for the triggering of the wind, but their validity is wide enough to be used in a more general context.

The modeling of the wind follows two routes. As a first option, “dry winds” are assumed to remove all mass from the bulge ejecting it to the halo. This gas is assumed to be heated to the inverse-Compton temperature of the AGN, $T \sim 2 \times 10^7$ K. This is what happens if the wind is generated by an injection of kinetic energy coming directly from the accreting BH. Further accretion is possible from the reservoir, which is not depleted by the wind. As a second option, “accreting winds” are assumed to trigger further accretion onto the BH. This is what happens if the wind is generated throughout the galaxy by SNe, then pushed away by radiation pressure of the shining AGN; in this case a fraction f_{center} (set to 0.1) of the ISM is assumed to be compressed to the center, and a fraction f_{lowJ} of this is given to the reservoir of the BH. For simplicity we neglect any star formation connected to this compressed gas; this is done to minimize the effect the highly uncertain mechanism of quasar winds on the host galaxy.

We saw in sec. 4.8.2 that another feedback mechanism is caused by jets emitted by the AGN, which can heat the hot halo gas and quench the cooling flows in large DM halos at low redshift. The importance of this feedback will

be highlighted in chapter 7. We incorporate a self-consistent implementation of this feedback by injecting energy from the accreting BH to the hot halo gas each time the accretion rate is less than 1 per cent of Eddington; in this case the radiative efficiency in jets is known to be highest (see, e.g., Merloni, Heinz & di Matteo 2003). This way the low-redshift cooling flows are slowed down but not quenched to the level required by observations. We also implement a simpler recipe, similar to that of Bower et al. (2005, see also sec. 1.5.1): we estimate the energy that the AGN would give to the hot halo gas if a fraction of the cooling flow was given directly to the BH, then quench the cooling flow each time this energy is higher than the radiated energy. This “forced quenching” is able to solve many of the symptoms of the low-redshift excess of cooling.

6.1.3 Computing LFs and X-ray background

We use the same PINOCCHIO run as the one used in chapter 4, a 512^3 PINOCCHIO realization of a 200 Mpc comoving box ($h = 0.7$). For each run, we compute the evolution of (up to) 100 trees (i.e. DM halos at $z = 0$) per logarithmic bin of halo mass of width 0.5 dex. This implies that while all the most massive halos are considered, smaller halos are randomly sparse-sampled. To properly reconstruct the statistical properties of galaxies we assign to each tree a weight w_{tree} equal to the inverse of the fraction of selected DM halos in the mass bin. The simulated comoving volume of $8 \times 10^6 \text{ Mpc}^3$ sets an upper limit n_{lim} to the number density of objects that can be studied with sufficient statistics. This limit depends on the probability of seeing an accretion event (with a given duty cycle) at a given redshift z in the box, and is computed as:

$$n_{\text{lim}} = \frac{10}{V} \frac{t_{\text{ed}}}{t_{\text{box}}(z)} \quad (6.6)$$

where the limit refers to 10 objects in the box, $t_{\text{ed}} \simeq 0.04 \text{ Gyr}$ is the Eddington time, used as a fiducial duration of an accretion event, and t_{box} is the cosmological time spanned by the box at the redshift z . For a box length of 200 Mpc this function takes values ranging from 10^{-7} Mpc^{-3} at $z = 0$ to 2×10^{-6} at $z = 5$. This way we cannot sample the brightest quasars, characterized by bolometric luminosities well in excess of $10^{47} \text{ erg s}^{-1}$. This allows us to address the bulk of AGN activity at $0 < z < 5$, but not to consider the important problem of the assembly of bright quasars at very high redshift $z \sim 6$. This topic will be addressed elsewhere, using a larger simulated volume.

As mentioned in chapter 4, the information on galaxies is output on a time grid of 0.1 Gyr. Due to the short duty cycle of the BH accretion events, this grid is too coarse to sample properly the AGN activity. Then, information on BH accretion for all the galaxies is given at each integration time-step, whenever this accretion is significant; we use $\dot{M}_{\text{BH}} > 1.76 \times 10^{-3} \text{ M}_{\odot} \text{ yr}^{-1}$, corresponding to bolometric luminosities in excess of $10^{43} \text{ erg s}^{-1}$. With this limit, the detailed information is issued only for a small fraction of integration time-steps. In particular, GALRISE outputs the cosmological time t , the integration time-step Δt , the BH mass M_{BH} , the mass of the reservoir M_{resv} , the bulge mass M_{B} ,

the accretion rate onto the BH \dot{M}_{BH} . Typically, every accretion event spans many contiguous timesteps; we treat each time-step as an independent event with duty cycle Δt . The accretion rate is converted into bolometric luminosity L_{bolo} through the equation $L_{\text{bolo}} = \eta \dot{M}_{\text{BH}}$, where we assume that the accreted mass is converted into radiation with an efficiency of $\eta = 0.1$. Each event is then counted w_{tree} times to correct for the sampling of the merger trees.

We choose to test our model against observed LFs in the B, soft X-ray (0.5-2 keV) and hard X-ray (2-10 keV) bands. The hard X-ray band is the most useful one to compare with (see sec. 2.2); its main advantage lies in the low level of extinction suffered by the radiation, especially for objects at high redshift (whose rest-frame emission is even harder). In this band we can assume that most objects are visible, with the only exception of Compton-thick AGNs, characterized by a hydrogen column density of $N_H > 10^{25} \text{ cm}^{-2}$; these however are thought to represent only a modest (though significant) fraction of the objects (see, e.g., La Franca et al. 2005). Moreover, as the observed hardness ratio of a source allows one to estimate N_H , it is possible to estimate the unabsorbed hard-X flux; this is related to the bolometric luminosity only through a bolometric correction but not through the uncertain fraction of absorbed objects. We compare our predictions with analytic fits of the observed LF, corrected for absorption, proposed by Ueda et al. (2003), Barger et al. (2005) and La Franca et al. (2005).

Unfortunately, data at such high energies are rather sparse, so it is useful to compare also with the better sampled soft X-ray band. The best available data (Miyaji, Hasinger & Schmidt 2001; Hasinger 2005) are restricted to unabsorbed objects with $N_H < 10^{22} \text{ cm}^{-2}$, so we need to correct for the fraction of absorbed objects before comparing model and data. One possible way would be to assign an N_H to each AGN event, then selecting only these that satisfy the selection criterion; this however would decrease the statistics of the model LF. We prefer then to compute the fraction of unabsorbed objects in luminosity bins, given the N_H distribution, and correct our LF by that fraction. For the N_H distribution we use the luminosity-dependent one proposed by La Franca et al. (2005).

We also compare our model to the B-band LFs (Kennefick, Djorgovski & Meylan 1996; Fan et al. 2003; Croom et al., 2004; Wolf et al. 2003; chapter 3), that are measured with the best statistics and in the widest redshift range. As a matter of fact, the most stringent constraint comes from the high-redshift ($3.5 < z < 5.2$), low-luminosity ($M_B \sim -22$ to -24) AGNs observed by GOODS (see chapter 3). To correct for the fraction of type I object we use the luminosity-dependent relation proposed by Simpson (2005). However, we warn that the assumption that only type I AGNs are observed is not good at low luminosities: for instance, of the two $z > 4$ AGNs found in the GOODS survey, one is type I and the other is type II. However, as pointed out by Cristiani et al. (2004), the real news from the GOODS fields is the dearth of faint AGNs, so that a further selection of type I objects would give differences well within the errorbars, and would not change or loosen significantly the constraint.

To transform from bolometric to band luminosities, we use the Elvis et al.

(1974) bolometric correction for the B-band, assuming a value of 10.4 ± 2 for the ratio $\nu_{4400\text{\AA}}/f_{\nu_{4400\text{\AA}}}$ and the bolometric luminosity L_{bolo} . In the X-ray bands we adopt the bolometric corrections proposed by Marconi et al. (2004):

$$\begin{aligned} \text{Log}\left(\frac{L_{\text{bolo}}}{L_{\text{soft}}}\right) &= 1.64 + 0.22L_{12} + 0.012L_{12}^2 - 0.0015L_{12}^3 \\ \text{Log}\left(\frac{L_{\text{bolo}}}{L_{\text{hard}}}\right) &= 1.53 + 0.24L_{12} + 0.012L_{12}^2 - 0.0015L_{12}^3 \end{aligned} \quad (6.7)$$

where $L_{12} = \text{Log}(L_{\text{bolo}}) - 12$. Marconi et al. (2004) also propose a luminosity-dependent bolometric correction for the B-band which is in agreement with the Elvis et al. (1994) correction in the L_{bolo} range of our interest.

To compute the X-ray background predicted by our model, we use the library of QSO template spectral energy distributions (SEDs) we describe in sec. 2.2.1. For each accretion event in our GALRISE output we associate a template spectrum and an N_H value, extracted from the La Franca et al. (2005) distribution, which includes also Compton-thick objects (for which the X-ray flux is set to zero). The N_H absorption is computed using the Morrison & McCammon (1983) cross section. We also compute absorption by the ISM following Madau, Haart & Rees (1999); this is important only at the lowest energies. The integration in redshift is easily performed with the GALRISE output, as this spans the whole range of cosmological times from recombination to the present.

6.2 Results

In this section we compare the results of our model to observations of LFs and number counts in the hard-X, soft-X and optical bands, and to the statistics of remnant BHs at $z = 0$. To best illustrate the constraints that can be obtained on physical processes we show results for five combination of parameters. The first model (STD) is our reference model presented in chapter 4, with the physical and inefficient quenching of the cooling flows by jet feedback. In this case the exponent α_{lowJ} is set to 1, and no winds are allowed. The resulting LFs for this model are always too steep (figures 6.1, 6.2 and 6.3) though the $z = 0$ black hole–bulge relation is roughly reproduced (figure 6.5). Within the range of parameters allowed by the constraints of galactic observables we have found no way to have shallower LFs. On the other hand, the introduction of quasar winds allows us to improve the agreement with AGN data without influencing much the results on galaxies. The second model (model DW) includes dry winds as follows. In order to flatten the AGN LF the α_{lowJ} exponent is set to the slightly higher value of 1.08, and in order to avoid a steepening of the black hole–bulge relation at $z = 0$ dry winds are assumed to take place, with a parameter $f_{\text{qw}} = 0.006$ as stated above. In this case we use $f_{\text{lowJ}} = 0.001$ in place of the 0.003 value of STD. The quenching of the cooling flow is performed with the forced quenching procedure in the third model DWQ. Another good combination of parameters is found by allowing

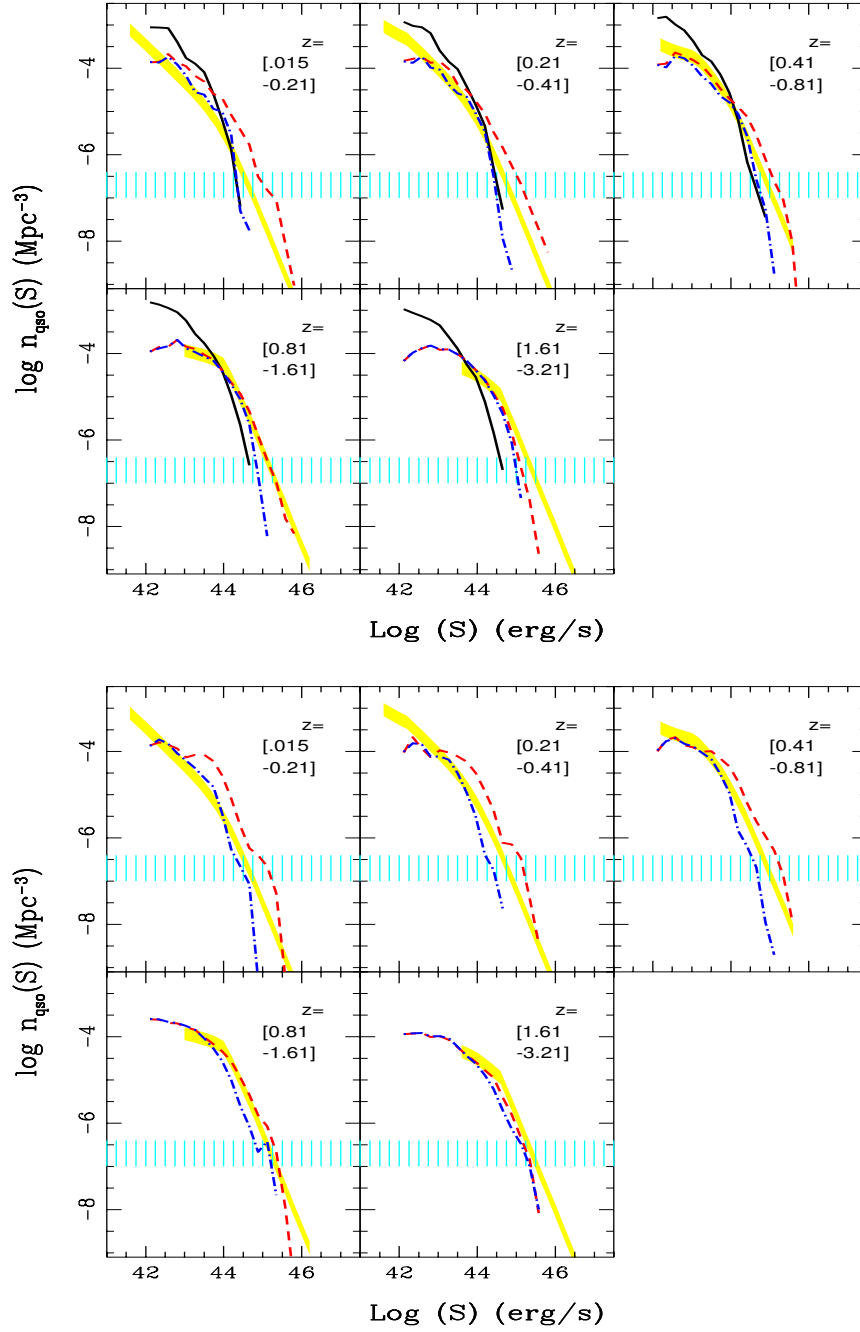


Figure 6.1: 2-10 keV X-ray Luminosity Function. Upper panel: STD model (black solid line), DW model (red dashed line), DWQ model (blue dot-dashed line). Lower panel: AW model (red dashed line), AWQ model (blue dot-dashed line). The cyan shaded area represents the completeness limit of the run (equation 6.6)

accreting winds (with $f_{\text{qw}} = 0.006$, $f_{\text{lowJ}} = 0.003$ and $f_{\text{center}} = 0.1$) and setting $\Sigma_{\text{lim}} = 300 M_{\odot} \text{pc}^{-2}$ (model AW). The fifth model is obtained by using the

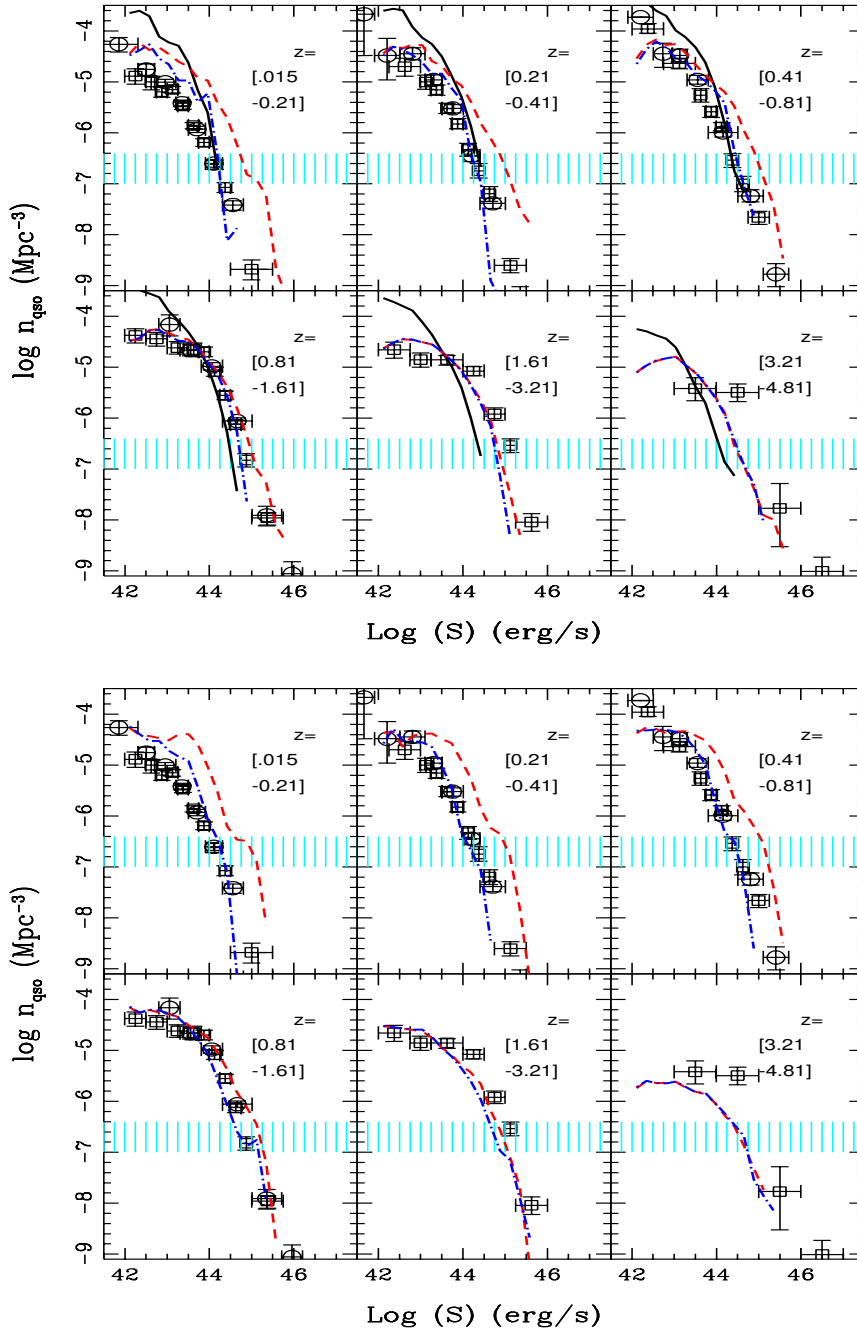


Figure 6.2: 0.5-2 keV X-ray Luminosity Function. Panels and lines refer to models as in fig 6.1. In both panels the data points refer to the observations of Miyaji et al. (2001).

same winds as AW and the forced quenching of the cooling flow (model AWQ).

Figures 6.1, 6.2 and 6.3 show that the models DW, DWQ, AW and AWQ

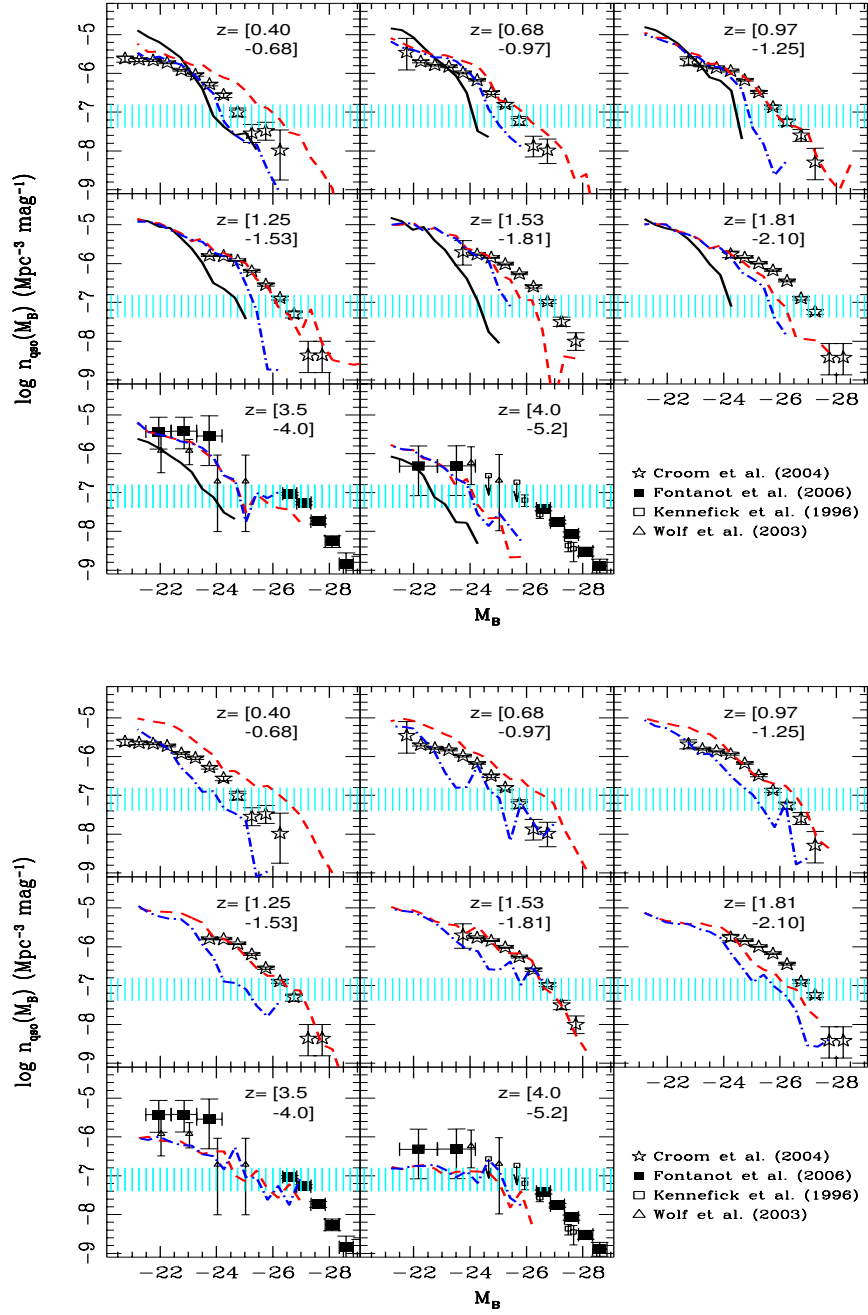


Figure 6.3: B-band Luminosity Function. Panels and lines refer to models as in fig 6.1. In both panels data are taken from Kennefick et al. (1996), Wolf et al. (2003), Croom et al. (2004), chapter 3.

give LFs that fit nicely the observed LFs. At high redshift the DW/DWQ and AW/AWQ predictions are very similar and agree with the observed LFs. At low redshift, the DW and AW models overpredict slightly the normalization

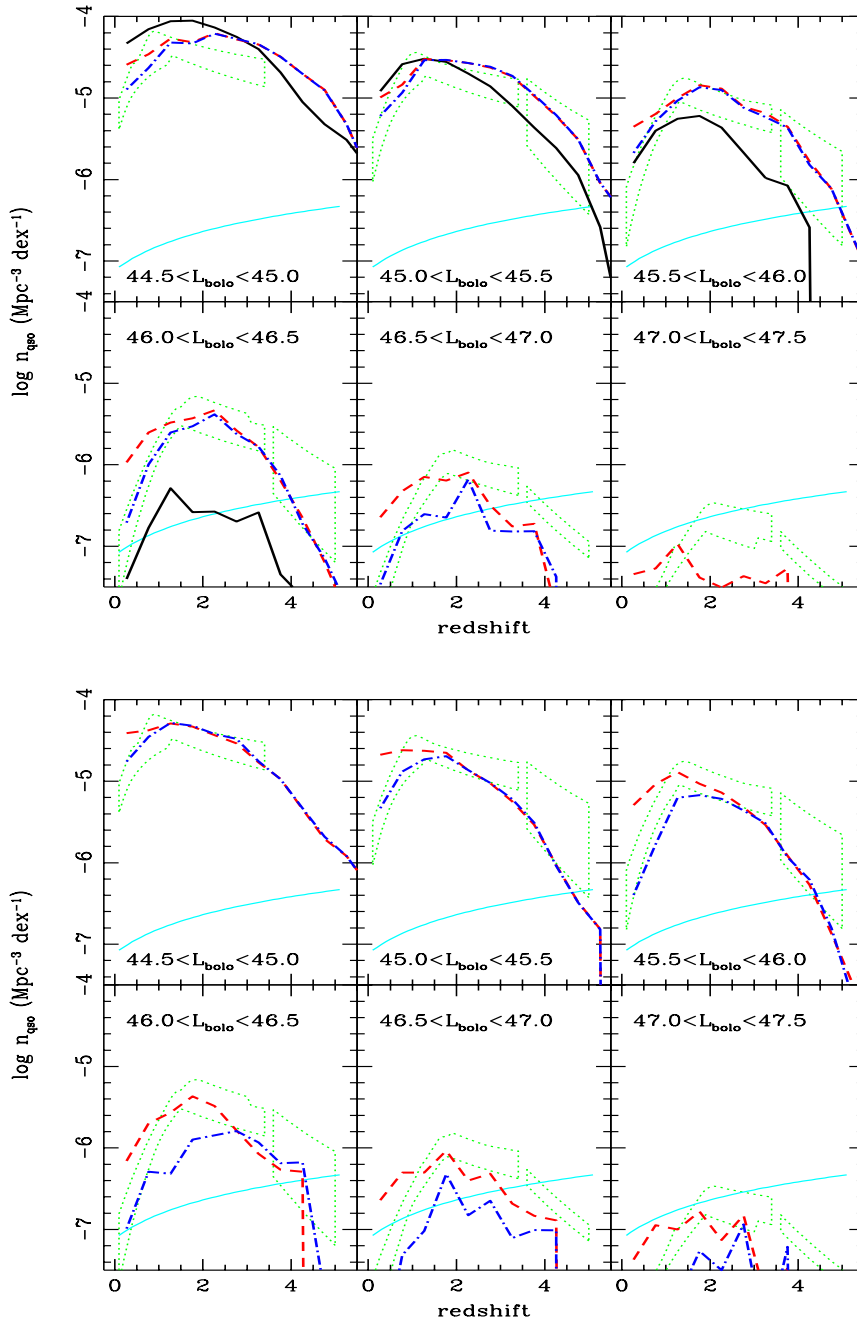


Figure 6.4: The evolution of QSOs number density with redshift in different bins of bolometric luminosity. See text for more details on the estimate of the number density from observational luminosity functions. Panels and lines refer to models as in fig 6.1.

of the LFs; this is expected, as the inefficient quenching of the cooling flow stimulates also the AGN activity. Besides, models DWQ and AWQ give a

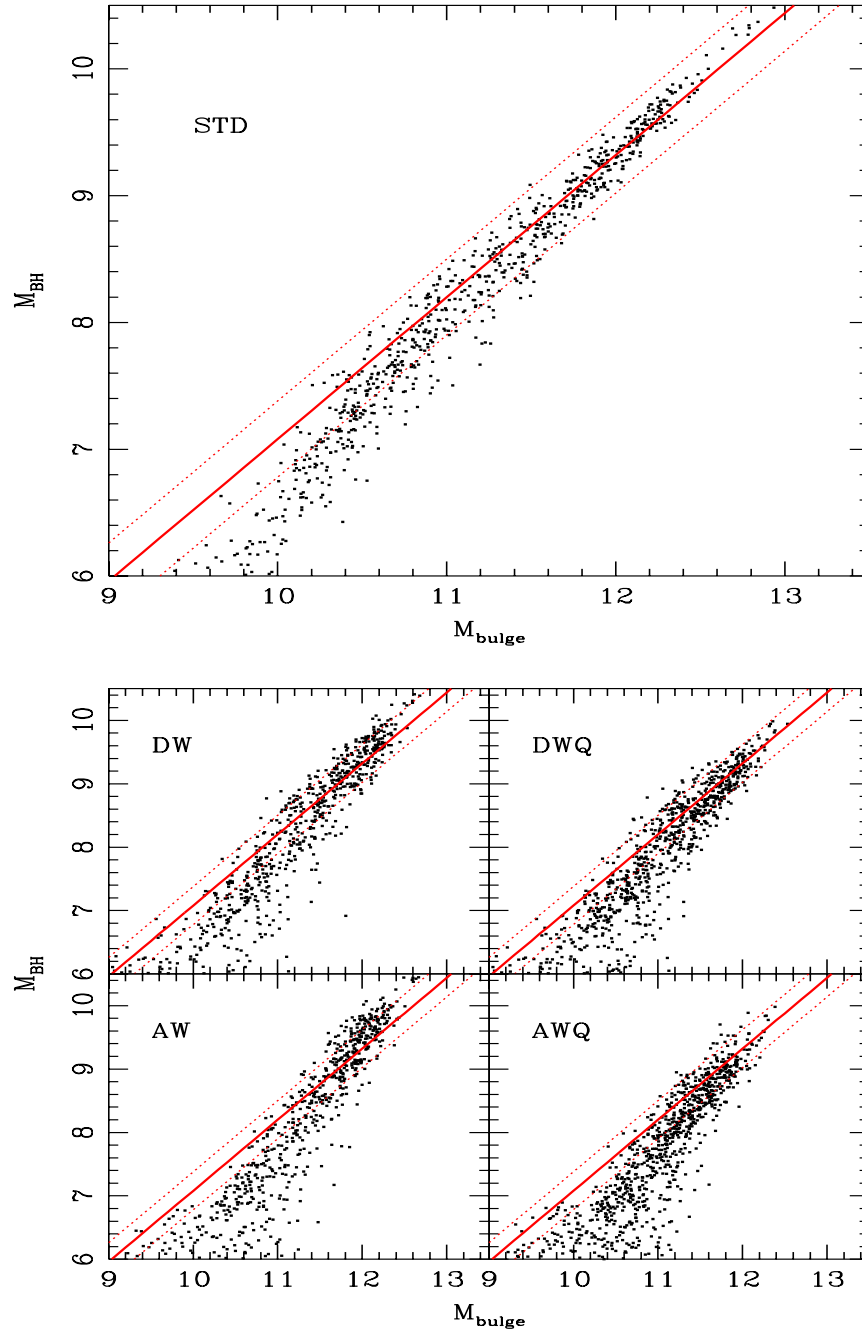


Figure 6.5: $M_{bulge} - M_{BH}$ relation at $z = 0$ for STD (left panel), DW, DWQ, AW and AWQ (right panels) models.

better fit, with a slight underestimate of bright quasars. These two cases should bracket the solution that would be obtained with a fully consistent quenching of the cooling flows.

Figure 6.4 shows the same results in a different way. The number density

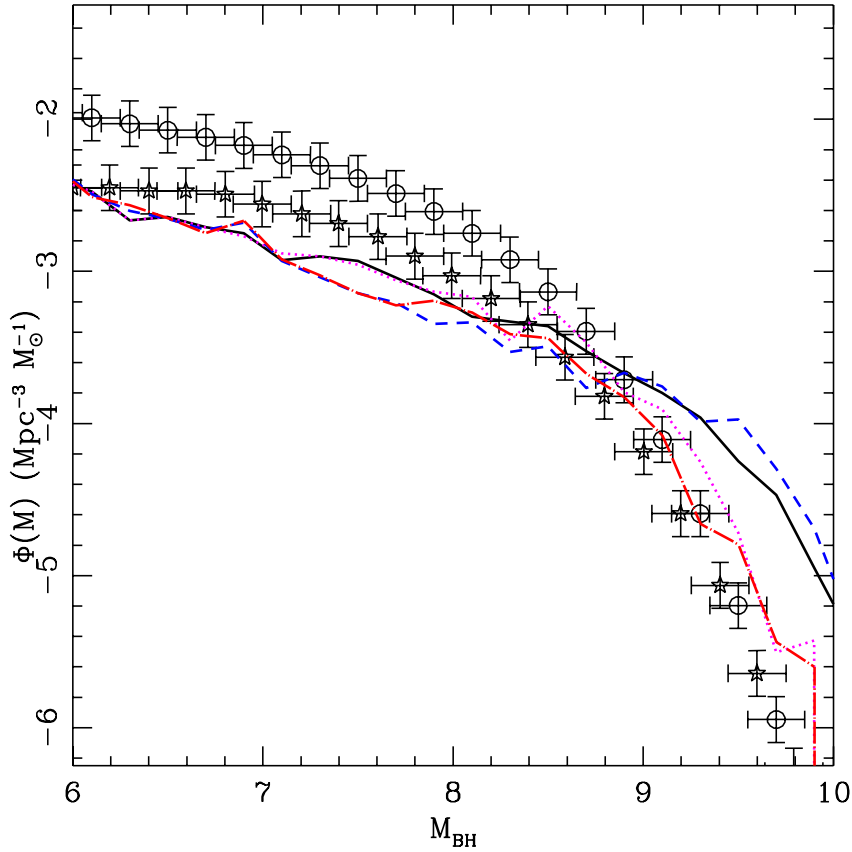


Figure 6.6: The BH mass function. Points refer to the Shankar et al. (2004) (open circles) and Marconi et al. (2004) (stars) estimates; an indicative error-bar of 0.15 dex bot in the x and y directions has been added. Solid line refer to DW model, magenta dotted line to DWQ model, blue dashed line to AW, red dot-dashed line to AWQ.

of AGNs in bins of bolometric luminosity is compared to the range of values inferred from observations (using mainly the analytic fit of the hard-X LFs of Ueda et al. 2003, Barger et al. 2003 and La Franca et al. 2005 for $z < 3.5$, and the results of chapter 3 at $z > 3.5$). The five models are all shown. It is clear that these model reproduce nicely the evolution of the AGN population, and that the forced quenching of the cooling flow is required to obtain the drastic drop of the accretion activity at $z < 2$, even though it causes an excessive decrease of the activity of bright quasars. This figure shows clearly that the peak of the activity as a function of bolometric luminosity is reproduced; in other words, the downsizing or anti-hierarchical behaviour of AGNs can be recovered in the context of the hierarchical Λ CDM cosmogony.

The physical process at the origin of this downsizing is the kinetic feedback active in star-forming bulges. This is shown in figure 6.7, where the DW model is shown with σ_0 values ranging from 0 to 120 km s⁻¹. The kinetic feedback causes a strong cold galactic wind in small bulges, thus decreasing the number

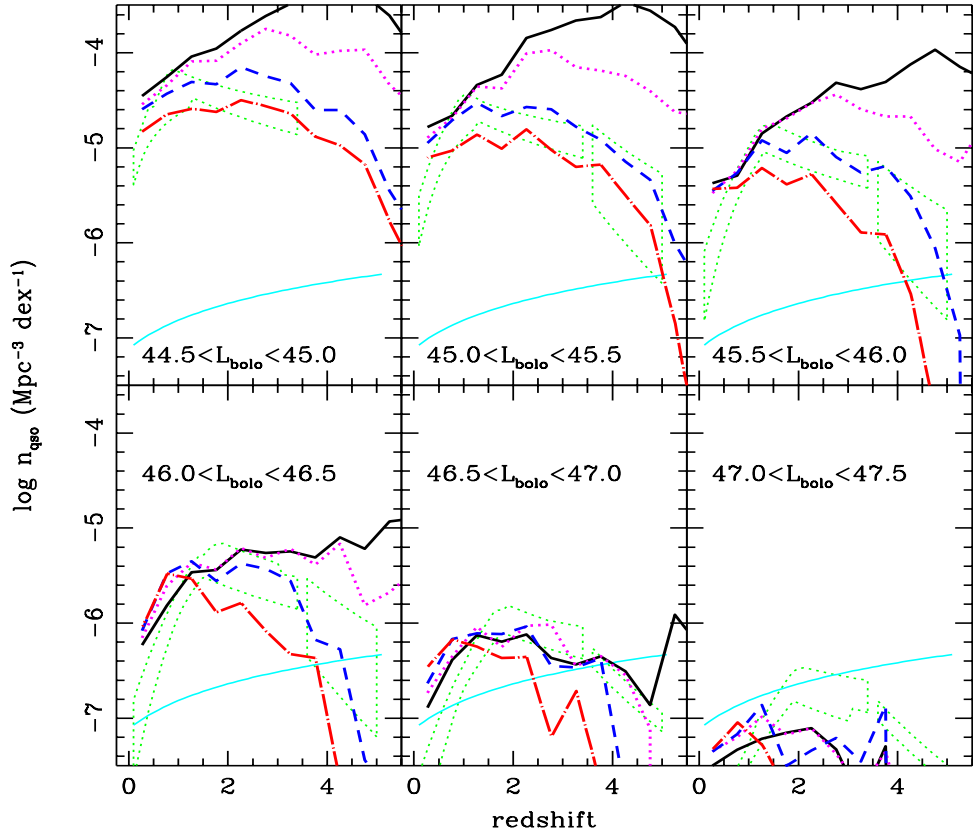


Figure 6.7: The evolution of QSOs number density for the DW model as a function of σ_0 . The black solid line refers to $\sigma_0 = 0 \text{ km s}^{-1}$, the magenta dotted line to $\sigma_0 = 40 \text{ km s}^{-1}$, the blue dashed line to $\sigma_0 = 80 \text{ km s}^{-1}$, the red dot-dashed lines to $\sigma_0 = 120 \text{ km s}^{-1}$.

of faint AGNs without changing much the number of bright quasars. From this comparison we obtain a best-fit value for σ_0 of 80 km s^{-1} ; this is the most effective way to constrain this parameter.

Figure 6.5 shows the black hole–bulge relation at $z = 0$ predicted by the models, while figure 6.6 shows the resulting mass function of BHs. All models, included STD, reproduce the observed range of values for massive bulges ($M_b > 10^{11} M_\odot$), while a slight steepening is predicted at smaller masses, especially for the AW and AWQ models. This shows that this relation is not after all a very strong constraint to the models, despite its fundamental importance in demonstrating the connection between AGNs and their host bulges. A similar reasoning applies to the BH mass function at $z = 0$; here the difference between DW, AW and DWQ, AWQ models is visible in the high-mass cutoff. In all cases the mass function is underpredicted (slightly with respect to Marconi et al. 2004, more significantly with respect to Shankar et al. 2004); this is a consequence of the underprediction of the BH–bulge relation at moderate masses. This is an effect of the same kinetic feedback that allows

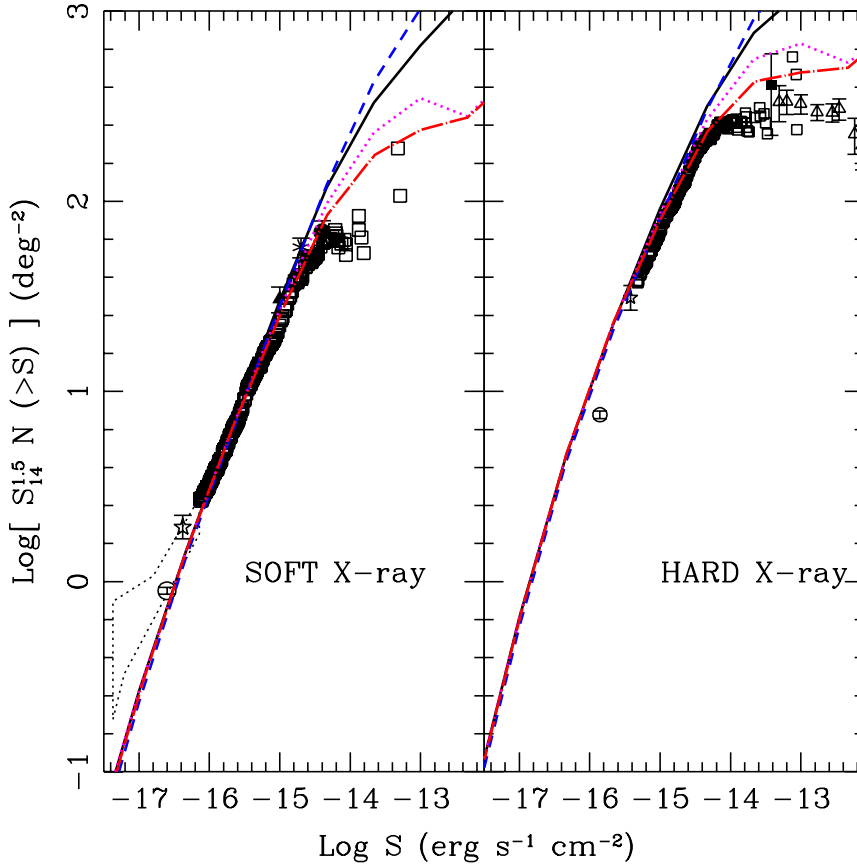


Figure 6.8: Cumulative Source Number Counts in x-ray bands. Left Panel: soft (0.5-2 KeV). Estimates from Hasinger et al., (1993) (*dotted yellow region and filled square*); Brandt et al., (2001) (*empty star*); Bauer et al., (2004) (*empty circle*); Hasinger et al. (1998) (*filled triangle*); Zamorani et al. (1999) (*filled circle*); Rosati et al. (2002) (*empty squares*). Right Panel: hard (2-10 KeV). Estimates from Giommi et al., (2001) (*empty triangles*); Ogasaka et al. (1998) (*filled square*); Brandt et al., (2001) (*empty star*); Bauer et al., (2004) (*empty circle*); Rosati et al. (2002) (*empty squares*). Lines refer to models as in fig 6.6.

the downsizing of the luminosity function. As this range of masses is not very well sampled by observations at $z = 0$, we regard this discrepancy as marginal, and leave a deepening of this point to further work.

6.2.1 X-ray number counts and background

In order to strenghten our conclusions we compare our model predictions to X-ray number counts (figure 6.8) in the soft and hard X-ray bands. Apart from an overestimate at the brightest fluxes, which is more severe for the DW and AW models, the fit to the data is very good in the soft band, while a modest overestimate is visible in the hard band. All the models give very similar results, so that this comparison can be considered only as a very useful

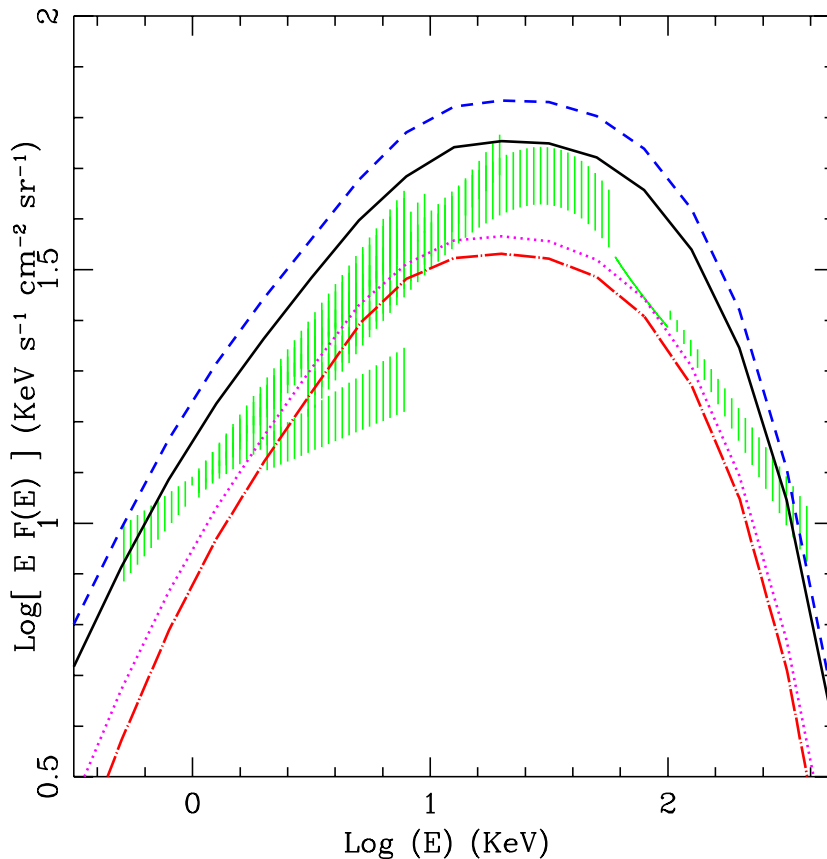


Figure 6.9: The contribution of GALRISE objects to the x-ray background. Observations are taken from Revinvtsev et al. (2003) (*blue region*), Wosley et al. (2004) (*red region*), Georgantopoulos et al (1996) (*cyan region*), Vecchi et al. (1999) (*green region*), Lumb et al., (2002) (*magenta region*), De Luca et al., (2004) (*yellow region*), Kinzer et al., (1997) (*red dashed region*), Gruber et al. (1992) (*cyan dot-dashed region*). Lines refer to models as in fig 6.6.

consistency check.

Figure 6.9 shows the prediction for the X-ray background from 0.5 to 300 keV. The predicted background follows nicely the observed one, though the peak at ~ 30 keV is underpredicted in the case of models AWQ/DWQ. This is in line with the results of La Franca et al. (2005), who claim a missing (though not dominant) population of Compton-thick AGNs, which is not included in this background synthesis as the heavily absorbed objects are neglected. Moreover, models with the physical but inefficient quenching of the cooling flows and models with the forced quenching procedure bracket the correct normalization.

This agreement shows that the population of faint sources is roughly reproduced by our model.

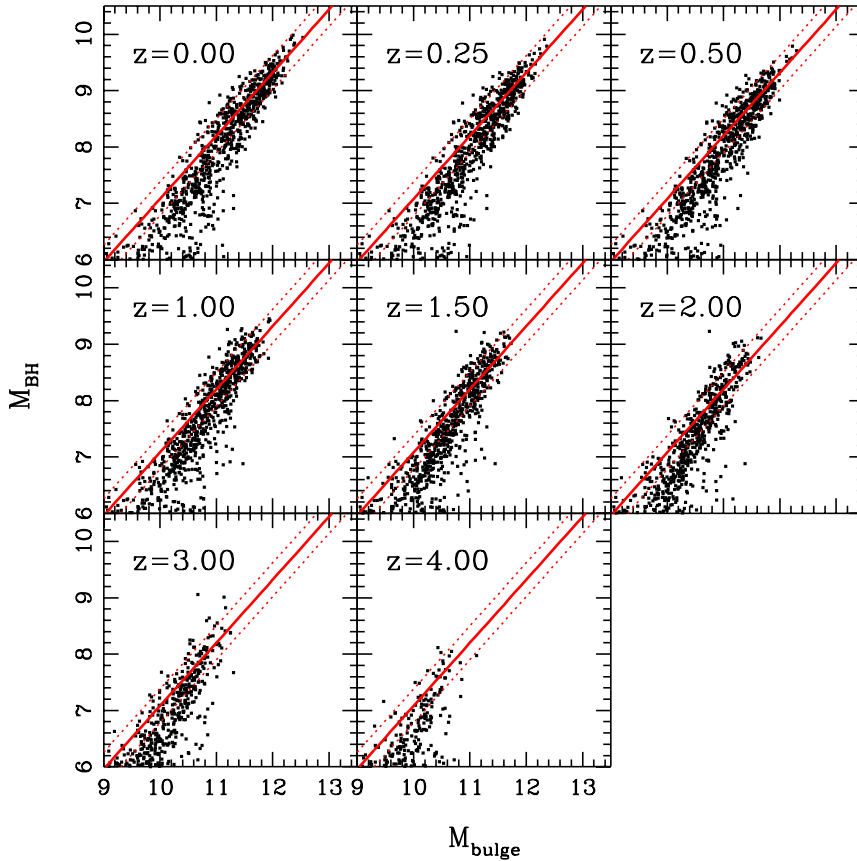


Figure 6.10: Evolution of the BH-bulge relation as a function of redshift for model DWQ.

6.2.2 Predictions

In fig. 6.10 we show the resulting evolution of the BH-bulge relation as a function of redshift for the model DWQ; similar conclusions hold also for the other models. The BH-bulge relation is already in place at high redshift, even though some outlier with relatively high BH masses is visible at high redshift. This can help in understanding the presence of bright quasars at high redshift, when very massive galaxies were not still assembled. This will be deepened elsewhere.

Another important prediction is the average accretion rate of BHs in units of the Eddington rate. This quantity is important to relate the accretion history of AGNs, estimated from the LFs, to the local BH mass function. As each accretion event is subdivided by our model into many sub-events, one per integration interval, we show this quantity averaged over bins in bolometric luminosity and redshift and weighted by the width of the time bin. Figure 6.11 shows the results for the models STD, DW and DWQ; the AW and AWQ models give similar results to DW and DWQ. While the STD rates are very

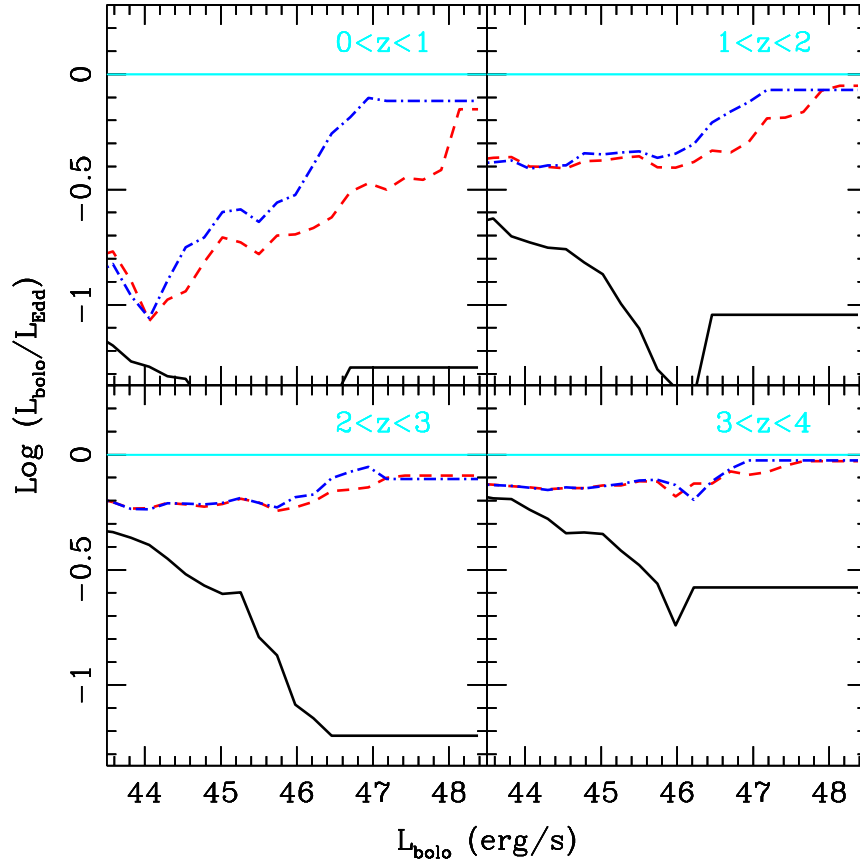


Figure 6.11: Average accretion rates in units of Eddington for the models STD (solid line), DW (red dashed line) and DWQ (blue dot-dashed line).

low, especially for the highest accretion rates, the Eddington ratios of the other models are rather high at high redshift and decrease at low redshift, especially for low AGN luminosities. This shows how the main effect of winds is to force massive black holes to accrete at high rates. The low level of accretion for low luminosity AGN at $0 < z < 1$ is consistent with the findings of Ballo et al. (2006).

6.3 Conclusions on the Effect of Stellar Feedback and Quasar Winds on the AGN Population

Our analysis confirms that models based on the Λ CDM cosmogony are able to roughly reproduce the properties of AGNs. However, in our model it is very difficult, in absence of quasar-triggered winds, to achieve a good fit of the AGN LFs without spoiling the good agreement with the galaxy data presented in next chapter. This can be explained as follows: despite the two-component modeling of the AGN (BH+reservoir), in most accreting black holes the loss rate of angular momentum is much slower than the viscous accretion rate, so

that the accretion rate is roughly proportional to the star-formation rate in bulges. This quantity is constrained by the sub-mm counts and, indirectly, by the almost passive evolution of massive galaxies in the K-band (see chapter 7). On the other hand, the AGN LFs resulting from this star-formation function are too steep, though the local black hole–bulge relation is recovered. This is due to the low level of accretion with respect to Eddington. To improve the fit of the AGN LFs without changing too much the star-formation function of bulges it is necessary to allow for further degrees of freedom of the system. This is most easily done by introducing quasar winds. By presenting two different cases that give similarly good results we aim to stress that the solution of the problem is not unique. Also, the solutions we present could be optimized by a more accurate tuning of the parameters; being the solution not unique, we see no need for such a careful tuning, as the main message is that it is possible to find solutions due to the wide parameter space, but we are not sure how far a given solution should be believed.

In particular, the two solutions that we propose are based on the same triggering criterion for the wind, requiring that (i) the accretion rate is high enough to perturb the ISM, (ii) the ISM to remove is not too massive, (iii) the AGN is accreting in a radiatively efficient mode. The first solution is based on a slight tilt of the relation between bulge star-formation rate and loss rate of angular momentum (where the exponent is 1.08 in place of 1), compensated by “dry winds”, where the kinetic energy injected by the central engine causes a removal of all the ISM from the host bulge. The second solution is based on the “accreting wind” mechanism proposed in chapter 5, where the wind is generated throughout the ISM, so that a fraction of the cold gas is compressed to the center and stimulates further accretion. A good fit of the AGN LFs is then obtained by assuming that discs with high gas density surface lose angular momentum (and then become bulges) by the expected change in the feedback regime (Monaco 2004a) and the consequent increase of the velocity dispersion of clouds.

Despite the uncertainties connected with the complex physics of AGN, there are some conclusions that can be drawn on the feedback mechanisms. In particular, kinetic feedback in star-forming bulges is the key mechanism to create the anti-hierarchical behaviour of the AGN population; the increased velocity dispersion of star-forming bulges leads to a depletion of the less massive bulges, and this hampers the accretion of the less massive BHs, especially at high redshift (where, due to the higher amount of gas available and to the stronger cooling flows, small bulges have stronger star-formation rates). Moreover, the best constraint to the role and value of kinetic feedback in star-forming bulges is given by high redshift faint AGNs, in particular by GOODS observations of faint high redshift quasars (Cristiani et al. 2004, see also chapter 3). However, this downsizing leads to a decrease in the mass of small black holes at $z = 0$ which is in marginal disagreement with observations. This highlights that the modeling of feedback in star-forming galaxies needs much more work.

Another important conclusion is that to reproduce correctly the decrease

of AGN activity at later times (low redshift) it is necessary to switch off the cooling in massive DM halos that host sufficiently large central bulges (and BHs). A self-consistent switching of the cooling flows by feedback from slowly accreting AGNs (such that the accretion rate is less than 1 per cent of the Eddington rate) is inefficient, while a drastic, forced quenching simply based on an energy criterion (similar to that proposed by Bower et al. 2005) gives good results in terms of galaxies, but results in an underprediction of bright AGNs at low redshift. So, the two cases (physical but inefficient quenching, forced quenching) bracket the true solution, which is still to be found.

This model has been extended, through a careful modeling of AGN SEDs, to predict many QSO properties, especially in the X-rays. It reproduces nicely LFs and number counts in the soft and hard X-ray bands, and the measured background from 0.5 to 300 keV, with an underestimate of the peak which confirms the claim for a significant though not dominant population of Compton-thick sources. This implies that the bulk of AGN accretion is roughly reproduced. We then predict the evolution of the BH–bulge relation, the Eddington ratios of accreting BHs at various redshifts and the fraction of mass acquired by mergers and accretions. It results that the BH–bulge relation is already in place at high redshift, though high BH masses in relatively small bulges are found at $z > 2$; (ii) the Eddington ratios of accreting BHs depend mostly on redshift, with low values for the faint AGNs at $0 < z < 1$ that give the bulk of the hard X-ray background (in line with the findings of Ballo et al. 2006).

Chapter 7

The assembly of massive galaxies in the hierarchical cosmogony.

¹We introduced in sec 1.2.4 the so called *downsizing scenario*, according to which more massive galaxies form before less massive ones. The most important evidence of the early assembly of elliptical galaxies comes from Near- (NIR) and Far-Infrared (FIR) observations (see also sec. 1.2.1). In particular, the *K*-band is a very good tracer of the stellar mass at $z \leq 1.5$ (Gavazzi et al., 1996), is almost unaffected by dust extinction, and requires small *K*-corrections that weakly depend on the morphological type, so it is ideal to follow the assembly of the bulk of stellar mass (a galaxy with stellar mass $\sim 10^{11} M_{\odot}$ has a magnitude of $18 < K < 20$ at redshifts $1 < z < 2$). Galaxy number counts in the *K*-band have been studied in great detail by many groups (Mobasher et al., 1986; Glazebrook et al., 1993; Gardner et al., 1993, 1996; Djorgovski et al., 1995; Moustakas et al., 1997; Szokoly et al., 1998; Maihara et al., 2001; Kochanek et al., 2001). The local *K*-band LF has recently been measured with great accuracy by the 2MASS collaboration (Cole et al., 2001; Kochanek et al., 2001). The redshift evolution *K*-selected galaxies has been measured by the recent K20 survey (Cimatti et al. 2002a), a *K*-band limited sample ($K < 20$) with a very high redshift completeness. The K20 collaboration has provided both the redshift distribution of these sources (Cimatti et al. 2002a) and the luminosity functions at redshift 0.5, 1.0, 1.5 (Pozzetti et al., 2003)

The FIR light of galaxies is instead dominated by the emission from warm dust (~ 50 K) present in the regions of massive star formation; this dust absorbs most of the UV/blue photons emitted by young stars and reprocesses it to the FIR. The FIR emission of young, strongly star-forming galaxies at high redshift is observed in the sub-mm, and the steeply decreasing shape of the galactic SEDs from $\sim 100\mu\text{m}$ to ~ 1 mm gives a negative *K*-correction that

¹The results presented in this chapter will be submitted for publication in Fontanot, Monaco et al. (2006b).

promotes the observation of starbursts up to $z \sim 5$. The sub-mm band then, more than the optical bands that probe the rest-frame UV emission of high-redshift galaxies, is useful to reconstruct the star-formation history of the strongest starbursts that presumably give rise to the most massive galaxies. The sub-mm emission is measurable in a few windows, most notably that at $850 \mu\text{m}$. Observations with the Submillimeter Common-User Bolometer Array (SCUBA) on the James Clerk Maxwell Telescope have highlighted the presence of a new population of galaxies (Smail et al. 1997, 2002; Hughes et al. 1998; Barger et al., 1999; Eales et al., 2000; Webb et al. 2002; Borys et al., 2002, 2003; Chapman et al., 2002; Cowie et al., 2002; Scott et al., 2002). These are commonly interpreted as high-redshift massive starbursts, forming stars at rates of hundreds if not thousands of $M_{\odot} \text{ yr}^{-1}$. Given the poor angular resolution of SCUBA images, the search for optical counterparts is very difficult, so that for a proper identification interferometric images at longer wavelengths are required. The resulting redshift distribution is claimed to peak at $z \sim 2.4$ (Chapman et al., 2003).

In this chapter we demonstrate the ability of GALRISE to reproduce the assembly of massive galaxies. To this purpose we concentrate on the $850\mu\text{m}$ band as a tracer of massive star formation at $z \sim 2 - 3$, and on the K band as a tracer of stellar mass at $z \sim 1 - 2$. To pass from physical predictions (stellar masses and star formation rates) to astronomical ones (magnitudes in various bands) we use the GRASIL spectro-photometric code (Silva et al. 1998), which is an ideal tool to produce predictions on galactic SEDs from the UV to the radio. The overall good agreement between predictions and observations demonstrates that, though many details are still to be understood, it is possible within the hierarchical cosmogony to reproduce the early build-up of massive galaxies.

We use the same PINOCCHIO run as the one used in chapters 4 and 6, a 512^3 PINOCCHIO realization of a 200 Mpc comoving box ($h = 0.7$). As shown in chapter 4, galaxies with stellar mass in the range from 10^9 to $10^{10} M_{\odot}$ are sensitive to the mass resolution, so the results we present are fully reliable for the high-mass part ($> 10^{10} M_{\odot}$) of the star mass function. For each run, we compute the evolution of (up to) 100 trees (i.e. DM halos at $z = 0$) per logarithmic bin of halo mass of width 0.5 dex. The implications of this choice have been already discussed in chapter 6.

7.1 Spectrophotometric Codes

Our model for the joint formation of galaxies and AGNs gives accurate predictions for the properties of galaxies in terms of the mass content, star formation rate, kinetic and thermal energy of the different gaseous and stellar phases. On the other hand multiwavelength observations map the electromagnetic spectrum of galaxies with great accuracy. In order to compare our results with observations we need to compute the SEDs of model galaxies at each redshift. The resulting spectra have a complex dependence on star formation and mass assembly history.

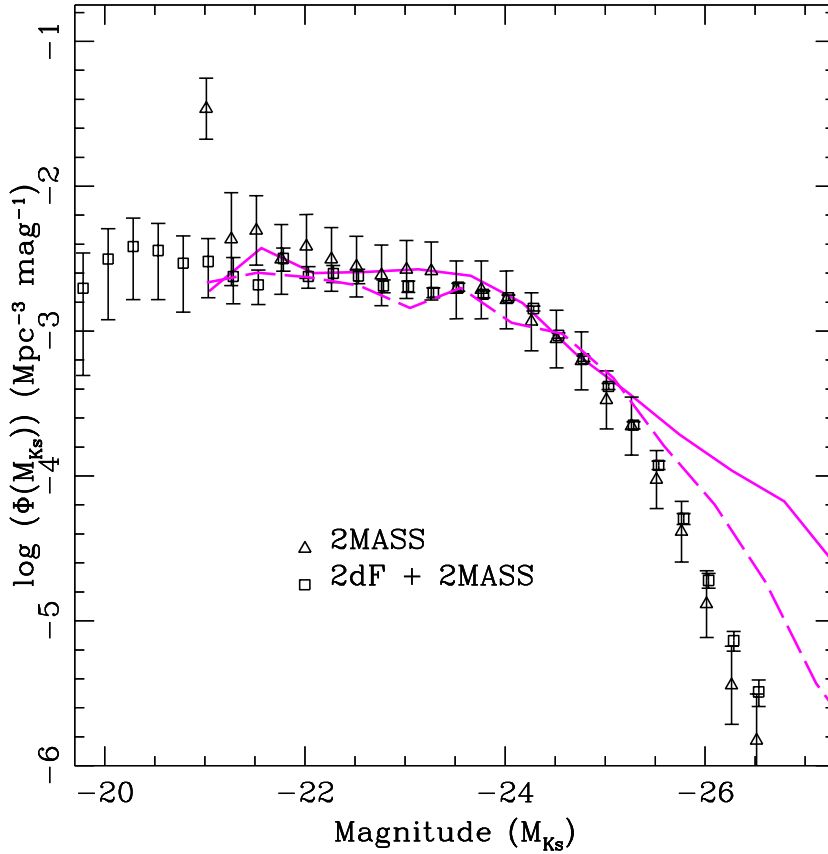


Figure 7.1: K -band Luminosity Function. Data refer to the observations of Cole et al. (2001) and Kochanek et al., (2001). Solid line refers to the GALRISE reference model (tab. 4.2), dashed line refers to the model with the forced quenching of the cooling flows.

7.1.1 Computing Galactic Spectra

The spectrum of a galaxy is the sum of the spectra of its single stars. The stellar content of a galaxy evolves with time because of the continuous death and rebirth of its stellar populations. The spectrum of a galaxy is depends on its star formation history.

We define *Simple Stellar Population* (SSP) an ensemble of coeval stars with the same chemical composition. The properties of an SSP are determined mainly by age, metallicity, and IMF. The IMF is particularly relevant because it determines how many stars of a certain mass form in each SSP: this way it regulates the relative number of long-living, low-mass stars and short-living, high-mass stars. As the age of an SSP increases, stars move along the color-magnitude space (Hertzsprung-Russell Diagram) populating different regions according to their mass. Different evolutionary stages (main sequence, sub-giant, red giant, horizontal branch) are characterized by different stellar spectra. We call the SED of an SSP at a given age *isochrone*. The stellar

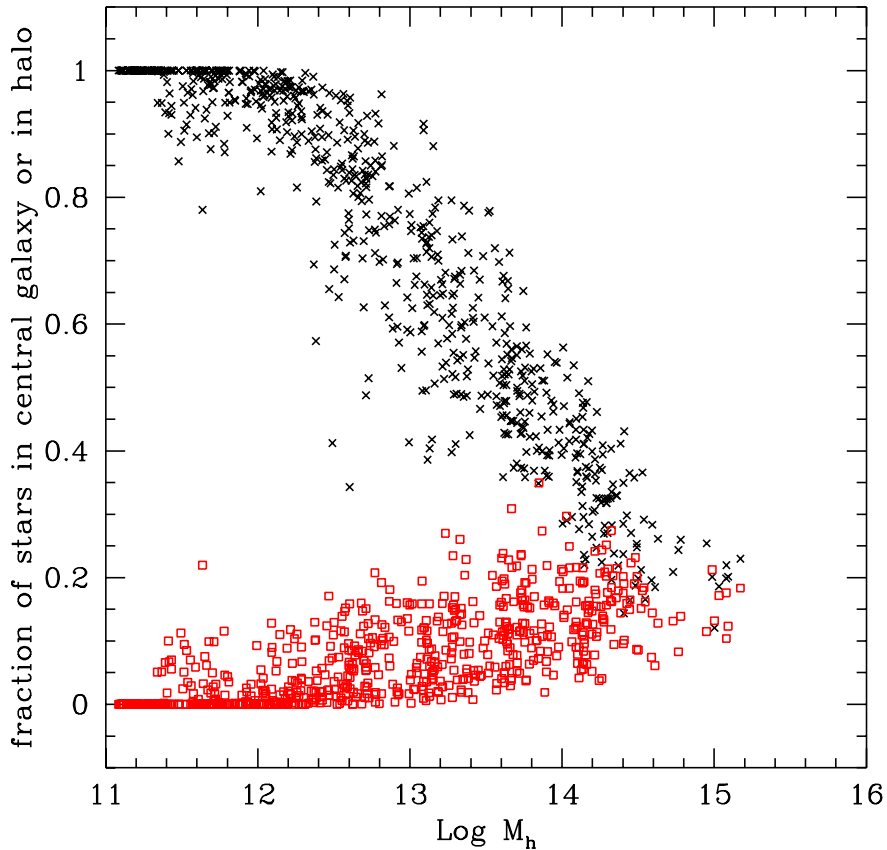


Figure 7.2: Fraction of stars in the central galaxy (crosses) or in the halo (squares) as a function of DM halo mass, in the forced quenching model.

content of a galaxy is better represented by a *Composite Stellar Population* (CSP) because it contains stars of different ages and chemical compositions: however we can define a CSP as the sum of SSP isochrones, each of them relative to the SFR at a given cosmic time.

A numerical code able to compute galactic SEDs using a combination of SSP isochrones is called *spectrophotometric code*. Typically it needs information on the star formation history of the object and its chemical evolution. It then computes the isochrones relative to different SSPs at a given time and performs a weighted average to produce the galactic spectrum. For a general overview of the techniques used in computing CSP from an SSP library and a given star formation history see i.e. Bruzual & Charlot (1991). The galactic spectrum is then convolved with passband filters so as to predict the magnitude of the galaxy.

There are several spectrophotometric codes available in the literature. A first difference between them is related to the adopted isochrone libraries. These differ for several reasons: (i) stellar evolutionary stages under consideration: some stages are poorly known and different models are present in literature (i.e. pulsating regime of AGB stars see Girardi et al., 1996); (ii)

computation of the isochrones: several groups use compilations of observed spectra, while others provide theoretical spectra based on stellar evolutionary models.

A major difference between spectrophotometric models is related to the treatment of the reprocessing of starlight due to the presence of *dust*.

7.1.2 Dust

Observations performed in the last decades have clearly demonstrated that dust is one of the most important components of the ISM. It contains a large fraction of the heavy elements produced by stars. The influence of dust grains on the transfer of radiation coming from stellar systems is of fundamental importance: dust is able to absorb and scatter optical and UV photons and, heated up at a temperature of $\sim 50K$, it reradiates the absorbed energy by thermal emission. The resulting effect is a radical change in the emerging SED of a galaxy. Dust reprocessing is particularly important if we consider the Optical-UV radiation coming from star-forming regions. In fact star formation is favored by the presence of dust, which is able to shield dense molecular clouds from the external UV radiation keeping them to the low temperatures necessary for the onset of gravitational instability. Following this argument it turns out that dust reprocessing is more severe in galaxies undergoing massive episodes of star formation. OB stars are important tracers of the Optical-UV radiation coming from star-forming galaxies. These stars are massive and hot and the maximum of their radiation lies in the UV region. They evolve on a short timescale, so their contribution to the total UV emission is important when the stellar population is young. On the other hand, the cloud is progressively disrupted by the newly born stars. The net effect is that dust obscuration is larger at the first stages after star formation in the cloud begins. We can conclude that the presence of dust has important consequences for what concern the observed galactic properties: neglecting the dust effects can lead to erroneous estimates of many interesting quantities such as the SFR estimated from the rest-frame UV. Also, the estimate of the age of a galaxy through the fit of its broadband SED is hampered by the degeneracy between the colors of an old galaxy and those of an extinguished young galaxy, further complicating the age-metallicity degeneracy (sec. 1.2.4).

At least three different dust environments must be taken into account: (i) dust in *HI* clouds heated by the interstellar radiation field (the so-called *cirrus* component); (ii) dust associated with star-forming molecular clouds; (iii) circumstellar dust regions (necessary for a proper modeling of the windy final stages of stellar evolution and of the SED of AGB stars).

A direct comparison of the luminosity functions of galaxies at optical and infrared wavelengths shows that about 30% of starlight is dust-reprocessed.

Only a few spectrophotometric codes include a detailed modeling of dust reprocessing, while many others include these effects only partially or with crude simplifications. This leads to several discrepancies in the resulting synthetic spectra. These discrepancies are most important at the wavelengths where dust reprocessing is most relevant. As an example, in the NIR and

in particular in the K -band (where radiation is dominated by old and slowly evolving low-mass stars) both dust obscuration and emission is negligible so there is no need for a complete modeling of dust processes; on the other hand in the UV (where starlight is heavily extinguished by dust) and FIR bands (where radiation is mainly dust thermal emission) only a detailed model of dust reprocessing can lead to an adequate reproduction of the observed spectra.

7.1.3 Bruzual & Charlot (2003)

The spectrophotometric code of Bruzual & Charlot (1993) is among the most widely used in the literature. In the following we refer to the most recent version of the code (Bruzual & Charlot, 2003). The model computes the spectral evolution of stellar populations of different metallicities at ages between $10^5 yr$ and $2 \times 10^{10} yr$. Different prescriptions for stellar evolution are available in the code. A first choice is the library of stellar evolutionary tracks computed by Alongi et al. (1993), Bressan et al. (1993), Fagotto et al. (1994a,b) and Girardi et al. (1996). In the original paper of Bruzual & Charlot they refer to these tracks as the “Padova 1994” library. This library encompasses a wide range of initial chemical compositions: $Z = 0.0001$, $Z = 0.0004$, $Z = 0.004$, $Z = 0.008$, $Z = 0.02$, $Z = 0.05$, $Z = 0.1$, with the Helium fraction assumed as $Y = 2.5Z + 0.23$. The range of initial masses is $0.6 \leq m \leq 120M_{\odot}$ for all metallicities, except for $Z = 0.0001$ ($0.6 \leq m \leq 100M_{\odot}$) and $Z = 0.1$ ($0.6 \leq m \leq 9M_{\odot}$). Tracks are computed using the radiative opacities of Iglesias, Rogers & Wilson (1992) and include all phases of stellar evolution from the zero-age main sequence to the beginning of the thermally pulsating regime of AGB stars (TP-AGB). For a solar composition the models are normalized to the temperature, luminosity and radius of the Sun at $4.6Gyr$. Tracks include mild overshooting in convective cores of $m > 1.5M_{\odot}$ stars and core overshooting with reduced efficiency for $1.0 < m < 1.5M_{\odot}$ stars. Girardi et al. (2000) produced a new version of this library, in which the main novelties are a revised equation of state and new low-temperature opacities. The revised library includes stars with masses down to $0.15M_{\odot}$, but does not contain stars more massive than $7M_{\odot}$. Bruzual & Charlot (2003) combined these new tracks of low- and intermediate-mass stars with high-mass tracks from the “Padova 1994” library and refer to this revised set as “Padova 2000”. The third prescription they consider is valid only for solar metallicities and is based on the work of Shaller et al. (1992, for $m \geq 2M_{\odot}$) and Charbonnel et al. (1996, for $0.8 \leq m < 2M_{\odot}$; 1999, for $0.6 \leq m < 0.8M_{\odot}$). The authors refer to these track as the “Geneva” library. Tracks include all phases of stellar evolution up to the beginning of TP-AGB and are normalized to the temperature, luminosity and radius of the Sun at $4.6Gyr$. There several differences between these tracks and the “Padova 1994” tracks, mainly due to the treatment of convection and overshooting. These tracks include a treatment of mass loss both in massive stars and along the red giant branch. Moreover, Bruzual & Charlot supplement the track of low- and intermediate-mass stars beyond the early AGB phases with TP-AGB and

post-AGB evolutionary tracks following the work of Vassiliadis and Woods (1993).

To account for the attenuation of starlight by dust, they adopt the simple prescription of Charlot & Fall (2000), based on the definition of an “effective absorption” $\tau_\lambda(t)$, which describes the attenuation of photons emitted at all directions by stars of age t in a galaxy.

$$\tau_\lambda(t) = \begin{cases} \tau_V(\lambda/5500\text{\AA})^{-0.7} & \text{for } t \leq 10^7\text{yr} \\ \mu\tau_V(\lambda/5500\text{\AA})^{-0.7} & \text{for } t > 10^7\text{yr} \end{cases} \quad (7.1)$$

where τ_V is the total effective V -band optical depth seen by young stars. The characteristic age 10^7yr corresponds to the typical lifetime of a giant molecular cloud. The adjustable parameter μ defines the fraction of the total optical depth of the galaxy contributed by the diffuse interstellar medium ($\mu \sim 1/3$ on average, with substantial scatter).

7.1.4 GRASIL

One of the most important distinctive features of GRASIL is the inclusion of the effect of age-selective extinction (i.e. the observed trend of younger stellar populations of being more affected by dust obscuration). In fact, young stars are systematically found in the dense, chemically enriched and dusty molecular clouds. The massive, newly born stars progressively destroy the cloud (see, e.g., Monaco 2004b) and/or escape the star-forming region due to their peculiar motions. As a result, the earlier stages of a star formation episode – when the most massive OB stars are still alive – are more affected by dust obscuration.

Given the star formation and chemical enrichment history of a model galaxy, GRASIL computes the time-dependent UV-to-radio SED of the galaxy, with a state-of-the-art treatment of radiative transfer in a dusty ISM. This requires an assumption on the geometry of the system; we follow Silva et al. (2005) in assuming that the system is a superposition of an exponential disc and a bulge with a King profile. The cold gas is sub-divided into two phases, a diffuse one corresponding to cirrus dust, and a denser molecular one. The effect of selective extinction is taken into account by assuming that a fraction of the starlight radiated within a molecular cloud is a function of the star age. If t_{esc} is the time-scale for the destruction of the molecular cloud (or equivalently for the exit of stars from the cloud), all stars are assumed to radiate within the cloud up to t_{esc} , after which the fraction of radiation from exited stars linearly increases from 0 to 1 at $2t_{\text{esc}}$. The timescale t_{esc} is inferred to be longer in starbursts than in normal disk-like galaxies (Silva et al. 1998).

Another important parameter is the ratio f_{mc} of molecular to total gas, for which we assume a value of 0.50. The resulting molecular mass is subdivided into spherical clouds of mass m_{mc} and radius r_{mc} . The ratio $m_{\text{mc}}/r_{\text{mc}}^2$ is assumed to vary within the typical range of Milky Way molecular clouds. We also assume that the ratio δ_{dust} of dust to gas mass scales linearly with the metallicity, while the quantity $\tau_{\text{mc}} = \delta_{\text{dust}}m_{\text{mc}}/r_{\text{mc}}^2$, which gives an estimate of the optical depth of the clouds, is set to $\tau_{\text{mc}} = 45$ (Silva et al. 2004). As

for dust composition, the model assumes a mixture of graphite, silicate grains and polycyclic aromatic hydrocarbons (PAHs) with size distributions tuned to match the extinction and emissivity properties of the local ISM (Silva et al., 1998).

The SSP isochrone library included in the code is based on the Padova stellar models (Fagotto et al. 1994a,b, updated by Girardi et al. 2000) and covers a wide range of ages and metallicities. Starlight reprocessed by dust in the envelopes of AGB stars is included directly into the SSPs as described by Bressan et al. (2002).

7.2 From physical to astronomical quantities

The output of GALRISE consists (see chapter 4), for each galaxy, in a time sampling (with time bins of 0.1 Gyr) of the main dynamical variables of the model: for each component (halo, bulge, disc) the code issues mass, kinetic energy and metal mass of cold gas; mass, thermal energy and metal mass of hot gas; mass and metals of stars; average (over the time bin) and punctual (at the end of the time bin) star formation rate (these are given only for bulge and disc). For each galaxy it gives also expelled mass and metals, black hole mass, cooling radius, bulge and disc radii and velocities, punctual values of the accretion rate onto the black hole. In order to compare these predictions with observations we need to compute the Spectral Energy Distributions (SEDs) of the model galaxies, and convolve them with the filters used in a set of observations so as to obtain the magnitudes. Moreover, in order to compute the number counts of sources this computation must be repeated at several redshifts.

7.2.1 Interfacing the Spectrophotometric code with GALRISE

For each galaxy generated by GALRISE we give its star-formation history and metallicity of cold gas to GRASIL or Bruzual & Charlot (2003); only the bulge and disc components are used, the halo component is neglected.

The width of the time bin used for sampling the output quantities is larger than the lifetime of massive stars (which contribute mostly to B/UV and to FIR through dust-reprocessing), so for these the time sampling is too poor. We then split the last time bin into a sub-bin of 10 Myr, to which we assign the punctual value of the star-formation rate at the end of the bin, and a larger, earlier one of 90 Myr, to which we assign a star formation rate such that the integral in the two sub-bins gives the correct final amount of stars. The final time bin may be smaller than 100 Myr, because the age of the Universe is not a multiple of the bin width; in this case the earlier sub-bin will be consistently smaller than 90 Myr, while the later one is kept fixed to 10 Myr.

Once this information is provided to the spectrophotometric code, the restframe SEDs are computed, and from these the absolute restframe magnitudes (or fluxes for FIR and radio bands) and the apparent observer-frame magnitudes/fluxes for many passband filters. For apparent magnitudes

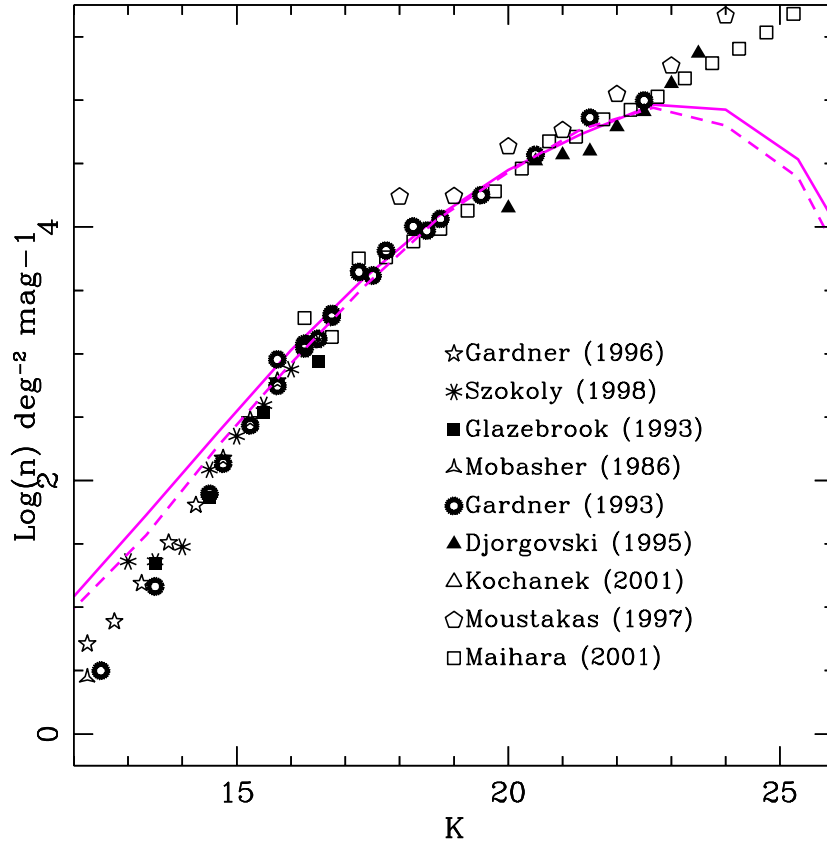


Figure 7.3: K -band Source Number Counts. Data refer to observations as listed in the figure. Lines refer to models as in fig. 7.1.

of high-redshift objects we model the IGM absorption by convolving the redshifted SEDs with the Madau, Haardt & Rees (1999) templates. We also include (on request) the AGN SED, modeled according to the punctual value of the accretion rate onto the black hole using the AGN library described in sec. 2.2.1.

Finally, it is worth mentioning that running the spectro-photometric code on model galaxies is the main bottleneck of the computation; it is then necessary to devise strategies to optimize the computation of observables, especially number counts, by estimating the minimal number of galaxies needed to have a reliable result.

In this chapter we will focus on the results obtained using GRASIL, even if the interface is designed to work both with GRASIL and Bruzual & Charlot (2003) code. We adopt a Salpeter (1955) IMF, both for the bulge and disc component.

7.2.2 Luminosity functions, number counts and redshift distributions

We run GRASIL on catalogues of model galaxies at several redshifts. As explained in chapter 4, the sparse-sampling of trees results in an over-sampling of small satellites with respect to central galaxies of similar (bulge plus disc) mass. These satellites also require a great amount of computing time. We correct for this over-sampling by further sparse-sampling the satellites as follows. First, we construct from the results of the run at $z = 0$ an average curve of mass of the central galaxy as a function of DM halo mass; second, we randomly sparse-sample the satellites with a probability equal to the ratio between the weights w_{tree} of the tree the satellite belongs to and that of the DM halo whose central galaxy has the same mass as the satellite. The inverse of this probability is a new weight, w_{gal} . Central galaxies are all selected and assigned a unity weight. Galaxies destroyed by mergers or tides are assigned a weight according to their mass at the merging or disruption time. This procedure gives a roughly constant number of galaxies in logarithmic intervals of mass. To further decrease the number of galaxies (which is useful when computing number counts) we add a further random selection which is applied to all galaxies; as a consequence, the weight w_{gal} can be less than unity even for central galaxies.

The two samplings (of merger trees and of galaxies) are both computed at $z = 0$, but the weights w_{tree} and w_{gal} assigned to the galaxies are used at any redshift. This is done with no loss of generality, as a fair reconstruction of luminosity functions or number counts only requires that the weights are used consistently with the sparse-sampling procedure.

Luminosity functions are then computed simply by weighting the galaxies by the product of the tree weight w_{tree} and the satellite weight w_{gal} . In the following we use $w_{\text{gal}} = 1$ for the central galaxies to compute the LFs at $z = 0$, and $w_{\text{gal}} = 0.5$ at $z = 0.5, 1$ and 1.5 .

Number counts are computed by sampling a line of sight with the same box replicated N times at several redshifts z_n , starting from $z \sim 6.5$ to the present time. Assuming that the line of sight is aligned with one of the sides, a box centered at z_n spans a redshift range $[z_{n,\text{dw}}, z_{n,\text{up}}]$, where:

$$z_{n,\text{dw}} = z \left(t(z_n) + \frac{l_{\text{box}}/2}{c(1+z_n)} \right) \quad (7.2)$$

where l_{box} is the box length, $t(z_n)$ is the cosmic time at z_n and c is the speed of light. A similar equation, with a $-$ sign, holds for $z_{n,\text{up}}$. For each box at redshift z_n (with n increasing with the cosmic time) we randomly associate to each galaxy a redshift in the interval $[z_{n,\text{dw}}, z_{n-1,\text{dw}}]$ (for $n = 1$ we use $z_{n,\text{up}}$); in this way the whole line of sight is sampled. Moreover, we do not take into account the spatial position of the galaxy, so that the large-scale structure within the box does not influence the redshift distribution of sources. Apparent magnitudes and fluxes of model galaxies are then computed at the given redshift. The contribution of a galaxy to the number counts is computed according to the angle subtended by a square of comoving side l_{box} at the

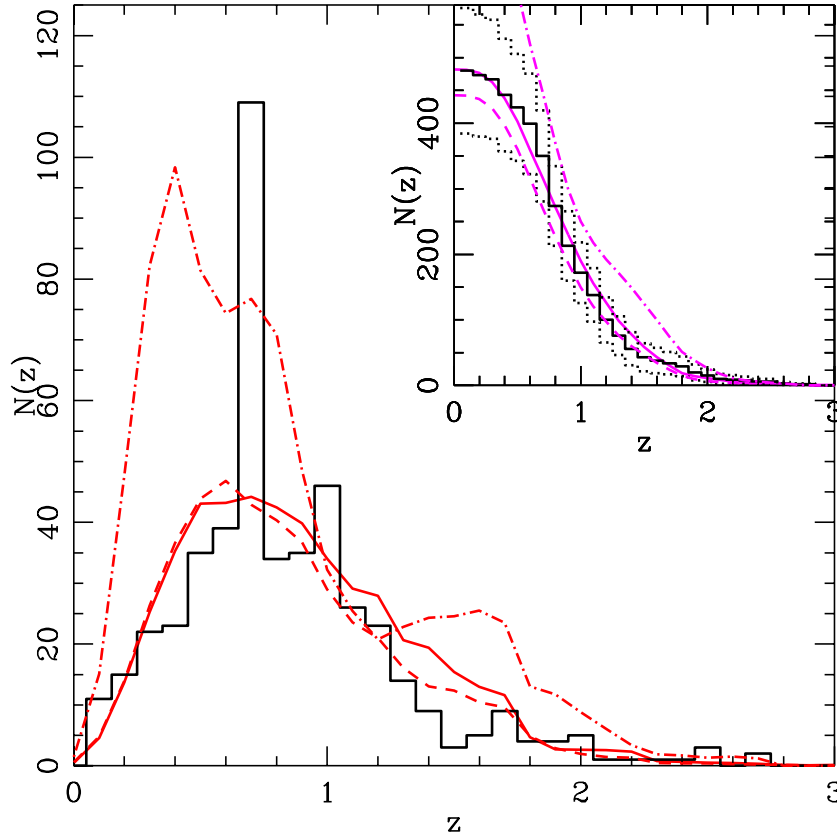


Figure 7.4: Redshift source distribution compared to K20 sample (Cimatti et al., 2002). Lines refer to models as in fig. 7.1. Dot-dashed line refers to a model without stellar feedback. The panel in the upper-right corner gives the cumulative distribution with $1\text{-}\sigma$ poisson errors.

corresponding redshift.

To compute the optimal number of boxes needed to sample the line of sight, we have performed tests with a complete coverage and a sampled coverage of the redshift range. In the case of complete coverage the redshift intervals are chosen so as for each $n > 1$ $z_{n,\text{up}} = z_{n-1,\text{dw}}$; in other words, the line of sight is sampled by adjoining boxes. Starting from $z \sim 6.5$, this requires 43 boxes, of which 17 are used at $z < 1$. In the case of sampled coverage, the boxes do not touch but are distributed over regular grids in some time-dependent quantity. In this case we associate to each object a further, third weight w_{counts} proportional to the ratio of l_{box} and the comoving distance that separates $z_{n-1,\text{dw}}$ and $z_{n,\text{dw}}$. We have tested several sampling schemes, based on uniform sampling in redshift, in cosmic time, in scale factor and in comoving distance. For each scheme we vary the number N of boxes, checking the value at which the resulting number counts reproduce these computed with complete coverage with a smaller error than ~ 0.15 dex, estimated to be the observational error of galaxy counts in the K -band. This way the result is insensitive of the sampling

strategy, which is then chosen so as to minimize the number of boxes needed. The best strategy results in a sparse sampling on scale factor, for which 11 boxes at intervals of 0.08 in a are sufficient. However, this sampling guarantees a numerical convergence of the number counts, but not a proper sampling of the redshift space, which is very good at later times but rather poor at $z > 1$. We then resort to a mixed sampling strategy by forcing a minimal redshift interval of 0.5 for $z < 3$ (where most of the K -band and $850\mu\text{m}$ objects are located) and 1 for $z > 3$. This means that the galaxies evolved up to some redshift z_n will be scattered in a redshift interval not larger than that quoted above; this is considered adequate given the relatively slow evolution of the population of galaxies with z . Finally, the last box is located at $z = 0.023$, so that $z_{N,\text{dw}} = 0$. With this procedure we obtain 15 boxes, located at $z = 6.33, 5.33, 4.33, 3.33, 2.83, 2.33, 1.83, 1.33, 0.96, 0.70, 0.49, 0.33, 0.21, 0.10$ and 0.023 (all these numbers are relative to $l_{\text{box}} = 200$ Mpc). For each box we set $w_{\text{sat}} = 0.2$ for the central galaxies; in this way a line of sight is sampled by roughly 3200 galaxies. Also, the sparse sampling is re-done for each box, so as not to choose always the same galaxies. There is clearly a redundancy in this procedure, but the galaxy sample is wide enough to be a fair tracer of the whole population.

7.3 Results

7.3.1 K -band LF

The resulting K -band LF is compared in figure 7.1 (where the prediction of the reference model is the solid line) to the data of the local 2MASS sample (Jarrett et al., 2000), limited to $K_s < 13.5$ (Kochanek et al., 2001), and to the estimate of Cole et al. (2001) obtained combining the 2MASS and 2dF samples. This comparison is analogous to the one of stellar mass functions presented in figure 4.6. The K -band LF is recovered correctly for $M_{K_s} > -25$, while the high-luminosity tail presents objects that are too bright by nearly two magnitudes, corresponding to a difference in stellar mass of factor ~ 5 . In the same figure we show also the prediction for the model with the forced quenching of the cooling flows (see sec. 4.11). Also in this case the model with this prescription is able to recover the exponential cut of the luminosity function.

Another possible explanation for the problem of the overprediction of luminous and massive galaxies is shown in figure 7.2, where we show for the trees at $z = 0$ the fraction of stars in the central galaxy and in the halo. This latter quantity is predicted to lie between 10 and 20 per cent in halos corresponding to rich clusters ($M_H > 10^{15} M_\odot$). Observational estimates (Gonzalez et al. 2000; Feldmeier et al. 2002; Gal-Yam et al. 2003) suggest higher values for this fraction, ranging from 20 to 40 per cent. A high fraction of halo stars in rich galaxy clusters is supported also by Nbody/SPH simulations (Murante et al. 2004). This evidence should be taken with care, but if this disagreement is true, then the stellar mass to be found in the halo should be obviously taken from the central galaxy, thus lowering its mass as needed. This

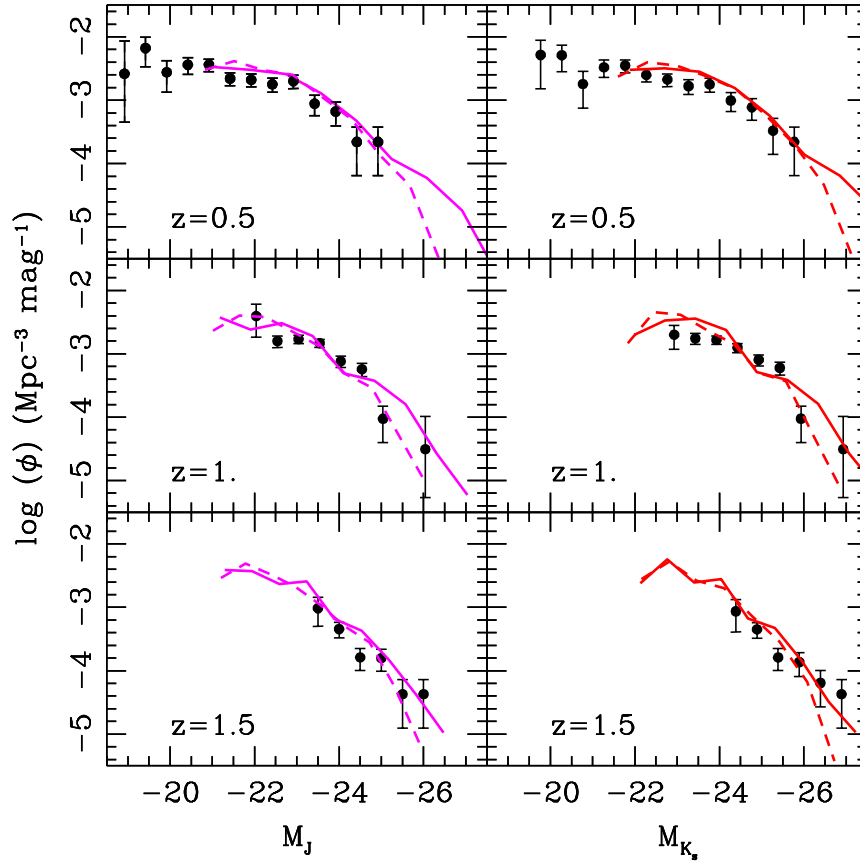


Figure 7.5: LF Redshift Evolution in the K20 sample. Data points are taken from Pozzetti et al. (2003). Lines refer to models as in fig. 7.1.

possibility is currently under investigation.

Figure 7.3 shows the predicted K -band number counts compared to the data indicated by the labels. The model fits the data with a remarkable accuracy in the range $16 \leq K \leq 22$. There is a clear overestimate at bright fluxes, which is another signature of the poor cutoff of the luminosity function, while the drop at the faint end is due to the mass limit.

The importance of number counts as a strong constraint to the model is subject to the requirement of recovering at the same time the redshift distribution of the sources. We then compare our results with the redshift distribution of $K_s < 20$ sources in the 52. arcmin² of the K20 survey. The total number of objects in the K20 survey is 480 versus a predicted number of objects of 490 for the same area². Model and data are then consistent. Figure 7.4 shows the predicted redshift distribution compared to the K20 data; the overall agreement is excellent: the position of the peak at $z \sim 0.8$ and the long tail of galaxies at $z > 1.5$ are both recovered.

Figure 7.5 shows the comparison of models and K20 data in terms of

²We use the actual limit of 19.8, see Cimatti et al. (2002)

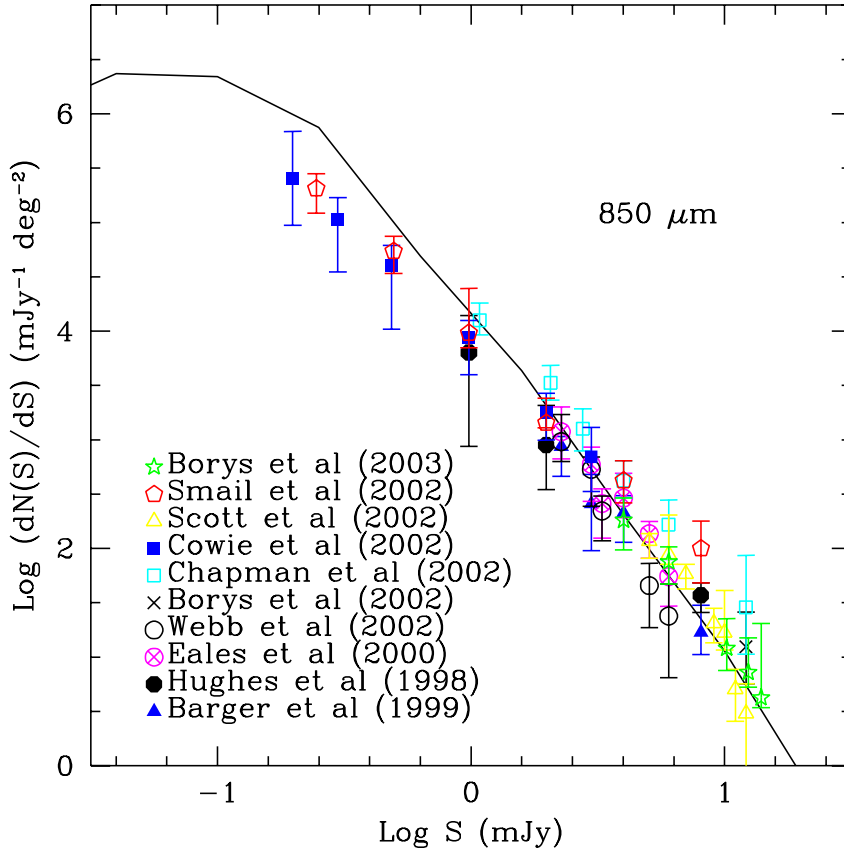


Figure 7.6: 850μ Source Number Counts. Data refer to observations as listed in the figure. Solid line refers to the model as in fig. 7.1.

luminosity functions at $z = 0.5, 1$ and 1.5 (Pozzetti et al. 2003). In this case the box at a single redshift is used, so any evolutive effect within the observative redshift bin is neglected; however, the evolution of these objects is so similar to passive that this effect is unlikely to be important. The agreement is again very good, with a possible marginal overestimate of the low-luminosity tail.

The figure 7.4 shows also the predictions for a model with AGN+stellar feedback switched off (dash-dotted lines). Clearly, a proper modeling of stellar feedback is the key ingredient to obtain the peak of the distribution, while AGN feedback helps but not in a determinant way.

We conclude from this comparison that the stellar mass of massive objects is correctly predicted by our model to be in place at $z \sim 1 - 2$; however, the biggest model galaxies continue growing in mass at $z < 1$, though this growth could be compensated for by the loss of stars to the halo by gravitational scattering.

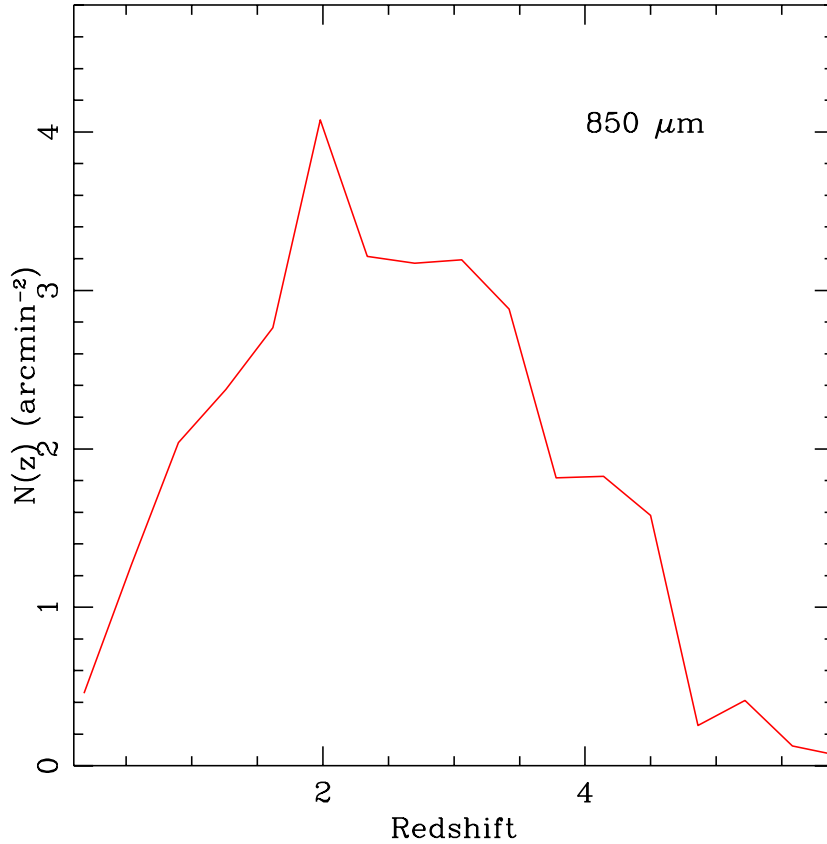


Figure 7.7: Predicted Redshift Distribution for 850μ sources. Solid line refers to the model with the feedback prescription of Monaco (2004ab).

7.3.2 $850\mu\text{m}$ counts

The results presented above show that GALRISE is able to reproduce the early assembly and late passive evolution of the bright galaxies. We now test whether these stars were formed in small chunks that were later assembled together, or in big starbursts at $z > 2$. This is best tested by comparing the reference model to number counts at $850\mu\text{m}$, where massive starbursts at $1 < z < 5$ are easily observed. Fig. 7.6 shows our prediction compared to SCUBA observations (see references in the figure). The model reproduces very well the data, with some overestimate at fluxes $< 1\text{mJy}$. Figure 7.7 gives the redshift distribution of the objects with flux $> 0.8\text{mJy}$. The distribution is peaked at $z \sim 2.4$ with a quartile range of $1.9 < z < 2.8$, in agreement with the estimate of Chapman et al. (2003). We conclude that GALRISE is able to reproduce the apparent “monolithic” of the formation of the most massive galaxies.

In figure 7.8, left panel, we show the star-formation function of galaxies at $z = 2.5$, divided into bulges and discs. In this case, the punctual value of the star formation rate of a component is computed at the end of the corresponding time-bin. An interesting feature is that the bulge star-formation is dominant

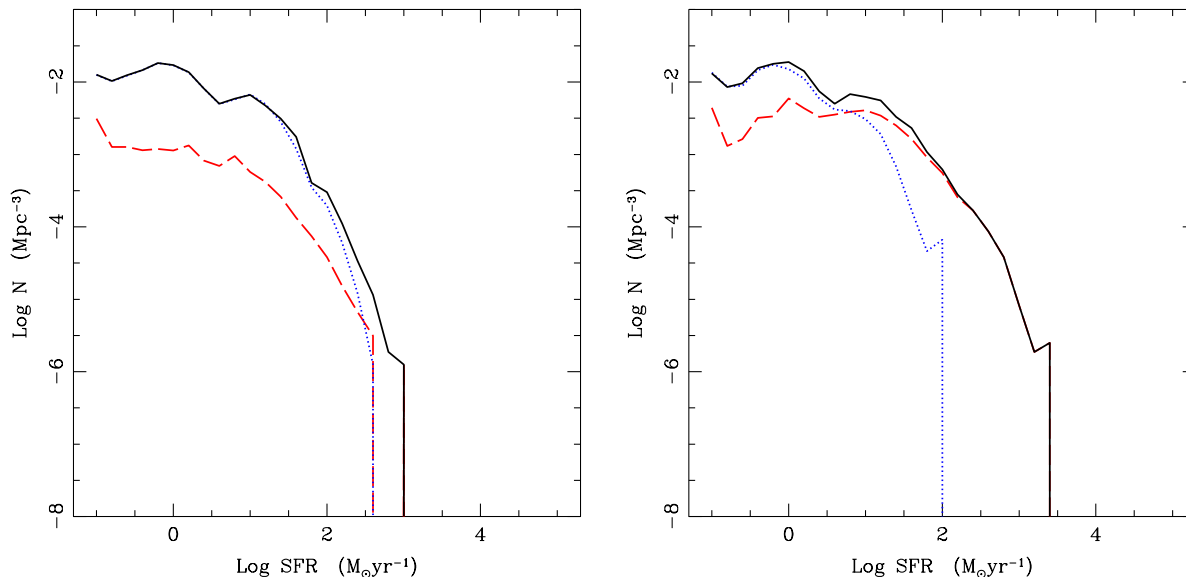


Figure 7.8: Left panel: SFR function at $z = 2.5$ for discs (dotted line) and bulges (dashed line). The continuous line gives the total SFR function. Right panel: the integral SFR in the 100 Myr time bin is shown in place of the SFR value at the end of the time bin.

only for the most massive starbursts of $> 300 M_{\odot} \text{ yr}^{-1}$. This is at variance with the dominance of the starburst mode for star formation found by Somerville, Primack and Faber (2000). This implies that our starbursts are triggered by cooling/infall more than by mergers, but it does not imply that massive starbursts are associated with spiral galaxies. In the right panel of figure 7.8 the star formation rate is computed as the total amount of stars, found at the end of the time bin in a bulge or disc component, that have formed in that time bin (but not necessarily in that component). This time bulges clearly dominate the star-formation function. This shows that such massively star-forming discs merge to form bulges (disc instabilities are not relevant at this redshift) in less than 100 Myr (the width of the time bin). It is then rather unlikely to observe these galaxies with a spiral morphology. We conclude that the cooling/infall domination of high-redshift starbursts does not change the conclusion that these events are responsible for the nearly “monolithic” character of massive ellipticals.

7.4 Conclusions on the Assembly of Massive Galaxies

In this chapter we have demonstrated that our model is able to reproduce the early assembly and late almost-passive evolution of massive galaxies by concentrating on observations in the NIR (especially in the K -band), most sensitive to the stellar mass, and the FIR (especially the $850\mu\text{m}$ channel), especially sensitive to the strongest and most obscured episodes of star formation. In particular, consistency between model and observations is

demonstrated by fitting the number counts in the K -band and the redshift distribution of the source in the K20 sample and the SCUBA sub-mm counts at $850\mu\text{m}$. For these counts we predict a redshift distribution with a median at $z \sim 2.4$ and quartiles at $z = 1.9$ and 2.8 ; this is consistent with the sparse evidence currently available.

This agreement is obtained at the cost of an over-prediction by a factor up to ~ 5 of the most massive galaxies; this over-prediction can nearly be corrected for by quenching the cooling flow in a physically motivated but not self-consistent way (forced quenching); a residual disagreement can be due to the (still very uncertain) scattering of stars into the halo component in galaxy clusters.

We also obtain that most star formation at high redshift is not stimulated by starbursts (which are anyway very abundant) but is due to the strong cooling/infall flows that take place at early times. This does not imply necessarily a disc-like morphology of such galaxies because galaxy mergers are very abundant at these times. We then conclude that the most important difference between this model and previous one lies in the improved cooling model, where infall is treated as a different physical process, more than to the improved model for feedback. This is anyway of fundamental importance to obtain the correct position of the peak in the redshift distribution of the K20 sample.

Chapter 8

Conclusions

In this work we studied the joint formation and evolution of galaxies and AGNs, both from the observational and the theoretical point of view.

- We extended the available information on the evolution of the AGN space density, studying the QSO luminosity function at high redshift. We have selected QSOs candidates in GOODS fields, defining suitable color criteria and matching optical candidates with X-ray surveys, and we discussed the results of the spectroscopic follow-up of targets. We have estimated the QSOs number density evolution and we conclude that the space density of moderate luminosity AGNs is insufficient to ionize the IGM at redshift between $3.5 < z < 5.2$. In the same redshift interval we have developed an algorithm able to estimate the QSO luminosity function by comparing datasets coming from GOODS and SDSS surveys. This algorithm employs Monte Carlo techniques, in order to estimate the completeness of the catalogues against selection criteria; then it simulates the surveys and computes the luminosity function through a statistical comparison of the resulting mock catalogues with the observations. The results indicate that pure density evolution models based on low-redshift observations reproduce the observed distribution of QSOs with higher accuracy with respect to pure luminosity evolution models. This is the first estimate of the faint-end of the QSO LF at such high redshift.
- We presented GALRISE, a new model for the joint formation and evolution of galaxies and AGNs. This model improves with respect to previous semi-analytical models in several details: (i) the evolution of the various components and phases of a galaxy is followed by integrating a differential system of equation along each branch of a merger tree, thus allowing for the most general (and non-linear) set of equations for mass and energy flows; (ii) in each galaxy component (halo, bulge, disc) the gas is modeled as two-phase; (iii) the evolution of the thermal and kinetic energies of the hot and cold phases is taken into account; (iv) the halo gas components (hot gas, cooling flows, halo stars) are described by a simple model that treats cooling and infall as separated processes, takes into account the mass and energy injection by galaxy winds and allows for galactic super-

winds; (v) feedback and star formation are inserted following the results of the model by Monaco (2004a,b), plus an additional prescription for kinetic feedback; (vi) accretion onto BHs and its feedback onto the galaxy are built-in. This increased level of sophistication allows to move from a phenomenological description of gas physics (especially of feedback), based on simple scalings with the depth of the DM halo potential, towards a physically motivated one. The comparison between real and model data was based on the definition of mock multiwavelength catalogues, built up by interfacing GALRISE with a spectrophotometric code. In particular we have used Bruzual & Charlot (2003) and GRASIL (Silva et al., 1998). We have adopted the former code because it is the most widely used code in previous semi-analytical models; on the other hand GRASIL provides a more detailed modeling of both the starlight extinction due to dust and the dust contribution of the emitted galactic radiation.

- We also took into account the energy released during accretion as a source for QSO feedback. We have shown that a massive removal of ISM from a large star-forming spheroid can be triggered by the joint action of SNe and quasar light; when the evaporation of gas due to AGN activity is strong enough, the stellar feedback regime changes, giving rise to the percolation of SNe remnants and to the creation of an expanding super-shell that can be pushed out of the galaxy by the combined stellar and AGN radiation pressure as a galactic wind. We demonstrated that this mechanism can lead to a self-limited black hole–bulge relation similar to the observed one.
- We studied the X-ray properties of the AGN population predicted by GALRISE. We have used the hard-X band observations, where it is possible to assume that most objects are visible, due to the low level of extinction suffered by the radiation. We have also taken into account soft X-ray samples, in order to recover a complete view of the X-ray emission properties, and optical observation in order to gain advantage of the larger amount of data available. We demonstrated that a proper modeling of stellar feedback is crucial to reproduce the observed “downsizing” behavior of galaxies and AGNs. In particular kinetic feedback in star-forming bulges is the key mechanism to create the anti-hierarchical behavior of the AGN population.
- We analysed the near-infrared (K -band) and sub-millimeter ($850\mu m$) properties of galaxy population. We have focus our attention both on the K -band, to follow the assembly of the bulk of stellar mass, and on FIR observations as a key tool for determining the Star Formation History of the Universe. The combined study of K -band and sub-mm observations provides us important clues on the assembly mechanisms leading to the formation of massive galaxies, owing to the fact that we are able to sample both the star-forming and the passive phases of their evolution. We demonstrated that the improved cooling model, where infall is treated as a different physical process, is crucial to reproduce at the same time both the evolution of the K -band galaxy luminosity

function, the redshift distribution of $K < 20$ galaxies and the sub-mm population of star-forming galaxies at a redshift $z \sim 2$.

Our analysis confirms that models based on the Λ CDM cosmology are able to reproduce at the same time the properties of both AGNs and galaxies.

Several improvements to this work should be taken into account both from the theoretical and the observational point of view.

- **Extremely Red Objects.** In order to strengthened our conclusion about the early assembly of massive galaxies, it will be very important to analyse GALRISE predictions on EROs, which can be subdivided into a passive and a star-forming population. We plan to compare GALRISE prediction with the EROs number counts and with their redshift distribution, trying to reproduce both the properties of the population as a whole and the relative importance of the two separate subclasses. The correct prediction of this set of observations will provide even stronger constraints on the physical processes leading to the assembly of massive galaxies.
- **Optical and UV properties.** We also leave to future analysis the optical and UV wavebands, which are fundamental to gain insight on the stellar population properties of galaxies. In particular we will focus on the cosmic luminosity density and on local optical luminosity functions. Besides we will also take into account the color properties of our model galaxies: in particular the observed color bimodality of local galaxies, which highlights the presence of two distinct galaxy populations. A preliminary analysis of the color distribution shows that GALRISE is able to reproduce the observed bimodality. We plan to deepen this point in future work, with the quantitative analysis of the predicted color distribution. The prediction of the UV properties of galaxies is another topic we leave to future work. This spectral region will be suitable for studies relative to the star formation activity of galaxies, especially when compared to recent UV surveys as GALEX.
- **PAHs and dust composition** We plan to study GALRISE predictions in the 15 and $24\mu m$ bands. The comparison with the source number counts in these bands will be very useful to study the physical properties of dust in galaxy (e.g. the relative importance of PAHs) and to test spectrophotometric models for dust absorption and emission, both in terms of the physical processes involved and of dust composition.
- **Cosmic Infrared Background.** The correct reproduction of this observational constraint over a wide range of wavelength will allow us to give prediction on the expected galaxy number counts for future infrared telescopes, such as Herschel mission.

- **Radio emission.** Also the analysis of the radio emission will be of fundamental importance in order to gain insight on the interplay between stellar and nuclear emission. In fact radio emission due to stellar activity traces star-formation regions, whereas roughly half of AGN population is composed by strong and complex radio sources. A careful modeling of radio emission will be also useful to gain insight on the joint evolution of stellar populations and SMBH growth.
- **Chemical Evolution.** An important improvement to be tested on our model is related to the possible interfacing of GALRISE with a detailed model for the chemical evolution of galaxies, in order to predict the relative abundances of a variety of metal species. In particular the abundance of α -elements (carbon, oxygen, silicon, magnesium) with respect to iron is very sensitive to the explosion rate of SNeII and SNeIa and as a consequence to the detailed star-formation histories of galaxies. Such an analysis will strengthen our conclusion about the assembly history of massive galaxies: the combination of near-infrared information and chemical abundances will provide strong constraints on the mass assembly history of early type galaxies predicted by models of galaxy formation and evolution.
- **Multiwavelength Catalogues.** The definition of multiwavelength galaxy/AGN catalogues covering a spectral range from X-rays to radio will be very useful to study the color properties of high-redshift counterparts and to tailor selection criteria to be proposed in real surveys in order to select specific galaxies and AGNs populations at various redshift.
- **Faint AGNs.** Our approach is able to disentangle between the nuclear AGN emission and the radiation coming from the host galaxy, at optical wavelength: a careful treatment of this effect will allow us to give estimates on the correction to AGN optical magnitudes, which is particularly important for faint AGN studies.
- **Luminosity Functions of high-redshift sources.** Our algorithm for computing the high- z QSO LF can be easily implemented to the analysis of other samples of color-selected high-redshift objects. The comparison of the AGN and galaxy high-redshift population will provide new and stringent constraints on different models of joint galaxy and AGN formation. In fact the estimate of the high- z QSO luminosity function can be used as a test on the black hole accretion mechanisms as far as an estimate of the QSO contribution to the UV background, while the luminosity function of high- z galaxies provide a wide range of information on the selected galaxy population, depending on the corresponding restframe luminosity. As a starting point we plan to apply it to a color-selected sample of $z \sim 6$ Lyman Break Galaxies in order to give relevant constraints both on the star-formation rate and on the galaxy assembly process at these redshifts.

Bibliography

- [1] Alexander, D.M., et al. 2003, AJ, 126, 539
- [2] Allen, S. W., Schmidt, R. W., & Fabian, A. C. 2002, MNRAS, 334, L11
- [3] Alongi M., Bertelli, G., Bressan, A., Chiosi, C. 1993, A&AS, 97, 851
Fagotto, F., Greggio L., Nasi E.,
- [4] Arimoto, N., & Yoshii, Y. 1987, A&A, 173, 23
- [5] Arnouts, S., Cristiani, S., Moscardini, L., Matarrese, S., Lucchin, F.,
Fontana, A., Giallongo, E., 1999, MNRAS, 310, 540
- [6] Abazajian, K., et al, 2005, AJ, 129, 1755
- [7] Babul, A., & Rees, M. J. 1992, MNRAS, 255, 346
- [8] Bahcall, N. A., Dong, F., Hao, L., Bode, P., Annis, J., Gunn, J. E., &
Schneider, D. P. 2003, ApJ, 599, 814
- [9] Baldry, I. K., Glazebrook, K., Brinkmann, J., Ivezić, Ž., Lupton, R. H.,
Nichol, R. C., & Szalay, A. S. 2004a, ApJ, 600, 681
- [10] Baldry, I. K., Balogh, M. L., Bower, R., Glazebrook, K., & Nichol, R. C.
2004b, AIP Conf. Proc. 743: The New Cosmology: Conference on Strings
and Cosmology, 743, 106
- [11] Ballo, L., et al., 2006, ApJ submitted
- [12] Balogh, M. L., Baldry, I. K., Nichol, R., Miller, C., Bower, R., &
Glazebrook, K. 2004, ApJL, 615, L101
- [13] Barger, A. J., Cowie, L. L., Sanders, D. B., 1999, ApJL, 518, L5
- [14] Barger, A.J., Cowie, L.L., Richards, E.A., 2000, AJ, 119, 2092
- [15] Barger, A.J., Cowie, L.L., Bautz, M.W., Brandt, W.N., Garmire, G.P.,
Hornschemeier, A.E., Ivison, R.J, Owen, F.N., 2001, AJ, 122, 2177
- [16] Barger, A.J., Cowie, L.L., Brandt, W.N., Capak, P., Garmire, G.P.,
Hornschemeier, A.E., Steffen, A.T., Wehner, E.H., 2002, AJ, 124, 1839
- [17] Barger, A.J., Cowie, L.L., Capak, P., Alexander, D.M., Bauer, F.E.,
Brandt, W.N., Garmire, G.P., Hornschemeier, A.E., 2003, ApJ, 584, L61
- [18] Barger, A. J., Cowie, L. L., Mushotzky, R. F., Yang, Y., Wang, W.-H.,
Steffen, A. T., & Capak, P. 2005, AJ, 129, 578

- [19] Bauer, F. E., Alexander, D. M., Brandt, W. N., Schneider, D. P., Treister, E., Hornschemeier, A. E., & Garmire, G. P. 2004, *AJ*, 128, 2048
- [20] Baugh C.M., Lacey C.G., Frenk C.S., Granato G.L., Silva L., Bressan A., Benson A.J., Cole S., 2005, *MNRAS*, 356 ,1191
- [21] Baumgartner, W. H., Loewenstein, M., Horner, D. J., & Mushotzky, R. F. 2005, *ApJ*, 620, 680
- [22] Begelman M.C., 1985, *ApJ*, 297, 492
- [23] Begelman M.C., 2004, in L.C. Ho ed., *Coevolution of Black Holes and Galaxies*. Cambridge University Press, Cambridge, p. 375
- [24] Begelman M.C., McKee C.F., Shields G.A., 1983, *ApJ*, 271, 70
- [25] Bell, E. F., McIntosh, D. H., Katz, N., & Weinberg, M. D. 2003, *ApJS*, 149, 289
- [26] Bender, R., Burstein, D., & Faber, S. M. 1992, *ApJ*, 399, 462
- [27] Bennett C.L. et al., 2003, *ApJS*, 148, 1
- [28] Benson, A. J., Pearce, F. R., Frenk, C. S., Baugh, C. M., & Jenkins, A. 2001, *MNRAS*, 320, 261
- [29] Benson, A. J., Lacey, C. G., Frenk, C. S., Cole, S., & Baugh, C. M. 2001, *Bulletin of the American Astronomical Society*, 33, 871
- [30] Benson, A. J., Bower, R. G., Frenk, C. S., Lacey, C. G., Baugh, C. M., & Cole, S. 2003, *ApJ*, 599, 38
- [31] Bernardi, M., et al. 2003, *AJ*, 125, 1866
- [32] Bernardi, M., Sheth, R. K., Nichol, R. C., Schneider, D. P., & Brinkmann, J. 2005, *AJ*, 129, 61
- [33] Bertin, E., & Arnouts, S. 1996, *A&AS*, 117, 393
- [34] 1987, *Nat*, 326, 219
- [35] Blanton, M. R., et al. 2003, *ApJ*, 594, 186
- [36] Blanton, M. R., et al. 2003a, *ApJ*, 592, 819
- [37] Blanton, M. R., Lupton, R. H., Schlegel, D. J., Strauss, M. A., Brinkmann, J., Fukugita, M., & Loveday, J. 2005, *ApJ*, 631, 208
- [38] Bond, J. R., Cole, S., Efstathiou, G., & Kaiser, N. 1991, *ApJ*, 379, 440
- [39] Borgani, S. 2004, *Ap&SS*, 294, 51
- [40] Borgani, S., et al. 2001, *ApJ*, 561, 13
- [41] Borys, C., Chapman, S. C, Halpern, M., Scott, D., 2003, *MNRAS*, 344, 385
- [42] Borys, C., Chapman, S. C., Halpern, M., Scott, D., 2002, *MNRAS*, 330, L63

- [43] Bouchet, F. R., Colombi, S., Hivon, E., & Juszkiewicz, R. 1995, *A&A*, 296, 575
- [44] Buchert, T. & Ehlers J., 1993, *MNRAS*, 264, 375
- [45] Boyle, B.J., Shanks, T., Croom, S.M., Smith, R.J., Miller, L., Loaring, N., & Heymans, C., 2000, *MNRAS*, 317, 1014
- [46] Bower, R. G., Lucey, J. R., & Ellis, R. S. 1992, *MNRAS*, 254, 601
- [47] Bower, R. G., et al. 2005, (astro-ph/0511338)
- [48] Brandt et al., 2001, *AJ*, 122, 2810
- [49] Bressan, A., Silva, L., Granato, G.L., 2002, *A&A*, 392, 377
- [50] Bressan, A., Fagotto, F., Bertelli, G., Chiosi, C. 1993, *A&AS*, 100, 647
- [51] Brinchmann, J., & Ellis, R. S. 2000, *ApJL*, 536, L77
- [52] Bromley J.M., Somerville R.S., Fabian A.C., 2004, *MNRAS*, 350, 456
- [53] Bruzual, G., & Charlot, S. 1993, *ApJ*, 405, 538
- [54] Bruzual, G., & Charlot, S. 2003, *MNRAS*, 344, 1000
- [55] Bullock, J. S., Dekel, A., Kolatt, T. S., Kravtsov, A. V., Klypin, A. A., Porciani, C., & Primack, J. R. 2001, *ApJ*, 555, 240
- [56] Cagnoni I., Della Ceca R., Maccararo T., 1998, *ApJ*, 493, 54
- [57] Calzetti D., 1997, in *Proc. of The Ultraviolet Universe at Low and High Redshift: Probing the Progress of Galaxy Evolution*, AIP Conference Proceedings, 408, p.403
- [58] Capak, P., et al. 2004, *AJ*, 127, 180
- [59] Caputi, K.I., Dunlop, J.S., McLure, R.J., & Roche, N.D., 2004, *MNRAS*, 353,30
- [60] Cardelli J., Clayton G. & Mathis J., 1989, *ApJ*, 345, 245
- [61] Carollo, C. M., Danziger, I. J., & Buson, L. 1993, *MNRAS*, 265, 553
- [62] Catelan, P., & Theuns, T. 1996, *MNRAS*, 282, 436
- [63] Catelan, P., 1995, *MNRAS*, 176, 115
- [64] Cattaneo A., 2001, *MNRAS*, 324, 128
- [65] Cavaliere, A., Colafrancesco, S., & Menci, N. 1992, *ApJ*, 392, 41
- [66] Cavaliere, A., & Menci, N. 1993, *ApJL*, 407, L9
- [67] Cavaliere A. & Vittorini V., 2002a, *ApJ*, 570, 114
- [68] Cavaliere A. & Vittorini V., 2002b, *ApJ*, 543, 599
- [69] Cavaliere A., Fusco-Fermiano R., 1976, *A&A*, 49, 137
- [70] Ciardi, B., & Ferrara, A. 2005, *Space Science Reviews*, 116, 625
- [71] Cimatti, A., et al. 2004, *Nat*, 430, 184

- [72] Cimatti, A., et al. 2002b, A&A, 391, 1
- [73] Cimatti, A., et al. 2002a, A&A, 381, 68
- [74] Cimatti, A., et al., 2003, A&A, 412, L1
- [75] Cioffi, D.F., McKee, C.F., Bertschinger, E., 1988, ApJ, 334, 252
- [76] Ciotti L., Ostriker J.P., 1997, ApJ, 487, L105
- [77] Chapman, S. C., Scott, D., Borys, C., Fahlman, G. G., 2002, MNRAS, 330, 92
- [78] Chapman, S.C., Blain, A.W., Ivison, R.J., Smail, I.R., 2003, Nat., 422, 695
- [79] Charbonnel C., Meynet G., Maeder A., Schaerer D., 1996, A&AS, 115, 339
- [80] Charbonnel C., Däppen W., Schaerer D., Bernasconi P.A., Maeder A., Meynet G., Mowlawi N., 1999, A&AS, 135, 405
- [81] Charlot, S., & Bruzual, G., 1991, ApJ, 367, 126
- [82] Charlot, S., & Fall, S.M., 2000, ApJ, 539, 718
- [83] Christodoulou, D.M., Shlosmann, I., Tohline J.E., 1995, ApJ, 443, 551
- [84] Cohen, J., 2002, ApJ, 567, 672 Society, 34, 1274
- [85] Cohen, J.G., Hogg, D.W., Blandford, R., Cowie, L.L., Hu, E., Songaila, A., Shopbell, P., Richberg, K., 2000, ApJ, 538, 29
- [86] Cole, S., et al. 2001, MNRAS, 326, 255
- [87] Cole, S., Lacey, C.G., Baugh, C.M., & Frenck, C.S., 2000, MNRAS, 319, 168
- [88] Cole, S., 1991, ApJ, 367, 45
- [89] Colless, M.M., et al., 2001, MNRAS, 328, 1039
- [90] Comastri A., Setti G., Zamorani G., Hasinger G., 1995, A&A, 296, 1
- [91] Condon, J. J., Cotton, W. D., & Broderick, J. J. 2002, AJ, 124, 675
- [92] Cowie, L.L., Gardner, J.P., Hu, E.M., 1994, ApJ, 434, 114
- [93] Cowie, L.L., Gardner, J.P., Hu, E.M., & Cohen, J.G., 1996, AJ, 112, 839
- [94] Cowie, L. L., Barger, A. J., Kneib, J.-P., 2002, AJ, 123, 2197
- [95] Cowie, L. L., Barger, A. J., Hu, E. M., Capak, P., & Songaila, A. 2004, AJ, 127, 3137
- [96] Cristiani S., Vio R., 1990, A&A, 227, 385
- [97] Cristiani, S., et al., 2000, A&A, 359, 489
- [98] Cristiani S., et al., 2004, ApJL, 600, 119
- [99] Croom, S. M., Smith, R. J., Boyle, B. J., Shanks, T., Miller, L., Outram, P. J., & Loaring, N. S., 2004, MNRAS, 349, 1397

- [100] Daddi, E., Cimatti, A., & Renzini, A., 2000, A&A, 362, 45
- [101] Daddi, E., et al. 2002, A&A, 384, L1
- [102] Daddi, E., et al. 2005, ApJ, 626, 680
- [103] Dalla Vecchia, C., Bower, R. G., Theuns, T., Balogh, M. L., Mazzotta, P., & Frenk, C. S. 2004, MNRAS, 355, 995
- [104] Danese, L., Granato, G. L., Silva, L., Magliocchetti, M., & de Zotti, G. 2003, The Mass of Galaxies at Low and High Redshift, 99
- [105] Davis, M., Efstathiou, G., Frenk, C. S., White, S. D. M., 1985, ApJ, 292, 371
- [106] Dawson, S., Stern, D., Bunker, A.J., Spinrad, H., Dey, A., 2001, AJ, 122, 598
- [107] Dawson, S., Spinrad, H., Stern, D., Dey, A., van Breugel, W., de Vries, W., Reuland, M., 2002, ApJ, 570, 92
- [108] de Bernardis, P., et al. 2000, Nat, 404, 955
- [109] Dekel, A., & Silk, J. 1986, ApJ, 303, 39
- [110] De Luca A., Molendi S., 2004, A&A, 419, 837
- [111] A. Dekel & O. Lahav, 1999, ApJ, 520, 24D
- [112] Desert, F.-X., Boulanger, F., & Puget, J. L. 1990, A&A, 237, 215
- [113] Devriendt, J. E. G., Guiderdoni, B., & Sadat, R. 1999, A&A, 350, 381
- [114] Djorgovski, S., & Davis, M. 1987, ApJ, 313, 59
- [115] Djorgovski, S., et al. 1995, ApJ, 438, L13
- [116] Dickinson, M., 1998, in *The Hubble Deep Field*, ed. M. Livio, S. M. Fall, P. Madau (Cambridge: Cambridge Univ. Press), 219
- [117] Dickinson, M., Papovich, C., Ferguson, H. C., & Budavári, T. 2003, ApJ, 587, 25
- [118] D'odorico V., Cristiani S., Romano D., Granato G.L., Danese L., 2004, MNRAS, 351, 976
- [119] Dressler, A., Lynden-Bell, D., Burstein, D., Davies, R. L., Faber, S. M., Terlevich, R., & Wegner, G. 1987, ApJ, 313, 42
- [120] Drory, N., Bender, R., Feulner, G., Hopp, U., Maraston, C., Snigula, J., & Hill, G. J. 2004, ApJ, 608, 742
- [121] Dunlop J.S., McLure R.J., Kukulka M.J., Baum S.A., O'Dea C.P., Hughes D.H., 2003, MNRAS, 340, 1095
- [122] Eales, S., Lilly, S., Webb, T., Dunne, L., Gear, W., Clements, D., Yun, M., 2000, AJ, 120, 2244
- [123] Edge A.C., Frayer D.T., 2003, ApJ, 594, L13
- [124] Efstathiou, G., Lake, G., Negroponte, J., 1982, MNRAS, 199, 1069

- [125] Efstathiou, G., Frenk, C. S., White, S. D. M., & Davis, M. 1988, MNRAS, 235, 715
- [126] Efstathiou, G., 1992, MNRAS, 256, 43
- [127] Elmegreen B.G., 2002, ApJ, 564, 773
- [128] Elvis, M., Wilkes, B. J., McDowell, J.C., Green, R.F., Bechtold, J., Willner, S.P., Oey, M.S., Polomski, E., Cutri, R., 1994, ApJS, 95,1
- [129] Eke, V. R., Cole, S., Frenk, C. S., & Patrick Henry, J. 1998, MNRAS, 298, 1145
- [130] Faber, S. M., & Jackson, R. E. 1976, ApJ, 204, 668
- [131] Fabian, A. C. 1994, ARA&A, 32, 277
- [132] Fabian A.C., 1999, MNRAS, 308, 39
- [133] Fagotto, F., Bressan, A., Bertelli, G., Chiosi, C. 1994a, A&AS, 104, 365
- [134] Fagotto, F., Bressan, A., Bertelli, G., Chiosi, C. 1994b, A&AS, 105, 29
- [135] Fall, S.M., Efstathiou, G., 1980, MNRAS, 193, 189
- [136] Fan, X., Strauss, M.A., Schneider, et al., 2001, AJ, 121,54
- [137] Fan, X., Strauss, M.A., Schneider, D.P., Becker, R.H., 2003, AJ, 125, 1649
- [138] Feldmeier, J.J., et al. 2002, ApJ, 575, 779
- [139] Ferrara A., Bianchi S., Cimatti A., Giovanardi C., 1999, ApJS, 123, 423
- [140] Firth, A.E., Somerville, R.S., McMahon, R.G., et al., 2001
- [141] Fontana, A., et al. 2004, A&A, 424, 23
- [142] Fontana, A., et al. 2003, ApJL, 594, L9
- [143] Fontanot et al., 2006a, in preparation
- [144] Fontanot et al., 2006b, in preparation
- [145] Fontanot et al., 2006c, in preparation
- [146] Fukugita M., Ichikawa T., Gunn J.E., Doi M., Shimakasu K., Schneider D.P., 1996, AJ, 111, 1748
- [147] Fukugita, M., & Peebles, P. J. E. 2004, ApJ, 616, 643
- [148] Gal-Yam, A., et al. 2003, AJ, 125, 1087
- [149] Gardner, J.P., Cowie, L.L., Wainscoat, R.J., 1993, ApJ 415, 9
- [150] Gardner, J.P., Sharples, R.M., Carrasco, B.E., Frenk, C.S., 1996, MNRAS, 282, 1
- [151] Gavazzi, G., Pierini, D. & Boselli, A., 1996, A&A, 312, 397
- [152] Gentile, G., Salucci, P., Klein, U., Vergani, D., & Kalberla, P. 2004, MNRAS, 351, 903

- [153] Georgantopoulos I., Steward G.C., Shanks T., Boyle B.J., Griffiths R.E., 1996, MNRAS, 280, 276
- [154] Giacconi, R., et al. 2002, ApJS, 139, 369, G02
- [155] Giavalisco et al. 2004a, ApJ, 600, L93
- [156] Giavalisco et al. 2004b, ApJ, 600, L103
- [157] Giommi P., Perri M., Fiore F., 2000, A&A, 362, 799
- [158] Girardi L., Bressan, A., Chiosi, C., Bertelli, G., Nasi E. 1996, A&AS, 117, 113
- [159] Girardi L., Bressan, A., Bertelli, G., Chiosi, C. 2000, A&AS, 141, 371
- [160] Glazebrook, K., Peacock, J.A., Collins, C.A., Miller, L. 1994, MNRAS, 266, 65
- [161] Gonzalez, A.H., et al. 2000, ApJ, 536, 561
- [162] Governato, F., Babul, A., Quinn, T., Tozzi, P., Baugh, C. M., Katz, N., & Lake, G. 1999, MNRAS, 307, 949
- [163] Governato, F., et al. 2004, ApJ, 607, 688
- [164] Granato G.L., Silva L., Monaco P., Panuzzo P., Salucci P., De Zotti G., Danese L., 2001, MNRAS, 324, 757
- [165] Granato G.L., De Zotti G., Silva L., Bressan A., Danese L., 2004, ApJ, 600, 580
- [166] Grazian A. & Fontana, A., in preparation
- [167] Gruber D.E., 1992, In: Barcons X., Fabian A.C., (eds.) The Proceedings of: The X-ray Background. Cambridge Univ. Press, Cambridge, p.44
- [168] Gwyn, S. D. J., & Hartwick, F. D. A. 2005, AJ, 130, 1337
- [169] Haehnelt M.G. & Rees M.J., 1993, MNRAS, 263, 168
- [170] Haehnelt M.G., Natarajan P., Rees M.J., 1998, MNRAS, 300, 817
- [171] Haiman, Z., & Hui, L., 2001, ApJ, 547, 27
- [172] Haiman, Z., Madau, P., & Loeb, A., 1999, ApJ, 514, 535
- [173] Haiman Z., Ciotti L., Ostriker J.P., 2004, ApJ, 606, 763
- [174] Hamann F. & Ferland, G., 1999, ARA&A, 37, 487
- [175] Hao, L., et al. 2005, AJ, 129, 1795
- [176] Häring N. & Rix H.W., 2004, ApJ, 604, 89
- [177] Hasinger, G., Miyaji, T., & Schmidt, M. 2005, A&A, 441, 417
- [178] Hasinger, G., Burg, R., Giacconi, R., Hartner, G., Schmidt, M., Trumper, J., & Zamorani, G. 1993, A&A, 275, 1
- [179] Hasinger G., 1998, Astron. Nacht., 319

- [180] Hatton S., Devriendt J.E.G., Ninin S., Bouchet F.R., Guiderdoni B., Vibert D., 2003, MNRAS, 343, 75
- [181] Hatziminaoglou E., Mathez G., Solanes J., Manrique A., Salvador-Solé E., 2003, MNRAS, 343, 692
- [182] Helly, J. C., Cole, S., Frenk, C. S., Baugh, C. M., Benson, A., Lacey, C., & Pearce, F. R. 2003, MNRAS, 338, 913
- [183] Hopkins, A. M. 2004, ApJ, 615, 209
- [184] Hughes, D. H., et al. 1998, Nat, 394, 241
- [185] Kaiser N., 1984, ApJ, 284L, 9K
- [186] Kang X., Jing Y.P., Mo H.J., Böerner G., 2005, ApJ, 631, 21
- [187] Katz, N., Weinberg, D. H., & Hernquist, L. 1996, ApJS, 105, 19
- [188] Kauffmann, G., et al. 2003, MNRAS, 341, 54
- [189] Kauffmann G., Haehnelt M.G., 2000, MNRAS, 311, 576
- [190] Kauffmann, G., & Charlot, S. 1998, MNRAS, 297, L23
- [191] Kauffmann, G., Colberg, J.M., Diaferio, A., & White S.D.M., 1999, MNRAS, 303, 188
- [192] Kauffmann, G. 1996, MNRAS, 281, 487
- [193] Kauffmann, G. & White S.D.M., 1993, MNRAS, 261, 921
- [194] Kawakatu, N., Umemura, M. & Mori, M., 2003, ApJ, 583, 85
- [195] Kenefick, J.D., Djorgovski, S.G., & de Carvalho, R.R., 1995, AJ, 110, 2553
- [196] Kenefick, J.D., Djorgovski, S.G., & Meylan, G., 1996, AJ, 111, 1816
- [197] Kennicutt R.C., 1983, ApJ, 498, 541
- [198] Kennicutt, R. C. 1998, ASP Conf. Ser. 142: *The Stellar Initial Mass Function (38th Herstmonceux Conference)*, 142, 1
- [199] Kinzer R.L., Jung G.V., Gruber, D.E., Matteson J.L., Peterson L.E., 1997, ApJ, 475, 361
- [200] Knop, R. A., et al. 2003, ApJ, 598, 102
- [201] Kochanek, C.S., Pahre, M.A., Falco, E.E. et al. 2001, ApJ, 560, 566
- [202] Kormendy J., Richstone D., 1995, ARA&A, 33, 581
- [203] Koushiappas S.M., Bullock J.S., Dekel A., 2004, MNRAS, 349
- [204] Kriss G.A., Davidsen A., Zheng W., Lee G., 1999, ApJ, 527, 683
- [205] Krolik J.H., McKee C.F., Tarter C.B., 1981, ApJ, 249, 422
- [206] Kroupa, P., Tout, C. A., & Gilmore, G. 1990, MNRAS, 244, 76
- [207] Jorgensen, I., Franx, M., & Kjaergaard, P. 1996, MNRAS, 280, 167

- [208] Iglesias C.A., Rogers F.J. & Wilson B.G. 1992, ApJ, 397, 717
- [209] Lacey, C., & Cole, S., 1993, MNRAS, 262, 627
- [210] La Franca, F., Cristiani, S., 1997, AJ, 113, 1517
- [211] La Franca, F. et al., 2005 (astro-ph/0509081)
- [212] Lanzoni, B., Guiderdoni, B., Mamon, G.A., Devriendt, J., Hatton, S., 2005, MNRAS, 361, 369-384
- [213] Li, Y., Mo, H.J., van den Bosch, F.C., 2005 (astro-ph/0510372)
- [214] Lombardi M., Bertin G., 2001, A&A, 375, 1091
- [215] Loveday J., 1996, MNRAS, 278, 1025
- [216] Lumb D.H., Warwick R.S., Page M., De Luca A., 2002, A&A, 389, 93
- [217] Mac Low, M.-M. 2002, AP&SS, 281, 429
- [218] Madau, P., Haardt, F., Rees, M.J., 1999, ApJ, 514, 648
- [219] Magorrian J., Tremaine S., Richstone D. et al., 1998, ApJ, 115, 2285
- [220] Makino J. & Hut P., 1997, ApJ, 481, 83
- [221] Mahmood A., Devriendt J.E.G., Silk J., 2005, MNRAS, 359, 1363
- [222] Maihara, T., et al. 2001, PASJ, 53, 25
- [223] Maiolino R., Oliva E., Ghinassi F., Pedani M., Mannucci F., Mujica R., Juarez Y., 2004, A&A, 420, 889
- [224] Marconi A., Hunt L.K., 2003, ApJ, 589, 21
- [225] Marconi, A., Risaliti, G., Gilli, R., Hunt, L. K., Maiolino, R., & Salvati, M. 2004, MNRAS, 351, 169
- [226] Marinoni, C., Monaco, P., Giuricin, G., & Costantini, B., 1999, ApJ, 521, 50
- [227] Matteucci F. & Padovani, 1993, ApJ, 419, 485
- [228] Matteucci F., 1994, A&A, 288, 57
- [229] Matteucci, F. 1996, ASP Conf. Ser. 98: *From Stars to Galaxies: the Impact of Stellar Physics on Galaxy Evolution*, 98, 529
- [230] Matzner, C. D. 2002, ApJ, 566, 302
- [231] Menci N., Cavaliere A., Fontana A., Giallongo E., Poli F., 2002, ApJ, 578, 18
- [232] Menci N., Cavaliere A., Fontana A., Giallongo E., Poli F., Vittorini V., 2003, ApJ, 587, 63
- [233] Menci, N., Cavaliere, A., Fontana, A., Giallongo, E., Poli, F., & Vittorini, V. 2004, ApJ, 604, 12
- [234] Menci N., Fontana, A., Giallongo E., Salimbeni S., 2005, ApJ, 632, 49
- [235] Merloni, A., Heinz, S., & di Matteo, T. 2003, MNRAS, 345, 1057

- [236] Merloni, A., 2004, MNRAS, 353, 1035
- [237] Miyaji T., Hasinger G., Schmidt M., 2001, A&A, 369, 49
- [238] Miyazaki, M., et al., 2003, PASJ, 55, 1079
- [239] Mo, H.J., Mao, S., White, S.D.M., 1998, MNRAS, 295, 319
- [240] Mobasher, B., Ellis, R.S., Sharples, R.M., 1996, MNRAS, 223, 11
- [241] Monaco, P., Fontanot, F., Taffoni, G., 2006, in preparation
- [242] Monaco, P., & Fontanot, F. 2005, MNRAS, 359, 283
- [243] Monaco, P., 2004a, MNRAS, 352, 181
- [244] Monaco, P., 2004b, MNRAS, 354, 151
- [245] Monaco P., 2004c, in eds. A. Merloni, S. Nayakshin, R. Sunyaev, Growing Black Holes. Springer-Verlag, Berlin, in press
- [246] Monaco P., Theuns T., Taffoni G., Governato F., Quinn T., Stadel J., 2002, ApJ, 564, 8
- [247] Monaco P., Theuns T., Taffoni G., 2002, MNRAS, 331, 587
- [248] Monaco P., Salucci P. & Danese L., 2000, MNRAS, 311, 279
- [249] Monaghan, J. J. 1992, ARA&A, 30, 543
- [250] Moore, B., Katz, N., Lake, G., Dressler, A., & Oemler, A. 1996, Nat., 379, 613
- [251] Moretti A., Campana S., Lazzati D., Tagliaferri G., 2003, ApJ, 588, 696
- [252] Mori M., Ferrara A., Madau P., 2002, ApJ, 571, 40
- [253] Morrison, R., & McCammon, D., 1983, ApJ, 270, 119
- [254] Moustakas, L.A., Davis, M., Graham, J.R., Silk, J., Peterson, B.A., Yoshii, Y. 1997, ApJ, 475, 445
- [255] Moutarde, F., Alimi, J.-M., Bouchet, F. R., Pellat, R., & Ramani, A. 1991, ApJ, 382, 377
- [256] Murante, G., et al. 2004, ApJL, 607, L83
- [257] Murray N., Quataert E., Thompson T.A., 2005, ApJ, 618, 569
- [258] Natali, F., Giallongo, E., Cristiani, S., La Franca, F., 1998, AJ, 115, 397
- [259] Navarro J.F., Frenk C.S., White S.D.M., 1995, MNRAS, 275, 720
- [260] Navarro, J. F., Frenk, C. S., & White, S. D. M. 1996, ApJ, 462, 563
- [261] Navarro, J. F., Frenk, C. S., & White, S. D. M. 1997, ApJ, 490, 493
- [262] Norberg, P., et al. 2002, MNRAS, 332, 827
- [263] Norman, C., et al. 2002, ApJ, 571, 218
- [264] Ogasaka Y., Kii T., Ueda Y., et al., 1998, Astron. Nacht., 319, 47
- [265] Ostriker J.P., McKee C.F., 1988, RvMP,60, 10

- [266] Ostriker J.P., Ciotti L., 2005, Royal Society of London Philosophical Transactions Series A, 363, 667
- [267] Padmanabhan T., *Structure formation in the Universe*, Cambridge University Press, 1995
- [268] Pahre, M.A., Djorgovski, S.G., & de Carvalho, R.R., 1995, ApJ, 453, L17
- [269] Peacock J.A., *Cosmological Physics*, Cambridge University Press, 1999
- [270] Peacock, J. A., & Heavens, A. F. 1990, MNRAS, 243, 133
- [271] Perlmutter, S., et al. 1999, ApJ, 517, 565
- [272] Péroux, C., Dessauges-Zavadsky, M., D'Odorico, S., Sun Kim, T., & McMahon, R. G. 2005, MNRAS, 363, 479
- [273] Persic, M., Salucci, P., & Stel, F. 1996, MNRAS, 281, 27
- [274] Peterson, J. R., et al. 2001, A&A, 365, L104
- [275] Popesso, P., Böhringer, H., Brinkmann, J., Voges, W., & York, D. G. 2004, A&A, 423, 449
- [276] Pozzetti, L., Cimatti, A., Zamorani, G. et al., 2003, A&A, 402, 837
- [277] Press W.H. & Schechter P., 1974, ApJ, 187, 425
- [278] Prochaska, J. X., & Herbert-Fort, S. 2004, PASP, 116, 622
- [279] Quilis, V., Bower, R. G., & Balogh, M. L. 2001, MNRAS, 328, 1091
- [280] Rao, S. M., Prochaska, J. X., Howk, J. C., & Wolfe, A. M. 2005, AJ, 129, 9
- [281] Recchi, S., Matteucci, F., & D'Ercole, A. 2001, MNRAS, 322, 800
- [282] Rees, M. J. 1976, MNRAS, 176, 483
- [283] Rees M., 2004, in eds. A. Merloni, S. Nayakshin, R. Sunyaev, *Growing Black Holes*. Springer-Verlag, Berlin, in press
- [284] Renzini A., 2004, in eds. J.S. Mulchaey, A. Dressler, A. Oemler 2004, *Clusters of Galaxies: Probes of Cosmological Structure and Galaxy Evolution*. Carnegie Observatories Astrophysics Series. Pag 261
- [285] Renzini, A., & Ciotti, L. 1993, ApJL, 416, L49
- [286] Revintsev M., Gilfanov, M., Sunyaev R., Jahoda K., Markwardt C., 2004, A&A, 411, 329
- [287] Richards, G. T., et al. 2002, AJ, 123, 2945
- [288] Richards, G. T., et al. 2005, MNRAS, 360, 839
- [289] Risaliti G., Elvis M., 2004, ASSL Vol. 308: *Supermassive Black Holes in the Distant Universe*, 187
- [290] Romano D., Silva L., Matteucci F., Danese L., 2002, MNRAS, 334, 444

- [291] Rosati P. et al., 2002, ApJ, 566, 667
- [292] Ruszkowski, M., Brüggén, M., & Begelman, M. C., 2004, ApJ, 615, 675
- [293] Salpeter E.E., 1955, ApJ, 121, 61
- [294] Salucci P., Szuszkiewicz E., Monaco P., Danese L., 1999, MNRAS, 307, 637
- [295] Salucci, P., & Persic, M. 1999, MNRAS, 309, 923
- [296] Saunders W., Rowan-Robinson M., Lawrence A., Efstathiou G., Kaiser N., Ellis R.S., Frenk C.S., 1990, MNRAS, 242, 318S
- [297] Sazonov S.Yu., Ostriker J.P., Ciotti L., Sunyaev R.A., 2005, MNRAS, 358, 168
- [298] Sazonov S.Yu., Ostriker J.P., Sunyaev R.A., 2004b, MNRAS, 347, 144
- [299] Scalo, J. M. 1986, IAU Symp. 116: Luminous Stars and Associations in Galaxies, 116, 451
- [300] Scalo J., 1998, in Gilmore G., Howell D., eds., *The Stellar Initial Mass Function*, ASP Conf. Ser., Vol. 142, Astron. Soc. Pac., San Francisco, p.201
- [301] Schneider, D. P., et al. 2005, AJ, 130, 367
- [302] Schmidt M., 1959, ApJ, 129, 243
- [303] Schmitt, H.R., Kinney, A.L., Calzetti, D., Storchi-Bergmann, T., 1997, AJ, 114, 592
- [304] Scodeggio, M. 2001, AJ, 121, 2413
- [305] Scott, S. E., Fox, M. J., Dunlop, J. S., Serjeant, S., et al., 2002, MNRAS, 331, 817
- [306] Shaller G., Schaerer D., Meynet G., Maeder A., 1992, A&AS, 96, 269
- [307] Shang, Z., et al. 2005, ApJ, 619, 41
- [308] Shankar F., Salucci P., Granato G.L., De Zotti G., Danese L., 2004, MNRAS, 354, 1020
- [309] Schaye, J. 2004, ApJ, 609, 667
- [310] Silk J., Rees M.J., 1998, A&A, 331, 1
- [311] Silk, J. 2003, MNRAS, 343, 249
- [312] Silva, L., Granato, G.L., Bressan, A., Danese, L., 1998, ApJ, 509, 103
- [313] Silva, L., De Zotti, G., Granato, G. L., Maiolino, R., & Danese, L. 2005, MNRAS, 357, 1295
- [314] Simpson, C. 2005, MNRAS, 360, 565
- [315] Smail, I., Ivison, R., Blain, A., 1997, ApJ, 490, L5
- [316] Smail, I., Ivison, R., Blain, A., Kneib, J.-P., 2002, MNRAS, 331, 495

- [317] Smith, G.P., Smail, I., Kneib, J.P., et al., 2001
- [318] Somerville, R., & Primack, J.R., 1999, MNRAS, 310, 1087
- [319] Somerville, R. S., & Kolatt, T. S. 1999, MNRAS, 305, 1
- [320] Somerville, R. S., Primack, J. R., & Faber, S. M. 2001, MNRAS, 320, 504
- [321] Songaila A., 2004, AJ, 127, 2598
- [322] Spergel, D. N., et al. 2003, ApJS, 148, 175
- [323] Springel V., Yoshida, Y., White, S.D.M., 2001, New Astron., 6, 79
- [324] Springel, V., & Hernquist, L. 2003, MNRAS, 339, 289
- [325] Springel V., Di Matteo T., Hernquist L., 2005, MNRAS, 361, 776
- [326] Springel, V., et al. 2005, Nat., 435, 629
- [327] Srianand R., Petitjean P., 2000, A&A, 357, 414
- [328] Strickland, D. 2002, ASP Conf. Ser. 253: *Chemical Enrichment of Intracluster and Intergalactic Medium*, 253, 387
- [329] Strickland, D. K. 2004, IAU Symposium, 222, 249
- [330] Sutherland R. & Dopita M., 1993, ApJS, 88, 253
- [331] Szokoly, G.P., Subbarao, M.U., Connolly, A.J., Mobasher, B., 1998, ApJ, 492, 452
- [332] Szokoly, G. P., et al. 2004, ApJS, 155, 271
- [333] Taffoni G., Mayer L., Colpi M., Governato F., 2003, MNRAS, 341, 434
- [334] Taffoni G., Monaco P., Theuns T., 2002, MNRAS, 333, 623
- [335] Terlevich, A. I., Caldwell, N., & Bower, R. G. 2001, MNRAS, 326, 1547
- [336] Thomas D., 1999, MNRAS, 306, 655
- [337] Thomas D., Maraston C. & Bender R., 2002, A&ASS, 281,371
- [338] Tinsley B.M., 1980, Fundam. Cosmic Phys., 5, 287
- [339] Tormen G., 1997, MNRAS, 290, 411
- [340] Tozzi et al., 2001, ApJ, 562, 42
- [341] Trager S.C., Faber S.M., Worthley G., Gonzalez J.J., 2000a, AJ, 119, 1645
- [342] Trager S.C., Faber S.M., Worthley G., Gonzalez J.J., 2000b, AJ, 120, 165
- [343] Trentham, N., Sampson, L., & Banerji, M. 2005, MNRAS, 357, 783
- [344] Tully, R. B., & Fisher, J. R. 1977, A&A, 54, 661
- [345] Vanzella, E., et al. 2004, A&A, 423, 761
- [346] Vanzella, E., et al., 2005, A&A submitted

- [347] Vanzella, E., et al., 2006, in preparation
- [348] Vassiliadis E., Woods P.R., 1993 ApJ, 413, 641
- [349] Vecchi A., Molendi S., Guainazzi M., Fiore F., Parmar A.N., 1999, A&A, 349, 73
- [350] Verde, L., et al. 2002, MNRAS, 335, 432
- [351] Viel, M., Weller, J., & Haehnelt, M. G. 2004, MNRAS, 355, L23
- [352] Vignali C., Brandt W.N., Schneider D.P., 2003, ApJ, 125, 433
- [353] Volonteri, M., Haardt, F., & Madau, P. 2003, ApJ, 582, 559
- [354] Ueda Y., Akiyama M., Ohta K., Miyaji T., 2003, ApJ, 598, 886
- [355] Umemura M., 2001, ApJ, 560, L29
- [356] Urry C.M. & Padovani P., 1995, PASP, 107, 803
- [357] Yu Q., Tremaine S., 2002, MNRAS, 335, 965
- [358] Waddington, I., Windhorst, R.A., Cohen, S.H., Partridge, R.B., Spinrad, H., Stern, D., 1999, ApJ, 526, L77
- [359] Wang B., Heckman T., 1996, ApJ, 477, 8
- [360] Warren, M. S., Quinn, P. J., Salmon, J. K., & Zurek, W. H. 1992, ApJ, 399, 405
- [361] Weaver R., McCray R., Castor J., Shapiro P., Moore R., 1977, ApJ, 218, 377
- [362] Webb, T., Eales, S., Lilly, S., Clements, D., Dunne, L., Gear, W., Flores, H., Yun, M., 2003, ApJ, 587, 41
- [363] White, S. D. M., & Rees, M. J. 1978, MNRAS, 183, 341
- [364] White, S. D. M., & Frenk, C. S. 1991, ApJ, 379, 52
- [365] White, S. D. M. 1996, Cosmology and Large Scale Structure, 349
- [366] Williams, R. E., et al. 1996, AJ, 112, 1335
- [367] Wirth, G. D., et al., 2004, AJ, 127, 3121
- [368] Wolf, C., Wisotzki, L., Borch, A., Dye, S., Kleinheinrich, M., Meisenheimer, K., 2003, A&A, 408, 499
- [369] Wosley M.A., Fabian A.C., Barcons X., Mateos S., Hasinger G., Brunner H., 2004, MNRAS, in press
- [370] Wu, K. K. S., Fabian, A. C., & Nulsen, P. E. J. 2000, MNRAS, 318, 889
- [371] Zamorani G., et al. 1981, ApJ, 245, 357
- [372] Zamorani G., Mignoli M., Hasinger G., 1999, A&A, 346, 731
- [373] Zanni, C., Murante, G., Bodo, G., Massaglia, S., Rossi, P., & Ferrari, A. 2005, A&A, 429, 399
- [374] Zehavi, I., et al. 2005, ApJ, 630, 1

- [375] Zel'dovich Y. B., Shandarin S. F., *Rev. Mod. Phys.*, Vol 61, No. 2, April 1989
- [376] Zhao, D. H., Mo, H. J., Jing, Y. P., Börner, G. 2003, *MNRAS*, 339, 12
- [377] Zwaan, M. A., Meyer, M. J., Staveley-Smith, L., & Webster, R. L. 2005, *MNRAS*, 359, L30